Repair of Reinforced Concrete Bridge Columns via Plastic Hinge Relocation

Volume 1: Repair Using Conventional Materials

Photo of Plastic Hinge Relocation Test #6 taken by Zachary Krish, September 2017

Prepared By:
Zachary F. Krish, Ph.D.
Mervyn J. Kowalsky, Professor, Ph.D.
James M. Nau, Professor, Ph.D.
Rudolf Seracino, Professor, Ph.D.

Prepared For:
Alaska Department of Transportation & Public Facilities
Research, Development, and Technology Transfer
P.O. Box 112500
3132 Channel Drive
Juneau, Alaska 99811-2500

and

Federal Highway Administration
P.O. Box 21648
709 West 9th Street
Juneau, Alaska 99802-1648

REPORT DOCUMENTATION PAGE

Form approved OMB No.

1. AGENCY USE ONLY (LEAVE BLANK)	2. REPORT DATE	3. REPORT TYPE AND DATES COVERED
4000(142)	September 30, 2018	Final Report, May 2015 through September 2018

4. TITLE AND SUBTITLE

Repair of Reinforced Concrete Bridge Columns via Plastic Hinge Relocation
Volume 1: Repair Using Conventional Materials

5. FUNDING NUMBERS
Federal #: 4000(142)
IRIS #: Z839740000

6. AUTHOR(S)
Zachary F. Krish, Ph.D.
Mervyn J. Kowalsky, Professor, Ph.D.
James M. Nau, Professor, Ph.D.
Rudolf Seracino, Professor, Ph.D.

7. PERFORMING ORGANIZATION NAME(S) AND ADDRESS(ES)
Alaska Department of Transportation and Public Facilities
Research, Development & Technology Transfer
3132 Channel Drive
Juneau, Alaska 99811-2500

8. PERFORMING ORGANIZATION REPORT NUMBER
4000(142)

9. SPONSORING/MONITORING AGENCY NAME(S) AND ADDRESS(ES)

State of Alaska, Alaska Dept. of Transportation and Public Facilities
Research and Technology Transfer
3132 Channel Drive
Juneau, AK 99801-7898

10. SPONSORING/MONITORING AGENCY REPORT NUMBER
4000(142)

11. SUPPLEMENTARY NOTES

12a. DISTRIBUTION / AVAILABILITY STATEMENT
Copies available online at http://www.dot.alaska.gov/stwddes/research/search_lib.shtml

12b. DISTRIBUTION CODE

13. ABSTRACT (Maximum 200 words)
Presented in this report is research aimed at challenging the assumption that severely damaged reinforced concrete bridge columns are not easily repaired. An experimental program was conducted in which six large scale bridge columns exhibiting buckled and fractured reinforcement were repaired using plastic hinge relocation and conventional materials. Discussion of several repair methods is presented along with the introduction of a simplified analytical approach by which the repair can be designed, and repaired member performance obtained. In addition, a rational approach to assessing the limits of residual drift in a damaged system is presented, considering the availability of such a repair.

14- KEYWORDS :
Reinforced concrete bridges, Repairing, Earthquake resistant design, Plastic hinge relocation, Buckled reinforcement, Fractured reinforcement

15. NUMBER OF PAGES
312

16. PRICE CODE
N/A

17. SECURITY CLASSIFICATION OF REPORT	18. SECURITY CLASSIFICATION OF THIS PAGE	19. SECURITY CLASSIFICATION OF ABSTRACT	20. LIMITATION OF ABSTRACT
Unclassified	Unclassified	Unclassified	None

SI* (MODERN METRIC) CONVERSION FACTORS

APPROXIMATE CONVERSIONS TO SI UNITS

Symbol	When You Know	Multiply By	To Find	Symbol
		LENGTH		
in	inches	25.4	millimeters	mm
ft	feet	0.305	meters	m
yd	yards	0.914	meters	m
mi	miles	1.61	kilometers	km
		AREA		
in^2	square inches	645.2	square millimeters	mm^2
ft^2	square feet	0.093	square meters	m^2
yd^2	square yard	0.836	square meters	m^2
ac	acres	0.405	hectares	ha
mi^2	square miles	2.59	square kilometers	km2
		VOLUME		
fl oz	fluid ounces	29.57	milliliters	mL
gal	gallons	3.785	liters	L
ft^3	cubic feet	0.028	cubic meters	m^3
yd^3	cubic yards	0.765	cubic meters	m^3
	NOTE: volumes greater than 1000 L shall be shown in m^3			
		MASS		
oz	ounces	28.35	grams	g
lb	pounds	0.454	kilograms	kg
T	short tons (2000 lb)	0.907	megagrams (or "metric ton")	Mg (or "t")
		TEMPERATURE (exact degrees)		
°F	Fahrenheit	5 (F-32)/9 or (F-32)/1.8	Celsius	°C
		ILLUMINATION		
fc	foot-candles	10.76	lux	lx
fl	foot-Lamberts	3.426	$candela/m^2$	cd/m^2
		FORCE and PRESSURE or STRESS		
lbf	poundforce	4.45	newtons	N
lbf/in^2	poundforce per square inch	6.89	kilopascals	kPa

APPROXIMATE CONVERSIONS FROM SI UNITS

Symbol	When You Know	Multiply By	To Find	Symbol
		LENGTH		
mm	millimeters	0.039	inches	in
m	meters	3.28	feet	ft
m	meters	1.09	yards	yd
km	kilometers	0.621	miles	mi
		AREA		
mm^2	square millimeters	0.0016	square inches	in2
m^2	square meters	10.764	square feet	ft^2
m^2	square meters	1.195	square yards	yd^2
ha	hectares	2.47	acres	ac
km^2	square kilometers	0.386	square miles	mi^2
		VOLUME		
mL	milliliters	0.034	fluid ounces	fl oz
L	liters	0.264	gallons	gal
m^3	cubic meters	35.314	cubic feet	ft^3 m^3
	cubic meters	1.307	cubic yards	yd^3
		MASS		
g	grams	0.035	ounces	oz
kg	kilograms	2.202	pounds	lb
Mg (or "t")	megagrams (or "metric ton")	1.103	short tons (2000 lb)	T
		TEMPERATURE (exact degrees)		
°C	Celsius	1.8C+32	Fahrenheit	°F
		ILLUMINATION		
lx	lux	0.0929	foot-candles	fc
cd/m^2	$candela/m^2$	0.2919	foot-Lamberts	fl
		FORCE and PRESSURE or STRESS		
N	newtons	0.225	poundforce	lbf
kPa	kilopascals	0.145	poundforce per square inch	lbf/in^2

*SI is the symbol for the International System of Units. Appropriate rounding should be made to comply with Section 4 of ASTM E380. (Revised March 2003)

TABLE OF CONTENTS

LIST OF TABLES

LIST OF FIGURES

LIST OF SYMBOLS AND TERMINOLOGY

$A_{g,c}$	Gross cross sectional area of original column
$A_{g,r}$	Gross cross sectional area of repair annulus
$A_{h,r}$	Area of transverse steel reinforcement in repair (taken as t_j if steel sleeve is used)
$A_{s,r}$	Total area of longitudinal steel in repair annulus
$c_{o,r}$	Cover to centroid of transverse steel in repair annulus
$d_{bl,c}$	Diameter of longitudinal repair bar
$d_{bl,r}$	Diameter of longitudinal bar in original column
D_c	Outer diameter of original column
D_r	Outer diameter of repair annulus
E_{conc}	Elastic modulus of repair concrete
E_{grout}	Elastic modulus of repair grout
$E_{s,c}$	Modulus of longitudinal steel in original column
$E_{sh,c}$	Modulus of transverse steel in original column (~29,000ksi, 400MPa)
$E_{s,r}$	Modulus of longitudinal steel in repair (~29,000ksi, 400MPa)
$E_{sh,r}$	Modulus of transverse steel in repair (~29,000ksi, 400MPa)
$f'_{c,c}$	Nominal unconfined concrete strength in original column
$f'_{c,r}$	Nominal unconfined concrete strength in repair
$f'_{cc,c}$	Nominal confined concrete strength in original column
$f'_{ce,c}$	Expected unconfined concrete strength in original column
$f'_{co,c}$	Overstrength concrete strength in original column (~1.7f'$_{c,c}$)
$f'_{ce,c}$	Expected concrete strength in original column (~1.3f'$_{c,c}$)
$f_{u,c}$	Nominal ultimate stress of column longitudinal bars
$f_{y,c}$	Nominal yield stress of column longitudinal bars
$f_{y,r}$	Nominal yield stress of repair longitudinal bars
$f_{ye,c}$	Expected yield stress of longitudinal steel in original column
$f_{yhe,c}$	Expected yield stress of transverse steel in original column
$f_{yh,r}$	Nominal yield stress of transverse steel in repair
$f_{yo,c}$	Overstrength yield stress of longitudinal steel in original column
$I_{g,r}$	Gross moment of inertia of repair annulus

L_c Overall clear length of original column

L_{eff} Effective length of column above repair

L_{pt} Rectangular tension based plastic hinge length

L_{prt} Triangular tension based plastic hinge length

L_r Length of repair

$L_{sp,c}$ Strain penetration length of column longitudinal reinforcement

$L_{sp,r}$ Strain penetration length of repair longitudinal reinforcement

$M_{b,r}$ Proportion of total base moment demand distributed to the repair

$M_{ue,c}$ Expected ultimate moment at critical column cross section

$M_{ue,rup}$ Expected ultimate moment at critical column cross section with ruptured longitudinal bars

$M_{uo,c}$ Overstrength ultimate moment at critical column cross section

$M_{uo,rup}$ Overstrength ultimate moment at critical column cross section with ruptured longitudinal bars

$M_{ye,c}$ Expected yield moment at critical column cross section

$M_{ye,rup}$ Expected yield moment at critical column cross section with ruptured longitudinal bars

$M_{y,r}$ Yield moment of repair annulus

P Axial load

s_r Spacing of transverse steel in repair (taken as 1.0 if steel sleeve is used)

V_C Concrete component of shear strength

V_S Steel component of shear strength

$V_{cap,r}$ Shear capacity of repair annulus

V_r Repair shear demand

$\Delta_{e,c}$ Elastic component of displacement due to column flexure above repair

$\Delta_{e,r}$ Elastic component of displacement due to column rotation within the repair

$\Delta_{e,sp}$ Elastic component of displacement due to column strain penetration

$\Delta_{e,rr}$ Elastic component of displacement due to rigid repair rotation

$\Delta_{e,rr,rup}$ Elastic component of displacement due to rigid repair rotation considering column with ruptured longitudinal bars

$\Delta_{p,c}$ Plastic component of displacement due to column flexure above repair

$\Delta_{p,r}$ Plastic component of displacement due to column rotation within the repair

$\Delta_{p,sp}$	Plastic component of displacement due to column strain penetration
$\Delta_{p,rr}$	Plastic component of displacement due to rigid repair rotation
$\Delta_{p,rr,rup}$	Plastic component of displacement due to rigid repair rotation considering column with ruptured longitudinal bars
Δ'_y	Total yield displacement of repaired member
Δ_u	Total ultimate displacement of repaired member
ε_{bb}	Max tension strain prior to longitudinal bar buckling
ε_y	Yield strain of longitudinal steel
$\rho_{l,r}$	Longitudinal steel ratio in repair annulus ($A_{s,r}$ / $A_{g,r}$)
$\rho_{s,c}$	Volumetric ratio of transverse steel in original column
$\rho_{s,r}$	Volumetric ratio of transverse steel in repair
$\phi_{ue,c}$	Expected ultimate curvature of original column cross section
$\phi'_{ye,c}$	Expected yield curvature of original column cross section
ϕ_f	Flexural strength reduction factor
ϕ_s	Shear strength reduction factor

Greek Alphabet

Α	α	Alpha
Β	β	Beta
Γ	γ	Gamma
Δ	δ	Delta
Ε	ε	Epsilon
Ζ	ζ	Zeta
Η	η	Eta
Θ	θ	Theta
Ι	ι	Iota
Κ	κ	Kappa
Λ	λ	Lambda
Μ	μ	Mu
Ν	ν	Nu
Ξ	ξ	Xi
Ο	ο	Omicron
Π	π	Pi
Ρ	ρ	Rho
Σ	σ	Sigma
Τ	τ	Tau
Υ	υ	Upsilon
Φ	ϕ	Phi
Χ	χ	Chi
Ψ	ψ	Psi
Ω	ω	Omega

EXECUTIVE SUMMARY

This report discusses the investigation of a rapid repair strategy for modern, well designed reinforced concrete columns that have been subjected to extreme seismic attacks. Modern seismic design practice for bridge structures involves the implementation of capacity design principles which localize plastic hinges in columns, while protecting against other modes of failure or locations of damage. For large earthquakes, the formation of plastic hinges can lead to buckling and rupture of longitudinal steel, at which point columns are typically demolished and rebuilt since the cost to replace portions of them can be prohibitive. Replacement is deemed necessary since the inelastic strain capacity of reinforcing bars severely diminishes once buckling occurs, rendering the structure vulnerable to collapse in future earthquakes. This often results in significant durations of service interruption following a major event which is generally not acceptable, especially for lifeline critical bridges. A reliable option for repair of these structures, that is both rapid and cost effective, would certainly be an attractive alternative to the present ideology.

This research proposes such a solution, specifically focusing on a repair method known as plastic hinge relocation. Using this methodology, sections of the structure that experience inelastic behavior during the initial event are strengthened and future plastic deformation is relocated to a newly prescribed region. While bridge column repair has been studied for some time with regards to shear and confinement critical columns, there is limited data available on the repair of columns that are otherwise designed to modern standards. However, recent research has demonstrated the feasibility of plastic hinge relocation as a viable repair option for bridge columns exhibiting the levels of damage described above. The intent of this study is to expand on the work done previously and further develop plastic hinge relocation as a fully implementable repair solution.

The study includes an experimental investigation in which a total of six large-scale reinforced concrete cantilever bridge columns are subjected to varying levels of damage, repaired using the plastic hinge relocation technique, and retested. Each column is repaired using conventional materials including steel rebar for longitudinal strengthening, a continuous steel jacket or discrete rebar hoops for transverse strength and confinement, and ready-mix concrete or commercially available grout for backfill. Each column tests results in a clear relocation of the plastic hinge above the installed repair with measured strains on the longitudinal bars inside the repair below yield. Additionally, the repaired specimens achieve an equivalent or greater hysteretic

energy dissipation than the original columns and are capable of reaching equal displacement capacities.

An analytical model and design recommendations are developed based on the experimental results, both of which are discussed at length. The resulting model is based on engineering principles and provides the designer with all necessary information to design and implement this repair. A computational model is also devised to numerically investigate the impact of residual drift on the performance of the repaired system. This assessment consists of a parametric study considering L/D ratio, longitudinal steel ratio, and axial load ratio, in which performance is defined as the probability of reaching specified tension strain limit states for various defined hazard levels. Results of this limited study indicate that current prescriptive residual drift limits are potentially overly conservative and should be expanded to consider the properties and performance of the repaired system.

Chapter 1: Introduction

This report discusses the development of a repair technique for modern, well designed reinforced concrete bridge columns subjected to extreme inelastic loading, such as that encountered during a seismic event. Other loading conditions may also cause such damage, such as vessel or ice impacts, and would be equally applicable to the scope of this report. The repair method specifically addresses columns with significant damage, including buckled or fractured longitudinal reinforcement, crushed core concrete, and/or fractured transverse steel, and aims to provide a timely and economical solution to restore their functionality.

Modern reinforced concrete bridges implement performance based earthquake engineering (PBEE) and capacity design principles (Paulay & Priestley, 1992; Priestley, Seible, & Calvi, 1996), allowing them to sustain much greater deformations prior to collapse than their predecessors. These designs typically rely on inelastic deformation through plastic hinges in columns as the primary means of dissipating seismic forces which, in large earthquakes, can lead to extensive local damage while the rest of the structure remains intact. Current design guides aim to either retrofit existing structures (ACI Committee 341, 2007; FEMA, 1997) to achieve this behavior or repair those that have undergone lesser damage (ACI Committee 546, 2014; U.S. Army Corps of Engineers, 1995); however, repair of columns which are damaged to the extent described above is typically not considered feasible. Without reliable methods of repairing such damage, these structures are likely demolished and reconstructed as the cost to replace portions of the columns can be prohibitive.

Recent research demonstrates the feasibility of a repair technique, called plastic hinge relocation, in which the developed plastic hinge is sufficiently strengthened such that future inelastic action is forced to a prescribed, undamaged location in the column (Lehman, Gookin, Nacamull, & Moehle, 2001; Parks, Brown, Ameli, & Pantelides, 2016; Rutledge, Kowalsky, Seracino, & Nau, 2014). The primary goal of the research presented in this report is to expand on

these previous works and develop the plastic hinge relocation method into a complete and reliable repair technique capable of quickly restoring the functionality of severely damaged bridges. The study described herein includes an experimental portion in which six large-scale bridge columns are subjected to varying levels of damage, repaired using the plastic hinge relocation technique, and then retested. The results of these tests are then used to develop analysis and design techniques, as well as a novel modeling approach to accurately predict the global force-displacement response and local strain behavior of a repaired bridge column. Finally, an assessment of limits to reparability based upon residual deformations is conducted using a probabilistic methodology in which collapse fragility functions are determined for a repaired structure for a given residual displacement and future hazard.

1.1 Traditional Repair Philosophy

Traditional repair of reinforced concrete structures focuses on the restoration of member strength and serviceability as its primary goal and is limited to relatively minor states of damage. Many of the design guides currently available address issues such as deterioration due to corrosion and general strengthening of existing members to meet new code of load bearing requirements, as discussed subsequently. However, there is little or no guidance on members that have undergone extensive plastic deformation as would be the case during a severe earthquake.

The American Concrete Institute (ACI) has published the *Guide to Concrete Repair* (ACI Committee 546, 2014) which pertains to the issues stated above, but addresses seismic vulnerabilities of bridges specifically in a document titled *Seismic Evaluation and Retrofit Techniques for Concrete Bridges* (ACI Committee 341, 2007). The term retrofit is used explicitly in place of repair, as this represents the current philosophy with regards to seismic hazards. Past design methods have left many structures susceptible to collapse during extreme earthquakes as was recognized during the 1971 San Fernando, 1989 Loma Prieta, and 1994 Northridge earthquakes just to name a few (ACI Committee 341, 2007). As a result, the initial strategy to address this vulnerability has been to retrofit existing structures to mitigate any damage that might occur. Other similar documents arose in the aftermath of these events, such as the Applied Technology Council's (ATC) *Seismic Evaluation and Retrofit of Concrete Buildings* (ATC, 1996) which specifically addresses California structures, and multiple Federal Highway Association (FHWA) documents focusing on bridge retrofits specifically, culminating in the most recent

document: *Seismic Retrofitting Manual for Highway Structures* (FHWA, 2006). Due to the often catastrophic nature of failure of these deficient structures, repair is typically not considered beyond minor instances that could be addressed through ACI 546 and similar documents.

1.2 Modern Reinforced Concrete Design Principles

In addition to the investigation of retrofitting existing structures, a great deal of research has also focused on the development of improved seismic design methodologies for new bridges and buildings. This has led to a better understanding of how structures respond to earthquakes and how to properly detail them to be more resilient. The following sections outline the principles of Performance Based Seismic Engineering (PBSE) and Capacity Design, each of which play critical roles in the reparability of modern designed structures.

1.2.1 Performance Based Seismic Engineering

A major shortcoming in early seismic design was the inability to accurately predict the performance of a structure for a given hazard. Most code-based design methodologies used prescriptive approaches that resulted only in an assurance that the structure would have a sufficiently low probability of collapse given the assumed hazard. However, recent advancements have expanded the understanding of how structures behave under seismic loading and provide the basis of the more modern PBSE approach in which structures are designed to achieve predefined levels of performance at various levels of seismic hazard. An example of performance limit states, as defined in a report issued by the Structural Engineer's Association of California (SEAOC) (2003), is shown in Figure 1.1, where hazard levels range from EQ-1 to EQ-4, with EQ-1 being the lowest energy event. These hazards correspond to various performance levels 1 to 4, where level 1 represents the smallest amount of acceptable damage and level 4 represents life safety performance. As with current codes, different objectives can be assigned to different structures depending on importance or acceptable risk.

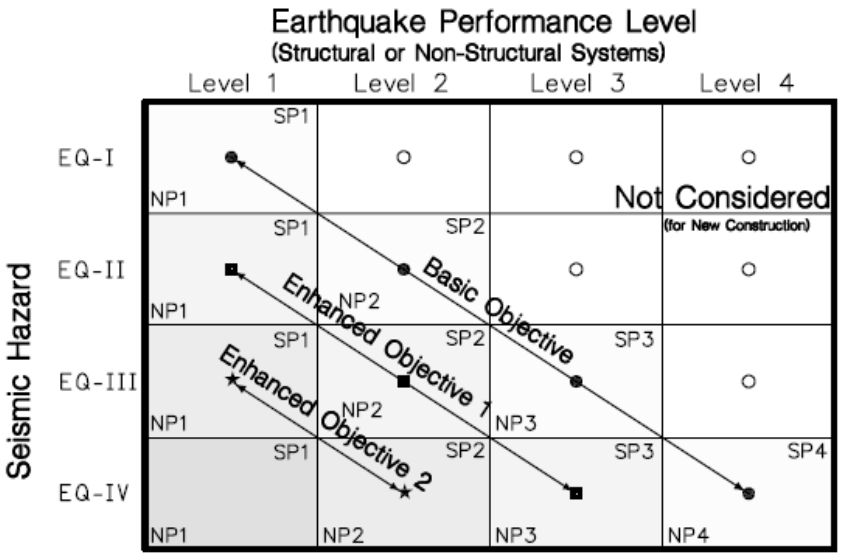

Figure 1.1: Typical Seismic Performance Objectives for Buildings (SEAOC, 2003).

The definition of performance objectives requires a basis for quantifying said performance at a given level of hazard. Specifying acceptable levels of damage can have subjective interpretations depending on which stakeholder that is asked and the design intent of the structure itself. Damage to buildings is often controlled by the state of the contents inside the building envelope following an earthquake, which is most closely related to building drift. Bridges on the other hand do not typically have this concern and are driven by damage accumulation within individual elements, which can be predicted via strains of the constituent materials. A great deal of research has focused on quantifying these strain limits and relating them to specific limit states (Goodnight, Kowalsky, & Nau, 2013). Through precise detailing and an understanding of how these limit states relate to damage and performance, modern structures can be designed to undergo large levels of deformation and accumulate damage while maintaining ductile behavior. Figure 1.2 illustrates how this deformation can be used to define performance levels, and the system can then be designed to reach these levels for different hazards.

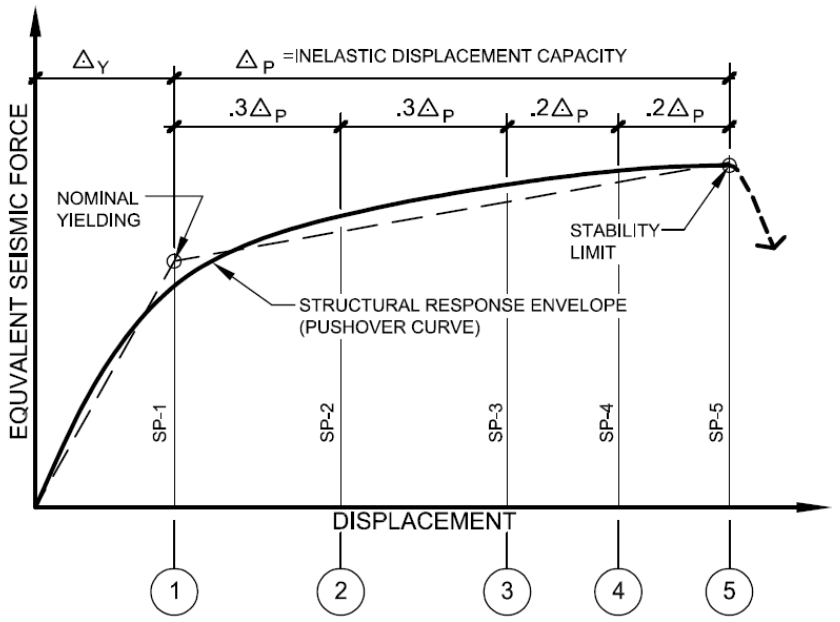

STRUCTURAL PERFORMANCE LEVEL	QUALITATIVE DESCRIPTION	SYSTEM DISPLACEMENT LIMIT	INELASTIC DISPLACEMENT DEMAND RATIO (IDDR)	NON-STRUCTURAL PERFORMANCE LEVEL	NON-STRUCTURAL DAMAGE RATIO
SP-1	OPERATIONAL	Δ_Y	0%	NP-1	0%-10%
SP-2	OCCUPIABLE	$\Delta_Y + .3\Delta_P$	30%	NP-2	5%-30%
SP-3	LIFE SAFE	$\Delta_Y + .6\Delta_P$	60%	NP-3	20%-50%
SP-4	NEAR COLLAPSE	$\Delta_Y + .8\Delta_P$	80%	NP-4	40%-80%
SP-5	COLLAPSED	$\Delta_Y + \Delta_P$	100%	NP-5	> 70%

Figure 1.2: Illustration of structural performance levels seismic response curve for structural systems (SEAOC, 2003).

The importance of PBSE, as it relates to the reparability of bridges, is that structures designed with this methodology behave in a much more controlled manner than those designed using prescriptive, code-based approaches. Whereas the development of severe local limit states such as bar buckling and rupture would likely have indicated catastrophic failure of an older bridge, these failure modes are directly considered and accounted for when using PBSE. Table 1.1 outlines how damage at the local level relates to the typical performance states illustrated in Figure 1.2. However, while bar buckling and rupture limit states are considered, they are only allowed in the most extreme and rare events in which life-safety is the performance objective. As a result, replacement of the structure is deemed acceptable, as noted in Table 1.2. This conclusion, of course, is predicated on the fact that no reliable repair method exists for this level of damage, which is the assertion the research presented in this report aims to challenge.

Table 1.1: Bridge Performance Assessment (Hose, 2001).

Damage Level	Performance Level	Qualitative Performance Description	Quantitative Performance Description
I	Cracking	Onset of hairline cracks	Barely visible residual cracks
II	Yielding	Theoretical first yield of longitudinal reinforcement	Residual crack width ~0.008in
III	Initiation of Local Mechanism	Initiation of inelastic deformation. Onset of concrete spalling. Development of diagonal cracks.	Residual crack width 0.04in – 0.08in Length of spalled region > 1/10 cross-section depth.
IV	Full Development of Local Mechanism	Wide crack widths/spalling over full local mechanism region.	Residual crack width > 0.08in. Diagonal cracks extend over 2/3 cross-section depth. Length of spalled region > ½ cross-section depth.
V	Strength Degradation	Buckling of main reinforcement. Rupture of transverse reinforcement. Crushing of core concrete.	Lateral capacity below 85% of maximum. Measurable dilation > 5% of original member dimension.

Table 1.2: Bridge Performance Classification (Hose, 2001).

Damage Level	Damage Classification	Damage Description	Repair Description	Socio-economic Description
I	None	Barely visible cracking	No Repair	Fully Operational
II	Minor	Minor residual cracking	Possible Repair	Operational
III	Moderate	Open residual cracks Onset of spalling	Minimum Repair	Life Safety
IV	Major	Very wide cracks. Extended concrete spalling	Repair	Near Collapse
V	Local Failure /Collapse	Visible permanent deformation. Buckling/rupture of reinforcement	Replacement	Collapse

1.2.2 Capacity Design Principle

Whereas PBSE provides a global framework in which structural performance is defined, *capacity design* ensures that these structures behave as intended (Paulay & Priestley, 1992; Priestley et al., 1996). Capacity design principles work by predefining a ductile mechanism through which inelastic behavior will occur and preventing other undesirable modes of failure. This concept is often described as analogous to that of a weak link in a chain, as illustrated in Figure 1.3. The ductile 'weak-link' is designed with a yield force equal to F_d and an ultimate overstrength force equal to $F_{d,o}$. With the properties of this link known, all other 'brittle-links' in the system are then designed such that their strength, $F_{i,b}$, is an acceptable margin above the ultimate overstrength of the ductile link. Therefore, any failure within the system is localized to the ductile regions, which are specifically designed to withstand very large plastic deformations thus dissipating energy during an earthquake. In reinforced concrete bridges, these ductile links are often in the form of plastic hinges within the columns, and brittle links represent modes of failure such as joint or column shear failure, or damage to the superstructure or foundation. Any damage associated with brittle modes of failure often results in complete loss of the structure.

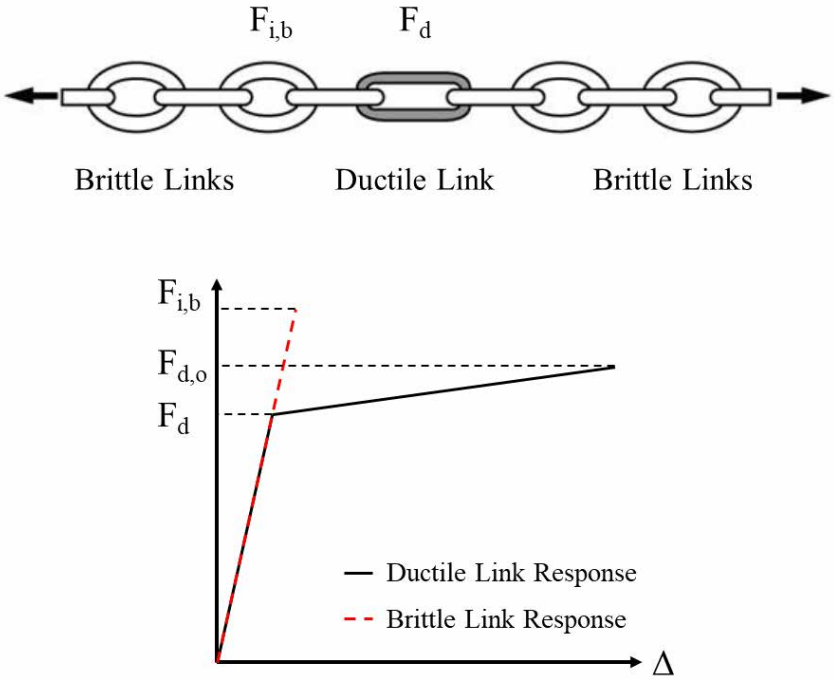

Figure 1.3: Capacity design "weak link" analogy illustration; adapted from (Paulay & Priestley, 1992).

The primary benefit of capacity design, from a repair perspective, is that damage localizes to specific areas and occurs through prescribed modes, thus narrowing the solution space for potential repairs. Knowing the location and mode of failure, combined with an understanding of extent of damage for a given hazard level from PBSE, means that considerations of a repair for a specific structure can be made before any damage occurs.

1.3 Plastic Hinge Relocation in Reinforced Concrete Members

Plastic hinges are typically the preferred mechanism through which RC members deform under earthquakes. Relocation of plastic hinges is essentially exactly how it sounds: the properties of the system are modified such that plastic rotation occurs in a different location within the member. Typically, in fixed moment reaction members the greatest demands are located at the joint interface, whether that is a beam-column joint or column-footing connection. These regions is notoriously difficult to repair, as damage spreads into the joint due to strain penetration from the plastic hinge. A group of researchers noted this and conducted a study to investigate whether columns could be designed such that plastic hinges were located away from the joint region in RC bridge columns (Hose, Priestley, & Seible, 1997). This is illustrated schematically in Figure 1.4 with experimental confirmation in Figure 1.5. The authors demonstrate that relocation of the plastic hinge is possible for new construction by terminating a portion of the longitudinal reinforcement a specified distance from the joint. While not considered as a repair, the research presented by the authors does provide the first known instance of this technique for RC structures.

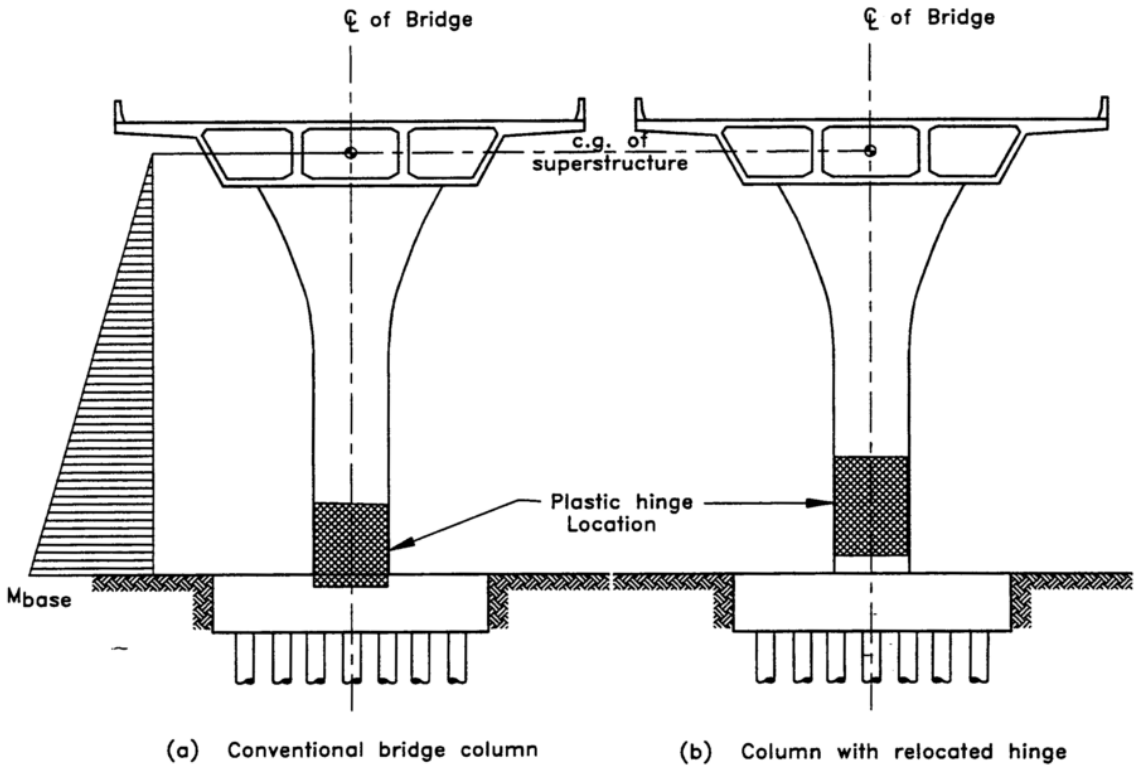

Figure 1.4: Plastic hinge formation in a typical single column bent (Hose et al., 1997).

Figure 1.5: Relocated plastic hinge in RC bridge column by (Hose et al., 1997) at USCD laboratory.

Despite their findings, most columns today are still designed with the plastic hinge occurring at the joint interface. Damage can be quite substantial following a design level earthquake, as illustrated in Figure 1.6, and requires immediate attention to ensure safe use of the structure. Past research demonstrates plastic hinge relocation as a viable repair method of severely

damaged columns (Lehman et al., 2001; Parks et al., 2016; Rutledge et al., 2014), but provides limited guidance for implementation in actual repairs.

(a) **(b)**

Figure 1.6: (a) Plastic hinge with buckled and fractured reinforcing bars; (b) Plastic hinge with buckled bars and fractured spiral.

Plastic hinge relocation has many advantages over other repair options, as the very nature of capacity protected hinge forming members lends itself to this type of repair. During an earthquake, if the structure performs as intended, all damage will localize in the plastic hinge regions leaving the rest of the structure intact. This provides the opportunity to locate a new plastic hinge anywhere in the undamaged member with similar properties to that of the original. This is very beneficial from a capacity protection perspective since the new location of the hinge alters the distribution of forces within the system, but does so predictably. Repairs that aim to restore the integrity of the initial hinge through strengthening may achieve their goal, but at greater uncertainty on the effects of the rest of the system.

Repairing a heavily damaged portion of a structure also brings about uncertainty as to how the repair itself will behave. While models do exist to predict the behavior of the distressed materials within the existing hinge, they are not as precise as would be needed to reliably protect the rest of the structure. To design a repair to directly form a new plastic hinge would be difficult at best. If the repaired region is capacity protected, however, it is possible to conservatively add strength to the repair in response to uncertainties in performance without fear of compromising other capacity protected regions of the structure.

1.4 Study Plan

1.4.1 Research Need

The design of modern reinforced concrete bridges extends beyond the traditional prescriptive, code-based approaches of the past where life safety and collapse avoidance were the only criteria for extreme seismic events. Using PBSE and capacity design principles, today's engineers understand the behavior and can predict the performance of their structures to far greater accuracy than in the past. This results in bridges that develop localized, well controlled damage through ductile plastic hinges and resist undesirable brittle modes of failure. As these advancements have pushed the boundary of design in new structures, it also stands to reason that previously established limits of repair should also be reevaluated.

Recent research indicates that modern structures with considerable damage, including buckling and fracture of longitudinal steel, fracture of transverse spirals, and crushed core concrete, are increasingly reparable, as will be discussed in greater detail in the following chapter. A method known as plastic hinge relocation has shown particularly promising results for rapid repair of RC bridge columns with buckled and fractured rebar; however, a need exists to build and expand upon these results to develop a reliable design procedure for practicing engineers. While the repair of damaged structures becomes an immediate issue in the aftermath of a major earthquake, it is unfortunately too late at that point to develop a strategy for repair. This is especially true for lifeline critical bridges that service essential facilities and must be operational as quickly as possible.

1.4.2 Research Scope and Objectives

To address the needs defined in the section above, the following research objectives are defined:

1. Conduct a series of experimental tests in which modern, well-designed RC columns are subjected to various levels of damage, repaired using the plastic hinge relocation method, and subsequently retested.
2. Develop analytical and computational models, validated by the results of the experimental tests, to accurately describe the observed behavior of the repaired structure.

3. Conduct a numerical study using the computational model devised in item 2 to investigate the global performance of a repaired column in a bridge structure, specifically as it relates to residual displacements from the initial event.
4. Establish clear criteria to determine when a plastic hinge relocation repair is truly needed, and the extents to which such a repair is feasible. These limits should consider both local damage states and global residual deformations of the structure.
5. Develop design guidelines for the repair of RC bridge column-to-footing connections and present in a manner which can be quickly and effectively implemented in the aftermath of a major event.

1.5 Document Layout

The focus of the research presented in this Volume is on the development of the plastic hinge relocation repair method using conventional materials (i.e. concrete, grout, rebar, and steel), whereas Volume II contains information relevant to the development and implementation of this repair technique using CFRP materials. Finally, Volume III contains a design guide that is meant to act as a standalone document containing all necessary information by which a plastic hinge relocation repair can be designed and installed. The remainder of this Volume is divided into individual chapters 2-8, the contents of which are summarized as follows:

Chapter 2: Literature Review – This chapter summarizes the current state of research as it is relevant to the topic of the repair discussed in this report.

Chapter 3: Experimental Methods – This chapter discusses all relevant details regarding the setup and execution of the experimental study that was conducted. This includes details of the original column specimens and of each repair, as well as discussion regarding the materials and typical construction sequence of each specimen. Additionally, this section provides information on the instrumentation and loading procedure of each test.

Chapter 4: Experimental Observations – This chapter reports the outcomes of each of the six experimental repair tests. Each repair is discussed individually with each section providing a detailed description of what was specifically investigated during each test as well as presentation and discussion of the observed results.

Chapter 5: Analytical Model – This chapter discusses the development and implementation of an analytical model which is used to describe the behavior observed in the experimental portion of the research. The intent of this model is to provide the basis for design procedures using a displacement based approach.

Chapter 6: Computational Model – This chapter will discuss the development of a numerical model which is based on the principles discussed in Chapter 5. This model will aim to directly represent the physical results of the experimental tests, thus confirming the assumed mechanisms acting in the repair and to provide a validated tool for use in future analytical studies, such as that in Chapter 7 of this report.

Chapter 7: Impact of Residual Drift on Repaired System Performance – This chapter investigates the impact of residual drift on the overall repaired structure's performance through a probabilistic fragility analysis. The intended outcome of this work is to define residual drift limits which are based on rational analysis as opposed to engineering judgement alone.

Chapter 8: Conclusions and Future Work – This chapter summarizes the work discussed throughout the report and provides conclusions and recommendations based on the observed results. Additional discussion is provided on application of this work to other connection types beyond the column-to-footing connection considered in this research as well as potential topics for future research in this field.

Chapter 2: Literature Review

A great deal of research has been completed in the past regarding repair of reinforced concrete bridge columns with regards to shear and confinement critical members; however, the available literature on repair of modern well-designed columns is limited. This literature review outlines some of what has been done to repair and retrofit older structures, as it applies to the problem at hand, but will focus primarily on the recent research that has been done with regards to modern structures, specifically addressing plastic hinge relocation as a repair technique.

2.1 Traditional Reinforced Concrete Column Repair

The following publications outline the general philosophy of the current state of reinforced concrete repair. The review of these documents represents only a small portion of the available literature on this topic and is not meant to summarize the total extent of current knowledge; however, additional information and sources can be found within the publications themselves if desired.

(ACI Committee 546, 2014) – ACI 546R-14: Guide to Concrete Repair

The Guide to Concrete Repair is published as a general use document that provides design engineers with recommendations for the selection and application of materials and methods for repairing, protecting, and strengthening concrete structures. The latest revision of this guide was published in 2014 and includes extensive revisions over the previous version from 2004. Although the purpose of the document is to provide a wide range of repair options, the scope is limited primarily to serviceability level repairs such as crack repair and surface patching. Structural repair and strengthening are addressed; however, these topics are discussed primarily from a design deficiency point of view as opposed to repair due to extensive damage due to plastic deformation and no mention is made of repairs specific to seismic applications. This describes the general scope of most other code based repair guides as well.

Special considerations for RC columns are discussed specifically in Section 7.7 of the guide, however these provisions relate primarily to the restoration of vertical load carrying capacity and not to seismic applications. Information regarding the use of jackets and collars applied to RC columns is also provided in Section 7.5. The guide defines jacketing as a process where a section of an existing structural member is increased in size by encasement in concrete and collars as jackets that surround only a portion of the column and are typically used to provide increased support for a floor slab. Although the intent and details of these repairs are not compatible with the ultimate goal of plastic hinge relocation in this research, the general form of the repair is very similar. The guide provides recommendations for backfill materials which include conventional concrete and grout which are used in this research, as well jacket materials including temporary cardboard forms and corrugated steel. Installation of epoxy bonded anchors for repair applications is also discussed, which relates directly to the repair employed within this research.

(U.S. Army Corps of Engineers, 1995) – Evaluation and Repair of Concrete Structures

This report, issued in June 1995, provides much of the same information that is found in the ACI 546 document, however it also includes information on the evaluation of damaged structures. Chapter 3 of the document discusses the potential causes of distress and deterioration of concrete by identifying 1) the mechanism through which damage is propagated, 2) symptoms of distress, and 3) prevention methods. Seismic loading is specifically addressed as an "accidental loading" as it may be characterized as a short-duration, one-time event and symptoms are typically evaluated by visual inspection (i.e. spalling or cracking of concrete). The document states that "Accidental loadings by their very nature cannot be prevented", however damage can be mitigated through proper design procedures. Table 4-1 defines the recommended repair approach for earthquake loading as "partial replacement" which is outlined in Table 4-2 as typical replacement of spalled concrete and jacketing to restore confinement and section loss. These repairs are again limited to serviceability levels of damage, and would not be applicable to the extreme cases which are of interest in this research. They do, however, represent the current state of member repair for extreme seismic events.

(ACI Committee 341, 2007) – ACI 341.3R-07: Seismic Evaluation and Retrofit Techniques for Concrete Bridges

As the title alludes, this document provides guidance on evaluation and retrofit of existing structures, but does not address repair of damaged structures. It is important to include this within the existing literature with regards to seismic repair, however, as retrofit has been the primary strategy for reducing seismic hazard. Beginning in 1971 with the San Fernando Earthquake, it has become evident that structural designs up until that time were deficient when dealing with large magnitude earthquakes. Most structures that failed in these events did so catastrophically thorough mechanisms such as joint and member shear failure, unseating of superstructure elements, lap splice failure or loss of confinement just to name a few. In light of these realizations, an emphasis was first put on recognizing these deficiencies and then finding appropriate solutions to address them, with repair being secondary.

The ACI 341.3 document is organized to do just this as it provides recommendations for evaluating and prioritizing existing structures for retrofit programs. Evaluation is based on both the seismic demand that the structure is likely to be subjected to as well as the capacity of the structure as it currently stands. While the retrofit measures that are described are not directly intended to be used as repairs, many of the concepts carry over. The discussion of column retrofit measures focuses much on confinement and jacketing wraps as a means of increasing the ductility of the member. Many of these principles are directly related to the restoration of confinement that is a necessary component of the repair proposed in this research. Plastic hinge relocation is also alluded to, not as a column retrofit, but instead as a means of reducing demands on a deficient cap beam by constructing a link beam that would force the hinge to form away from the cap beam. Although the development of plastic hinge relocation as a repair technique for extensively damaged members is a relatively modern concept, the principle should be generally familiar to engineers.

2.2 Repair of Modern RC Columns

(He, Yang, & Sneed, 2015) – Seismic Repair of Reinforced Concrete Bridge Columns: Review of Research Findings

This paper provides a review of the available literature at the time for repair of severely damaged RC bridge columns as well as the quantification of this damage. Much of the work

presented by the authors establishes the basis for this literature review. The research discussed is divided into two major categories: 1) Repair of RC bridge columns *without* fractured longitudinal bars, and 2) Repair of RC bridge columns *with* fractured longitudinal bars.

Of the research that discusses repair of columns without fractured longitudinal bars, most repairs focus on restoration of core confinement via some sort of jacketing system. Studies including steel, CFRP, GFRP, reinforced concrete and shape-memory alloy jackets are all described. In general, each of the repairs involved patching or somehow restoring the lost cross section prior to installation of the jacket. Some included additional measures such as high pressure epoxy injection, externally applied pre-stressing or cutting and replacing sections of buckled rebars with mechanical splices. A total of 15 studies are summarized in Table 1 of the report, where all of the tests either restored or enhanced the strength and displacement ductility capacity of the columns, however stiffness was less consistent. For the columns that failed through flexural failure in the plastic hinge, stiffness was almost always reduced in the repaired specimens.

Fewer tests have been conducted on columns with fractured longitudinal steel, with a total of only 6 studies summarized in Table 2 of the paper. The majority of the repairs were much more involved than those without fractured bars, and the results were not nearly as consistent. Most of the repairs aimed to restore the flexural capacity at the existing hinge location by mechanically coupling the fractured bars or welding a bridge material. Two of the referenced studies did utilize plastic hinge relocation (Lehman et al., 2001; Rutledge et al., 2014), and will be elaborated on in later sections. The author concludes that the overall time and effort to repair columns with fractured longitudinal steel is far greater than to repair those without and that many of these repairs are not suitable for rapid repair. One of the goals of the research found in this report is to challenge this conclusion and provide a truly rapid repair for all repairable levels of damage. Of the papers referenced within this review paper, only a select few which most closely relate to this research will be expanded on in the following sections. For additional information on any of the repairs mentioned, the reader is directed to the paper directly.

(Vosooghi & Saiidi, 2012) – Design Guidelines for Rapid Repair of Earthquake-Damaged Circular RC Bridge Columns using CFRP

The primary focus of this paper is to develop a design guide for rapid repair of reinforced concrete bridge columns using CFRP materials. It is assumed that the columns in question are

designed using modern principles and have not been damaged beyond slight buckling of the longitudinal steel. Part of the study aimed to quantify the contributions of each of the existing materials in the design of the repaired member. This included the determination of the shear strength provided by the concrete, spirals, and CFRP wrap and the confinement pressure provided by the spirals and CFRP wrap. These values are of great interest assuming that the repaired section will be required to undergo significant deformations in a future earthquake, however the repair method discussed in this paper will capacity protect the repaired region and force future deformations to occur in a previously undamaged section of the column. Thus confinement is not as critical and shear strength can be provided by the repair alone.

In addition to establishing a model for calculating the shear and confinement of the repaired column, the authors also present a simple trilinear constitutive model for the response of previously strained longitudinal steel as shown in Figure 2.1. This model will be beneficial in determining the contribution of the existing buckled and yielded steel in the damaged cross section to the response of the repaired section.

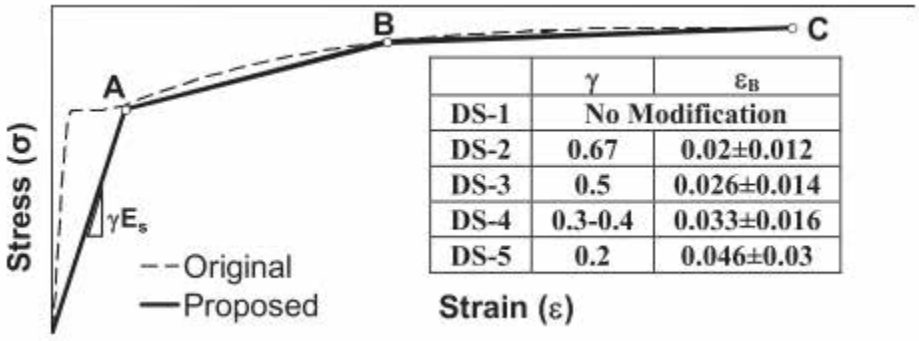

	γ	ε_B
DS-1	No Modification	
DS-2	0.67	0.02±0.012
DS-3	0.5	0.026±0.014
DS-4	0.3-0.4	0.033±0.016
DS-5	0.2	0.046±0.03

Figure 2.1: Original and modified stress-strain relationship for steel material (Vosooghi & Saiidi, 2013).

(Lehman et al., 2001) – Repair of Earthquake-Damaged Bridge Columns

The authors of this paper conducted experimental tests on four reinforced concrete bridge columns that were previously damaged. Only feasibility of the repairs was investigated with no particular concern given to rapid repair solutions. Three of the columns exhibited severe damage, including buckled and fractured longitudinal reinforcement while the fourth had only moderate levels of damage with no crushing of the core concrete and only yielding of the extreme fiber bars. For the purposes of this research, only the columns exhibiting severe damage will be discussed.

The first column that was repaired (labeled 407S in the report) exhibited spalled cover and crushed core concrete as well as fracture of 5 of the 11 longitudinal bars with the remaining bars

buckled. The transverse spiral was fractured in several locations within the hinge region as well. The column was repaired by severing the column just above and below the damaged regions and then mechanically splicing the longitudinal bars. New spiral reinforcement was placed around the new longitudinal bars and new concrete cast within the severed region. The repaired column performed very well reaching a displacement ductility level of seven, however the effort was quite extensive and would not be well suited for a rapid solution. Regardless, the concept of repairing a severely damaged column that is well beyond traditional definitions of "repairable" was proven.

A second column (labeled 430S in the report) was repaired using a reinforced concrete jacket with the intent of the new plastic hinge forming at the same location as the previous one. During initial testing, the column sustained cracking throughout the height, spalled cover and crushed core concrete and 44 buckled longitudinal bars, but none fractured. The design of the RC jacket provided equal flexural strength as the original design of the column. Since the contribution of the existing buckled bars was not known, they were all severed at the base so as to not contribute to the forces developed by the new hinge. This repair also behaved as intended with the flexural deformation occurring primarily at the base of the column and the response comparing closely to that of the original. While this repair successfully restored the serviceability of the specimen, it the effort expended by cutting and replacing the entirety of the steel in the original cross section would be too great for a rapid repair solution.

The third and final repair (labeled 415S in the report) uses plastic hinge relocation as the main design principle. This is the repair that most closely aligns with the design proposed in this research, and will be expanded on in the following section.

2.3 Plastic Hinge Relocation

2.3.1 Applications in Bridge Columns

In RC columns, plastic hinges are typically located near connections with adjacent members such as cap beams and footings. In a study conducted by (Hose et al., 1997), the plastic hinge was successfully relocated away from the adjacent members and further into the column. The goal of this research was not to repair damaged columns, but to design new columns to prevent the spread of plasticity into the joint regions where repairs can be especially difficult. Although the plastic hinge is not relocated as the result of a repair, the precedent was set that it is possible

given that the joint and column base are designed such that they are capacity protected thus forcing the inelastic action to the newly desired location.

Plastic hinge relocation as the result of a repair technique has also been successfully implemented previously, although the available information is limited. As mentioned in the previous section, one such experimental program was completed at the University of Washington (Lehman et al., 2001) and consisted of three columns that were severely damaged and one additional column that was moderately damaged. The study looked at several different repair techniques including plastic hinge relocation. This repair was implemented on one of the more severely damaged specimens where all 22 of the longitudinal bars were buckled and nine were ruptured during initial loading. Four of the transverse spirals were ruptured as well. An RC jacket was designed for the repair which utilized double headed steel bars grouted into the footing and secured along the length of the repair inside of the RC jacket in order to increase the flexural capacity of the base. A steel spiral was added around the perimeter of the new longitudinal steel to act as supplemental confinement and also to facilitate the transfer of the forces into the new reinforcement. Additionally, the flexural strength of the new hinge region was reduced by cutting six of the original 22 longitudinal bars such that the shear demand did not surpass the original design level. A depiction of the resulting design is illustrated in Figure 2.2 below. The results of the repair indicate that the hinge was successfully relocated with the column regaining its initial stiffness and a strength, but the displacement capacity was reduced which the authors attribute to the shorter effective length of the repaired column.

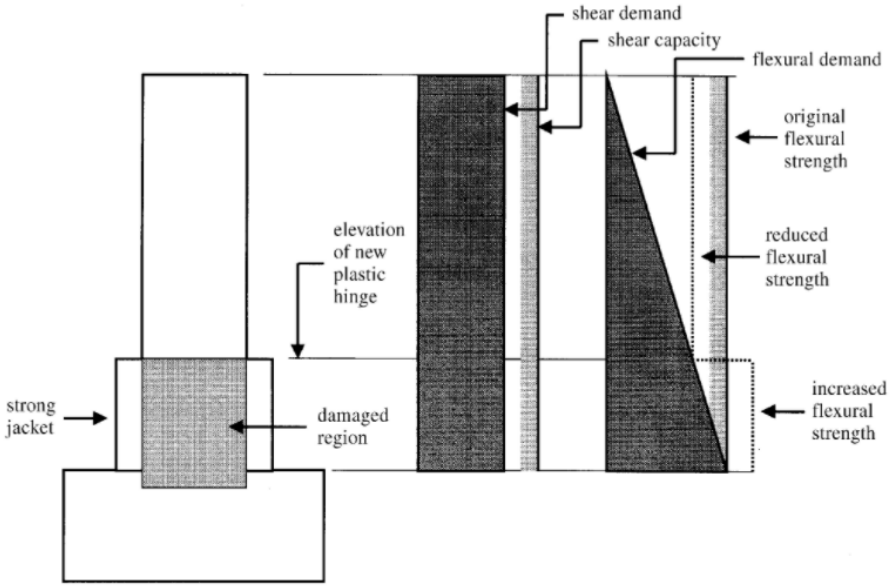

Figure 2.2: Repair concept of plastic hinge relocation via RC jacket (Lehman et al., 2001).

Other similar repairs have been completed using CFRP as the primary repair material (Parks et al., 2016; Rutledge et al., 2014) with the specific goal of rapid repair implementation. In the research completed by Rutledge et al., CFRP was used as both the primary flexural reinforcement and confinement. The flexural strengthening was achieved via CFRP anchors that were embedded into the footing with epoxy and then fanned onto the column over the length of the repair. Three columns were tested in this manner and each specimen contained buckled and/or fractured longitudinal steel. Of the columns tested, only one successfully relocated the plastic hinge. One repair developed a hinge at the footing interface, which the authors attributed to additional FRP confinement added above the repaired region which was intended to account for additional rotational demand anticipated at the new hinge location, however it also inadvertently resulted in larger forces developing in the system. This caused the new hinge region to exceed the predicted capacity and thus the column yielding at the base. The other specimen had a significantly reduced flexural strength due to several fractured longitudinal bars. The FRP anchors were determined to be inadequate to provide the strength necessary to relocate the plastic hinge. The authors state that additional research is necessary to quantify the capacity of these anchors prior to additional designs which will be conducted as part of this research program.

The study conducted by Parks et al. also utilized CFRP wraps for confinement of the new section, but used headed steel anchors for the flexural strengthening. It should be noted that this

test was conducted on prefabricated columns that were constructed with Grouted Splice Sleeve (GSS) connectors using Accelerated Bridge Construction (ABC) methods, however the repair technique should apply to conventionally constructed columns as well. The process and methodology was similar to that of Lehman et al., but instead of using a steel spiral and RC jacket the authors used a prefabricated CFRP shell as a type of stay in place form work which was then backfilled with non-shrink grout. The test matrix consisted of two damaged columns that both contained buckled and fractured longitudinal bars at the base. Both columns in the study successfully relocated the plastic hinge and fully restored the displacement, load and energy dissipation capacities as well as the stiffnesses of the original columns.

2.3.2 Applications in Buildings

In buildings, the desired location of plastic hinging is in the beam, as opposed to columns in bridge structures, since column hinging can lead to soft stories. Plastic hinge relocation in the beams of RC building frames has been investigated as a means to mitigate potential damage to the beam-column joints during a seismic event. An early experimental program by Abdel-Fatteh & Wight (Abdel-Fatteh & Wight, 1987) investigated the idea of relocating the plastic hinge away from the joint interface through careful detailing of new structures. This program was conducted similarly to that of Hose et al (1997) in that additional longitudinal reinforcement was added to the beam into the joint and terminated to create a "weakened" section at which the plastic hinge would form. The researchers concluded that this method could successfully move the hinge away from the column joint, thus localizing the damage within the beam. This was followed up with an analytical study (Al-Haddad & Wight, 1988) which revealed that relocation of plastic hinge had significant impact on the seismic response of the building system and that the degree of sensitivity was not uniform and varied widely depending on the response parameter chosen. A detailed discussion of the implementation of plastic hinge relocation as a design choice in RC frame buildings is also provided by Paulay & Priestley (1992, p. 194-198).

More recent studies have investigated plastic hinge relocation in RC frames as a means to retrofit deficient structures that have insufficient transverse reinforcement through the joint (Mahini & Ronagh, 2011; Shafaei, Hosseini, & Marefat, 2014). Mahini & Ronagh (2011) utilize a web-bonded CFRP approach in which CFRP sheets of specific lengths are placed along the sides of the beam the increase the flexural strength of the member along their lengths. Through an

experimental investigation of five retrofits, compared to two control specimens, the method is shown to effectively relocate the plastic hinge as predicted. Shafaei et al (Shafaei et al., 2014) enlarges the joint itself by installing steel angles that are mounted using pre-stressed cross ties. In their approach, the steel angles act as haunches to resist plastic deformations near the joint and the pre-stressing force acts to confine the joint therefore delaying the onset of tensile cracking. The method is shown to be effective through an experimental test program consisting of four retrofitted beam-column subassemblies and three control specimens. While much different in form and application than the repair addressed in this report, the concept of plastic hinge relocation as an application remains the same. Furthermore, these applications should be further investigated when extending the proposed repair strategy to other connection types, such as column-to-cap beam.

Chapter 3: Experimental Setup & Methods

The experimental portion of this research program consists of six large-scale tests on circular reinforced concrete columns that have been repaired using the plastic hinge relocation method. The columns were originally constructed and tested as part of a previous study investigating bidirectional load history effects on the definition of displacement-based performance limit states and the relationship between strain and displacement (Goodnight, Kowalsky, & Nau, 2017). As a result, these specimens developed significant damage through the formation of plastic hinges and represented ideal candidates for the implementation of this repair. This chapter outlines the laboratory test setup, repair material selection, specimen construction, instrumentation, and calculation methods for obtaining deformation quantities.

3.1 Test Setup

The test setup used was identical to that of the initial column testing by Goodnight, et. al. (2017). This section provides a summary of key elements describing the general layout and test methodology; however, for more detailed discussion the reader should reference the original report.

3.1.1 Laboratory setup

Each specimen consists of a footing, cantilever column, and loading cap. The front, side, and top views of the test setup are shown in Figure 3.1, Figure 3.2, and Figure 3.3 respectively with general dimensions of the setup shown in Figure 3.4. The footing sits on top of a second transfer footing which was necessary due to restrictions in capacity and spacing of holes in the strong floor. The specimen footing is secured to the strong floor and transfer footing via a total of eight 1-3/8” Dywidag bars, each post-tensioned to provide adequate force to prevent overturning and sliding of the column specimen during testing. The axial force is applied through a 1-3/4” Dywidag bar that passes through the center of the column inside of a 3” PVC duct. This bar is

anchored inside of the transfer footing at a blocked out pocket connection, visible in Figure 3.1 and Figure 3.2, and extends through the top of the column where it is loaded to a constant 191 kips with a single 200 kip hollow core hydraulic jack. The lateral load is supplied through two 220 kip hydraulic actuators, oriented in a 45-45-90 triangle from the strong wall, allowing for manipulation of the top of column displacement within the X-Y plane. Further discussion on the application and control of loads during the tests is provided in the next section.

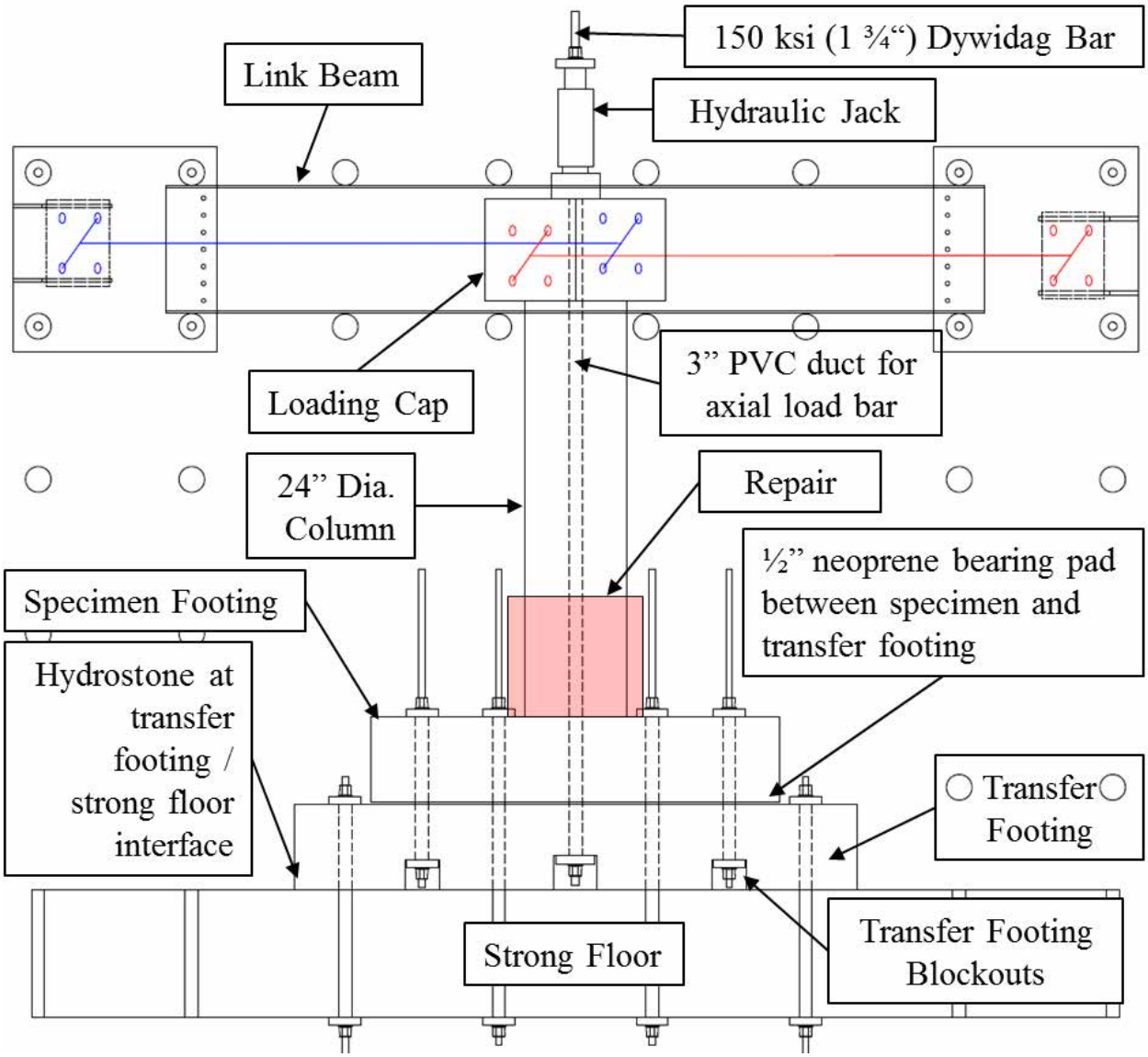

Figure 3.1: Laboratory setup – front view.

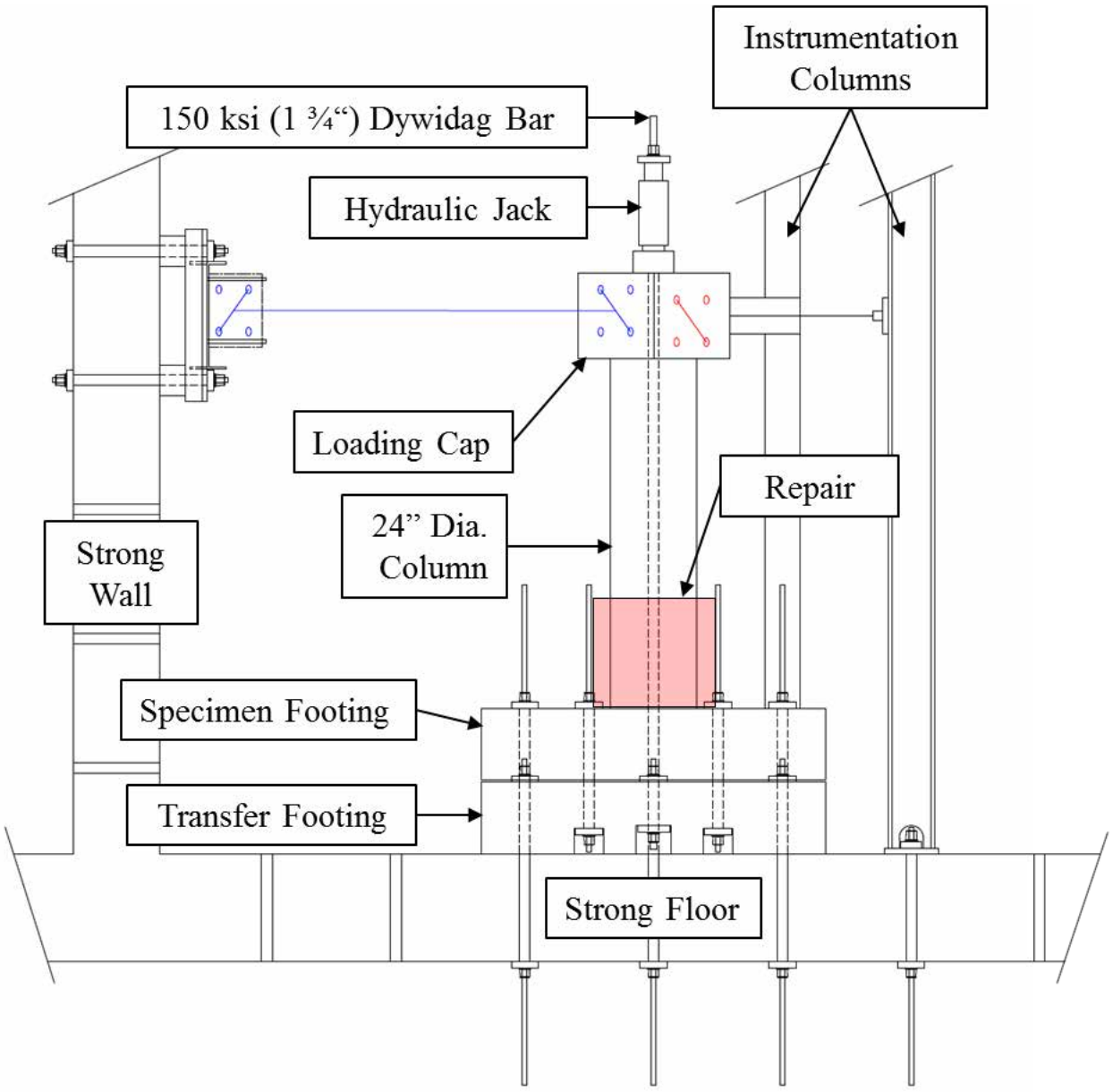

Figure 3.2: Laboratory setup – side view.

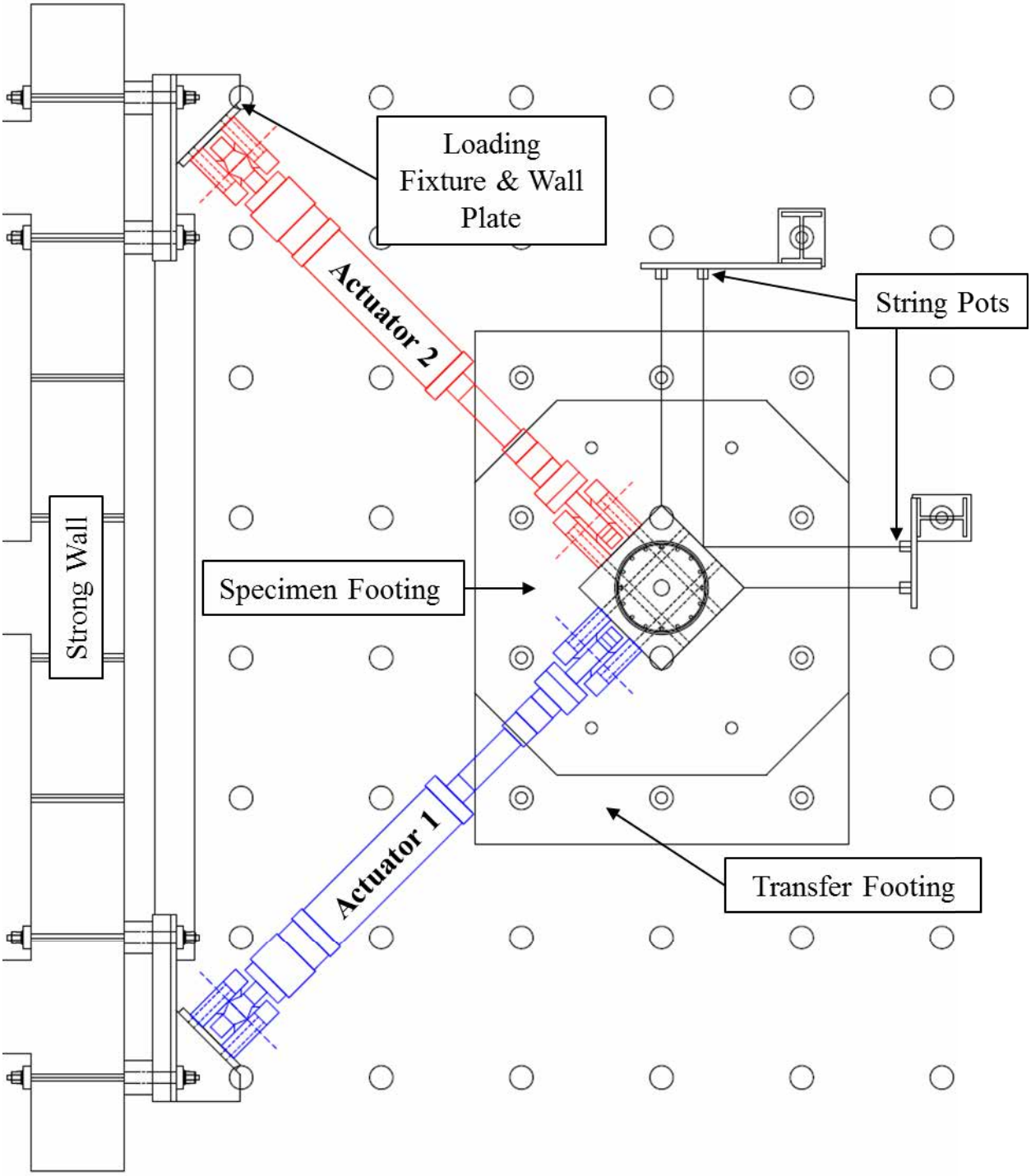

Figure 3.3: Laboratory setup – top view.

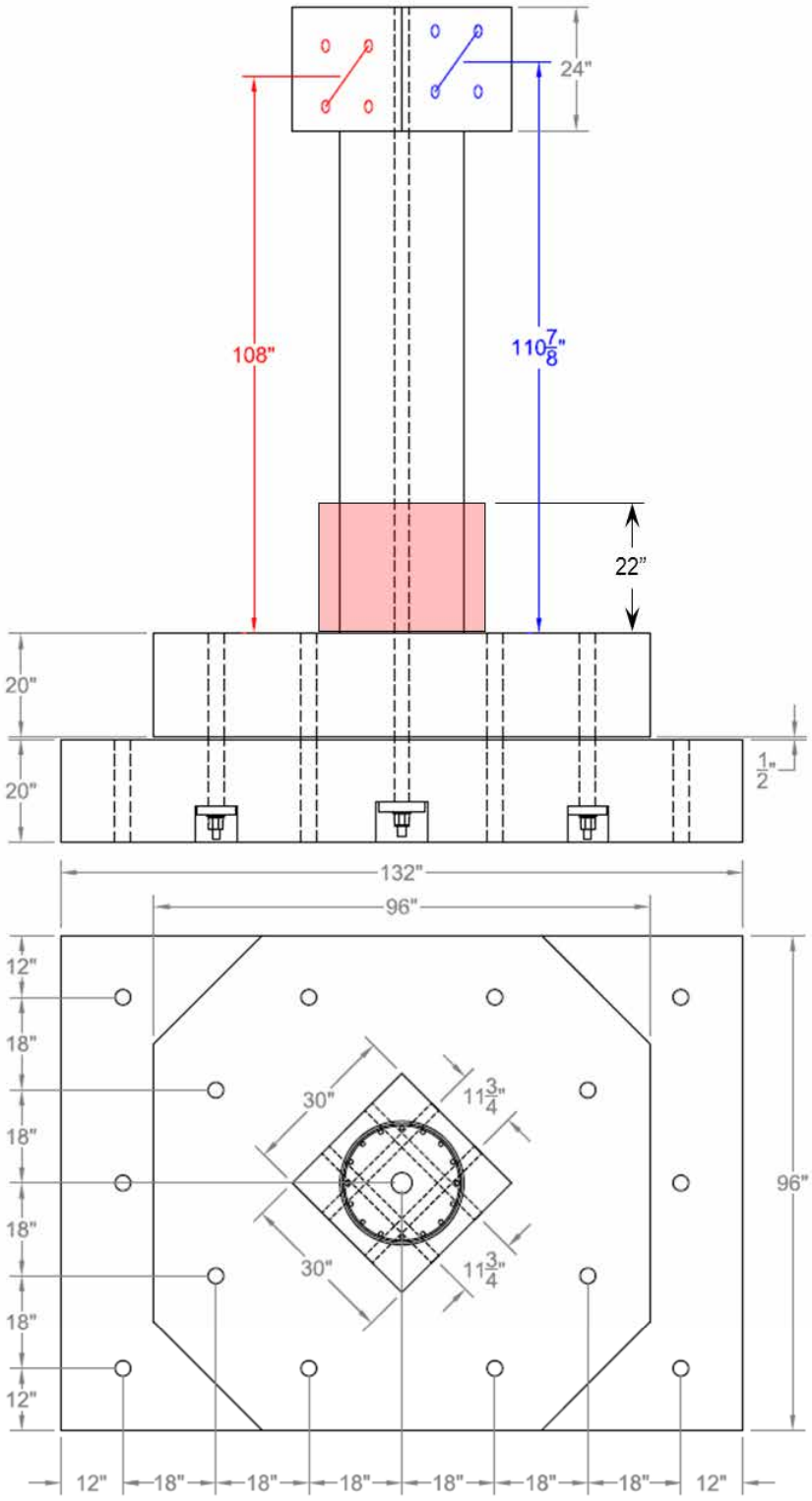

Figure 3.4: General test specimen dimensions.

3.1.2 Actuator control

The top of column displacement is manipulated in the X-Y plane by the linear extension and contraction of the two actuators shown in Figure 3.5. As each actuator deforms from the initial geometry, the center of rotation of each actuator head and the reinforced concrete loading block act as a rigid body translating through equivalent displacements. The configuration of the actuators in an arbitrary deformation state is shown in Figure 3.6, where the resulting geometry can be found as a function of the desired *(x, y)* location of the top of column. Therefore, the required change in actuator stroke to achieve a specified column displacement is simply the difference between the final *(L_f)* and initial *(L_i)* actuator lengths, calculated using Equation 3-1 through Equation 3-4 below. The actuators are then run in displacement control, where the top of column displacements are progressed through as prescribed in the given loading protocol.

The axial forces in each actuator *(F_1* and *F_2)* are measured using integrated load cells. Using similar triangles and the deformed geometry described above, each axial force can be broken into its respective global X and Y components and then combined to obtain the overall column shear forces in each direction, as described in Equation 3-5 through Equation 3-10 below. Since the test is run under a quasi-static displacement control procedure, any potential inertial forces in the column are considered negligible and therefore ignored the calculation of the overall response.

$L_{1i} = L_{2i} = L_i = 129.36in$	*Initial length between actuator pivot points measured from lab setup*	*Equation 3-1*
$a_1 = a_2 = \frac{L_i\sqrt{2}}{2} = 91.47in$	*Global X and Y components of the initial actuator length*	*Equation 3-2*
$L_{1f} = \sqrt{(a_1 - x)^2 + (a_1 + y)^2}$	*Deformed length of actuator #1*	*Equation 3-3*
$L_{2f} = \sqrt{(a_2 + x)^2 + (a_2 + y)^2}$	*Deformed length of actuator #2*	*Equation 3-4*
$F_{1x} = \frac{F_1(a_1 - x)}{\sqrt{(a_1 - x)^2 + (a_1 + y)^2}}$	*Global X-component of actuator #1 force*	*Equation 3-5*

$$F_{1y} = \frac{F_1\left(a_1 + y\right)}{\sqrt{\left(a_1 - x\right)^2 + \left(a_1 + y\right)^2}}$$ *Global Y-component of actuator #1 force* *Equation 3-6*

$$F_{2x} = \frac{F_2\left(a_2 + x\right)}{\sqrt{\left(a_2 + x\right)^2 + \left(a_2 + y\right)^2}}$$ *Global X-component of actuator #2 force* *Equation 3-7*

$$F_{2y} = \frac{F_2\left(a_2 + y\right)}{\sqrt{\left(a_2 + x\right)^2 + \left(a_2 + y\right)^2}}$$ *Global Y-component of actuator #2 force* *Equation 3-8*

$$F_x = F_{2x} - F_{1x}$$ *Global X-component of column shear force* *Equation 3-9*

$$F_y = F_{2y} + F_{1y}$$ *Global Y-component of column shear force* *Equation 3-10*

Under the assumption that the connections of each actuator to the specimen and strong wall are perfectly rigid, Equation 3-1 through Equation 3-4 should be sufficient to calculate the column displacement response when the actuator stroke is known. However, there is significant error using this approach due to slippage in the link-beam connection to the strong wall, among other factors, which result in inaccurate displacement values. To account for this, the top of column displacements are measured directly using an array of four string potentiometers, labeled SP_1 through SP_4 in Figure 3.5. The values of each are set to zero prior to beginning the test and are monitored in real-time throughout as the primary control for determining when the target displacements have been reached. Adjustments to the calculated actuator strokes are then made as necessary. During the test, the global X and Y displacements are calculated simply as the average of relative displacements in the two string-pots parallel to the axis considered, as shown in Equation 3-11 and Equation 3-12.

$$\Delta_x = \frac{SP_1 + SP_3}{2}$$ *Global X displacement as measured during test* *Equation 3-11*

$$\Delta_y = \frac{SP_2 + SP_4}{2}$$ *Global Y displacement as measured during test* *Equation 3-12*

During post-processing, the geometry of the system is considered such that effects of large displacements in one direction do no influence the readings of the displacements in the orthogonal direction. To illustrate this point, consider a very large displacement in the Y-direction where SP_2 and SP_4 contract, but SP_1 and SP_3 also extend resulting in erroneous X-displacement readings. To account for this, the system of equations formed by Equation 3-13 through Equation 3-16 is solved for values of x and y, which are taken as the final top of column displacements for analysis. Given that there are four equations and only two unknowns, a unique solution does not exist, therefore the system is solved such that the error is minimized. This solution is found using optimization algorithms available in most spreadsheet software, or the *minerr* function of MathCAD.

$$\sqrt{\left(SP_{1i}+x\right)^2+y^2}=SP_{1i}+\Delta_{SP_1} \qquad \textit{Deformed geometry of } SP_1 \qquad \textit{Equation 3-13}$$

$$\sqrt{\left(SP_{2i}-y\right)^2+x^2}=SP_{2i}-\Delta_{SP_2} \qquad \textit{Deformed geometry of } SP_2 \qquad \textit{Equation 3-14}$$

$$\sqrt{\left(SP_{3i}+x\right)^2+y^2}=SP_{3i}+\Delta_{SP_3} \qquad \textit{Deformed geometry of } SP_3 \qquad \textit{Equation 3-15}$$

$$\sqrt{\left(SP_{4i}-y\right)^2+x^2}=SP_{4i}-\Delta_{SP_4} \qquad \textit{Deformed geometry of } SP_4 \qquad \textit{Equation 3-16}$$

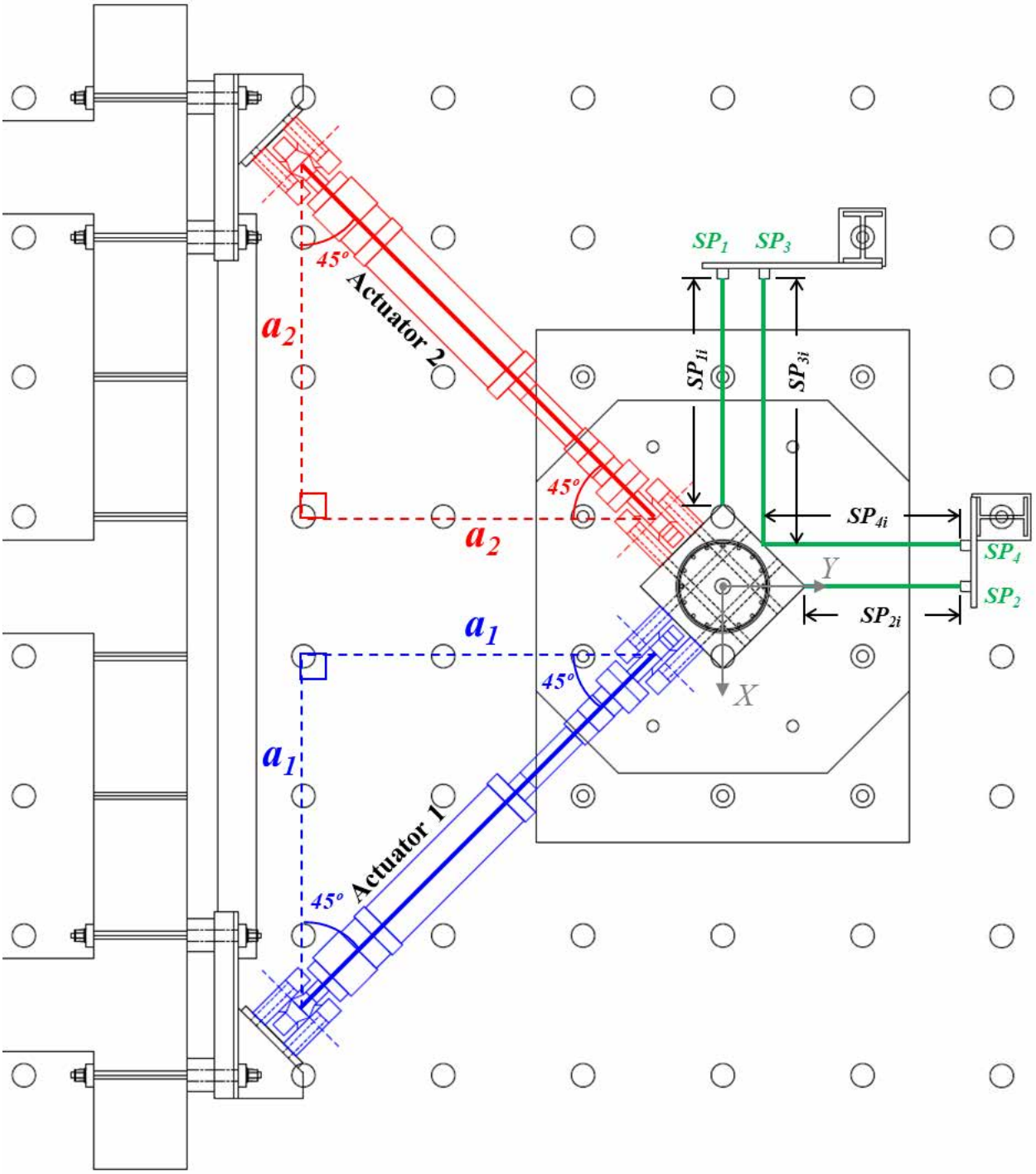

Figure 3.5: Initial actuator configuration at zero displacement.

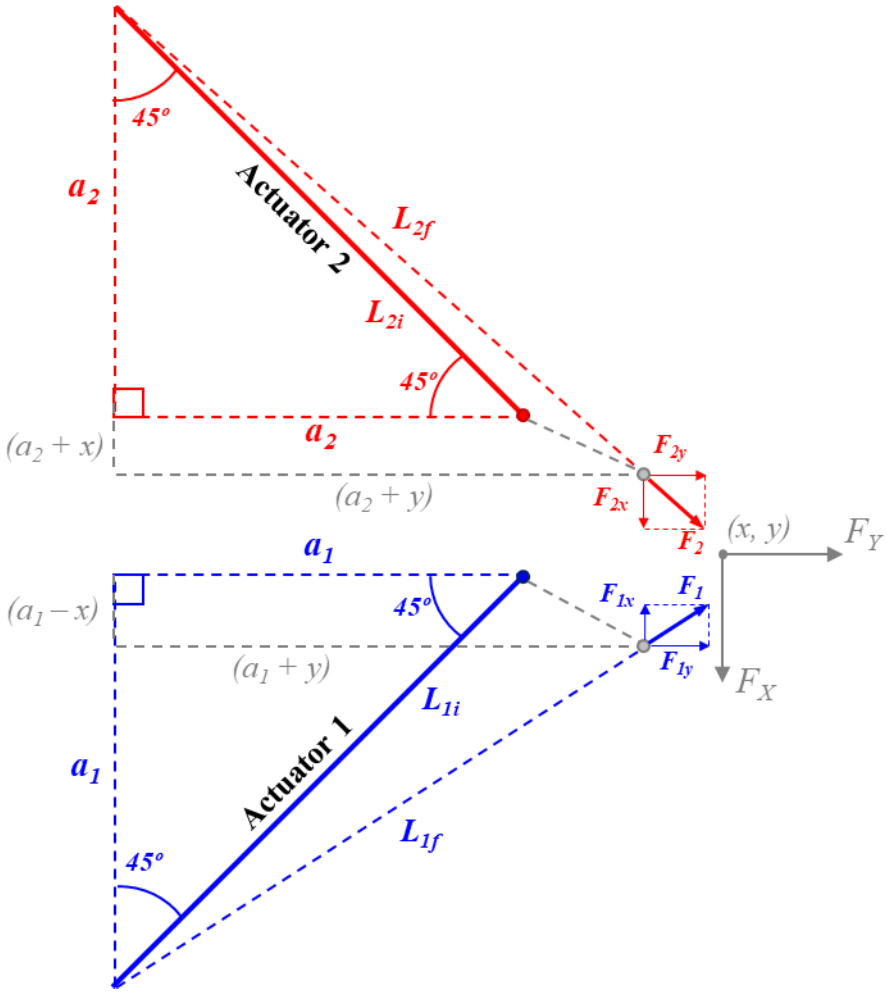

Figure 3.6: Deformed actuator configuration and global force components.

3.1.3 Method of axial load control

A constant axial load is applied via a hydraulic jack located at the top of the column to simulate the weight of the superstructure on the column. The jack applies load directly to the top of the column with a reaction provided by a steel plate which is secured to a Dywidag bar that passes through the length of the specimen. As the column undergoes deformation, the arc length of the bar also changes, resulting in fluctuations of the applied load assuming the jack is set and fixed prior to the start of the test. To address this, the oil pressure is regulated to maintain constant load through a second hydraulic jack placed into the MTS testing machine. The test machine is initially placed in displacement control while an external hydraulic pump applies the initial pressure to reach the desired axial load. The loading heads of the test machine are initially spaced such that the second jack extends to approximately half of its stroke capacity. Once the initial load is reached, the external hydraulic pump is isolated via a globe valve and the MTS test machine is

placed into force control. Now, as the column displaces, the MTS test machine regulates the volume of oil in the system to maintain the desired load. Oil overflow reservoirs are provided for each jack to allow for excess oil to be purged and returned to the jacks. Figure 3.7 illustrates the axial load application system described in this section.

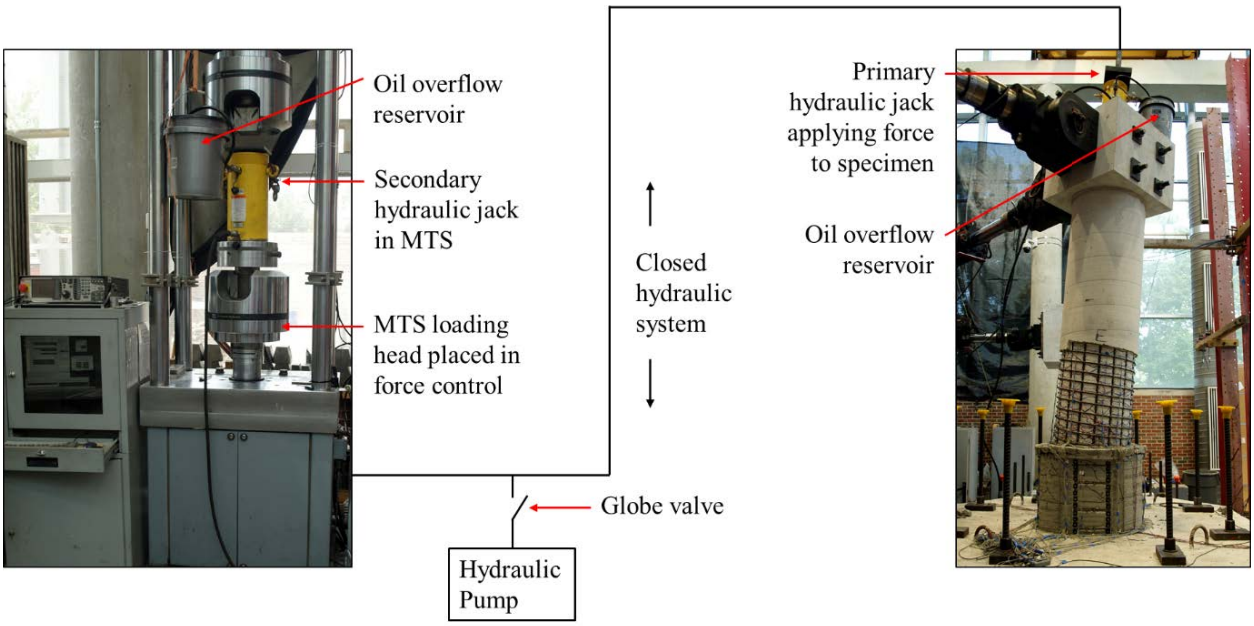

Figure 3.7: Diagram of axial load application system.

3.1.4 Loading protocol

The intent of the experiments presented in this report is to compare the performance of each repaired column to that of its original test, but to also have a direct comparison between the performances of each repair. Each of the six tested columns were initially subjected to different bidirectional loadings during the previous research project, therefore making it difficult to load the repaired columns in such a way to achieve sufficient comparability between all of the repaired columns and each of their individual original tests. In an effort to ensure adequate uniformity, a two-cycle set loading history, illustrated in Figure 3.8, was chosen for all of the repaired column tests, as at least one specimen with identical reinforcement details was subjected to this loading history during initial testing. This allows for comparisons to be drawn between the repaired column performance and that of the original test of that particular column, and to another nominally identical specimen subjected to the same loading history. Table 3.1 outlines which original tests presented in the Load Path Effects report (Goodnight et al., 2017) serve as comparisons for each of the repaired columns. The "Corresponding Load Path Tests" indicate the actual column that was

repaired and re-tested, while the "Nominal Comparison Tests" indicate which original test serves as the direct comparison (i.e., subjected to the same load history as the repaired column in addition to having identical reinforcement to the repaired column). Lastly, the use of the same two-cycle set for each repair test removes any influence of loading history when evaluating the performance of different repair configurations.

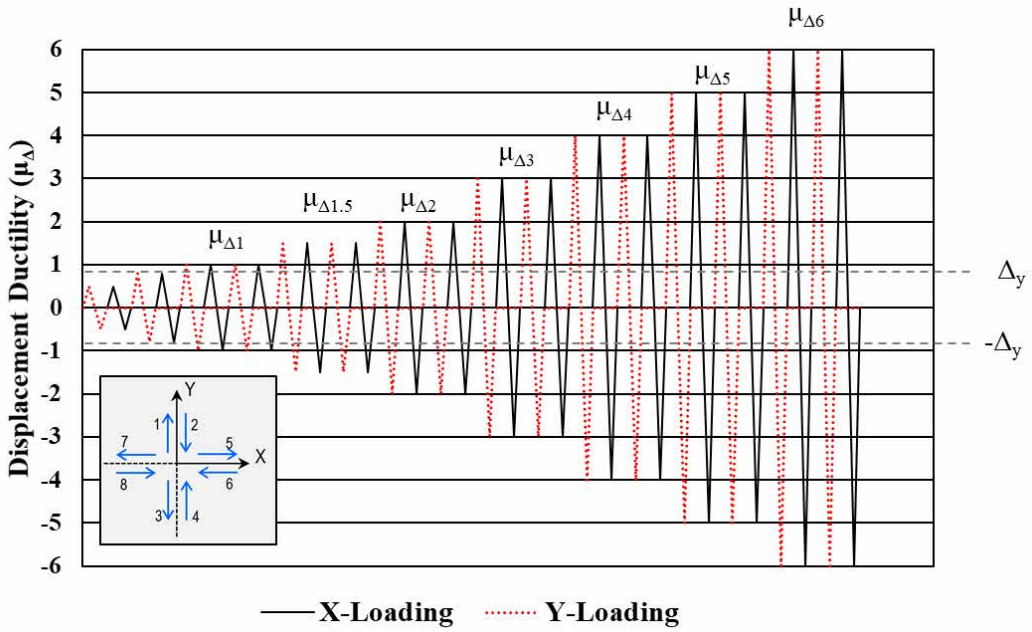

Figure 3.8: Definition of two-cycle set load history.

Table 3.1: Corresponding load path test columns to repair columns.

Repair#	Detailing	Corresponding Load Path Test#	Nominal Comparison Load Path Test#	Original Load History
1	(16) #7 / #3@2"	6	4	Asymmetric Two Cycle Set
2	(16) #7 / #3@2"	4	4	Two Cycle Set
3	(16) #7 / #3@2"	5	4	Three Cycle Set
4	(16) #6 / #3@2.75"	12	9	Megathrust
5	(16) #6 / #3@2"	11	8	Megathrust
6	(16) #7 / #3@1.5"	10	10	Two Cycle Set

Each test is run with two preliminary single-cycle sets at $1/2F'_y$ and F'_y before continuing into two-cycle sets at displacement ductility 1, 1.5, 2, 3 and so on through failure. In the original column tests, the displacement at first yield (Δ'_y) was defined as the measured displacement when the applied force vector produces the analytical first yield moment at the base cross section. The

equivalent yield displacement is then calculated as $\Delta_y = \Delta_y^{'}\left(M_n / M_y^{'}\right)$ with displacement ductility levels equal to multiples of the equivalent yield displacement. Since the steel at the critical cross section has already yielded during the initial testing of the column, it is unclear how to define these quantities for the repaired system. Therefore, for ease of comparison between the original and repaired performance, the equivalent yield displacement and resulting displacement ductilities defined for the original column are also used for the repaired specimens. Figure 3.9 indicates how displacement ductility cycles will be referenced in the discussion portions of this report. For reference, the example shown in the figure refers to the second cycle of displacement ductility 1.5 in the negative X-direction.

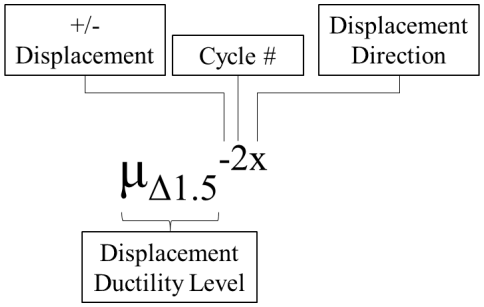

Figure 3.9: Definition of displacement ductility notation.

3.2 Repair Material Selection

This repair technique requires relatively few individual materials and, with the focus on conventional materials, all should be readily available. The materials required for the repair implemented in this report are listed below and illustrated in Figure 3.10:

1. Bond material of rebar into doweled holes
2. Steel bars for longitudinal reinforcement
3. Steel plate or hoops for transverse reinforcement
4. Grout or concrete for backfill

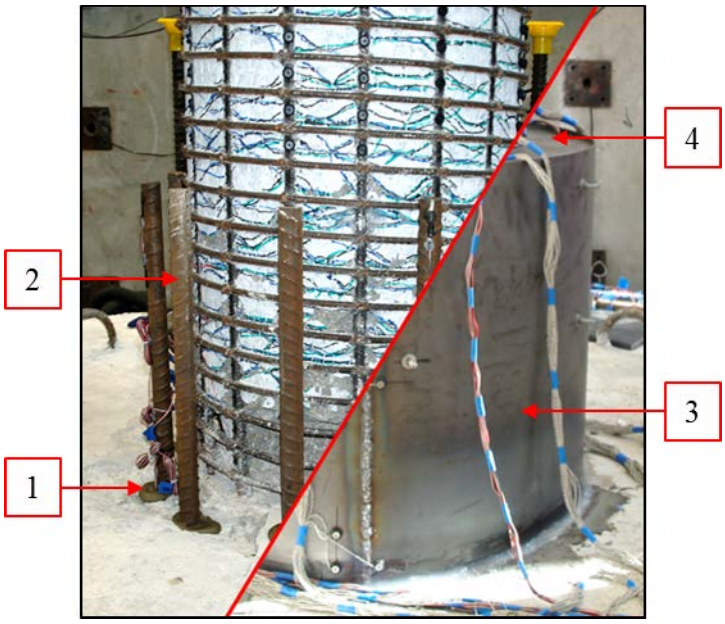

Figure 3.10: Illustration of repair materials as installed in repair.

This section outlines the considerations made in choosing the specific materials used in each test and summarizes the properties of each.

3.2.1 Repair bar bond material

Post installed bonded anchors can be installed with grout or epoxy, both of which provide force transfer from the new anchor to the parent concrete via bond shear stresses. While each material has its own set of benefits, grouted anchors were found to have longer set times and require larger diameter holes for installation than their epoxy counterparts (Burtz, 2003). The repair considered in this report will often be installed into already congested footings and must also provide a rapid solution. Therefore, it was decided to use a two-part epoxy system instead of grout in the connection of the longitudinal steel to the existing footing.

The selection of epoxies was dependent on several variables such as seismic rating, cold weather installation, low sensitivity to moisture during installation, bond strength and compatibility with rebar. Additionally, the product should be familiar with the Alaska DOT in order to facilitate rapid deployment. The following table was provided by AKDOT and shows chemical adhesive systems that are preliminarily approved for use:

Table 3.2: Prequalified chemical adhesive chart (Provided by AKDOT).

Manufacturer or Brand Name	Product Name	Threaded Rod			Reinforcing Bar (Gr. 60)	Concrete temp. at time of installation		Installation time at 25 °C [a]	
		ASTM A 307	ASTM A 449 (T1)	F 593		Min (°C)	Max (°C)	Set (hrs)	Cure (hrs)
Hilti (415) 507-1690	HTE 50	Yes	Yes	Yes	Yes	2	43	0.25	24.0
	RE500	Yes	Yes	Yes	Yes	-5	43	2.0	12.0
Adhesives Technology Corporation (800) 892-1880	Ultrabond HS200	Yes	Yes	Yes	Yes	2	43	0.25	24.0
	Ultrabond 365	No	Yes	No	Yes	-18	43	0.1	0.5
Unitex (816) 231-7700	Pro-Poxy 300 Fast [b]	No	Yes	No	No	5	43	2.5	24.0
Powers Fasteners (800) 659-1069	T308+ [b]	No	Yes	No	No	5	43	2.5	24.0
US Mix (303) 778-7227	US SPEC Gelbond NS Fast [b]	No	Yes	No	No	5	43	2.5	24.0
ITW Redhead (800) 368-9724	Acrylic 7	No	Yes	No	Yes	-18	43	0.1	0.5
Simpson Strong Tie (510) 460-9912	SET22 & SET56	No	Yes	No	Yes	5	43	1.0	24.0
Covert Operations / USP - (800) 328-5934	CIA Gel 7000	No	Yes	No	Yes	4	43	4.0	36.0

a. The installation times are based on information in the Manufacturer's product literature. Set time is the minimum time needed for the adhesive to harden and support the anchor; cure time is the minimum time required before the anchor may be loaded.
b. A 30-element mixing nozzle shall be used to place the chemical adhesive.

From the above table, the two products that best match the requirements of this research are the *Adhesives Technology Corporation (ATC) Ultrabond 365* and *ITW Redhead Acrylic 7*. From a material property standpoint, each of these products are essentially identical and therefore cost and availability are the deciding factor. As such, the *Redhead Acrylic 7* appears to be more readily available with comparable pricing and was therefore selected for use in all tests conducted in this report.

3.2.2 Repair Bars

The strengthening of the base cross section of the column requires an increased flexural capacity and therefore additional longitudinal reinforcement. In the context of the repair any reinforcing bar or material would be sufficient so long as it could be designed to remain elastic and provide sufficient strength to the cross section. To facilitate ease of installation and to maintain the philosophy of using conventional materials, steel rebar was chosen for use in this application. Its characteristics are well known and there is a great deal of research on the bond and development of these bars in both epoxy and grout materials. Since the repair is designed to remain elastic, any grade of rebar can be used so long as the steel does not exceed the yield strength.

Each repair was designed considering typical A706 grade 60 rebar properties, however A706 grade 80 steel was installed. The reasoning for this choice was twofold: 1) the extra strength

would provide additional assurance that the repair would remain elastic, even if it performed differently than expected; and 2) at the time of constructing these repairs, there was an abundance of A706 grade 80 rebar available from a previous study that had been conducted at NC State (Overby, Kowalsky, & Seracino, 2017). Although A615 steel is typically specified for capacity protected connections, it is recommended that A706 ductile steel be used as it provides additional protection in the event that a hinge does occur at the base and not in the relocated section.

The material properties for the #10 bars used in Repairs #1, #2, and #6 were taken from the database of tested specimens in Overby, et. al. (2017). This study investigated the material properties for A706 grade 80 steel bars from a variety of manufacturers and heats with the goal of expanding the available knowledge on the performance and variability of this steel. As a result, the bars used in each repair were labeled and corresponded to a specific manufacturer and heat number that had been previously tested. Table 3.3 shows the material properties corresponding to these bars.

Table 3.3: Reference material properties for #10 repair bars in Repairs #1, 2, and 6 (Overby et al., 2017).

E_s (ksi)	f_y (ksi)	ε_y (in/in)	f_u (ksi)	ε_{su} (in/in)
28729	83.6	0.0030	114.9	0.0970

The repair bars used in Repairs #3, #4, and #5 were not clearly marked, and therefore were tested directly. Table 3.4 through Table 3.6 summarize the material tests performed for each repair.

Table 3.4: Tested material properties for #7 repair bars in Repair #3.

Sample	E_s (ksi)	f_y (ksi)	ε_y (in/in)	f_u (ksi)	ε_{su} (in/in)
1	31386	89.6	0.0033	120.5	0.091
2	23883	89.8	0.0035	113.5	0.041
3	27735	88.9	0.0042	119.4	0.094
4	24215	91.9	0.0040	113.7	0.090
Average:	26805	90.1	0.0037	116.8	0.079

Table 3.5: Tested material properties for #7 repair bars in Repair #4.

Sample	E_s (ksi)	f_y (ksi)	ε_y (in/in)	f_u (ksi)	ε_{su} (in/in)
1	29961	84.0	0.0029	-*	-*
2	26171	83.3	0.0034	108.4	0.108
3	25391	84.6	0.0035	110.4	0.092
4	30931	85.4	0.0026	110.2	0.095
Average:	28113	84.3	0.0031	109.7	0.098

* Grips slipped prior to fracture

Table 3.6: Tested material properties for #7 repair bars in Repair #5.

Sample	E_s (ksi)	f_y (ksi)	ε_y (in/in)	f_u (ksi)	ε_{su} (in/in)
1	29491	82.5	0.0034	108.1	0.083
2	29547	83.2	0.0028	111.3	0.092
3	23142	83.7	0.0039	111.1	0.089
4	27890	83.2	0.0031	107.6	0.096
Average:	27517	83.2	0.0033	109.5	0.090

3.2.3 Transverse Steel

The transverse steel in Repairs #1 - #3, #5, and #6 is in the form of a steel sleeve that provides shear strength and confinement to the repair, but also acts as a stay-in-place formwork for construction. The sleeves were rolled into two half-moons from flat plates, each cut to a length of half the circumference of the repair and a width equal to the height of the repair. Figure 3.11 shows the sleeve fabrication process.

(a) (b) (c)

Figure 3.11: (a) Shear cutting of steel sheet; (b) Cold rolling of sleeve; (c) Final sleeve form.

To employ this process, the material must be thin enough to be cold rolled to the desired shape. Additionally, the material must be weldable as there will be two separate halves that will be joined in place around the column. Special considerations regarding the treatment and specifications of the material specifically relating to issues that could arise due to welding are

discussed in Section 3.3.3. A36 steel meets each of these requirements and is readily available, thus it was selected for use in the sleeve. Table 3.7 shows the material properties of the steel sheets used in Repairs #1 - #3, and Table 3.8 shows those if Repairs #5 and #6. All material specimens were made and tested per (ASTM A370, 2015).

Table 3.7: Tested material properties for 11-gauge A36 steel sheet in Repairs #1 - #3.

Sample	E_s (ksi)	f_y (ksi)	ε_y (in/in)	f_u (ksi)	ε_{su} (in/in)
1	33574	42.2	0.00145	54.1	0.211
2	34746	42.4	0.00146	54.3	0.214
3	30210	44.4	0.00153	55.2	0.211
Average:	32843	43.0	0.00148	54.6	0.212

Table 3.8: Tested material properties for 11-gauge A36 steel sheet in Repairs #5 - #6.

Sample	E_s (ksi)	f_y (ksi)	ε_y (in/in)	f_u (ksi)	ε_{su} (in/in)
1	30569	49.5	0.00162	55.9	0.230
2	30925	45.9	0.00148	56.7	0.233
3	31583	49.8	0.00158	56.8	0.221
4	32179	47.6	0.00148	57.2	0.224
5	28697	47.7	0.00166	56.2	0.236
Average:	31314	48.2	0.00154	56.7	0.227

For larger columns, it is recognized that fabrication from single flat sheets could be challenging. As an alternative, a prefabricated steel pipe with a diameter equal to that of the repair diameter could also be used. This would eliminate the need to cut and bend a flat sheet to the necessary dimensions and thus reduce fabrication time and effort. This option would likely be costlier assuming only a small portion of an entire pipe would be need to be purchased; however, if the material is readily available and easily obtainable it could be worth considering as an substitute to fabricating the sleeve from flat sheets.

Repair #4 uses individual rebar hoops as an alternative to the steel sleeve described above. The hoops are cut from continuous #3 A706 grade 60 spiral to lengths equal to half of the repair circumference plus an additional 16” to allow for 8” lap welds on either side of the repair. Rebar spiral is more conventional in reinforced concrete design and likely more readily available, therefore it is used to provide an alternative design approach to the steel sleeve while achieving the same end result. The test samples do not produce a sharp yield plateau since they are cold

rolled into shape, therefore Table 3.9 only provides yield stress taken at 0.2% offset and ultimate stress.

Table 3.9: Tested material properties for #3 A706 Grade 60 spiral in Repair #4.

Sample	f_y (ksi)	f_u (ksi)
1	66.0	96.7
2	65.0	97.8
3	69.6	97.4
4	69.3	96.7
Average:	67.5	97.2

3.2.4 Backfill material

Repairs #1 - #3 and part of Repair #6 utilize a rapid set, high strength, prepackaged grout mixture as the backfill material inside of the repair annulus. When considering the intended performance of this material within the repair, the connection can be seen as analogous to that of the grouted pocket connection utilized in Accelerated Bridge Construction (ABC). A grouted pocket connection consists of rebars that extend out from a precast concrete member, such as a column, and into a formed out void space in the adjoining member, which resembles the annular space between the original column and outer repair sleeve. Once each element is in place, the void is filled with grout to permanently connect the two members. Figure 3.12, which shows a grouted pocket connection between a precast pile and pile cap in a research study conducted at the University of Texas at Austin (Matsumoto et al., 2001), illustrates an example of this connection. Part of the work done in this previous study compares various grout products for use within these connections and outlines specific criteria for product selection. Since the grouted pocket connection so closely resembles the repair connection, the results of this research are used to form the basis of the selection of the grout to be used in the repair design.

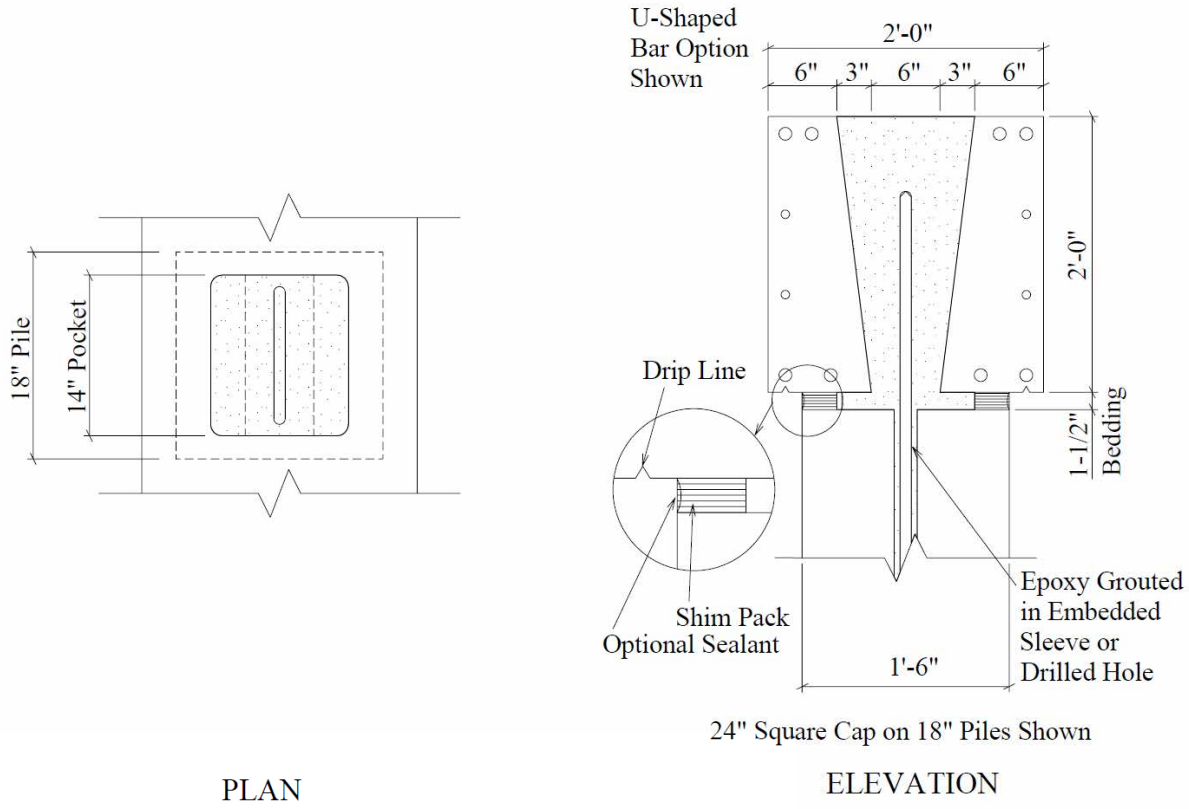

Figure 3.12: Grouted Pocket Connection in a precast bridge system (Matsumoto 2001).

The report by Matsumoto, et. al. (2001) outlines a grout specification which provides criteria for minimum requirements as well as applicable ASTM standards. The specification, shown in Table 3.10, has requirements for the mechanical, compatibility, constructability and durability properties of the grout. The mechanical requirements ensure a minimum compressive strength which is key for the overall strength of the repair and bond development of the new bars. The compatibility requirements ensure that the repair material and base material will interact consistently, and that the grout will not shrink. This is necessary as there must be contact between the steel sleeve and the grout to provide proper confinement to the repair region. The constructability requirements control the material's flowability and set times, both of which are critical in the repair scenario. The grout must be highly flowable to consolidate into the repair and the crushed core of the original column. Set time is also critical to achieve the rapid deployment objective of the repair. Finally, the durability of the grout is important to the repair as it is meant not only to be a rapid solution, but permanent as well. This factor is particularly important for extreme climates.

Table 3.10: Grout specification; adapted from (Matsumoto 2001).

Property	Values	
Mechanical Compressive strength (ASTM C-31, 4x8" cylinder)	Age 1 day 3 days 7 days 28 days	Compressive strength (psi) 2500 4000 5000 7000
Compatibility Expansion requirements (ASTM C 827 & ASTM C 1090) Modulus of elasticity (ASTM C-469) Coefficient of thermal expansion (ASTM C-531)	Grade B or C – expansion per ASTM C 1107 $3.0\text{-}5.0\times10^{6}$ psi $3.0\text{-}10.0\times10^{-6}$/deg F	
Constructability Flowability (ASTM C-939) Set Time (ASTM C-191) Initial Final	fluid consistency efflux time: 10-30 seconds 3-5 hrs 5-8 hrs	
Durability (as necessary) Freeze Thaw (ASTM C-666) Sulfate Resistance (ASTM C-1012)	300 cycles, RDF 80% expansion at 26 weeks < 0.1%	

The study completed by Matsumoto et al (2001) compares three different commercially available products that meet the criteria stated in Table 3.10. Of these three, *BASF Masterflow® 928* was used for most of the tests and the other two were used primarily as comparisons. This same grout was also used in a study conducted by NC State for the Alaska DOT in the development of a grouted shear stud connection for steel bridge column to pier cap connections (Fulmer, Kowalsky, & Nau, 2015). Since this product has been used successfully in previous tests and it has experimental results for connections which closely resemble that of the repair in question, BASF Masterflow® 928 was chosen as the backfill grout for the first three repairs.

The grout comes as a prepackaged dry powder in individual 55lb bags. Each bag was mixed with approximately 10lbs of water to achieve a flowable consistency, with the water content varying between 9.5lbs to 10.5lbs per bag. This results in a "milkshake-like" consistency that is easily poured and consolidated within the repair. Sample specimens were formed to determine compressive strength at the time of testing for each repair. Repair #1 considered the results of both 2x2 cube samples, tested per ASTM C109, and 4x8 cylindrical specimens, tested per ASTM C39.

The results, shown in Table 3.11, indicate that both tests produced similar strength measures, and therefore using the 2x2 cubes would be more economical and produce less waste. However, the material tests for Repair #2 show significant variation in measured strength due to imperfections in the samples. Table 3.12 summarizes the results of the testing performed, where samples 1 and 4 fall well below the average of the others. As a result, it is concluded that the 4x8 cylinder specimens should be used for the remaining tests and that this method should be used in field applications as they are less sensitive to imperfections in casting.

Table 3.11: Tested material properties for BASF Masterflow® 928 grout in Repair #1.

Sample	f'_c 2x2 cube (ksi)	f'_c 4x8 cylinder (ksi)
1	8.08	8.41
2	8.71	8.15
3	8.27	8.04
Average:	8.35	8.20

Table 3.12: Tested material properties for BASF Masterflow® 928 grout in Repair #2.

Sample	f'_c 2x2 cube (ksi)
1	5.83
2	7.94
3	7.74
4	6.29
5	7.34
6	7.85
Average:	7.16

Table 3.13: Tested material properties for BASF Masterflow® 928 grout in Repair #3.

Sample	f'_c 4x8 cylinder (ksi)
1	7.85
2	8.74
3	7.29
Average:	7.96

Table 3.14: Tested material properties for BASF Masterflow® 928 grout in Repair #6.

Sample	f'_c 4x8 cylinder (ksi)
1	11.9
2	10.8
3	11.3
Average:	11.3

Repairs #4 – #6 used a highly flowable pea gravel concrete mix designed to be placed by a concrete pump. The intent of using this material was to provide a more cost effective, and potentially more readily available, alternative to the BASF Masterflow® 928 grout. The mix design for Repair #4 includes a 0.46 w/c ratio, 4000 psi compressive strength, 4-8" slump with superplasticizer, 5-7% air content, and 3/8" pea gravel aggregate. While this mix performed well in the repair tests, it was found to have extremely low durability when tested according to ASTM C666, which is specified in Table 3.10 as the requirement for freeze-thaw performance. The w/c ratio was reduced to 0.40 in Repairs #5 and #6 to address this; however, additional investigation is needed into whether this material is suitable from a longevity standpoint. Table 3.15 summarizes the tested material properties for each repair, all of which were performed using 4x8 cylinder molds per ASTM C39. It should be noted that the reduced w/c ratio in Repairs #5 and #6 increased the specified 28 day compressive strength to 5000 psi, which was not achieved in either repair. The testing of Repair #5 was only 11 days after casting, but the testing of Repair #6 was 53 days after casting. Regardless, the concrete performed adequately in each test and did not show any signs of reduced function.

Table 3.15: Tested material properties for pea gravel concrete mix in Repairs #4 - #6.

Sample	f'_c Repair #4 (ksi)	f'_c Repair #5 (ksi)	f'_c Repair #6 (ksi)
1	5.02	3.86	4.72
2	4.64	3.88	4.93
3	4.87	3.78	4.93
Average:	4.84	3.84	4.86

3.3 Specimen Construction

3.3.1 Original Column Construction

As stated previously, the original columns were constructed as part of a separate research program at NC State University. The specifics of construction for each specimen are outlined in the report by Goodnight, et. al. (2017). The columns are designed with varying transverse and longitudinal steel details under very tight tolerances to isolate the impact of specific variables on column performance. Capacity design measures are employed in the footings explicitly considering the increased shear demand resulting from the plastic hinge relocation repair used in this study. Additional steel is located within the joint region to provide increased strength and prevent damage to the footing from the larger demand; therefore, no additional consideration for capacity design of the footings are required.

3.3.2 Repair Construction

This repair is intended to be rapidly deployable and require minimal preparation and installation time. Construction is conceptually straight forward; however, it was found that some difficulties could arise during field implementation requiring additional consideration. This section provides a detailed procedure for a typical installation, as well as a discussion of potential challenges and recommendations for each step. Repairs #4 - #6 have slight variations to the typical construction procedure which are discussed individually following the outline below. The estimated field installation time for this repair is approximately 48 hours, although installation time in the lab was substantially longer due to instrumentation requirements of each specimen.

Step 1: Straighten column if residual drift exceeds allowable limits

Following a major seismic event, it is likely that there will be some level of residual deformation due to large displacements of the structure. Prior to installation of the repair, the residual drift of the system should be checked to ensure that it is within the acceptable range and, if not, the structure should be adjusted as close to plumb as possible. Further discussion and recommendations on how to determine these limits is presented in Chapter 7 of this report. This was achieved in the lab by carefully manipulating the actuators such that the displacement at zero applied force was minimized; however, field applications will likely require the use of brute force through heavy machinery. This step is not included in the approximate installation time.

Step 2: Remove loose concrete from existing plastic hinge

The cover concrete will likely be completely spalled from the face of the column and will not require much effort to remove. The core concrete, however, will likely be crushed to some extent but still largely intact. To allow for the new grout to provide maximum continuity across the cross section, all the loose concrete must be removed from the core. This is achieved with light hand chiseling, removing only relatively loose concrete having large visible cracks. Once solid concrete is reached the removal process should be stopped. There is also likely to be substantial spalling of the footing concrete directly adjacent to the column which will require removal. An example of a test specimen before and after removal of crushed core concrete is shown in Figure 3.13.

(a) **(b)**

Figure 3.13: Existing plastic hinge (a) before and; (b) after crushed core removal.

Step 3: Drill holes for new bars into footing

Once the core is clear of loose concrete, holes are hammer drilled into the footing for the repair bars. The diameter and depth of the holes depends on the size of bar to be installed as well as the manufacturer's specifications for bond development of the epoxy. Since the top surface of the footing is likely to be cracked or spalled, it is recommended to measure the hole depth from top of sound concrete rather than from the top of footing to ensure adequate bond length of the bars. This will probably be just at or below the top mat of reinforcing steel.

Due to the heterogeneous nature of reinforced concrete and the inability to exactly locate reinforcing steel, the drilling of holes is likely to be the most labor intensive and potentially problematic step of installation. Although the spacing and layout of the steel should be known from design drawings, the exact location of bars, shear ties, and other miscellaneous inclusions will almost certainly require relocation of holes by some amount.

It is recommended to provide an envelope tolerance of +/- 1 bar diameter during the design phase such that the bars can be relocated in the field as needed. Considering this, a smaller bar diameter is preferable as it is easier to fit into a congested footing and requires a shallower embedment depth. Also, slight variations in the location of reinforcement did not appear to impact the repair's overall performance.

The specimens repaired in the lab had a large number of J-hooks within the repair region to account for increased joint shear, as the footing reinforcement plan in Figure 3.15 shows. During installation of the repair, it was found that avoiding the tails of these hooks was sometimes impossible due to the density of shear reinforcement, therefore it was decided to core drill the first 4" of each hole through the steel hooks and then proceed with the hammer drill for the remaining depth of holes, as illustrated in Figure 3.14. This approach was deemed acceptable as a review of the footing design revealed that the assumed increase in demand far exceeded the actual repair demand. However, coring of reinforcing steel should be avoided in practice unless the reduced steel area can be justified as acceptable. An alternative concept would involve placement of holes in the adjoining member during initial construction to accommodate the possibility of a future repair, should the need arise. Such a technique was considered, but not employed for these tests.

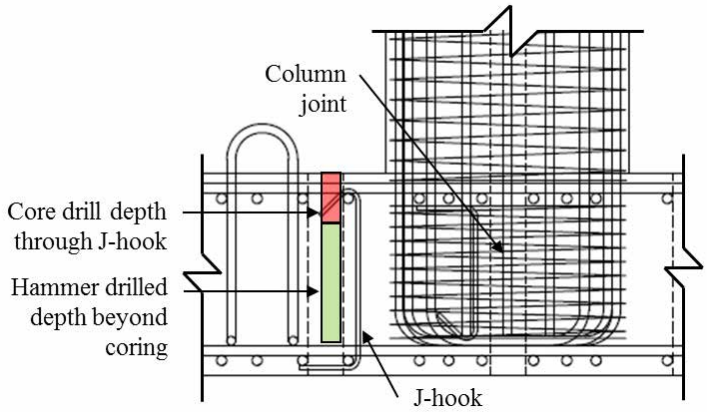

Figure 3.14: Repair bar drilling to avoid J-Hooks in specimen footing.

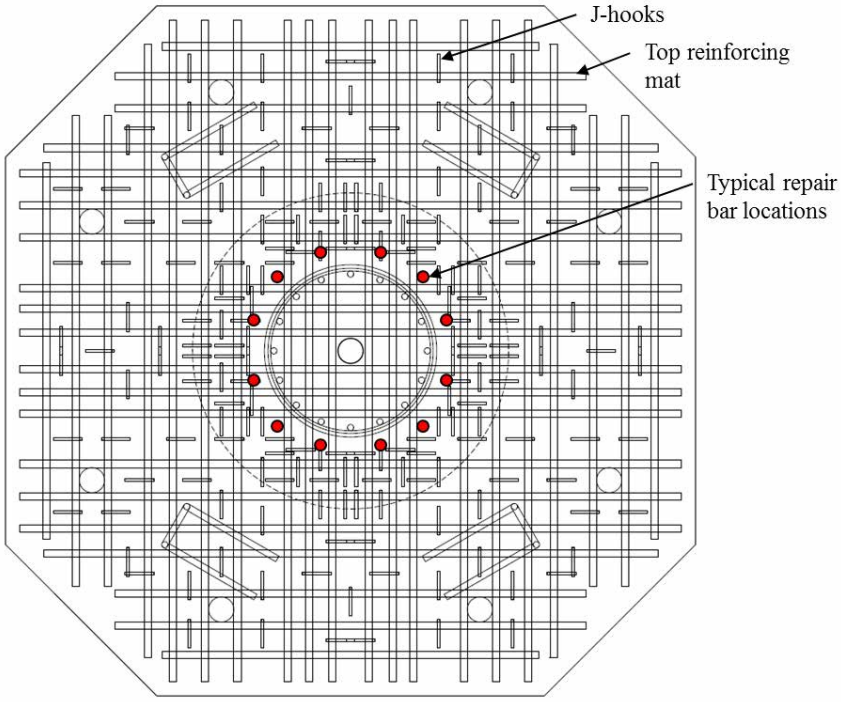

Figure 3.15: Typical footing reinforcement plan layout.

(a) **(b)**

Figure 3.16: Setup for (a) core drilling and; (b) hammer drilling.

Step 4: Install two-part epoxy and place repair bars into drilled holes

Once the holes are drilled into the footing the bars were then set with two-part acrylic epoxy. The selected product has a straight forward installation procedure and did

not require much effort; however, the set time at normal temperatures is about 6-7 minutes, so working quickly is necessary. Once the installation process begins it should continue through completion without interruption.

The holes are first cleared with compressed air to remove any loose debris from drilling. A wire brush is then run along the length of the hole to roughen the surface, followed by another burst of compressed air. Finally, a vacuum hose should be run into the hole to remove to ensure the hole is completely clean. It is recommended to complete this step for all holes, sealing the tops with a cloth to keep debris from entering, prior to beginning the epoxy process. Approximately ½ to ¾ of the depth of hole is then filled with epoxy using the mixing nozzle and applicator shown in Figure 3.17.

Figure 3.17: Redhead two-part epoxy application system.

The reinforcing steel is then installed into the hole by pushing downward through the epoxy while twisting to ensure that any air voids are removed as the bar is inserted. The bars should be fully set after about 30 minutes at normal temperatures, with total cure time being 24 hours. The bars are checked for vertical straightness using a level, as shown in Figure 3.18, and the viscosity of the epoxy was great enough that the bars did not require additional bracing to be held plumb once they were placed.

Figure 3.18: Installation of two-part epoxy into footing.

Step 5: Install level grout base at footing

If there is significant spalling of the top footing concrete, the interface will not provide a uniform, level base for the steel sleeve to be mounted. A rapid set grout should be used to fill the spalled surface after the repair bars are set. The BASF Masterflow® 928 grout used in the repair has an initial and final set time of 3 and 5 hours respectively, which was suitable for this application. Products with shorter set durations are available should that be required. It is not necessary to wait until the grout has fully cured to continue with the installation of the repair, but only until the grout has reached sufficient stiffness to support the weight of the steel sleeve. An example of the patched footing is shown in Figure 3.19 below.

Figure 3.19: Installation of patch grout on top of footing.

Step 6: Place steel sleeve halves around column base and weld in place

Once the top of the footing is flat and level, the steel sleeve is placed around the column base in two separate halves. The seam between each half is positioned with a 1/8”

gap between the two sheets and a backer bar placed behind. This is secured using vice grips, followed by a series of tack welds to hold the sleeve in place, as shown in Figure 3.20. Finally, a butt weld is run over the entire height of both seams creating a continuous ring around the column, shown in Figure 3.21 and Figure 3.22. Additional considerations for the welding process are discussed in Section 3.3.3.

Figure 3.20: Tack welds along seam to hold sleeve and backer bar in place.

Figure 3.21: Welding the two halves of steel sleeve.

Figure 3.22: Completed butt weld on steel sleeve.

Step 7: Position sleeve uniformly around column base

Once the sleeve has been welded, it must be positioned to ensure a consistent and stable spacing around the circumference of the column. The was accomplished in the lab by drilling a series of ¼ inch holes into the sleeve and running threaded rod through each hole. Bolts and washers are then placed on each side of the holes, which could then be adjusted and tightened such that the rods bear against the existing column. This provides a uniformly spaced annulus and prevents the sleeve from shifting while pouring the backfill.

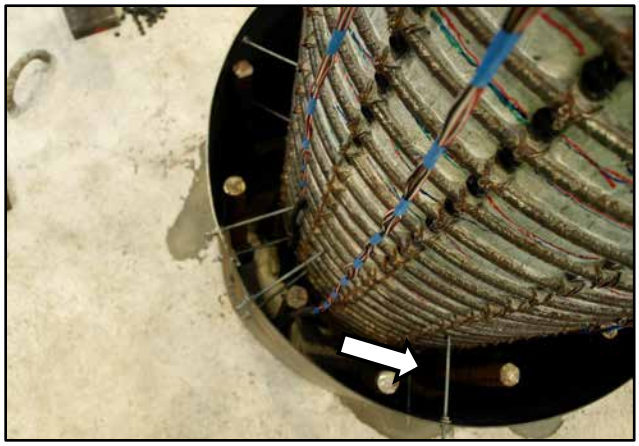

Figure 3.23: Steel sleeve with threaded rod spacers bearing against column.

Step 8: Provide watertight seal at interface of the steel sleeve and footing

A silicone sealant is used around the base of the steel sleeve to provide a water tight seal and prevent the fluid grout mixture from escaping when placed. The recommended cure time for the silicone is 24 hours, however in a field application it is likely acceptable

to backfill once the silicone has reached initial hardness which is approximately 1-2 hours. As long as this barrier is present, the aggregate in the grout will likely prevent catastrophic leakage from the sleeve.

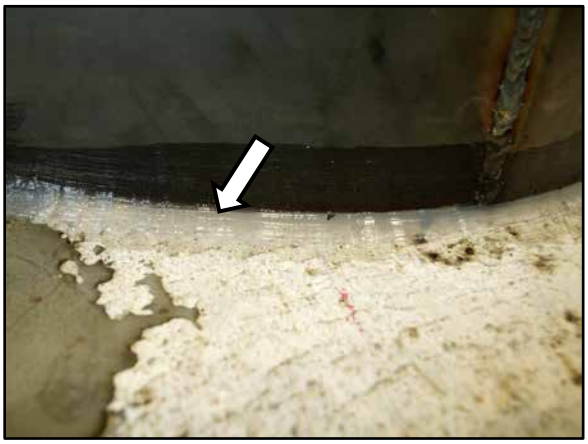

Figure 3.24: Silicone sealant at footing-steel sleeve interface.

Step 9: Place grout into annular void space between column and steel sleeve

Once the steel sleeve is set with the seal at the base, the backfill material is placed into the void space between the sleeve and the column. If the flowable grout mixture is used, a vibrator is not necessary to consolidate the material inside the repair; however, striking the outside of the sleeve with a rubber mallet does help to settle the mixture between lifts. The grout was mixed in the lab using an electric drum mixer, shown in Figure 3.25, and placed in lifts of one bag at a time using a five-gallon bucket, shown in Figure 3.26. Given that each mixing cycle requires approximately 3-5 minutes, this process would need to be scaled accordingly for field applications. A flowable ready-mix concrete mixture with small aggregate can be used as an alternative, as was done in Repairs #4 - #6, but a vibrator is recommended to ensure consolidation of this mix since it does have aggregate and is less fluid than the fluid grout mix.

Figure 3.25: Electric drum mixer and grout mixing station.

Figure 3.26: Placing grout into repair.

Figure 3.27: Top of repair once filled with grout.

Figure 3.28: Completed repair installation on lab specimen.

Repair #4 – Alternate transverse steel installation

Repair #4 uses individual rebar hoops for transverse reinforcement in place of the steel sleeve used in the other repairs. With the original column and superstructure in place, it is not practical or feasible to use continuous spiral reinforcement, therefore single layers of reinforcement are cut from a spiral coil with a diameter equal to that of the repair to the outside face of the new longitudinal bars. Each layer spans the full circumference plus an additional length to provide overlap for a splice weld to create a continuous hoop, as shown in Figure 3.29. The locations of the splice weld are staggered on each layer to prevent a potential weak direction. Once positioned, the hoops are tied directly to the longitudinal bars. The completed repair cage is shown in Figure 3.30.

Figure 3.29: Installation of rebar hoops in Repair #4.

Once the bars are tied, the lap splices are welded in place using a single sided groove weld. Figure 3.31 (a) shows an example of the completed splice weld, while Figure 3.31 (b) provides the weld detail. While this repair was successfully implemented in the lab, it should be noted that the longitudinal repair bars will not be placed in a perfectly circular layout. The #3 spiral used in this repair was somewhat easily manipulated by hand to match the reinforcement layout and tie directly to each bar, but this would likely not be the case in a field application where larger diameter bars are required for the hoops. This should be considered when designing a repair using this reinforcement option.

Figure 3.30: Completed rebar cage for Repair #4.

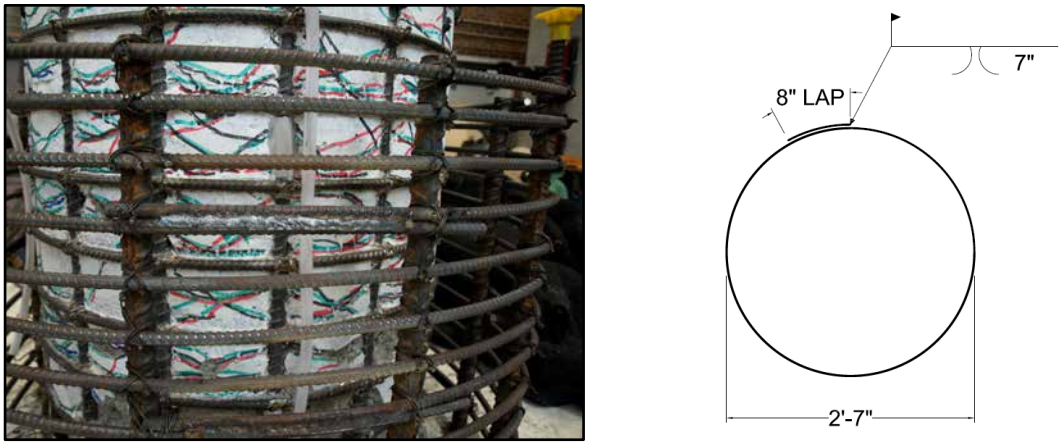

(a) **(b)**

Figure 3.31: (a) Repair #4 rebar hoop splice weld; (b) Repair #4 splice weld detail.

Repair #5 – Installation of bar development methods

Repair #5 follows the typical installation procedure, with the exception of special considerations made to the fractured bars in an attempt to improve their bond development. Two were fully exposed by chipping away the existing concrete, as per the ACI Guide to Concrete Repair (ACI Committee 546, 2014), and one was outfitted with a mechanical headed stud. An example of the first method is shown in Figure 3.32 (a) while the mechanical headed stud installation is shown in Figure 3.32 (b). Installation of each requires clear access to the existing column and should be done prior to installation of the repair bars.

(a) **(b)**

Figure 3.32: Installation of fractured bar anchorage mechanisms.

The existing concrete is chipped away using either a hammer drill or air chisel. The bar stripping method requires a clear spacing of approximately one bar diameter around the fractured bar over the height of the repair to be installed. The headed stud actually requires a much larger volume of concrete to be removed to make room for the device. Furthermore, the fractured bar needs to be cut above the buckled region to provide a straight section for installation, and the spirals covering the bar need to be cut up to the height of the installed device, as shown in Figure 3.32 (b). If multiple headed studs are to be installed on adjacent bars, it would likely be necessary to stagger their installation heights to prevent overlap. Once these steps are completed, the installation of the repair continues per the typical procedure. Further discussion of these methods and their performance is provided in Section 4.5.

Repair #6 – Installation of corrugated steel sleeve shear key mechanism

Repair #6 considers a shear key mechanism between the existing column and repair annulus as a means of developing compression struts spanning from the original fractured bars and the new repair bars. A corrugated steel pipe made from 16 gauge ASTM A-929 aluminized steel with a diameter between that of the original column and the inside of the repair bars is used for the deformed shear key interface. A length of this pipe was cut approximately 1” shorter than the height of the repair to ensure that the inner sleeve did not extend above the repair. This also corresponds to the length the repair bars extend above the footing. This section of pipe was then cut in half longitudinally to create two semicircular sections, similar to the steel sleeve sections described previously.

Once separated, these sections are placed around the base of the column and rejoined to create a continuous sleeve. A section of the pipe was cut to span across the gap between the two halves which was secured to each side using self-tapping sheet metal screws. Figure 3.33 illustrates how this patch section is used to rejoin the two halves around the column. This step should be performed after drilling the holes for the repair bars, but prior to their installation.

Figure 3.33: Corrugated steel sleeve shear key mechanism installed on column base.

Once the corrugated sleeve is installed, the repair bars should be place and the footing patching completed, as shown in Figure 3.34. The corrugated sleeve is then sealed and backfilled with fluid mix BASF Masterflow® 928 grout mix. To ensure consolidation of the grout mixture within the repair, the outside of the sleeve can be vibrated or tapped with a rubber hammer.

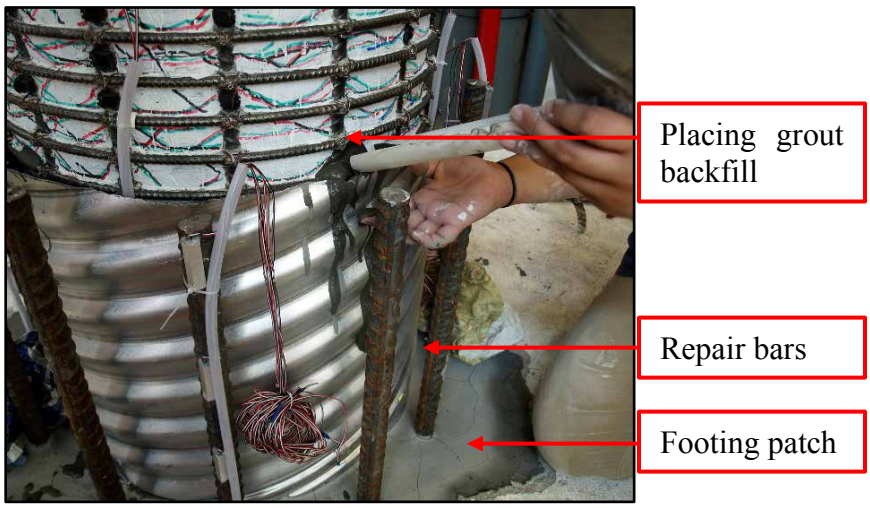

Figure 3.34: Placing grout inside of corrugated sleeve.

The grout should be given some time to cure once installed, but does not need to set fully before continuing the installation of the repair. Once this is completed, the outer steel sleeve is installed per the typical installation process. The completed system before and after concrete back fill has been placed is shown in Figure 3.35 (a) and (b) respectively. Further discussion on the theory and performance of this mechanism are provided in Section 4.6.

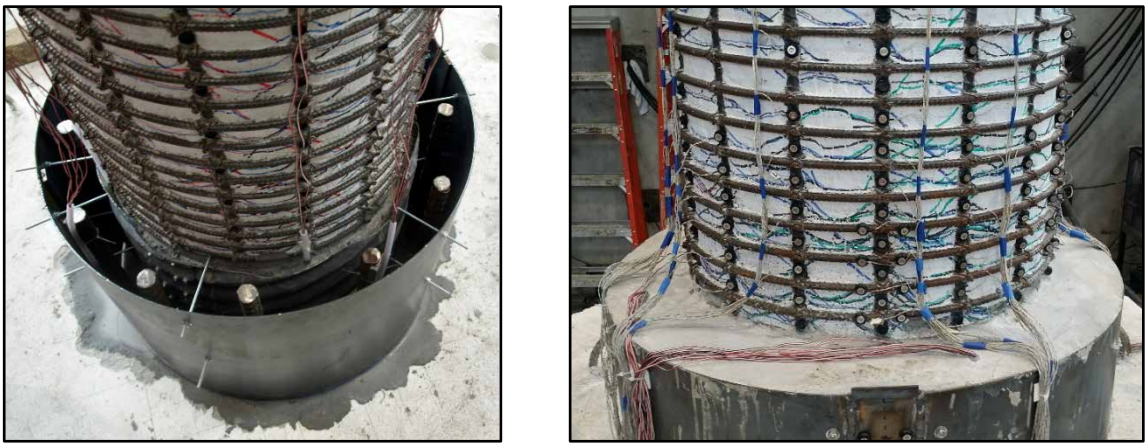

(a) **(b)**

Figure 3.35: Final installation of corrugated shear key (a) before and; (b) after concrete placement.

3.3.3 Considerations for welding of the steel sleeve

During testing of Repair #5, the seam welds between the two halves of the steel sleeve fractured on both the North and South faces of the repair. The following discussion outlines the potential causes of this failure and provides recommendations for welding of future repair installations. Additionally, the steps taken to ensure that a similar failure did not occur during the testing of Repair #6 are presented, as this repair had already been constructed with similar methods prior to the testing of Repair #5.

The most apparent difference between the welds in the first 3 repairs, which performed without issue, and Repair #5 was the process by which the sleeves were prepared. The sleeves for Repairs #1-3 were shear cut from a flat sheet in a shop, whereas the sleeve for Repair #5 was cut from a similar sheet using a plasma torch. It is possible that using this method on such thin material could have resulted in a large Heat Affected Zone (HAZ) thus hardening the edge and making it difficult for the weld to penetrate the base metal. While plasma cut edges are typically welded in the field without issue, these cuts are usually done on thicker materials. In their bridge seismic retrofit and strengthening details, (Caltrans, 2009) specifies a minimum sleeve thickness of 1/4” for columns less than or equal to 4’-4” diameter and 3/8” for anything greater, which would likely

reduce the effect of HAZ issues with proper edge preparation procedures. An investigation was conducted to test whether the HAZ in this thinner material influenced the performance of the sleeve welds in which two sets of coupons were created, one from a plate that was shear cut and welded back together and another that was plasma cut and welded. Each coupon was then subjected to tensile tests perpendicular to the welded joint. Figure 3.36 shows the welded plates from which each set of specimens was fabricated while Figure 3.37 shows examples of the finished coupons. The specimens were made and tested according to the Standard Test Methods and Definitions for Mechanical Testing of Steel Products (ASTM A370, 2015) with dimensions as shown in Figure 3.38.

(a) **(b)**

Figure 3.36: Welded plate specimens from which test coupons were fabricated (a) Shear cut; (b) Plasma cut.

Figure 3.37: Welded test coupons for cutting method comparison.

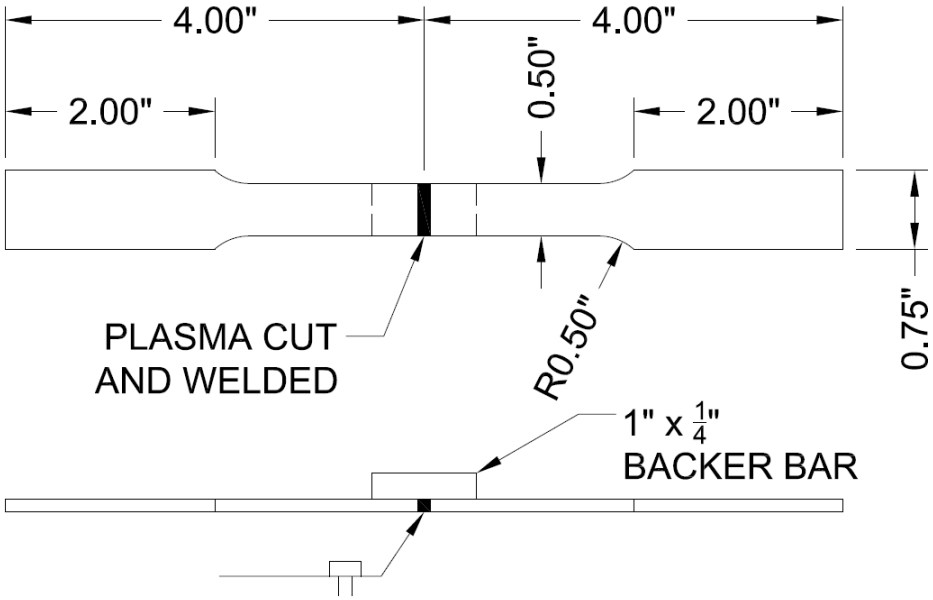

Figure 3.38: Example coupon detail for welded test specimens.

The test resulted in 3 of the 6 samples with plasma cut edges fracturing at the weld interface at about half of the strain of those that failed through the base metal alone. The shear cut samples only resulted in 1 of the 6 coupons failing at the weld, and the one that did fail was noted to have a significant dip in the weld metal resulting in a reduced cross section at that location. Figure 3.39 (a) and (b) show the tested coupons of the plasma cut and shear cut samples respectively, with weld failures circled in red. While it was clear that more of the plasma cut specimens failed through the weld, it is also noted that the quality of the weld on these specimens were much lower than on the shear cut samples. This could be a result of the weld metal not penetrating the base metal due to HAZ effects, but it is also noted that the edges of the plasma cut sections were much more jagged. This could have also contributed to the reduced capacity in the weld as well. From these results, it is concluded that extreme care should be taken in the edge preparation and weld quality when welding plasma cut thin gauge sheet metal for this repair. Should this process be used, the installer should ensure a clean cut and a properly prepared edge surface, and welding should be overseen by a certified weld inspector and performed by a certified welder.

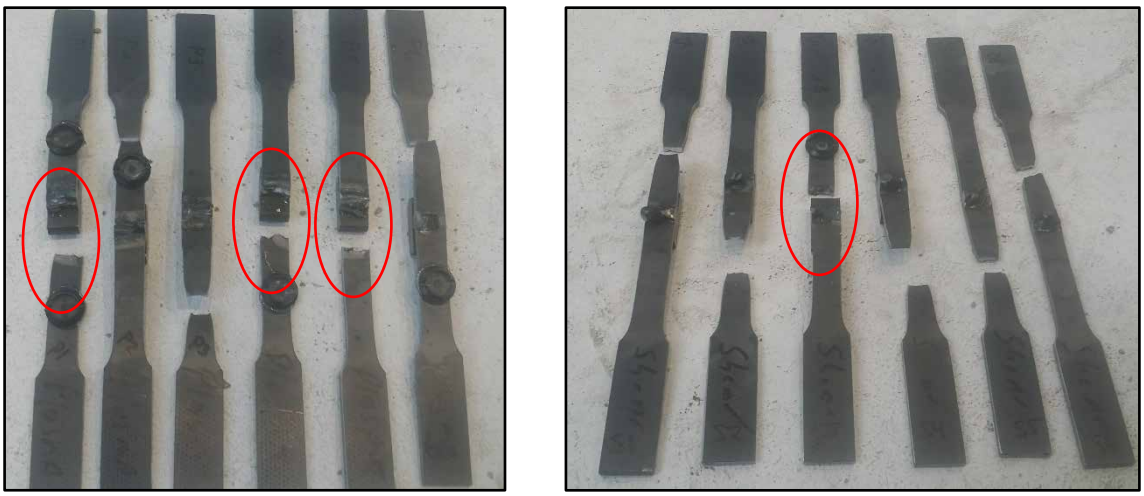

(a) **(b)**

Figure 3.39: Tested samples constructed using a welded edge cut by (a) plasma torch; and (b) shear cut.

An additional set of coupons were also made to test a "patch" weld that would be applied to the sleeve of Repair #6. This is intended not as a field application, but to ensure the weld failure observed in Repair #5 did not reoccur since the same cut and welding procedure had already been performed. Figure 3.40 illustrates the detail of the patch, and Figure 3.41 shows an example of the coupons that were tested. The first 5 coupons all failed through the base metal, indicating that the fix performed as intended, so the sixth coupon was notched along the original sleeve weld, simulating deficient section and ensuring it would fracture to test the capacity of the welded "patch". Figure 3.42 shows the tested specimens, with the far right being the notched coupon shown circled in red. This specimen did fail near the weld, however it still developed similar strength and strain to the first five specimens. It is also noted that the rotation of base metal around the weld would likely be restrained by the repair itself and the rest of the sleeve, reducing the local demand at the weld. After these tests, it was concluded that the patch would be sufficient to prevent the weld failure that was observed in Repair #5 and was installed on Repair #6, as shown in Figure 3.43.

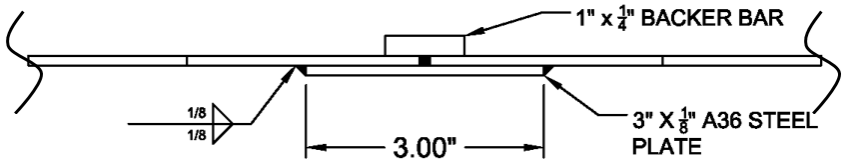

Figure 3.40: Repair #6 steel sleeve butt weld strengthening detail.

Figure 3.41: Welded coupon with patch repair.

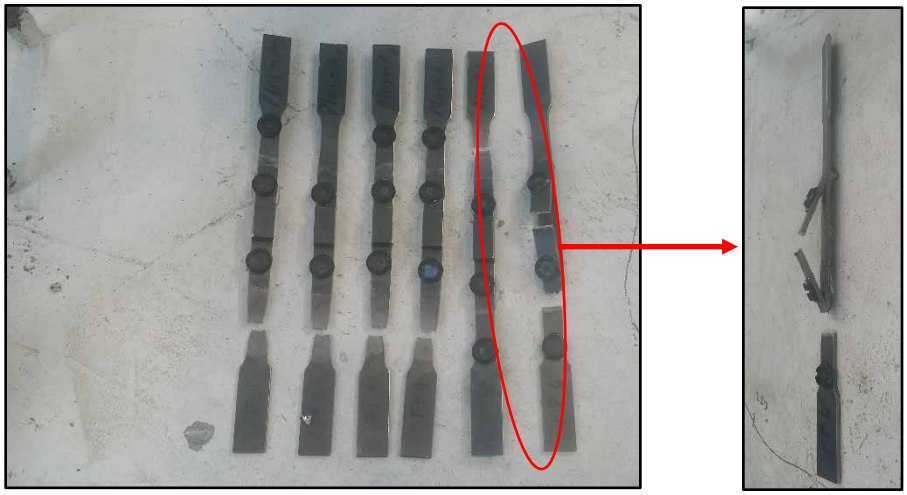

Figure 3.42: Tested samples with patch plate.

Figure 3.43: Repair #6 steel sleeve with patch of existing weld.

In conclusion, the primary cause of the weld failure was determined to likely be due to a combination of HAZ effects at the welded edge, improper edge preparation, and inadequate welding process. As such, the following recommendations are made to ensure sound welding of the repair sleeve:

1. The edge to be welded should be properly prepared with clean surfaces and straight edges.
2. Ensure all welding is conducted by a certified welder and supervised by a certified weld inspector.
3. Plasma cutting of thin gauge metal (< ¼") that is intended to be welded should be avoided as it has been shown to reduce the welded capacity of the connection.

3.4 Instrumentation

3.4.1 Optotrak Certus HD

The strains in the relocated plastic hinge reach levels that far exceed the measurable capacity of traditional instrumentation. This experimental program uses the Optotrak Certus HD 3D positioning system to track to column's deformation which uses infrared LED target markers applied to the specimen whose positions in 3D space are determined by an array of specially designed cameras. Each experiment records the positions of hundreds of LED sensors at a rate of 1Hz to generate an accurate picture of the overall deformation and response throughout the test. The accuracy of the Optotrak Certus HD system is reported by the manufacturer (Northern Digital, Inc.) to be 0.1mm with a resolution of 0.01mm, thus allowing for measurements of very small changes in geometry.

An extensive discussion of the instrumentation process and relative accuracy is provided by (Goodnight, Kowalsky, & Nau, 2015). Figure 3.44 illustrates a comparison between the strain measurement readings of the Optotrak Certus HD system to those of a traditional strain gauge and extensometer. Each method produces accurate results, but the Optotrak system is obviously capable of measuring significantly larger deformations.

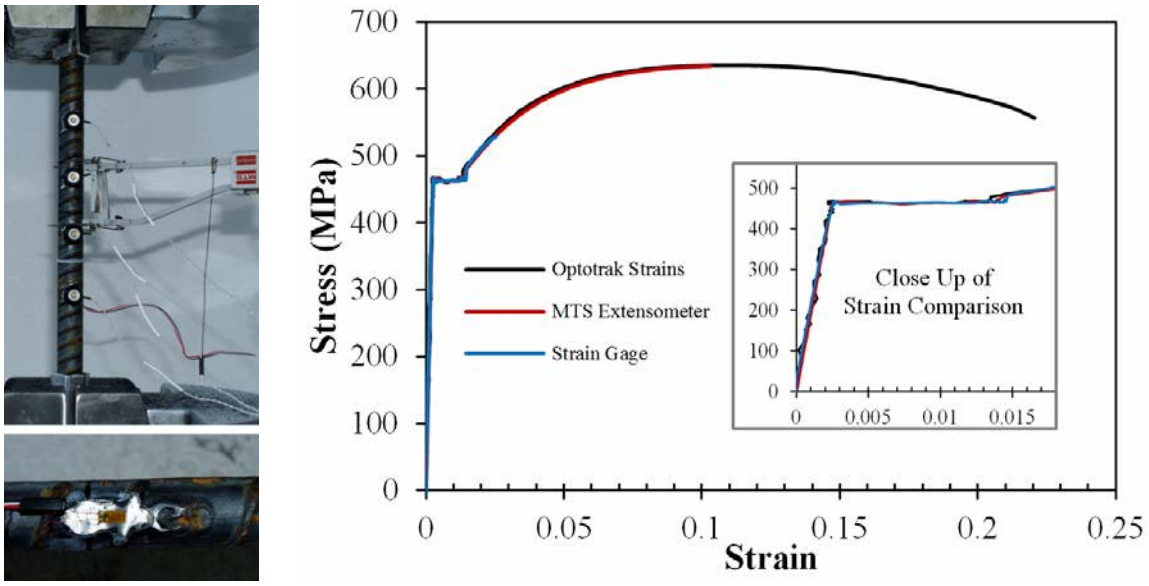

Figure 3.44: Comparison of Optotrak strain measurements to strain gauge and MTS extensometer (Goodnight et al., 2015).

The study conducted by Goodnight, et. al. (2017) used the same instrumentation system and constructed the specimens to allow for the LEDs to be installed directly to the reinforcing steel. The columns were cast with complete cover blockouts to a depth of the outside face of the longitudinal reinforcement over the bottom 4' of the column. The repaired specimens were able to utilize the exposed steel construction to measure the strains in the bars above the repair, but those within the repaired region were no longer visible. The repair sleeve was also instrumented to measure its total deformation, and Repair #4 was actually constructed using similar techniques to the original columns allowing for Optotrak sensors to be placed directly on the longitudinal repair bars. Figure 3.45 (a) shows an example of a repaired column with the new hinge and repair sleeve instrumented, while Figure 3.45 (b) shows Repair #4 with LED targets installed directly on the repair bars. Figure 3.46 shows the real-time computer tracking of the Optotrak data along with a 3D visualization of each target's location.

(a) **(b)**

Figure 3.45: Optotrak sensor installation on (a) typical steel sleeve and; (b) directly to repair bars.

Name	x [mm]	y [mm]	z [mm]
Marker_44	376.149	-335.282	-3750.749
Marker_45	376.830	-282.249	-3749.862
Marker_46	376.140	-232.263	-3751.242
Marker_47	377.317	-183.375	-3749.379
Marker_48	377.019	-133.437	-3750.110
Marker_49	375.921	-85.038	-3752.640
Marker_50	375.785	-36.822	-3752.473
Marker_51	376.501	13.014	-3752.285
Marker_52	376.927	63.270	-3751.766
Marker_53	376.284	112.122	-3752.656
Marker_54	378.655	163.652	-3749.071
Marker_55	377.408	211.579	-3752.340
Marker_56	377.094	262.128	-3752.339
Marker_57	391.317	-373.495	-3621.293
Marker_58	390.478	-323.581	-3621.847
Marker_59	392.046	-276.405	-3621.966
Marker_60	391.273	-227.674	-3621.185

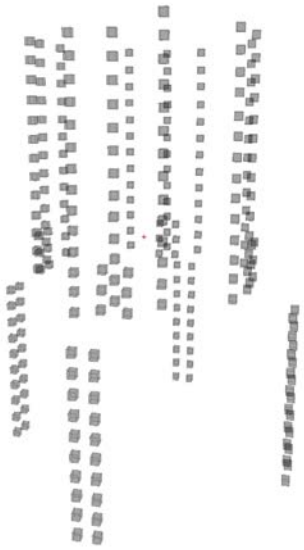

Figure 3.46: Computer visualization of Optotrak targets in 3D space for Repair #3.

3.4.2 Electrical resistance strain gages

For the majority of the tests, the repair bars were concealed inside of the steel sleeve and therefore not visible to the Optotrak cameras. These bars are designed to remain elastic, so it is of

interest to measure their strains to ensure this is the case. Several traditional electrical resistance strain gages were applied over the length of a single repair bar in each of the four extreme faces of the repair, as shown in Figure 3.47. Gages were also installed on the original column extreme fiber longitudinal bars below the top surface of the repair. Each strain gage was protected with a coating of acrylic as well as mastic, and the gages inside the repair, above the footing interface, also had aluminum angles installed to prevent the repair concrete from bearing onto the gage, as shown in Figure 3.48.

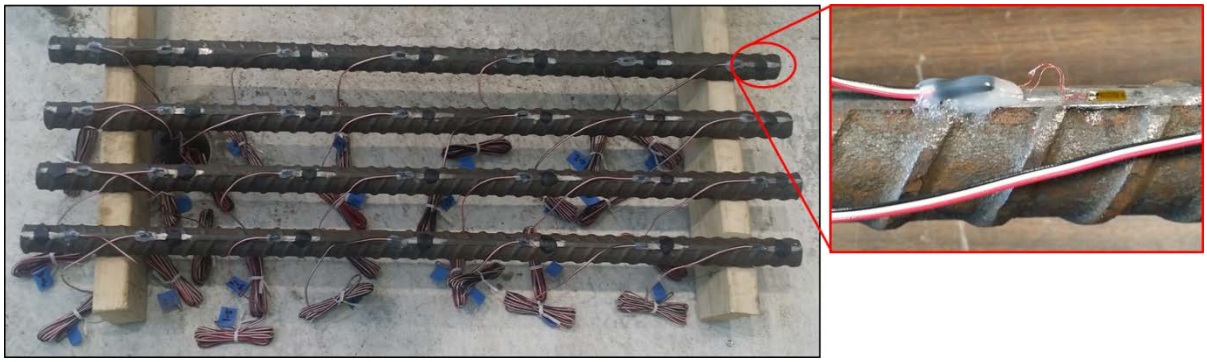

Figure 3.47: Strain gage installation on repair bars.

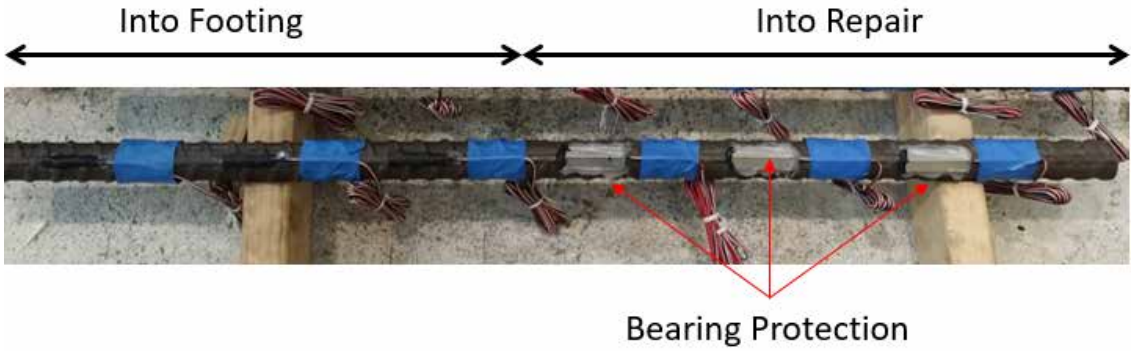

Figure 3.48: Protection of strain gages with aluminum angles.

The strain gage wires were also protected with rubber tubing to prevent the concrete or grout from bearing on, and potentially damaging, them during the experiment. Figure 3.49 shows how each set of strain gage wires were fed through a single rubber tube which would then extend above the top surface of the repair. Despite these measures, many of the strain gages would lose functionality before each test was completed; however, sufficient data was collected due in large part to the number of gages installed. The gages on the original column bars performed particularly poorly, but this is mostly attributed to the strains in these bars exceeding the capacity of the gages.

In future research, it is recommended to investigate more reliable methods of measuring strains on rebar embedded in concrete, especially for bars that extend into the plastic range of deformation.

Figure 3.49: Routing of strain gage wires with rubber tubing.

3.4.3 Electrical Potentiometers

String potentiometers were installed to measure the overall displacement at the top of the column, as described in Section 3.1.2. A total of eight linear potentiometers were also installed on the base of the footing to measure base translation and rotation. Two potentiometers, one vertical and one horizontal, were installed on each face of the column along the primary axes.

3.5 Calculation Methods of Column Deformation

3.5.1 Longitudinal Strains and Bar Buckling

Strains in the longitudinal bars (ε) above the repair are calculated using the Optotrak data collected during the experiment. Figure 3.50 illustrates the various states at which the bars are under throughout the test. Prior to buckling, the strains in the bars are determined simply as the ratio of the change in gage length to the initial gage length, shown in Equation 3-17. Each LED contains X, Y, and Z coordinate data, allowing for the determination of gage length between individual markers at every time step using Equation 3-18. The initial gage length, L_{g0}, is taken as the average of the first 100 recordings for purposes of analysis in this report. Once the bars have buckled, the gage length between the two Optotrak markers no longer accurately represents the

physical state of the bar, as shown in Figure 3.50 (d). When plotted, this behavior manifests as a clear deviation from what is to be expected, as shown in Figure 3.51.

$$\varepsilon = \frac{L_g - L_{g0}}{L_{g0}} \qquad \textit{Equation 3-17}$$

$$L_g = \sqrt{\left(LED2_x - LED1_x\right)^2 + \left(LED2_y - LED1_y\right)^2 + \left(LED2_z - LED1_z\right)^2} \qquad \textit{Equation 3-18}$$

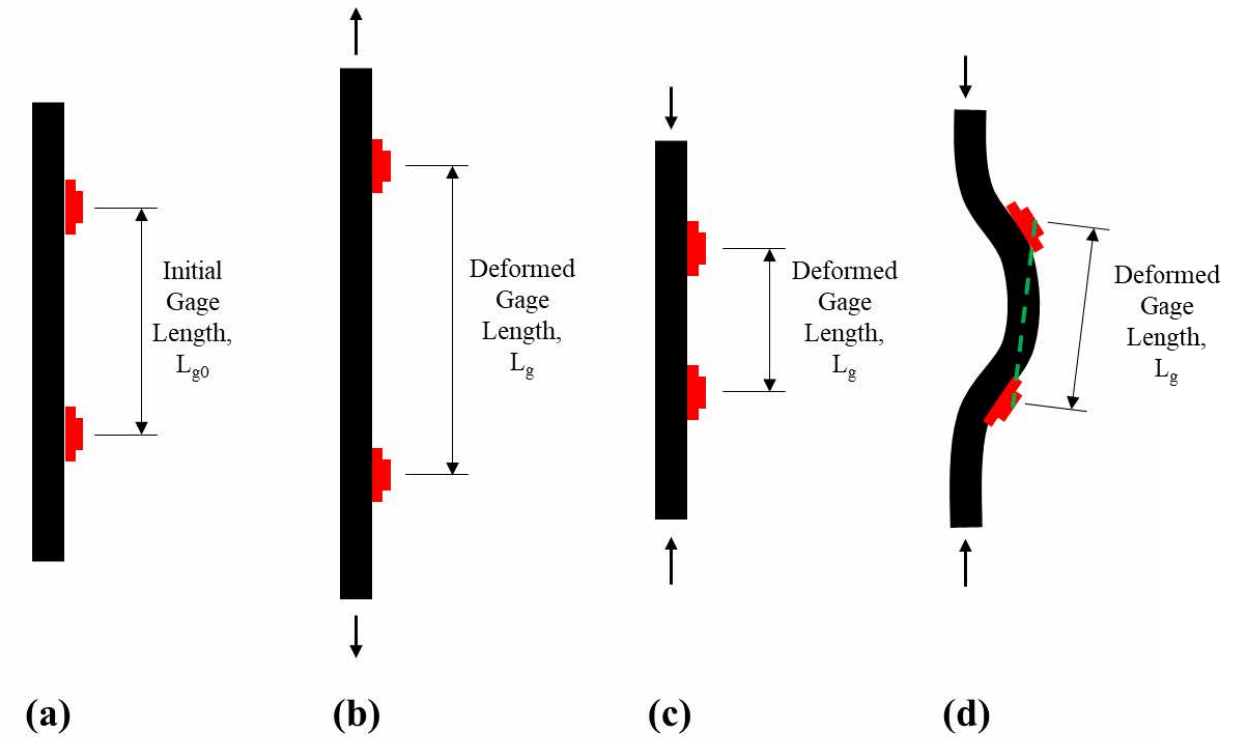

Figure 3.50: Longitudinal bar gage lengths as measured by Optotrak during (a) initial unloaded state; (b) tension state; (c) compression state and; (d) buckled state.

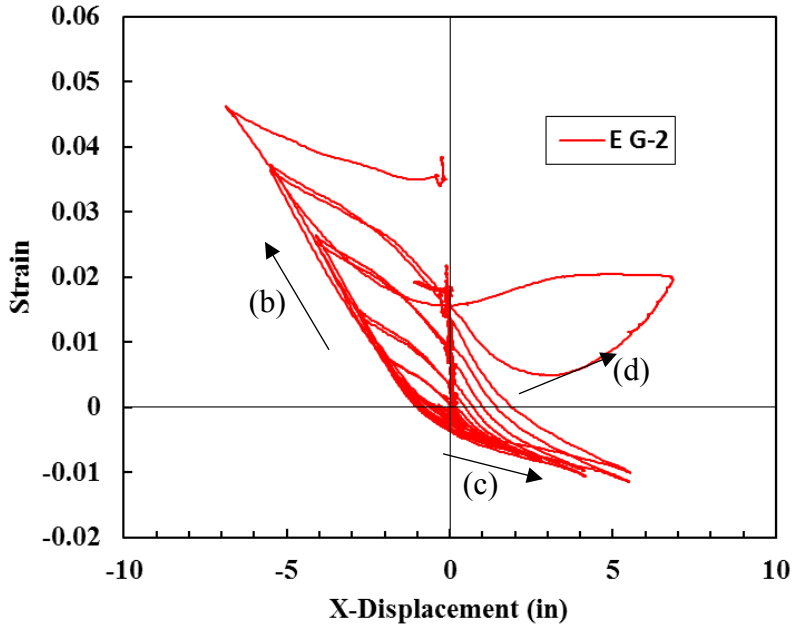

Figure 3.51: Strain vs. Displacement plot of East longitudinal bar in Repair #2 with events labeled corresponding to Figure 3.50.

3.5.2 Column Flexure

Once axial strains are calculated for individual gage lengths, cross sectional distributions of these strains are used to calculate curvatures. Assuming plane sections, the strain distribution at any cross section subjected to an external moment can be idealized as linear, as illustrated in Figure 3.52.

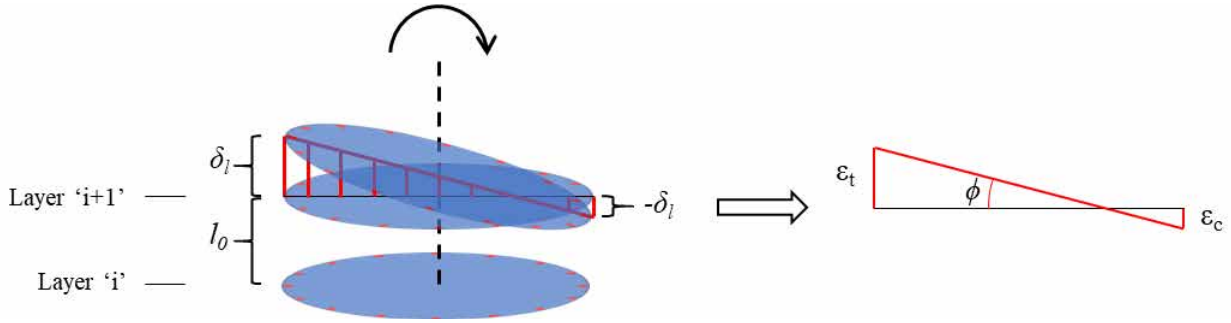

Figure 3.52: Cross section deformation under externally applied moment.

Optotrak LEDs are divided into "layers" of approximately the same elevation where a single LED is represented for each instrumented bar on each layer, as shown in Figure 3.53. The strains calculated at each bar location provide a full cross sectional distribution of the average strain between layers *'i'* and *'i+1'*. The slope of a linear fit through these strains as compared to

their physical location on the cross section represents the average curvature (ϕ) of the column over the gage length between two layers. Figure 3.54 shows an example of this, where each point represents the strains as calculated in the longitudinal bars plotted against their locations along the Y-axis. The red dashed line indicates the linear best fit through these points, the slope of which is taken as the curvature about the X-axis $\left(\phi_x = -0.00118\,{}^{1}/_{in}\right)$. The curvature about the Y-axis would be found in the same manner, except the strains would be plotted against their X-coordinate locations instead.

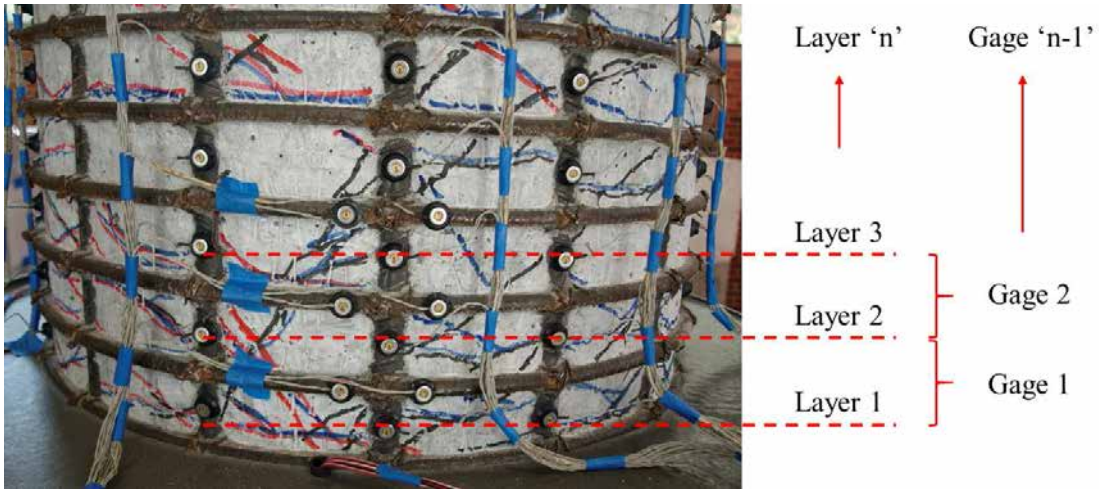

Figure 3.53: Division of column into sectional "layers" by Optotrak markers.

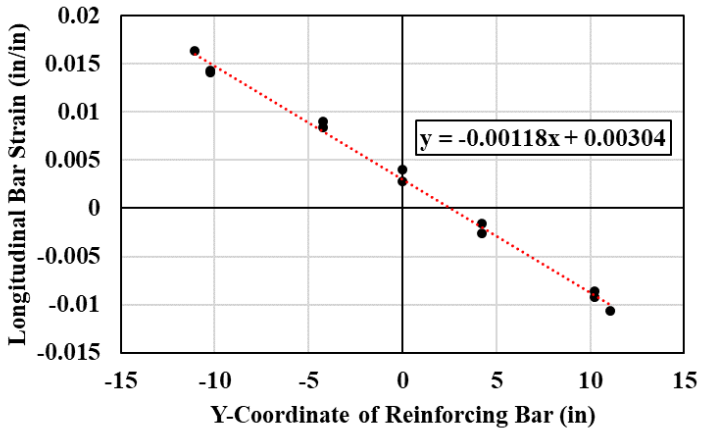

Figure 3.54: Example of linear fit through Optotrak strain data to calculate cross-section curvature.

Once the curvatures at each layer are determined, the flexural contribution to deformation $\left(\Delta_F\right)$ can be calculated using the first moment of area method, outlined in Equation 3-19. The

curvature is assumed to be constant over each gage length between layers on LEDs, resulting in discrete rectangular areas of curvature distribution over the instrumented region, as shown in Figure 3.55. Each of these areas are multiplied by the distance, $\left(\overline{z}_i\right)$, between their centroid and the location of measured displacement to find their individual contribution to the total flexural deformation. The sum of these values, along with that of an assumed triangular distribution of curvature above the instrumented region, represent the total flexural deformation of the column. Equation 3-19 outlines this process, where the first expression relates to the summation of integrated curvatures over the instrumented region, the second expression calculates the triangular distribution above the topmost layer of LEDs, and *n* is the total number of LED layers. The gage length between each layer, $Gage_i$, is taken as the difference in average elevations of the LEDs in each layer.

$$\Delta_F = \left[\sum_{i=1}^{i=n-1} \phi_i \cdot Gage_i \cdot \overline{z}_i\right] + \left[\frac{\phi_{n-1} \cdot \left(\overline{z}_{n-1} - Gage_{n-1}/2\right)^2}{3}\right] \qquad \textit{Equation 3-19}$$

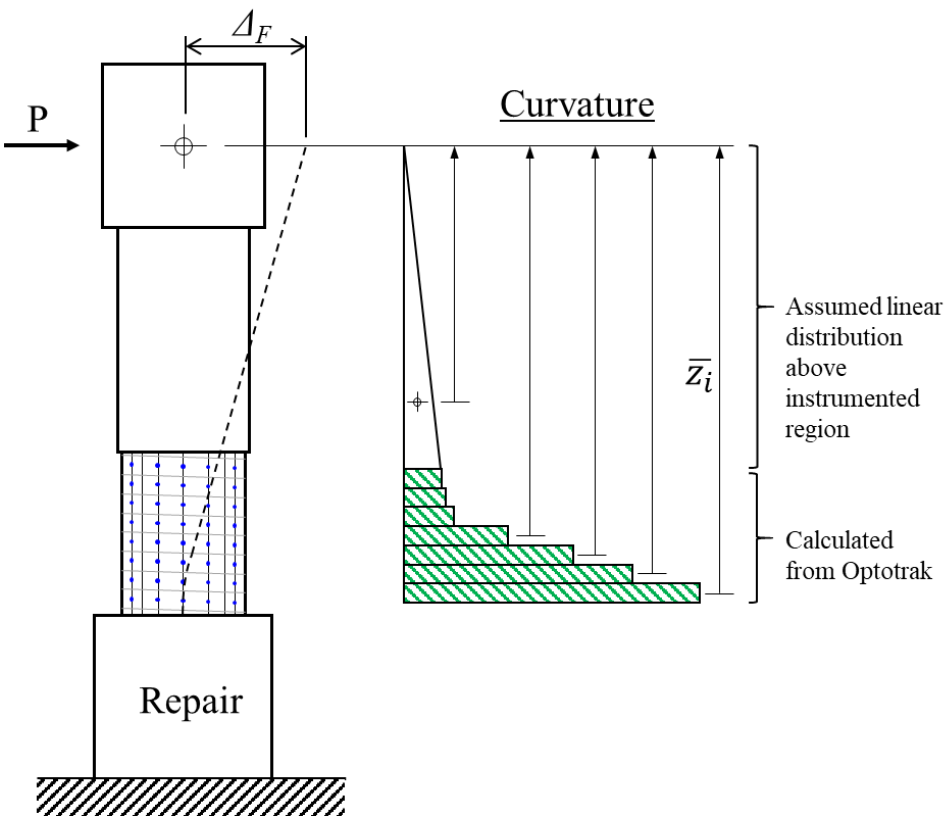

Figure 3.55: Curvature distribution over column height.

3.5.3 Column and Repair Base Rotation

In addition to flexural deformation, column base rotation from strain penetration and rigid body rotation of the repair contribute significantly to the overall global displacements. Figure 3.57 illustrates how each of these components behave when isolated from other modes of deformation. Calculation of each is similar to that of section curvature, except rotations are found using absolute relative displacement of the LEDs rather than strains. Assuming small angles, the repair rotation (θ_{RR}) is found as the slope of the linear fit to the change in absolute vertical position of the bottom most layer of LEDs on the repair compared to their locations on the cross section, as shown in Figure 3.56 (a). Rotation of the column due to strain penetration into the repair (θ_{SP}) is found using the same method for the bottom most layer of LEDs on the longitudinal bars, as shown in Figure 3.56 (b). Noting that these calculations are based on the absolute change in position of the LEDs and not relative change, θ_{SP} includes the rotation due to θ_{RR} as well. Thus, when calculating the displacement due to each component, the repair rotation angle must be subtracted from the calculated strain penetration rotation angle so as to not double count its contribution,

resulting in Equation 3-20 and Equation 3-21 which are used to find the top of column displacements due to repair rotation and column strain penetration respectively.

$$\Delta_{RR} = \theta_{RR} \cdot L_c \qquad \textit{Equation 3-20}$$

$$\Delta_{SP} = \left(\theta_{SP} - \theta_{RR}\right) \cdot \left(L_c - L_r\right) \qquad \textit{Equation 3-21}$$

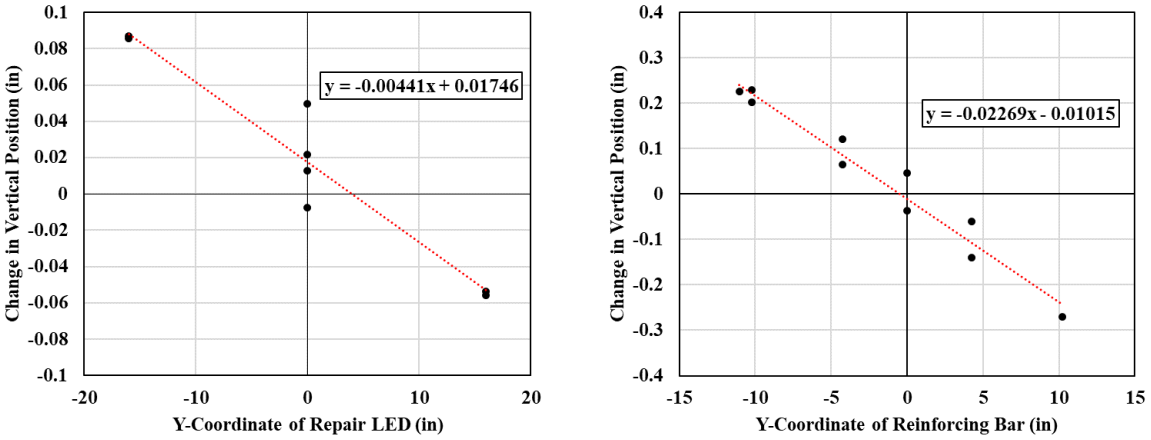

(a) **(b)**

Figure 3.56: Example of linear fit through Optotrak data to calculate (a) Repair rotation and; (b) Column strain penetration rotation.

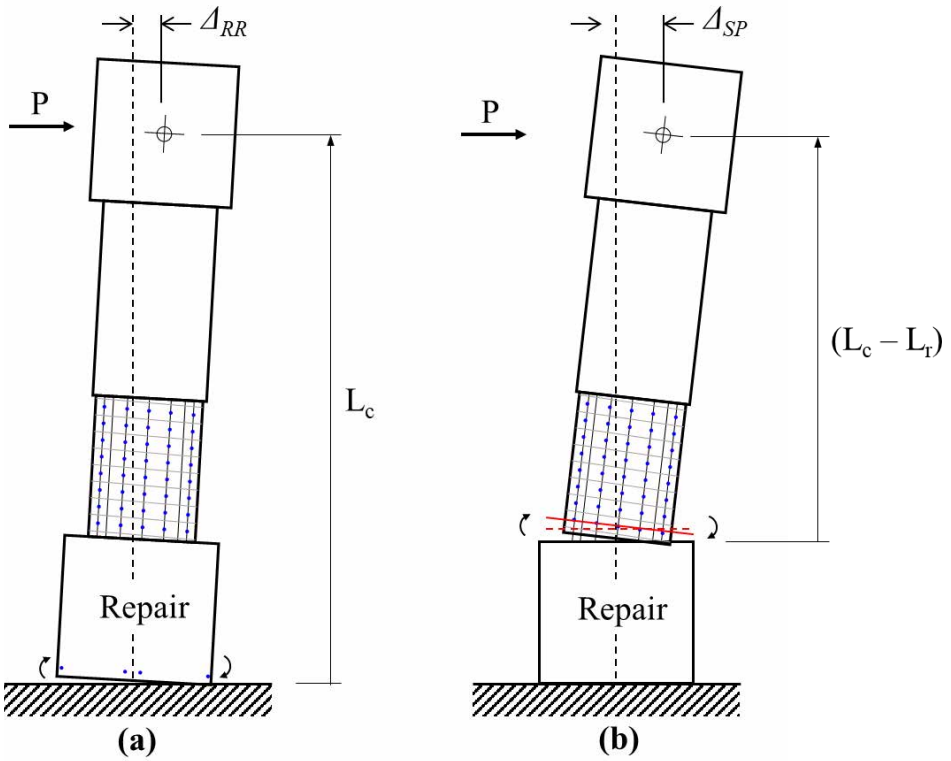

Figure 3.57: Isolated components of column displacement from (a) Rigid repair rotation and; (b) Rotation from strain penetration of column bars into repair.

3.5.4 Footing Translation and Rotation

Top of column displacements due to footing translation and rotation were subtracted from the measured displacements both actively during the test and during post processing. Translations were taken simply as the average readings of the horizontal linear potentiometers placed at the base of the footing along each axis. Rotations were taken as the difference between vertical potentiometer readings on opposite faces divided by the footing width along that direction. This angle was then multiplied by the distance from the bottom of footing to top of column to obtain the corresponding displacement at that location. In each test, the overall contribution to deformation from both of these factors was negligible.

Chapter 4: Experimental Observations

Each of the six repaired columns were designed, constructed and previously tested as part of a separate research program (Goodnight et al., 2017), under which they were exposed to a bidirectional cyclic loading history through failure. The typical damage state at the conclusion of each initial test included buckling in the majority of the longitudinal bars and some bar fractures. To investigate more severe damage states, additional damage was imposed manually prior to the installation of the repair. Each column specimen is 108 inches in height, from the top of footing to the center of loading, with an outer diameter of 24 inches (L/D = 4.56) and axial load of 191 kips ($P / f'_c A_g$ = 6.0 to 7.5%). A summary of each test's performance is shown in Table 4.1, and the reinforcement details, material properties, and damage states are outlined in Table 4.2. The following sections are meant to describe the specific considerations of each test and provide insight into how each repair performed from an experimental observations perspective. Further discussion on the significance of the data and how it will help to inform the design of future repairs is provided in Chapter 5.

Table 4.1: Summary of original and repaired column performance.

	Repair #:	1	2	3	4	5	6
Original Column	Δ_{max} (in.)	8.24	8.25	8.24	7.35	8.57	8.83
	F_{max} (kips)	79.9	78.0	77.7	62.4	64.2	79.9
	$\varepsilon_{t,max}$	0.044	0.049	0.047	0.034	0.051	0.053
	$\mu_{\Delta,max}$	6	6	6	6	7	6.5
Repair	Δ_{max} (in.)	8.31	8.28	6.88	7.51	5.0	8.9
	F_{max} (kips)	95.1	86.2	80.6	75.4	73.2	93.1
	$\mu_{\Delta,max}$	6	6	5	6	4	6.5

Table 4.2: Column Repair Test Matrix.

	Repair #:	1	2	3	4	5	6
Original Column	**Long. Steel ρ_l**	(16) #7 2.1%	(16) #7 2.1%	(16) #7 2.1%	(16) #6 1.6%	(16) #6 1.6%	(16) #7 2.1%
	σ_y (ksi)	71.2	71.2	71.2	70.3	70.3	69.6
	σ_u (ksi)	97.9	97.9	97.9	98.7	98.7	96.7
	Trans. Steel ρ_v	#3 @ 2in. 1.0%	#3 @ 2in. 1.0%	#3 @ 2in. 1.0%	#3 @ 2.75 in. 0.7%	#3 @ 2in. 1.0%	#3 @ 1.5in. 1.3%
	σ_y (ksi)	67.6	67.6	67.6	63.9	63.9	69.6
	σ_u (ksi)	105.6	105.6	105.6	93.6	93.6	96.7
	Column f'_c (ksi)	7.81	7.68	7.60	6.13	6.11	6.13
	Damage State	All long. bars buckled	3 extreme fiber bars on N & S faces fractured, all other bars buckled	All long. bars buckled, spiral fracture, initial torsional deformation	Extreme fiber bar on S face fractured, all other bars buckled	2 bars on E face and 1 on W face fractured, all others buckled, 1.5% residual drift in W direction	3 extreme fiber bars on N & S faces fractured, all other bars buckled
Repair	**Long. Steel**	(12) #10	(12) #10	(16) #7	(12) #7	(16) #7	(12) #10
	σ_y (ksi)	83.6	83.6	90.1	84.3	83.2	83.6
	Trans. Steel ρ_v	11ga A36 steel sleeve 1.5%	11ga A36 steel sleeve 1.5%	11ga A36 steel sleeve 1.5%	#3 @ 1.5in 1.0%	11ga A36 steel sleeve 1.5%	11ga A36 steel sleeve 1.5%
	σ_{yv} (ksi)	43.0	43.0	43.0	67.5	48.2	48.2
	Backfill Material	Grout	Grout	Grout	Ready-Mix Concrete	Ready-Mix Concrete	Concrete / Grout
	Repair f'_c (ksi)	8.20	7.20	7.96	4.84	3.84	4.86 11.3

4.1 Repair #1

4.1.1 Summary of Repair Considerations

The objective of the first repair is to establish a lower bound of damage for which this technique is applicable. Simpler, less involved methods have been shown to be acceptable for damage states preceding bar buckling, therefore a column with each of the longitudinal bars buckled was selected as the minimum damage state for which this repair would be utilized. The initial state of the column prior to repair installation is shown in Figure 4.1. The repair was designed using a moment-curvature analysis of the composite cross section consisting of the original column and the repair. The design strength was determined as the moment at which the extreme longitudinal steel fiber in the repair reached first yield, assuming steel strength of 60 ksi and yield strain of $\varepsilon_y = 0.002$. The repair height was chosen to be 22 in., corresponding to the height at which the previous tensile strain was limited to approximately 0.02, which resulted in design forces of:

$$M_R = \frac{M_o \cdot L_C}{L_C - L_R} = \frac{(680kip \cdot ft)(9\,ft)}{9\,ft - 1.833\,ft} = 854kip \cdot ft$$

$$V_R = \frac{M_o}{L_C - L_R} = \frac{(680kip \cdot ft)}{9\,ft - 1.833\,ft} = 94.9kips$$

Where M_o is the ultimate moment capacity of the original column cross section, which was found via a moment-curvature analysis using known material properties; however, in a typical design, overstrength factors would have been used on nominal material properties. A repair cross section of 12 #10 repair bars, along with the 16 original buckled #7 bars, was found to have a moment capacity of 836 kip-ft. Although this capacity falls just short of the calculated demand, it is recognized that the A706 Grade 80 longitudinal bars, which are actually used in the repair as discussed in Section 3.2.2, would provide additional strength not accounted for in the initial design. Therefore, this repair cross section was selected and assumed to provide adequate strength to ensure relocation of the plastic hinge. Furthermore, the repair is instrumented such that the previous design assumptions could be verified and ensure the repair remains elastic. An 11-gauge

A36 hot rolled steel sheet was used for the transverse steel along with the BASF MasterFlow® 928 prepackaged grout mix for the backfill. Figure 4.1 shows the damage state of the original column and Figure 4.2 shows the layout of the repaired cross-section along with the definition of instrumentation tags referenced later in this section.

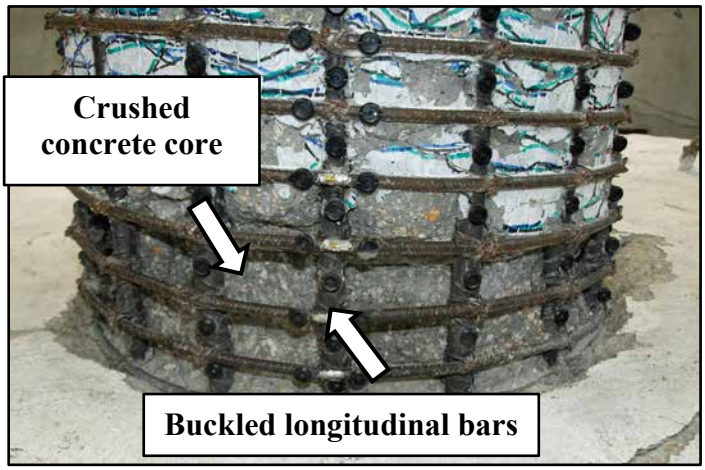

Figure 4.1: Repair #1 damage state prior to repair installation.

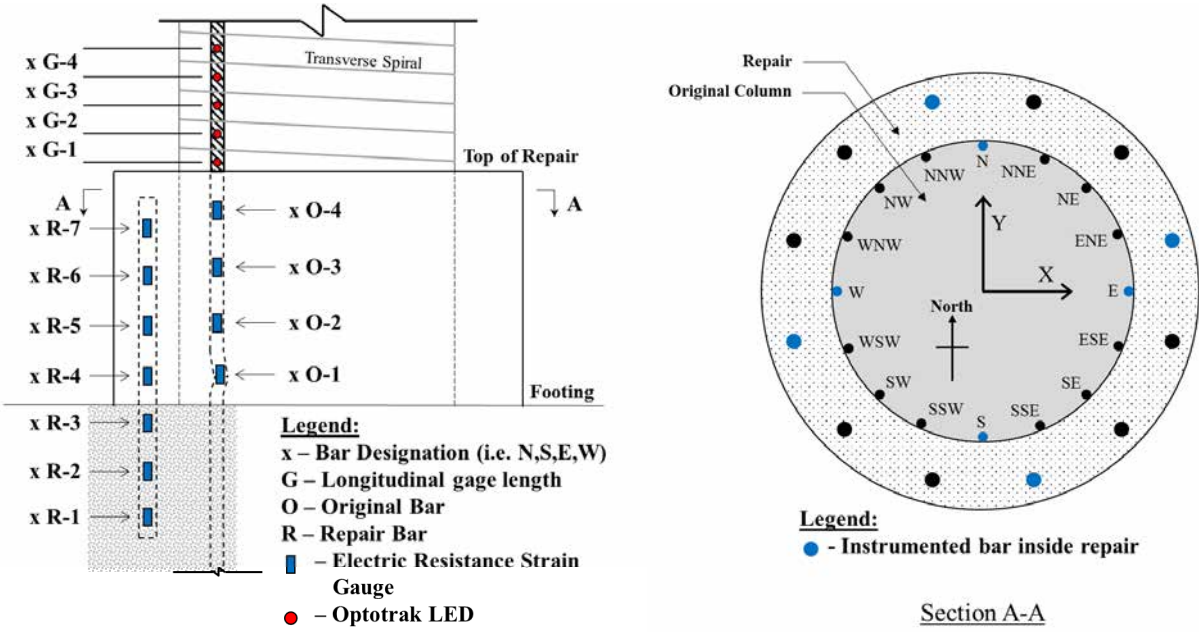

Figure 4.2: Repair #1 Instrumentation labels and repair cross section layout.

Table 4.3: Repair #1 summary of values of interest.

Original Column Properties	
Load History	Asymmetric Two Cycle Set
Column Geometry	L = 9 *ft*, D = 24 *in*, (L/D = 4.56)
Longitudinal Steel Detailing	16 #7 for $\rho_l = A_{st} / A_g$ = 2.1%
Longitudinal Steel Properties	f_y = 71.2 *ksi*, f_u = 97.9 *ksi*, ε_y = 0.00254
Transverse Steel Detailing	#3 @ 2 *in for* $\rho_s = 4A_{sp} / D'$ s = 1.0%
Transverse Steel Properties	f_y = 67.6 *ksi*, f_u = 105.6 *ksi*, ε_y = 0.00448
Column Concrete Strength	f'_c = 7.81 *ksi*
Footing Concrete Strength	f'_c = 9.67 *ksi*
Equivalent Yield Displacement	Δ_y = 1.37 *in*
Damage State	Buckling of all longitudinal bars
Repair Properties	
Load History	Symmetric Two Cycle Set
Repair Geometry	H = 22 *in*, D = 32 *in*
Longitudinal Steel Detailing	12 #10 *A706 Grade 80*
Longitudinal Steel Properties	f_y = 83.6 *ksi*, f_u = 114.9 *ksi*, ε_y = 0.0030
Transverse Steel Detailing	11ga A36 steel sheet $\rho_s = 4t_j / D'$ = 1.5%
Transverse Steel Properties	f_y = 43.0 *ksi*, f_u = 54.6 *ksi*, ε_y = 0.00148
Repair Grout Strength	f'_c = 8.20 *ksi*

4.1.2 Discussion of test results

4.1.2.1 Summary of Events

Overall, the repair performed as expected with the plastic hinge developing just above the annular ring and the strength and displacement capacities restored. Visible cracks began to appear on top of the repair during the F'$_y$ cycle as shown in Figure 4.3 (a). These cracks grew progressively larger through later cycles with the top portion of repair grout spalling away, as seen in Figure 4.3 (b). The first cycles of $\mu_{\Delta 3}$ = 4.2 in. showed signs of core concrete crushing with further deterioration through ductility cycles 4 and 5, shown in Figure 4.4. Finally, visible buckling was observed during $\mu_{\Delta 6}$ = 8.22 in. along with complete crushing of the concrete core and spalling of the top surface of the repair concrete shown in Figure 4.5. The test was terminated after visible buckling was observed in 13 of the 16 longitudinal bars in the relocated plastic hinge above the repair.

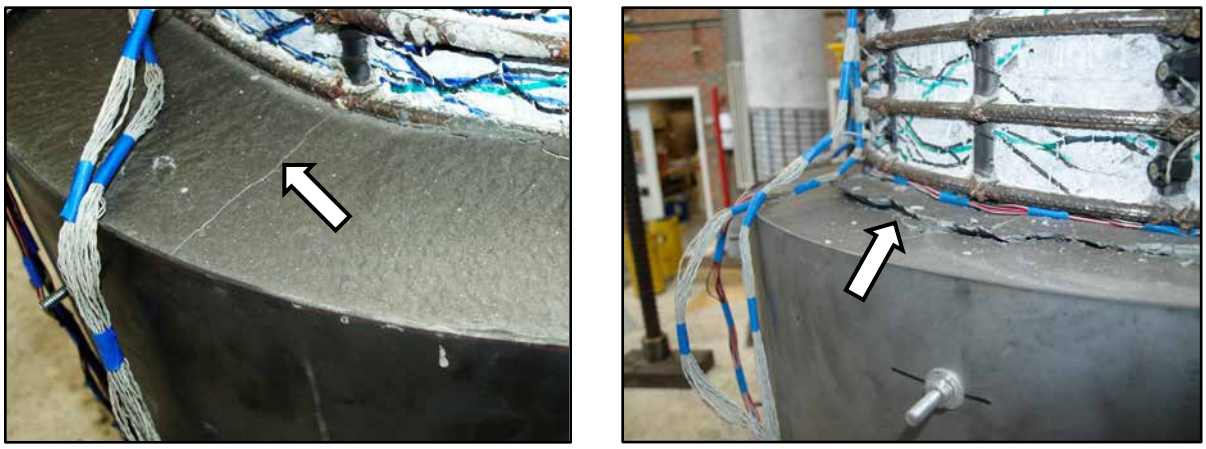

(a) **(b)**

Figure 4.3: Repair #1 (a) Slight cracking on top of repair during F'$_y$ cycle; (b) progression of top surface cracking during cycle $\mu_{\Delta 2}^{-2x}$.

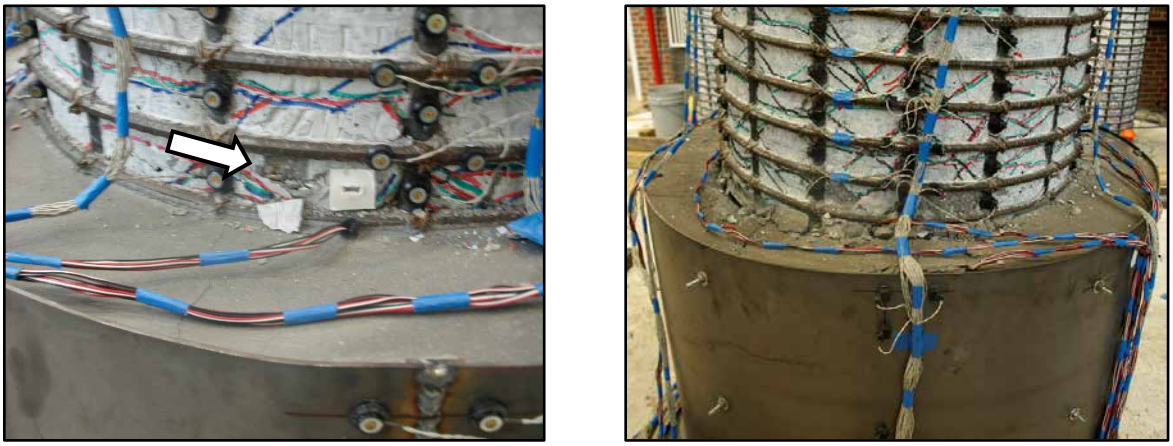

(a) **(b)**

Figure 4.4: Repair #1 (a) Onset of core crushing during cycle $\mu_{\Delta 3}^{-y}$; (b) Further deterioration of hinge core and top of repair region during $\mu_{\Delta 4}^{-2y}$.

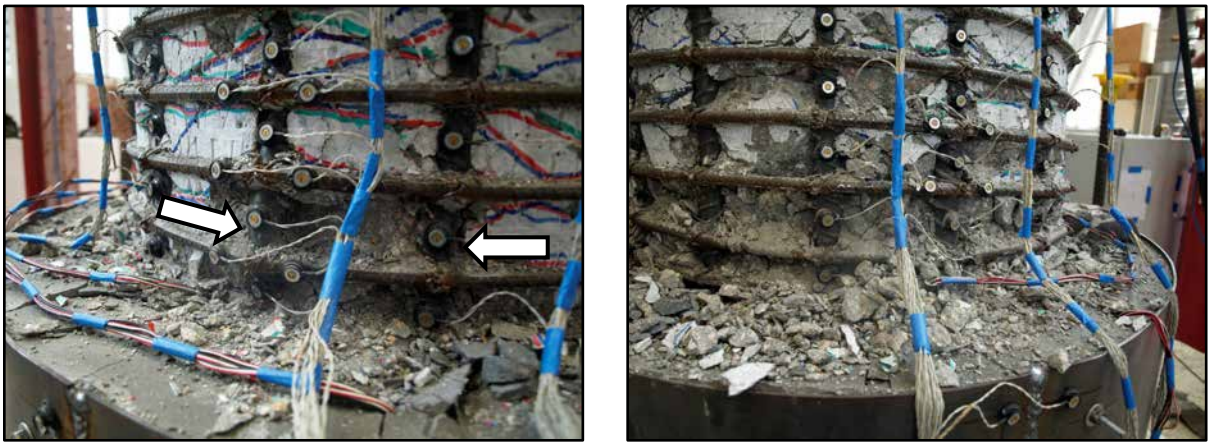

(a) **(b)**

Figure 4.5: Repair #1 (a) Buckled longitudinal bars during $\mu_{\Delta 6}^{-2y}$; (b) Final state of relocated plastic hinge.

4.1.2.2 Global Column Response

The global force vs. displacement hysteresis for Repair #1 in the Y and X directions is plotted in Figure 4.6 through Figure 4.9 below. Figure 4.6 and Figure 4.7 compare the repaired column response to that of Load Path Test #4 in the Y and X directions respectively. This corresponds to a different specimen, but nominally identical in terms of longitudinal and transverse reinforcement as well as symmetric two-cycle set load history. Figure 4.8 and Figure 4.9 alternatively compare the response of the repaired column to that of Load Path Test #6, which corresponds to the asymmetric two-cycle set that was initially run on the actual specimen on which Repair #1 was installed. The asymmetric two-cycle set protocol follows the same load history in the Y-direction, but the X-direction lags behind by two full cycles following the first yield cycle, as can be seen in the figures. Both sets of plots show that the repaired column restores the overall strength and displacement capacity of the original specimen, with the original and repaired columns both reaching a maximum ductility of $\mu_{\Delta 6}$ at displacement of 8.31 in. and a peak shear force of 95.1 kips, an increase from the original column strength of 79.9 kips. The resulting base moment demand was 855.9 kip-ft. which slightly exceeded the design moment of 836 kip-ft., but there was no noticeable damage to the repair that would indicate inelastic behavior. This observation is confirmed by the strain data that was collected from inside of the repair as well, which is discussed in the following section.

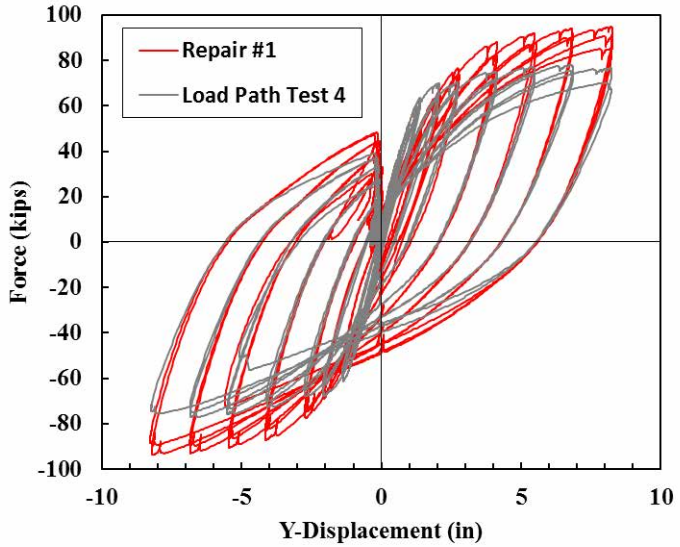

Figure 4.6: Repair #1 Y-Direction Force vs. Displacement comparison to Load Path Test 4.

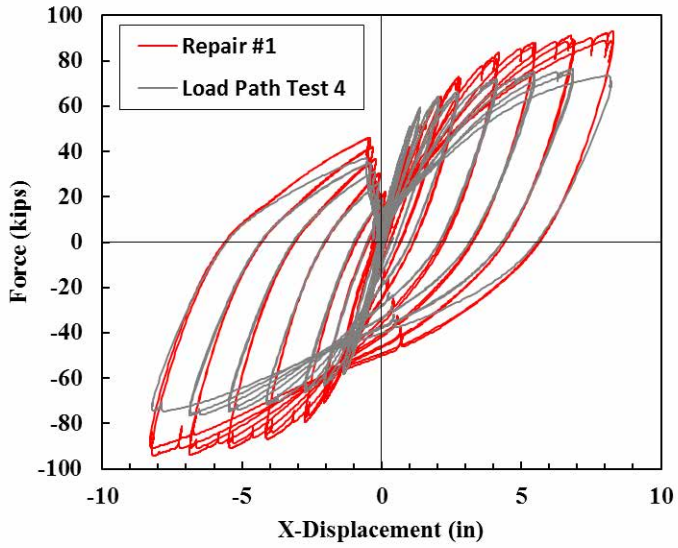

Figure 4.7: Repair #1 X-Direction Force vs. Displacement comparison to Load Path Test 4.

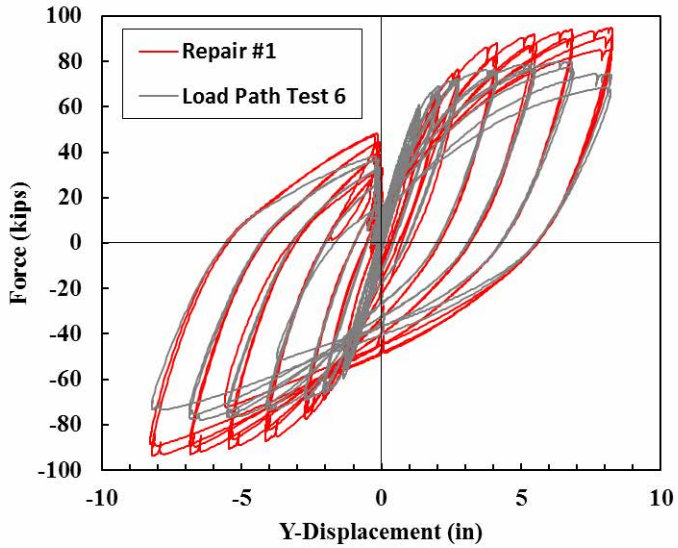

Figure 4.8: Repair #1 Y-Direction Force vs. Displacement comparison to Load Path Test 6.

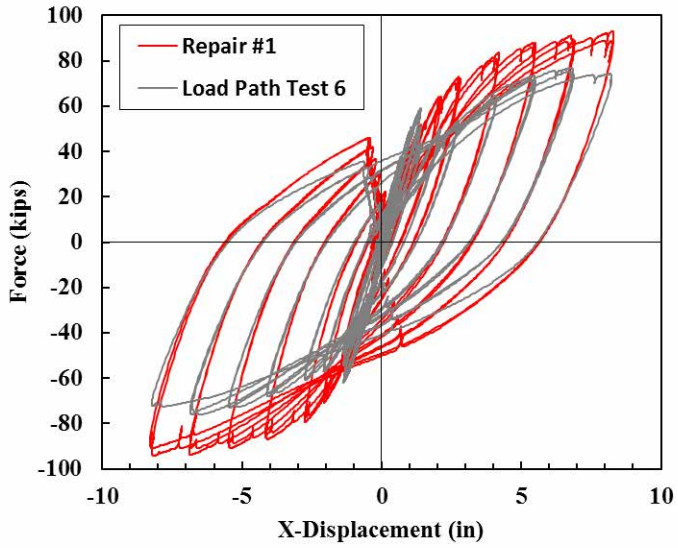

Figure 4.9: Repair #1 X-Direction Force vs. Displacement comparison to Load Path Test 6.

4.1.2.3 Local Behavior

The instrumentation of the repaired column allowed for the calculation of strains in both the repaired region and the column region above the repair. Figure 4.10 and Figure 4.11 show the strain vs. displacement histories of the longitudinal steel bars directly above the repair region. The peak strains in each of these bars reach well above yield in both the tension and compression directions. Tension strains of approximately 0.04 and compression strains of -0.01 to -0.02 are observed on all four faces which indicates significant plastic behavior at this location, as observed during the test. Comparing these strains to those of the original test at approximately the same location within the plastic hinge, shown in grey, reveals that the strains in the repaired column's plastic hinge are about equal to, or lower than, those in the original column for a given tip displacement. The notation of 'G-2' for Load Path Test #6 refers to the second Optotrak gage length above the footing, approximately the same distance above the repair as the second gage length in Repair #1. Furthermore, the onset of measurable bar buckling appears to be at approximately the same strain for both the repaired and original columns, indicating that the strain limit states for new columns would likely be applicable for the repaired columns as well so long as the deformation can be accurately predicted.

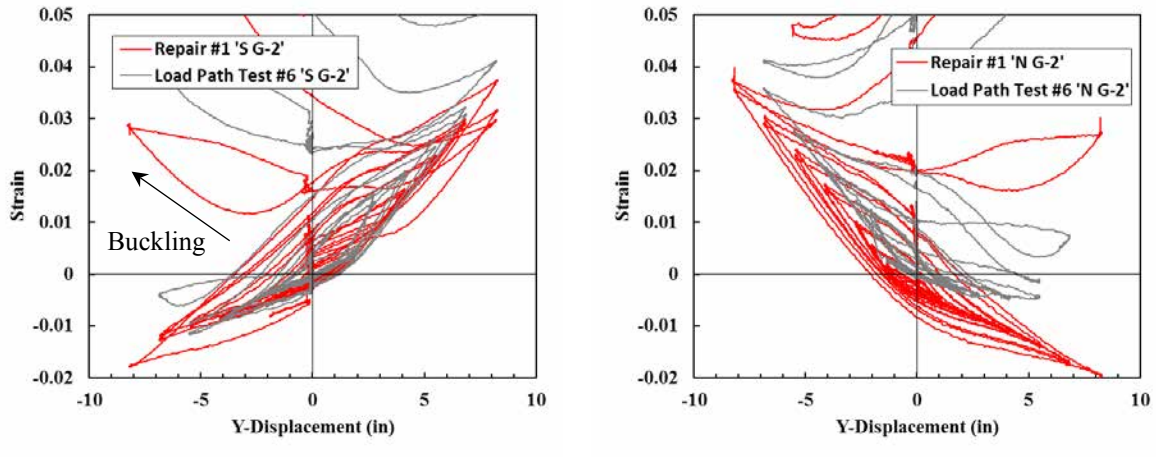

(a) **(b)**

Figure 4.10: Repair #1 Strain vs. Y-Displacement above the repaired region on the (a) South and (b) North faces of the column.

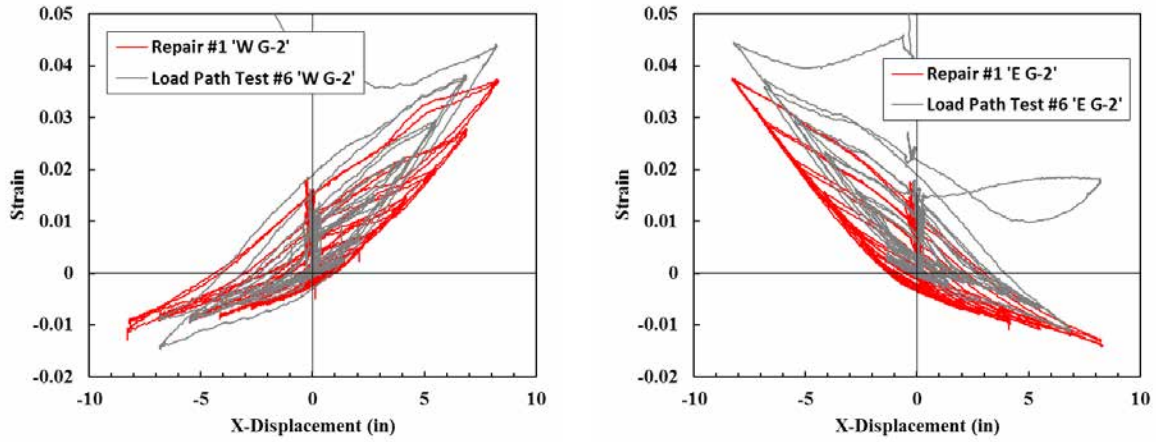

(a) **(b)**

Figure 4.11: Repair #1 Strain vs. X-Displacement above the repaired region on the (a) West and (b) East faces of the column.

The measured longitudinal strains in the repair bars were far below yield with a maximum tension strain of 0.0011 in gauge 'S R-4'. This was despite the forces in the column actually exceeding the design strength of the repair cross section, as discussed in the previous section. Figure 4.12 and Figure 4.13 show the strain vs. displacement histories for the original column bars and repair bars at the location just above the footing interface. Noting that the strains in the original column bars exceed those of the repair bars in each plot, it is clear that the strain distribution along the cross section is not linear as initially anticipated. Instead, the high plastic strains at the relocated hinge are penetrating farther into the repair than expected, resulting in a far greater strength contribution from the initially buckled bars than originally accounted for and lower demand on the

newly installed repair bars. While this appears to have little impact on the performance of the repaired column, it will need to be accounted for in both the design of the repair itself and in describing the means by which forces are transferred between the original column and the repair.

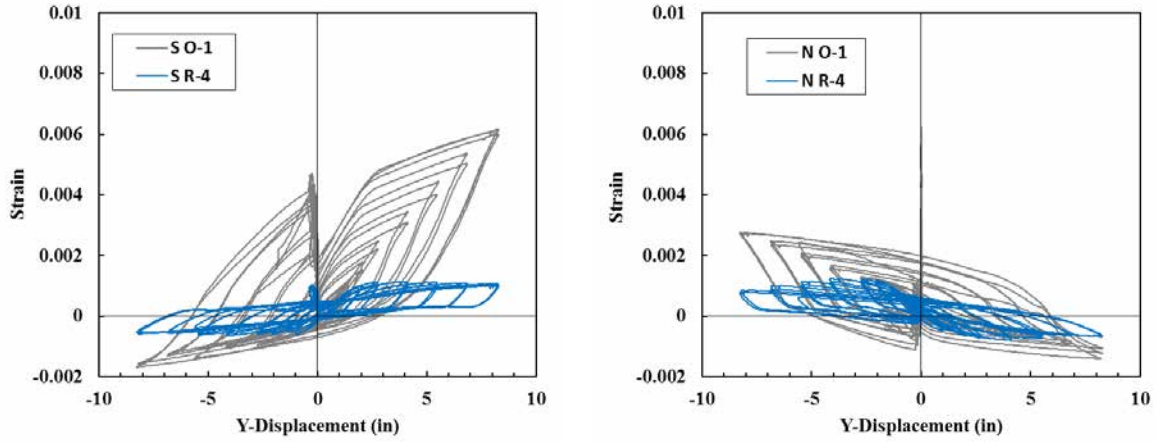

(a) **(b)**

Figure 4.12: Repair #1 Strain vs. Y-Displacement inside the repaired region on the (a) South and (b) North faces of the column.

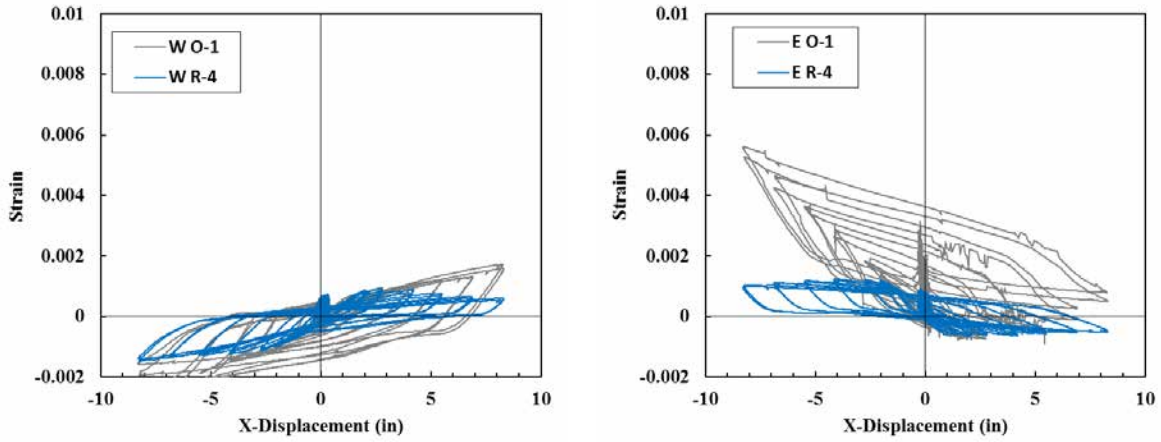

(a) **(b)**

Figure 4.13: Repair #1 Strain vs. X-Displacement inside the repaired region on the (a) West and (b) East faces of the column.

4.2 Repair #2

4.2.1 Summary of Repair Considerations

The second repair aimed to investigate a more extensively damaged specimen and establish whether columns with several fractured longitudinal bars could be repaired using this technique. This test included three fractured bars on the extreme North and South faces for a total of six out of sixteen bars fractured at the base cross section. Figure 4.14 shows the extent of damage in the original column prior to installation of the repair. The three fractured bars on this face are mirrored on the opposite side of the column. The concrete core is considerably deteriorated and the remaining bars are buckled, representing levels of damage similar to that of Repair #1. Since rapid deployment is of interest, there was no attempt to patch or splice the fractured bars prior to installing the repair. Although the demand on the repair is certainly higher than in Repair #1 with no fractured bars, the geometry and configuration of the repair were unchanged following the results of the first test since the observed strains were well below predicted values.

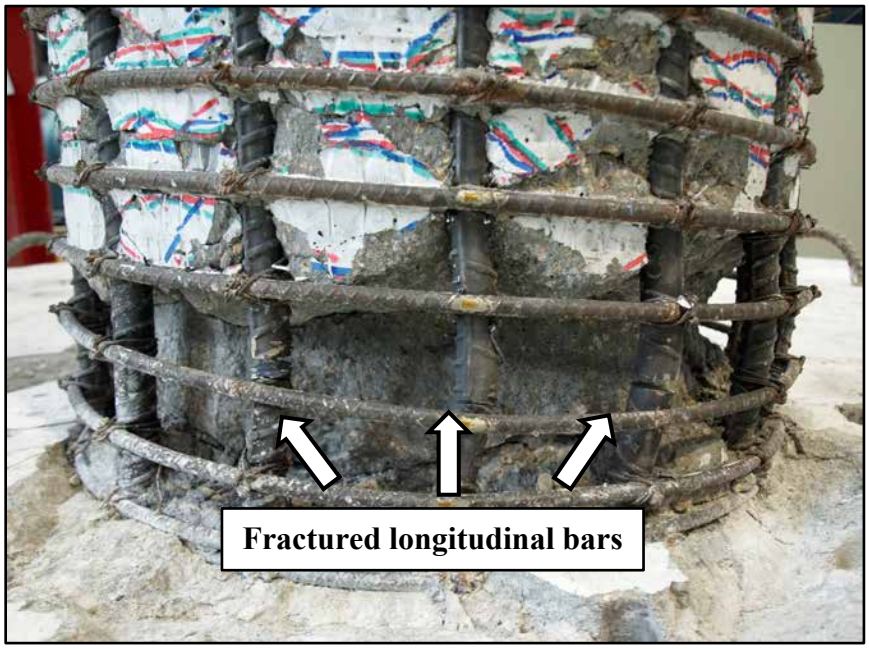

Figure 4.14: Repair #2 damage state prior to repair installation.

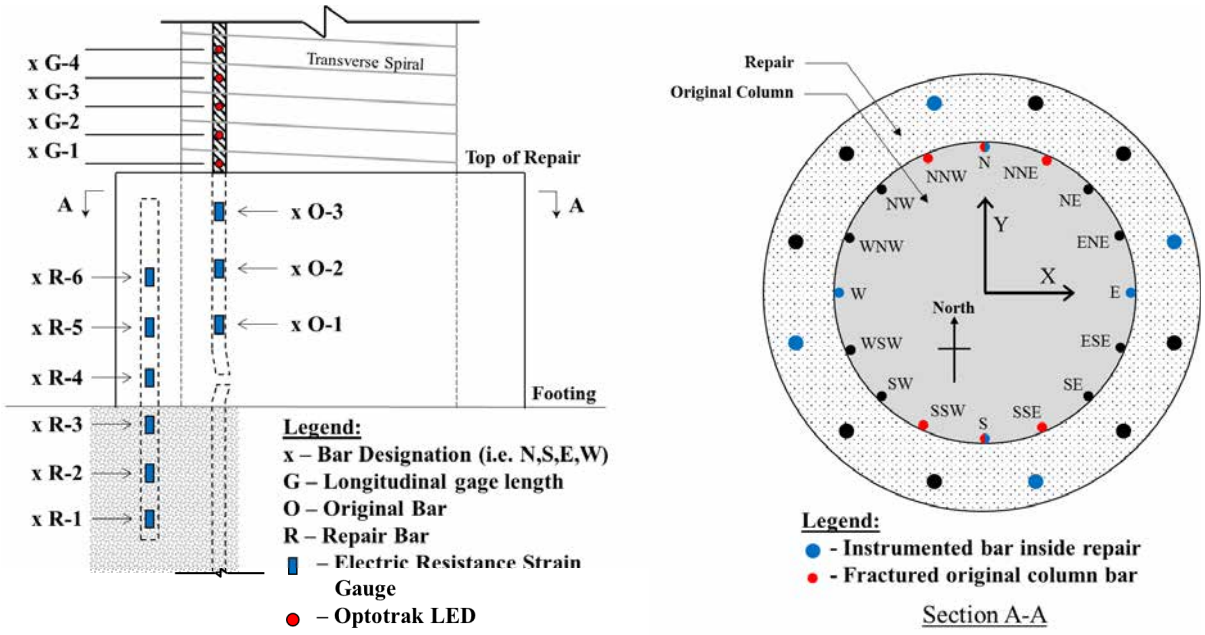

Figure 4.15: Repair #2 Instrumentation labels and repair cross section layout.

Table 4.4: Repair #2 summary of values of interest.

Original Column Properties	
Load History	Symmetric Two Cycle Set
Column Geometry	L = 9 *ft*, D = 24 *in*, (L/D = 4.56)
Longitudinal Steel Detailing	16 #7 for $\rho_l = A_{st} / A_g$ = 2.1%
Longitudinal Steel Properties	f_y = 71.2 *ksi*, f_u = 97.9 *ksi*, ε_y = 0.00254
Transverse Steel Detailing	#3 @ 2 *in for* $\rho_s = 4A_{sp} / D'$ *s* = 1.0%
Transverse Steel Properties	f_y = 67.6 *ksi*, f_u = 105.6 *ksi*, ε_y = 0.00448
Column Concrete Strength	f'_c = 7.68 *ksi*
Footing Concrete Strength	f'_c = 10.33 *ksi*
Equivalent Yield Displacement	Δ_y = 1.37 *in*
Damage State	Buckling of all longitudinal bars and fracture SSW, S, SSE, NNE, N, and NNW bars
Repair Properties	
Load History	Symmetric Two Cycle Set
Repair Geometry	H = 22 *in*, D = 32 *in*
Longitudinal Steel Detailing	12 #10 *A706 Grade 80*
Longitudinal Steel Properties	f_y = 83.6 *ksi*, f_u = 114.9 *ksi*, ε_y = 0.0030
Transverse Steel Detailing	11ga A36 steel sheet $\rho_s = 4t_j / D'$ = 1.5%
Transverse Steel Properties	f_y = 43.0 *ksi*, f_u = 54.6 *ksi*, ε_y = 0.00148
Repair Grout Strength	f'_c = 7.16 *ksi*

4.2.2 Discussion of test results

4.2.2.1 Summary of Events

The overall performance of Repair #2 was similar to that of Repair #1 with the strength and displacement capacities restored to that of the original column. Visible cracks began to appear on top of the repair during the F'_y cycles, as shown in Figure 4.16 (a), and grew progressively larger through later cycles as it had in the first test, shown in Figure 4.16 (b). Core crushing also began during the $\mu_{\Delta 3}$ cycles, as it had during the Repair #1 test, with damage progressing through further deterioration of the core and complete crushing of the top repair surface during ductility cycles 4 and 5, shown in Figure 4.17. Finally, visible buckling was observed during the first cycle of $\mu_{\Delta 6}^{+1x} = 8.22$ in. and was immediately followed by fracture of the SE and ESE bars on the subsequent cycle of $\mu_{\Delta 6}^{-1x}$, shown in Figure 4.18, thus terminating the test. Following the completion of the test, the specimen was deconstructed for removal from the lab allowing for the image in Figure 4.19. With the repair jacket removed, there is a clear visual of the initial and relocated plastic hinge regions, defined by the buckled longitudinal bars, separated by a span of straight reinforcing bars along the height of the repair. This is shown simply to illustrate the effectiveness of the repair in relocating the plastic hinge as it is intended.

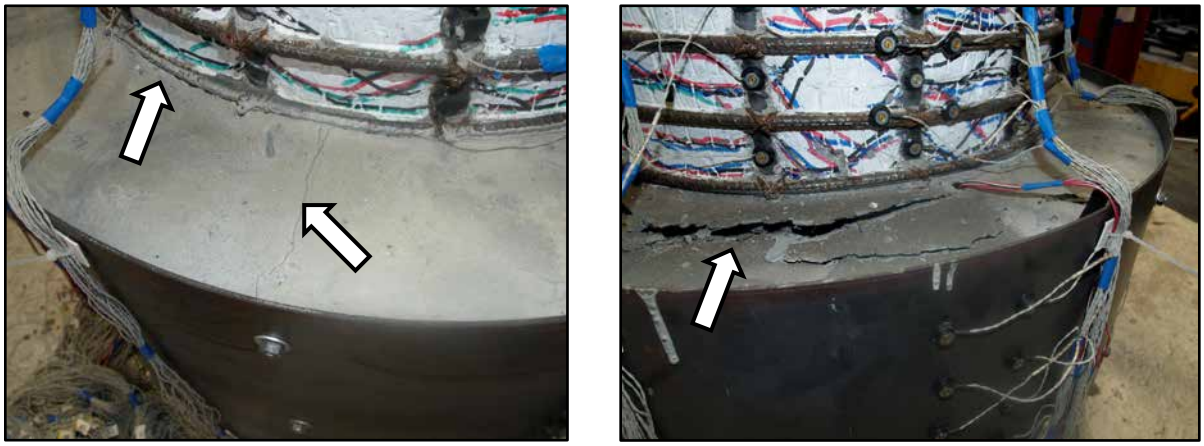

(a) **(b)**

Figure 4.16: Repair #2 (a) Slight cracking on top of repair during F'_y cycle; (b) progression of top surface deterioration during cycle $\mu_{\Delta 2}$.

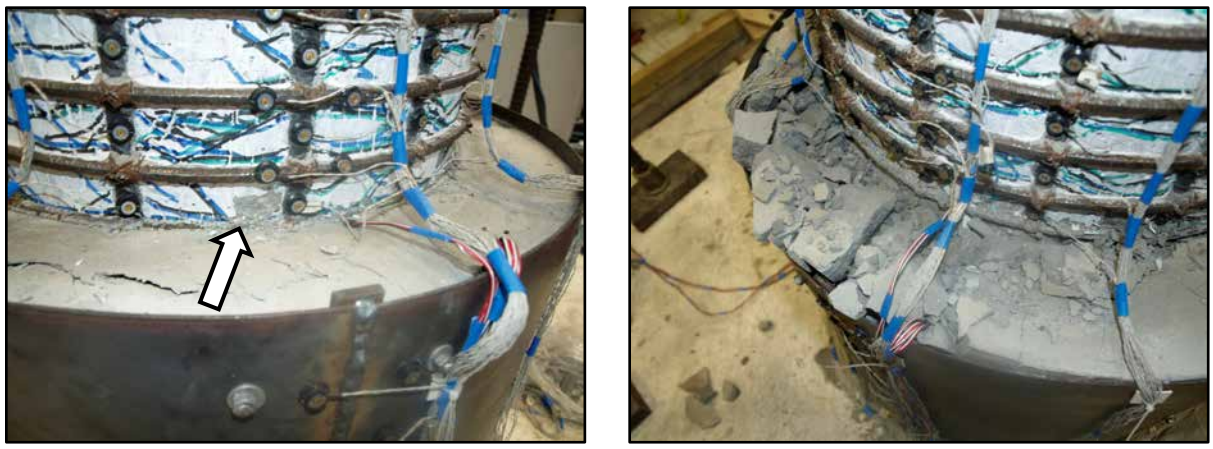

(a) **(b)**

Figure 4.17: Repair #2 (a) Onset of core crushing during cycle $\mu_{\Delta 3}^{+1y}$; (b) Further deterioration of hinge core and top of repair region during $\mu_{\Delta 5}^{-1y}$.

(a) **(b)**

Figure 4.18: Repair #2 (a) Visible bar buckling during $\mu_{\Delta 6}^{+1x}$; (b) Final damage state after multiple bar fractures during $\mu_{\Delta 6}^{-1x}$.

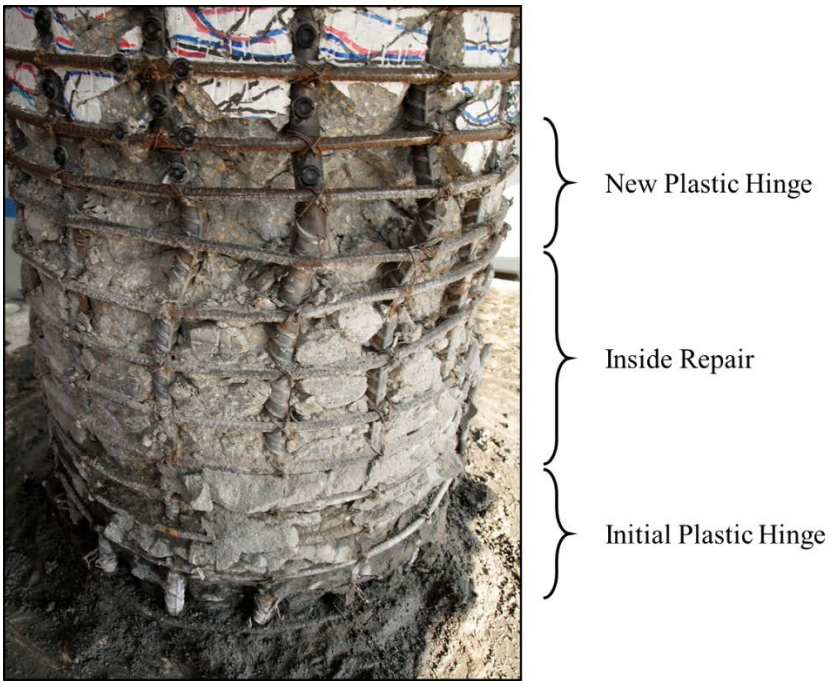

Figure 4.19: Repair #2 column state after test completion and removal of repair jacket.

4.2.2.2 Global Column Response

The global Force vs Displacement hysteresis responses of Repair #2 compared to the original column test are plotted in Figure 4.20 and Figure 4.21. The original test of this column corresponds to Load Path Test #4 which also used the symmetric two-cycle set, therefore this repair can be directly compared to the original test. Note that the X-direction response shown in Figure 4.21 contains only buckled reinforcement at the extreme fibers while the Y-direction response shown in Figure 4.20 has the three most extreme fiber bars fractured in both directions. The response of the repaired column is noticeably different between the two directions in these plots, as the Y-direction exhibits pinching behavior and member softening beyond $\mu_{\Delta 3}$ = 4.08 in. whereas neither of these are present in the X-direction plot. The repaired column reached a peak displacement of $\mu_{\Delta 6}$ = 8.22 in. in both directions, with failure occurring via rupture of the NE and ENE longitudinal bars, in that order, during the -X push in the first cycle of the $\mu_{\Delta 6}$ set. While failure from bar rupture alone is a significantly different outcome from the first test, it is specifically notable that these bars were the first to rupture since the NE bar is in what would presumably be the lowest strained position on the cross section. Further investigation of the local bar strains, discussed in the following section, provides additional information and insight into why this was the case.

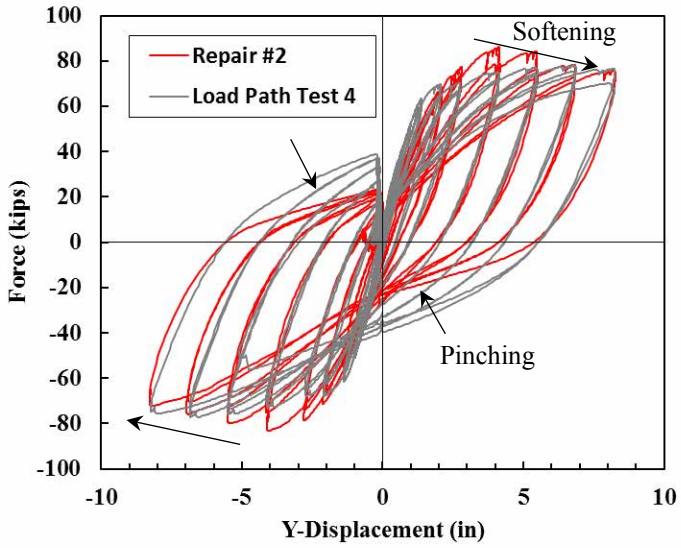

Figure 4.20: Repair #2 Y-Direction Force vs. Displacement comparison to Load Path Test 4.

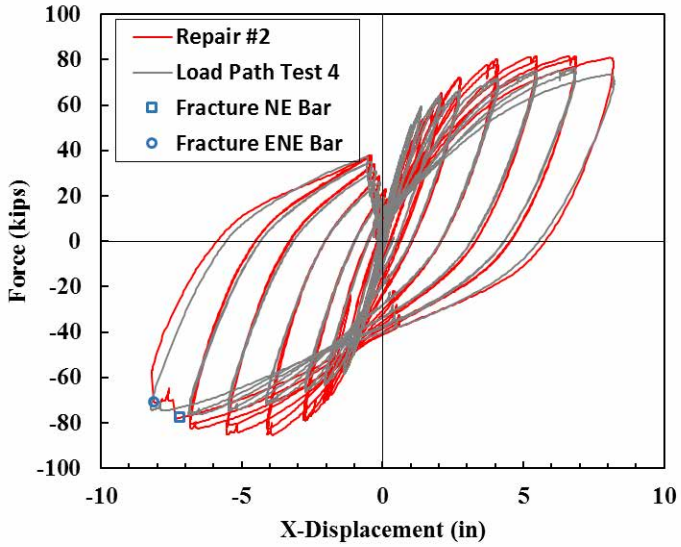

Figure 4.21: Repair #2 X-Direction Force vs. Displacement comparison to Load Path Test 4.

4.2.2.3 Local Behavior

The local strain behavior of each extreme fiber bar in the primary directions is plotted in Figure 4.22 and Figure 4.23 below. While the strains of the East and West bars match closely to those of Repair #1, those of the North and South bars are noticeably different. As the test proceeds beyond displacement ductility 3, there is a noticeable drop in strain generated in the bar, coinciding with the drop in global force discussed in the previous section. This drop in strain is attributed to the fractured bars debonding from inside the repair during cycles of increasing displacement, and

is consistent in each of the fractured bars on the North and South faces. As a result, the NE, SE, NW, and SW corner bars become the extreme fiber tension bars in the Y-direction loading and therefore under the highest demand, thus explaining why these were the first bars to fracture. Although this behavior is undesirable, it does not appear to have too great of an impact on the overall performance of the repair, as the column was still capable of achieving equal displacements despite the bars debonding. This behavior, along with specific means to prevent it, is addressed further in Repairs 4 through 6.

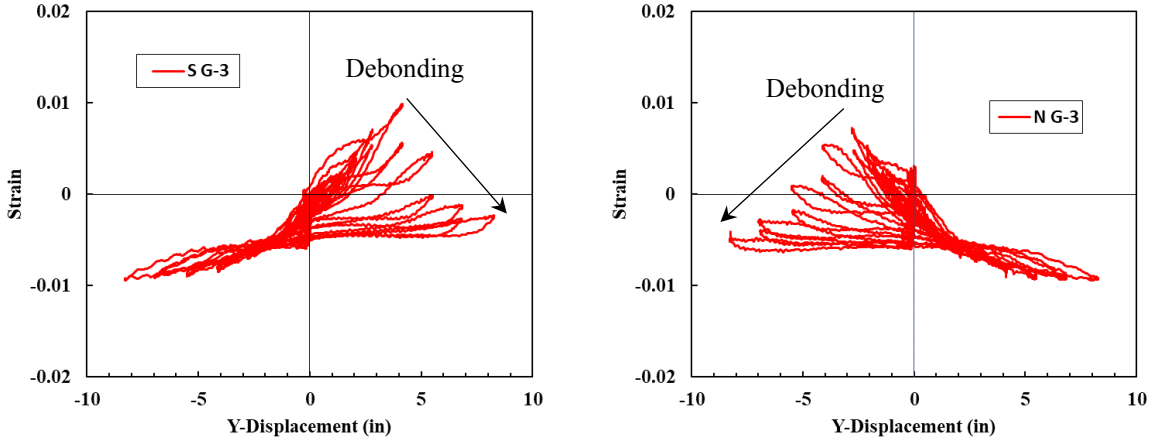

(a) **(b)**

Figure 4.22: Repair #2 Strain in longitudinal bars vs Y- Displacement on (a) South face; (b) North face.

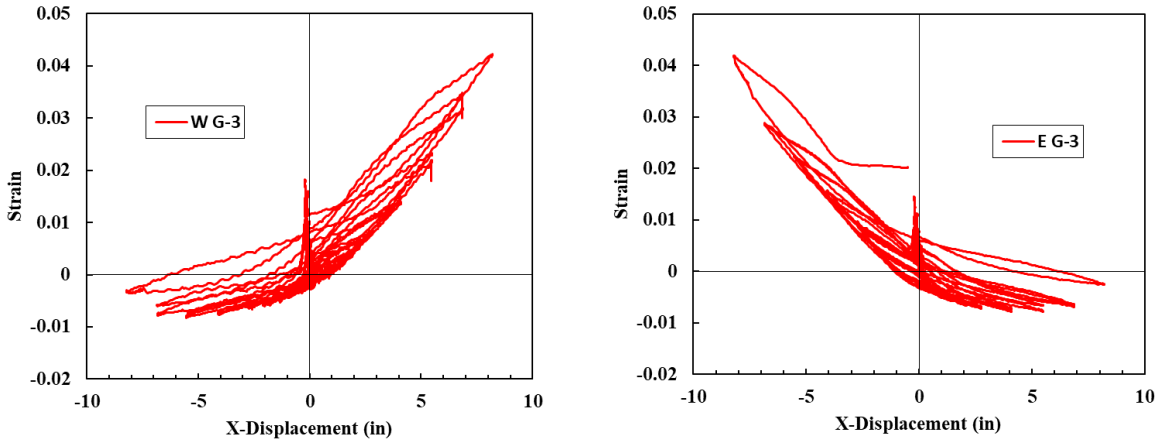

(a) **(b)**

Figure 4.23: Repair #2 Strain in longitudinal bars vs X- Displacement on (a) West face; (b) East face.

The repair bars all showed similar behavior to those in Repair #1, with plots of strain vs. displacement in these bars shown in Figure 4.24 and Figure 4.25. The longitudinal strains in the Y-direction repair bars were approximately 20% higher than in the first test, reaching values of

0.0013 despite a lower global force demand of only 86.2 kips. This was expected since the original column bars were not capable of resisting any force across their fracture surface and all of their demand would then be transferred to the repair bars. However, as the bond of the original bars deteriorates it is also evident that the demand in the repair bars decreases since there is less force transferred from the original bars. In conclusion, Repair #2 remained elastic as intended and the global behavior of the column reached the desired performance; however, it is clear that further investigation into the development of fractured bars inside of the repair is needed.

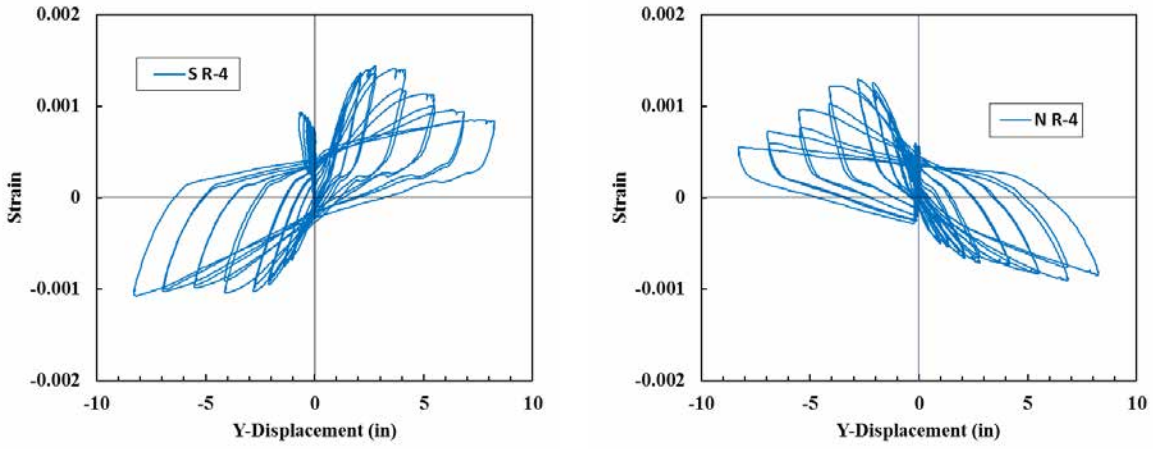

(a) **(b)**

Figure 4.24: Repair #2 Strain in repair bars vs. Y-Displacement on the (a) South and (b) North faces of the column.

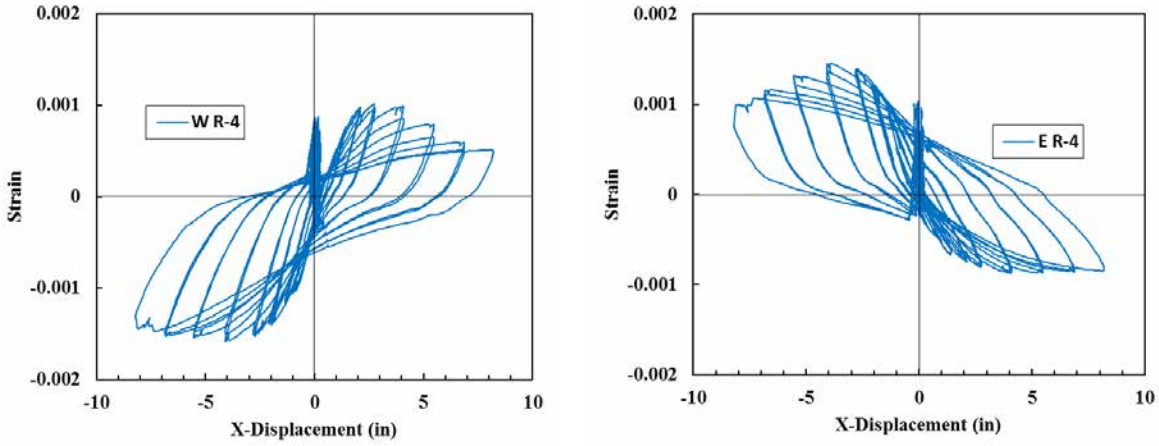

(a) **(b)**

Figure 4.25: Repair #2 Strain in repair bars vs. X-Displacement on the (a) West and (b) East faces of the column.

4.3 Repair #3

4.3.1 Summary of Repair Considerations

The goals of Repair #3 are to refine the design through the use of an alternate reinforcement configuration and address potential overstrength issues that could impact the capacity protected elements of the original bridge. Repairs #1 and #2 retained the same cross section at the relocated plastic hinge as was at the base of the original column, resulting in an increase in overall force demand due to the reduced column span. The footings of the tested specimens directly considered these effects in their designs by accounting for the potential increased force demands; however, actual bridge structures may not have such strength margins. To account for this, the shear force demand of the repaired column was reduced to that of the original by cutting the SE, NE, SW, and NW longitudinal bars *above* the repair. As a result, the moment capacity of the relocated plastic hinge is reduced such that it develops under the same shear force as the original column, and no additional force is introduced into the system. No further consideration is required for the capacity protected elements of the bridge since the original design has already satisfied this requirement.

The second modification to Repair #3 was to consider using a larger number of smaller diameter repair bars. The first repairs aimed to use the smallest number of reasonably well distributed repair bars, resulting in the configuration of 12 #10 bars. However, In doing so, it was determined that larger diameter bars are disproportionately more difficult to install than smaller bars as they are more difficult to place in congested footings and require much deeper embedment holes. Therefore, from a constructability perspective, smaller bars should be favored over fewer bars. Furthermore, it was theorized that a larger density of smaller diameter bars could contribute to a more flexurally dominated response than the larger bars as they would provide far less stiffness from dowel action in the transverse direction. The damage state of the column included only buckled longitudinal bars, matching the damage state of Repair #1; however, the transverse spiral reinforcement was fractured during the initial test. The damage state of the original column is shown in Figure 4.26.

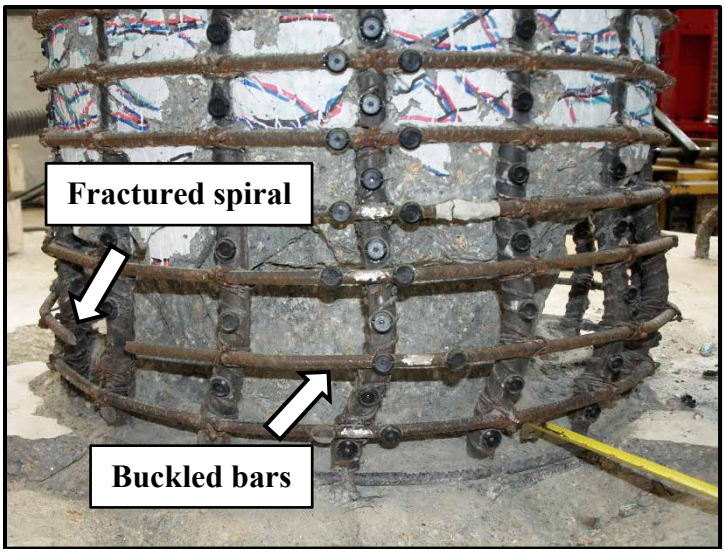

Figure 4.26: Repair #3 damage state prior to repair installation.

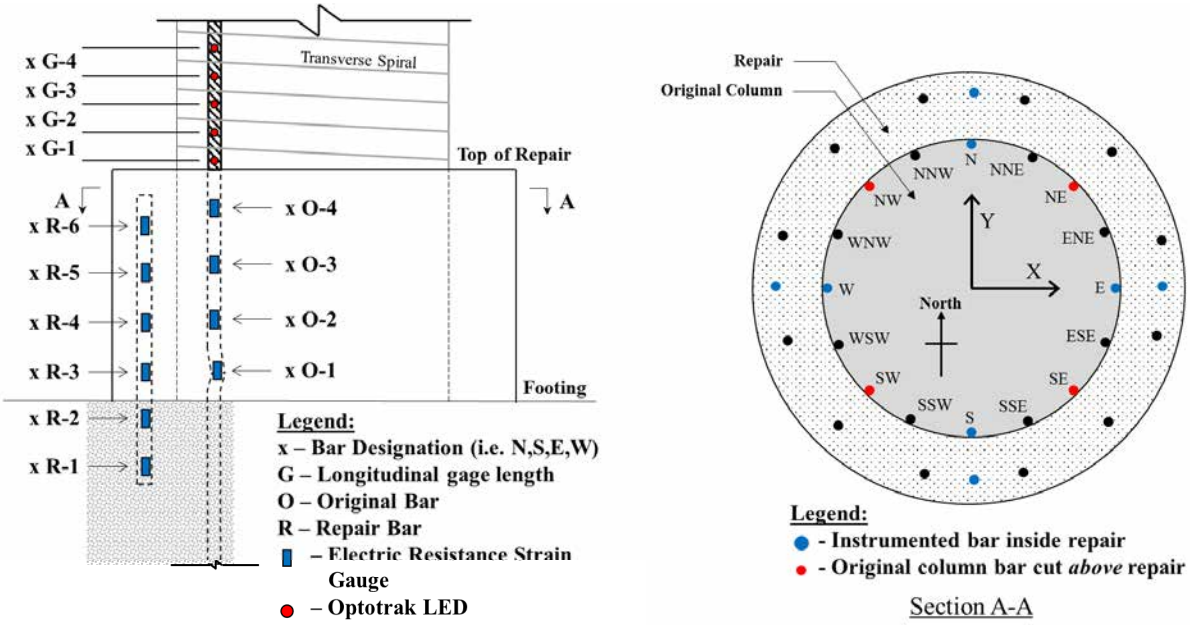

Figure 4.27: Repair #3 Instrumentation labels and repair cross section layout.

Table 4.5: Repair #3 summary of values of interest.

Original Column Properties	
Load History	Symmetric Three Cycle Set
Column Geometry	L = 9 *ft*, D = 24 *in*, (L/D = 4.56)
Longitudinal Steel Detailing	16 #7 for $\rho_l = A_{st} / A_g$ = 2.1%
Longitudinal Steel Properties	f_y = 71.2 *ksi*, f_u = 97.9 *ksi*, ε_y = 0.00254
Transverse Steel Detailing	#3 @ 2 *in for* $\rho_s = 4A_{sp} / D' s$ = 1.0%
Transverse Steel Properties	f_y = 67.6 *ksi*, f_u = 105.6 *ksi*, ε_y = 0.00448
Column Concrete Strength	f'_c = 7.60 *ksi*
Footing Concrete Strength	f'_c = 10.38 *ksi*
Equivalent Yield Displacement	Δ_y = 1.37 *in*
Damage State	Buckling of all longitudinal bars, fracture of spiral
Repair Properties	
Load History	Symmetric Two Cycle Set
Repair Geometry	H = 22 *in*, D = 32 *in*
Longitudinal Steel Detailing	16 #7 *A706 Grade 80*
Longitudinal Steel Properties	f_y = 90.1 *ksi*, f_u = 116.8 *ksi*, ε_y = 0.0037
Transverse Steel Detailing	11ga A36 steel sheet $\rho_s = 4t_j / D'$ = 1.5%
Transverse Steel Properties	f_y = 43.0 *ksi*, f_u = 54.6 *ksi*, ε_y = 0.00148
Repair Grout Strength	f'_c = 7.96 *ksi*

4.3.2 Discussion of test results

4.3.2.1 Summary of Events

Repair #3 performed as intended with the plastic hinge forming above the repair and no apparent damage to the repaired region. One notable observation throughout the test was that the grout in the repair remained far less damaged than it had during previous tests, which is demonstrated in Figure 4.28 (a). This figure shows only minor cracking on the top surface of the repair at $\mu_{\Delta 1.5}$ while this level of damage was seen during the F'_y cycles of previous tests. Although the reduced forces acting on the system likely contributed to this, the peak strains inside the repair were higher during this test than either of the previous two, indicating larger total deformation which should result in more damage. Thus, the apparent durability of this repair was likely due to the more equal distribution of steel within the repair.

Another observation relates to the reinforcing bars that were cut above the repair to reduce the force demand on the system. Figure 4.28 (b) shows a large gap opening while this section is in tension, which contributes to the formation of a large crack in the core concrete and eventual damage to this location. While the performance of the column was adequate from a seismic

response perspective, it is recommended that these cuts be placed just below the surface of the repair when used in practice to prevent the development of cracks and surface spalling under service loads.

The remainder of the test carried out similar to the first two with eventual deterioration of the top layer of grout in the repair during $\mu_{\Delta 4}$ followed by the onset of bar buckling during $\mu_{\Delta 5}$, shown in Figure 4.29 (a) and (b) respectively. The test concluded after the SSW bar ruptured during the second reversal in the Y-direction of $\mu_{\Delta 5}$, resulting in the first repair that did not reach the displacement capacity of the original test. This is a logical outcome, however, when considering that the reduction of longitudinal steel results in a shallower neutral axis depth and therefore greater tension strain demand on the bars for a given base rotation. Thus, these bars are likely to buckle and subsequently rupture sooner than in previous tests. This will be discussed in greater detail in the following sections.

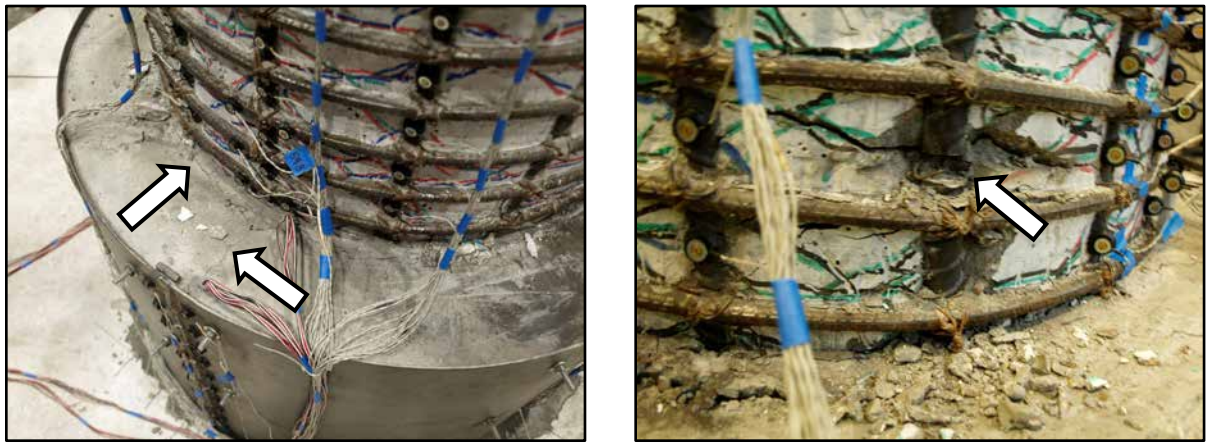

(a) **(b)**

Figure 4.28: Repair #3 (a) Slight cracking on top of repair during $\mu_{\Delta 1.5}$ cycle; (b) accumulation of damage and large crack width opening during $\mu_{\Delta 3}{}^{-1y}$.

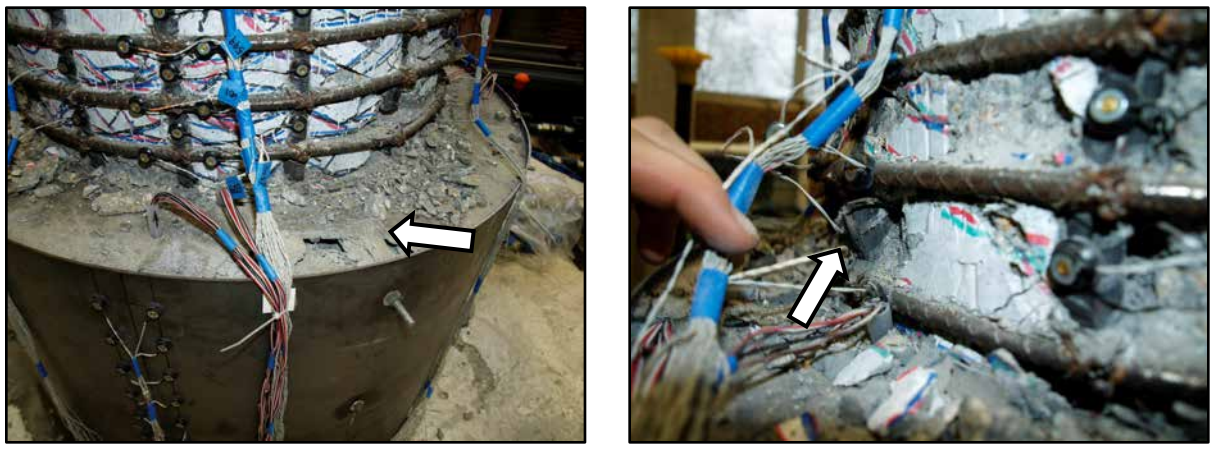

(a) **(b)**

Figure 4.29: Repair #3 (a) beginning of top of repair deterioration during $\mu_{\Delta 4}^{-1y}$; (b) Onset of bar buckling during $\mu_{\Delta 5}^{-1y}$.

(a) **(b)**

Figure 4.30: Repair #3 (a) Fracture of SSW bar during $\mu_{\Delta 5}^{+2y}$; (b) Final damage state.

4.3.2.2 Global Column Response

The global force vs. displacement responses of the repaired column in the Y and X directions are shown in Figure 4.31 and Figure 4.32 respectively. A comparison is provided to load path test 4, which was nominally identical in load history and reinforcement detailing, instead of load path test 5, which corresponds to the actual initial test of the repaired column but used a different load history. The global responses of each were similar enough not to warrant comparison to both. It is immediately noticeable that the repaired column response matches very closely to that of the original column response, especially considering the peak values. The original column had a peak applied force of 77.7 kips, while the repaired column only slightly exceeded that at 80.6 kips. This corresponds to an overstrength of only 3.7%, compared to 19.2% and 10.8% in

Repair #1 and #2 respectively, which should be well within the capacity protection margin for design. Therefore, the design goal of reducing the overall forces in the system to prevent failure through capacity designed elements was realized, but at the expense of reducing the displacement capacity of the member. However, depending on the desired performance of the repaired bridge, this could be a perfectly acceptable tradeoff. For example, if a critical bridge needs to be made operational for only a brief period while a new bridge is constructed, it would be unlikely to see an event where its full displacement capacity is required. This is especially true considering the rare event that would require such a response had likely just taken place to cause the initial damage. Furthermore, this approach ensures that no other strengthening measures are required given that the damage is localized to the plastic hinges.

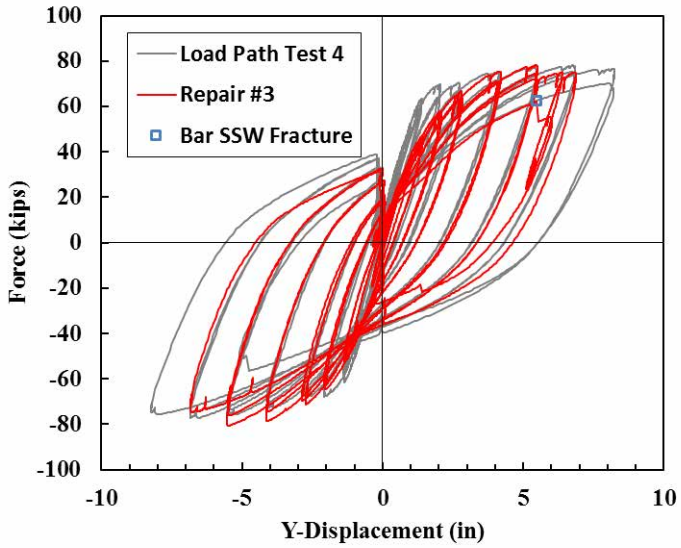

Figure 4.31: Repair #3 Y-Direction Force vs. Displacement comparison to Load Path Test 4.

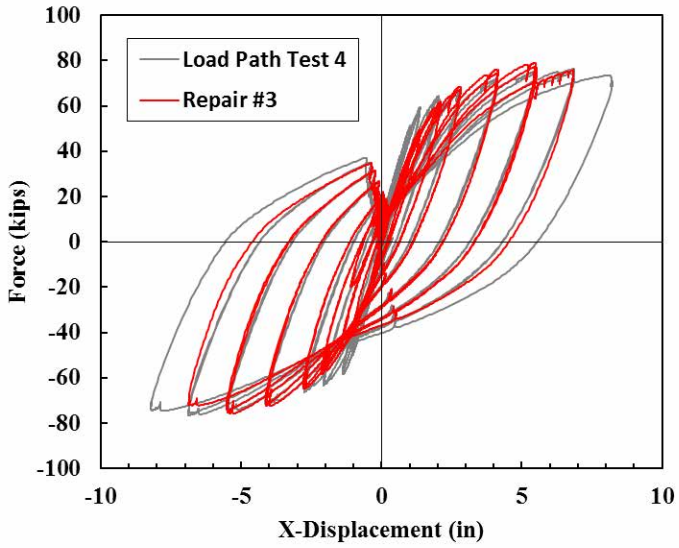

Figure 4.32: Repair #3 X-Direction Force vs. Displacement comparison to Load Path Test 4.

4.3.2.3 Local Behavior

Analysis of the strain behavior in the column bars above the repair confirms the statements in the discussion above. Figure 4.33 and Figure 4.34 show the strains in the plastic hinge region of the repaired column vs. the top of column displacement. As with Repairs #1 and #2, it is first evident that large inelastic strains did accumulate in this location confirming the development of a plastic hinge. Figure 4.33 (a) also shows a comparison between the strains in the extreme South bar in Repair #1 and Repair #3 which indicates larger tension strains in Repair #3 at equal levels of displacement. This is to be expected due to the lower steel content and therefore shallower neutral axis depth. It is also interesting to note that both bars begin to buckle after reaching almost identical levels of strain ($\varepsilon_t \approx 0.035$) implying that strain limit states remain consistent between the two repairs.

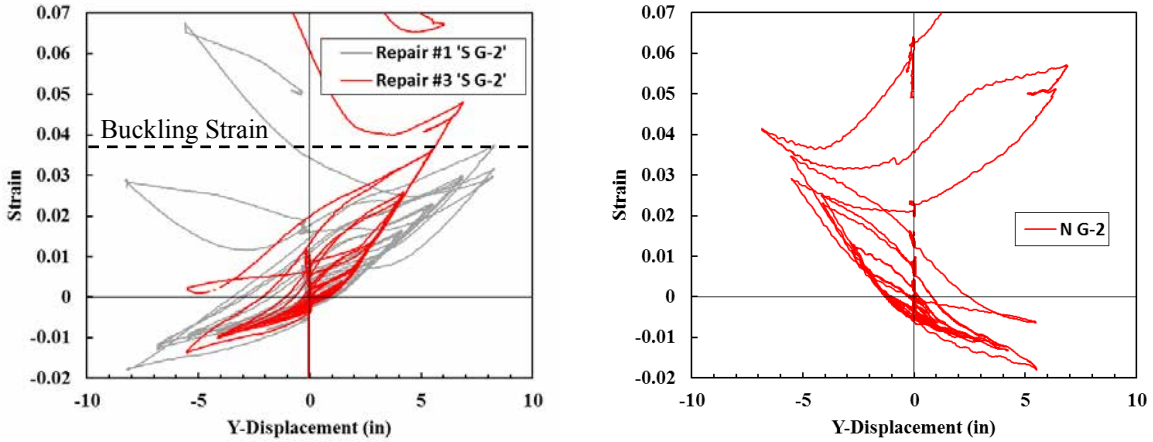

Figure 4.33: Repair #3 Strain in longitudinal bars vs Y- Displacement on (a) South face; (b) North face.

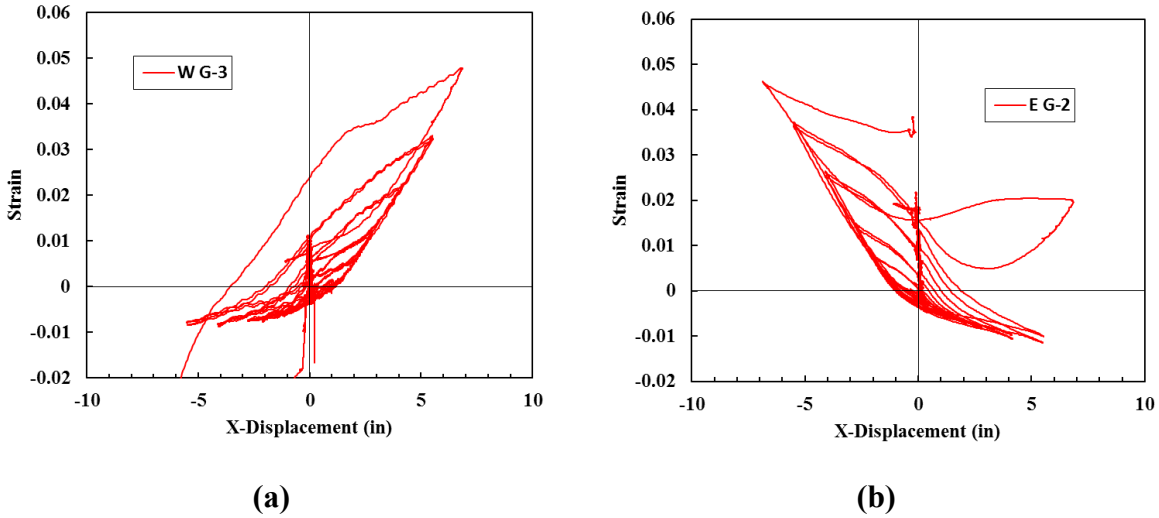

Figure 4.34: Repair #3 Strain in longitudinal bars vs X- Displacement on (a) West face; (b) East face.

Figure 4.35 compares the strains in the SSW and S bars, both in Repair #3. Assuming plane sections behavior, the S bar should have larger strains than the SSW bar, but this is not the case. This explains why this bar was the first to fracture, but also indicates that the removal of longitudinal steel from the cross section has a disproportionate impact on the bars directly adjacent to those cut.

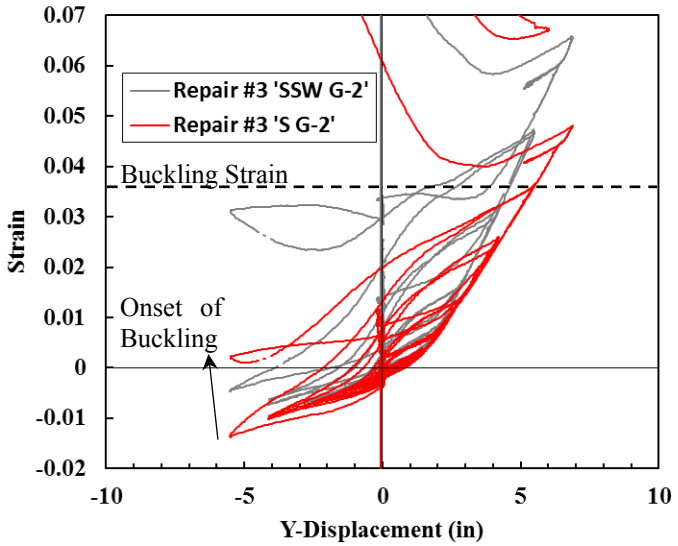

Figure 4.35: Repair #3 comparison of strain vs. displacement in the SSW and S longitudinal bars.

The strains in the repair bars show similar behavior to those of Repairs #1 and #2 as well. Each bar remained below the design yield strain of $\varepsilon_y = 0.002$, but reached a peak of 0.0018 which is substantially higher than either of the first two tests. This exceeds what is predicted given the ratio of longitudinal steel content in this repair to the force demand, which indicates that a larger proportion of forces were transferred flexurally into the repair than in the previous tests. This is likely due to the increased flexibility in the repair itself from the smaller diameter bars. Figure 4.36 and Figure 4.37 below show the strains in the extreme fiber repair bars as a function of the top of column displacement.

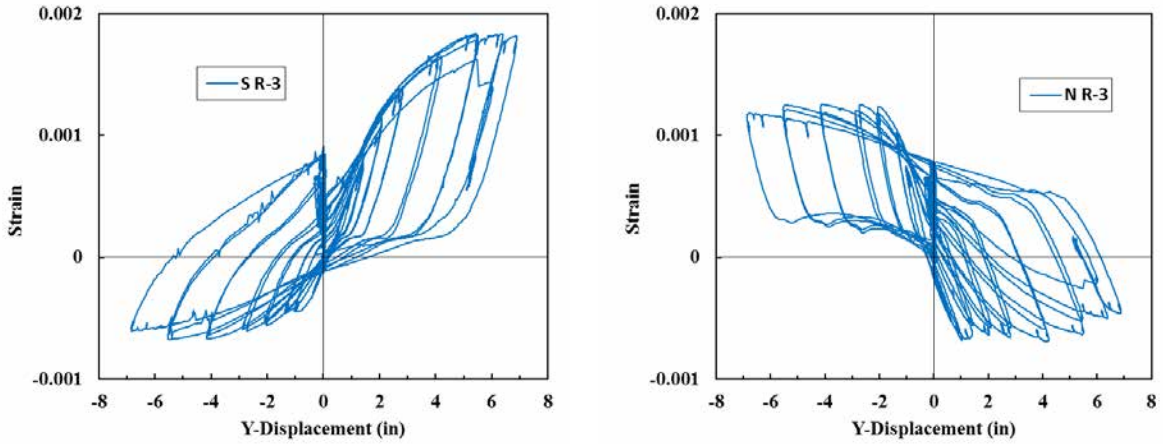

Figure 4.36: Repair #3 Strain in repair bars vs. Y-Displacement on the (a) South and (b) North faces of the column.

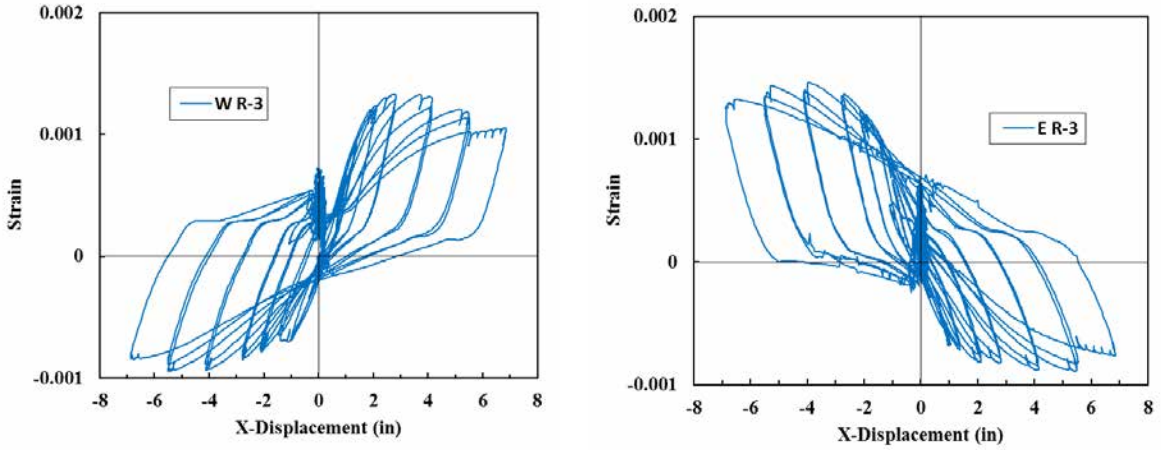

(a) **(b)**

Figure 4.37: Repair #3 Strain in repair bars vs. X-Displacement on the (a) West and (b) East faces of the column.

4.4 Repair #4

4.4.1 Summary of Repair Considerations

The primary objective of the fourth repair was to investigate the impact of different materials and configurations on the performance of the repaired specimen while keeping the overall concept the same. These modifications included replacing the steel sleeve with discrete rebar hoops tied directly to the longitudinal repair bars and exchanging the commercial grout with a flowable pump mix from a local ready-mix supplier, as shown in Figure 4.38. Each of these materials is meant to represent a more traditional reinforced concrete repair and provide alternative solutions to the design engineer. The design methodology remained the same as in the previous tests, although the longitudinal steel content in the original column was lower than in the previous tests allowing for a reduction to 12 #7 repair bars.

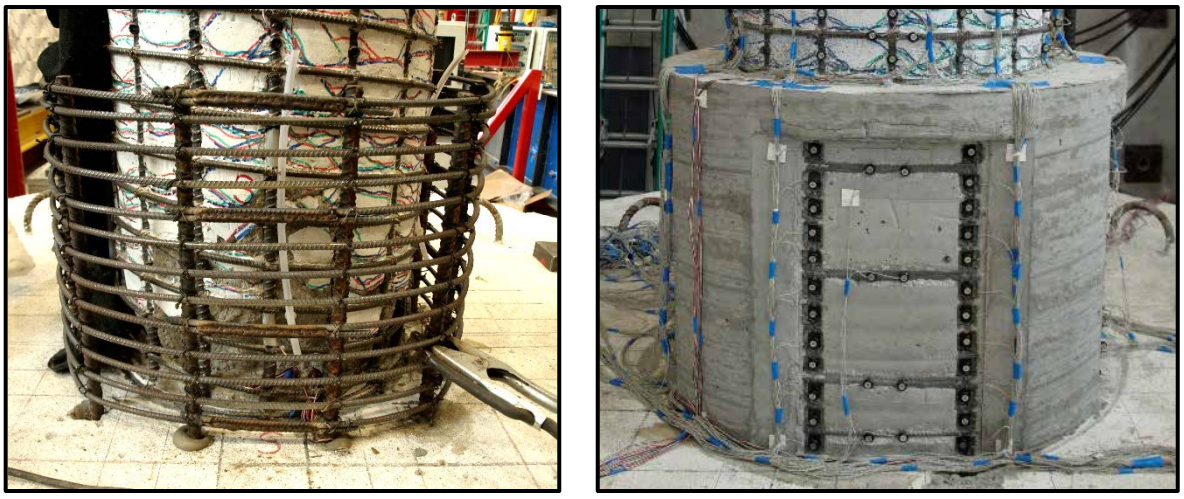

(a) **(b)**

Figure 4.38: Repair #4 (a) welded rebar hoop construction; (b) blocked out repair section.

Repairs #4 – #6 also specifically aim to investigate the development of ruptured longitudinal bars within the repair. Recall that, following the second repair test, it was discovered that each of the fractured bars debonded after reaching a displacement ductility of 3, as illustrated in Figure 4.39. Both plots show the strain of the extreme fiber bar above the repair vs. top of column displacements on the North and South faces of Repair #2. Both of these bars were fractured at the base of the repair. The reduction in strain as the test progresses beyond a displacement of about 4 inches ($\mu_{\Delta 3}$) indicates that these bars are no longer contributing to the flexural resistance of the repaired cross section. While the global performance of the second repaired column was

satisfactory, it is of interest to provide a means of reliably developing these bars such that the repaired response can be accurately predicted. Repair #4 reduces the number of fractured bars to just one on the South face of the column to address whether a single fractured bar behaves any differently from a group of fractured bars. No additional consideration for anchoring the bar was made.

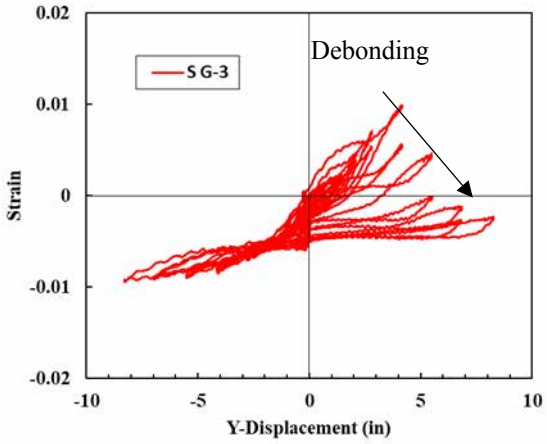

Figure 4.39: Observed debonding behavior in South repair bar in Repair #2.

An additional benefit of this repair configuration is that the repair bars were able to be blocked out and instrumented directly with Optotrak similar to that of the original column. This provides the opportunity to compare the results from strain gauges used in prior tests and also gain more data on the actual deformation of the repair section rather than just the longitudinal bar strains. The blocked out repair section can be seen in Figure 4.38.

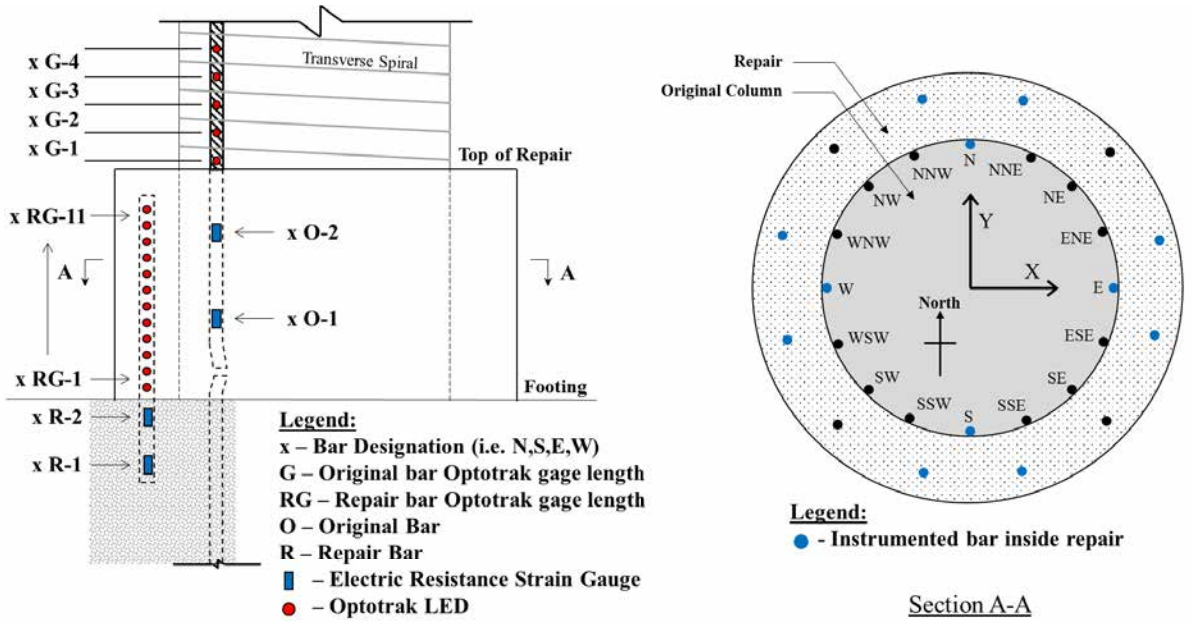

Figure 4.40: Repair #4 Instrumentation labels and repair cross section layout.

Table 4.6: Repair #4 summary of values of interest.

Original Column Properties	
Load History	Scaled Bidirectional Megathrust
Column Geometry	L = 9 *ft*, D = 24 *in*, (L/D = 4.56)
Longitudinal Steel Detailing	16 #6 for $\rho_l = A_{st} / A_g$ = 1.6%
Longitudinal Steel Properties	f_y = 70.33 *ksi*, f_u = 98.68 *ksi*, ε_y = 0.00283
Transverse Steel Detailing	#3 @ 2.75 *in for* $\rho_s = 4A_{sp} / D' s$ = 0.7%
Transverse Steel Properties	f_y = 63.89 *ksi*, f_u = 93.64 *ksi*, ε_y = 0.00418
Column Concrete Strength	f'_c = 6.23 *ksi*
Footing Concrete Strength	f'_c = 6.61 *ksi*
Equivalent Yield Displacement	Δ_y = 1.22 *in*
Damage State	Buckling of all longitudinal bars, fracture of extreme South bar
Repair Properties	
Load History	Symmetric Two Cycle Set
Repair Geometry	H = 22 *in*, D = 32.75 *in*
Longitudinal Steel Detailing	12 #7 *A706 Grade 80*
Longitudinal Steel Properties	f_y = 84.3 *ksi*, f_u = 109.7 *ksi*, ε_y = 0.0031
Transverse Steel Detailing	#3 @ 1.5 *in for* $\rho_s = 4A_{sp} / D' s$ = 1.0%
Transverse Steel Properties	*A706 Grade 60* f_{yv} = 67.5*ksi*
Repair Concrete Strength	f'_c = 4.84 *ksi*

4.4.2 Discussion of test results

4.4.2.1 Summary of Events

The repaired specimen performed as intended with the plastic hinge forming above the annular ring and no visible damage occurring within the repaired region. Visible cracks began to appear on top of the repair during the F'_y cycle as shown in Figure 4.41 (a). This was followed by slight flexural and shear cracking that developed during the first $\mu_{\Delta 1.5}$ cycles as shown in Figure 4.41 (b). Cracking in the repair continued throughout the rest of the test and did not exceed widths of 0.01", except at the top region above the confinement and longitudinal steel which spalled off at higher ductility levels. This behavior was similar to what was observed in previous tests; however, since there was no sleeve to restrain the spalled concrete the spalled regions appeared to have more damage. Further damage localized in the original column at the top of the repair with the onset of core crushing during $\mu_{\Delta 3}$, shown in Figure 4.42 (a), followed by visible bar buckling during $\mu_{\Delta 5}^{-2x}$ = 6.1 in., shown in Figure 4.42 (b). The test continued through a full cycle of $\mu_{\Delta 6}$ = 7.32 in. prior to rupture of the SW and SSW bars during the second +Y cycle, shown in Figure 4.43 (b).

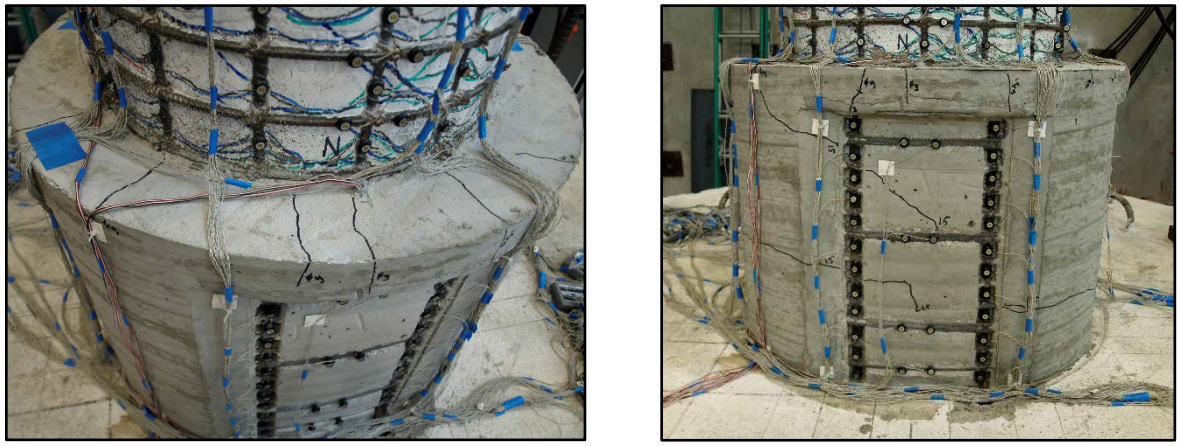

(a) **(b)**

Figure 4.41: Repair #4 (a) Slight cracking on top of repair during F'_y cycle; (b) Flexural and shear cracking in body of repair during cycle $\mu_{\Delta 1.5}^{-x}$.

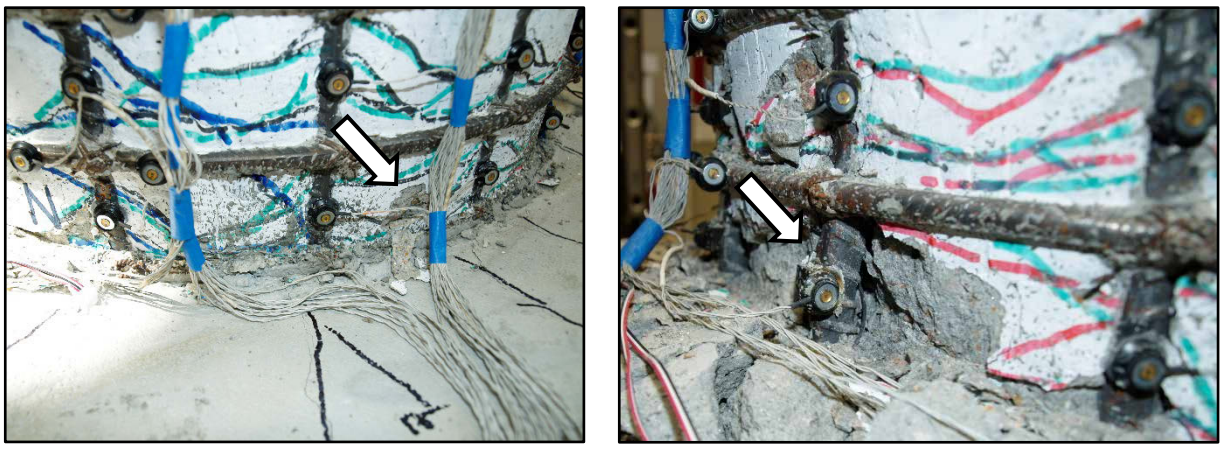

(a) **(b)**

Figure 4.42: Repair #4 (a) Onset of core crushing during cycle $\mu_{\Delta 3}{}^{+y}$; (b) Onset of bar buckling during $\mu_{\Delta 5}{}^{-2x}$.

(a) **(b)**

Figure 4.43: Repair #4 (a) Buckled longitudinal bars on West face; (b) Fractured longitudinal bars on South face.

4.4.2.2 Global Column Response

The global Force vs Displacement hysteresis responses are plotted in Figure 4.44 through Figure 4.47 below. Figure 4.44 and Figure 4.45 provide a comparison of the repaired column response to that of the load path study test #9, which corresponds to the nominally identical column subjected to the same load history as the repaired specimen, while Figure 4.46 and Figure 4.47 compare the repair performance to that of load path study test #12, which corresponds to the exact column used in Repair #4. Both sets of plots indicate that the repaired column restores the system's overall strength and displacement capacity, therefore it is concluded that the overall performance of the repaired column meets the design goal. A final observation between the two specimens is that the initial stiffness of the repaired column matches very closely to that of the original test,

whereas previous repairs displayed a reduced stiffness between the original and repaired columns. This is likely attributable to an increased shear stiffness of the repair itself due to the aggregate in the concrete mix.

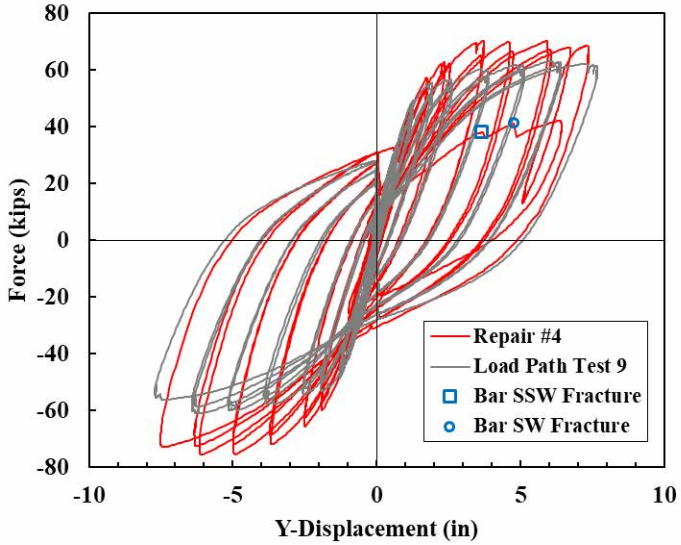

Figure 4.44: Repair #4 Y-Direction Force vs. Displacement comparison to Load Path Test 9.

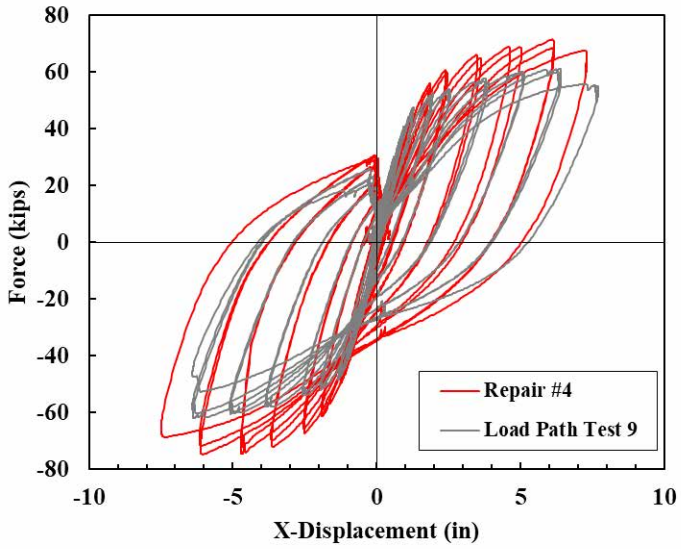

Figure 4.45: Repair #4 X-Direction Force vs. Displacement comparison to Load Path Test 9.

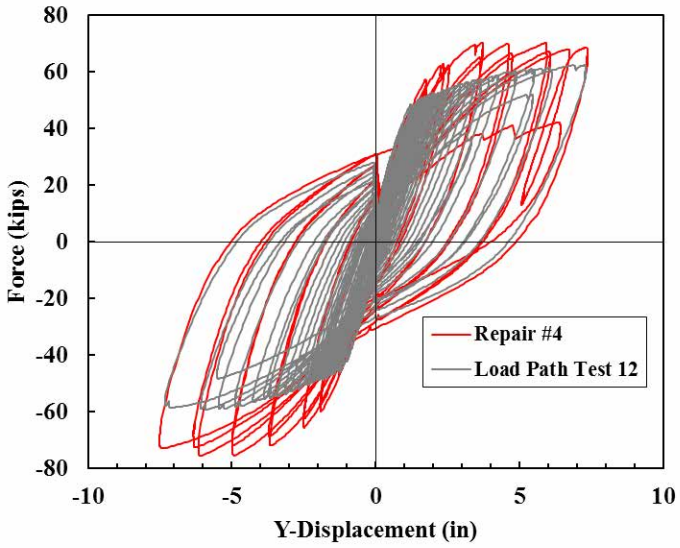

Figure 4.46: Repair #4 Y-Direction Force vs. Displacement comparison to Load Path Test 12.

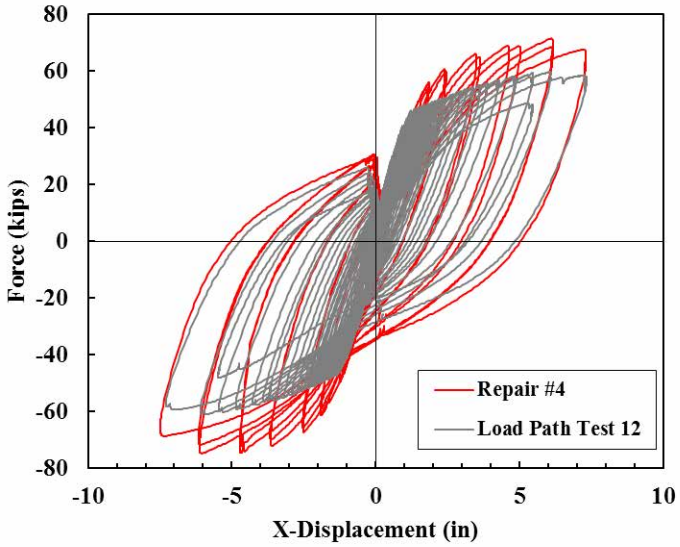

Figure 4.47: Repair #4 X-Direction Force vs. Displacement comparison to Load Path Test 12.

4.4.2.3 Local Behavior

Figure 4.48 and Figure 4.49 compare the strains of the longitudinal bars in the relocated plastic hinge to the top of column displacements in the Y and X directions respectively. Note that the South bar was fractured at the base of the repair and shows similar behavior to those of Repair #2. It is clear from Figure 4.48 (a) that this bar debonded during $\mu_{\Delta 3}$ and no longer contributed to the flexural strength of the column. Thus, reducing the number of fractured bars does not have an impact on their development into the repair. The remaining extreme fiber bars

performed as expected, reaching tension strains between approximately 0.04 and 0.05. It is worth noting that the West bar did buckle much more severely than the data indicates, however the bottom LED marker on this bar was not visible for much of the test, therefore the plot shown represents the second gage length which did not capture much of the buckling behavior.

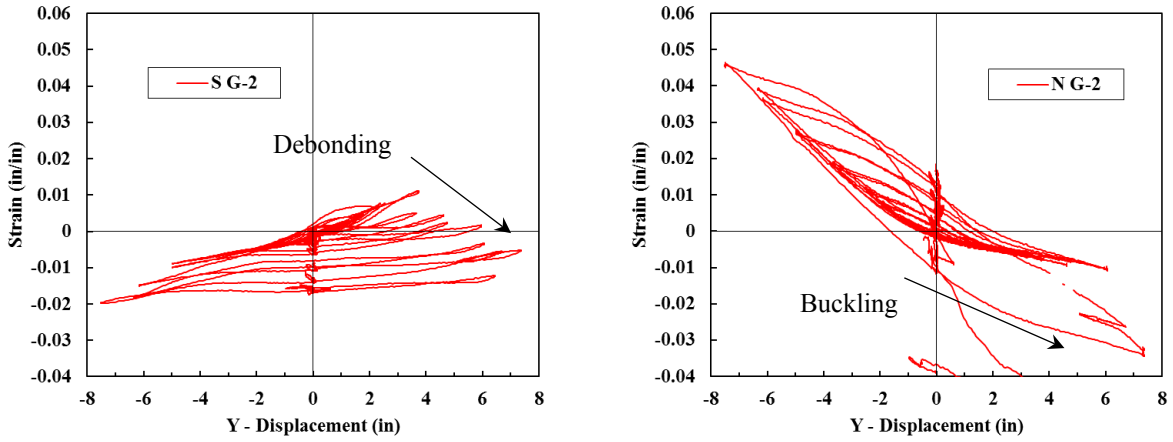

(a) **(b)**

Figure 4.48: Repair #4 Strain in longitudinal bars vs Y- Displacement on (a) South face; (b) North face.

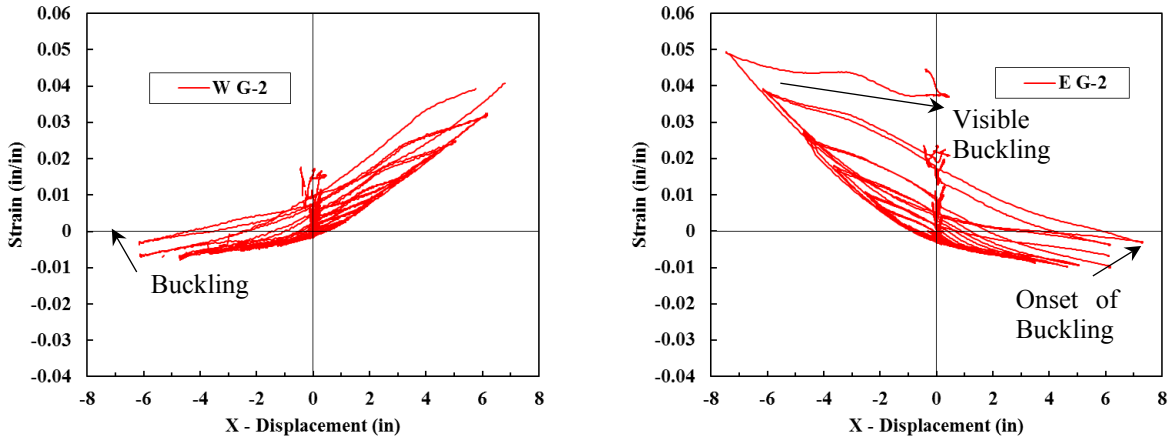

(a) **(b)**

Figure 4.49: Repair #4 Strain in longitudinal bars vs X- Displacement on (a) West face; (b) East face.

A side by side comparison of strains determined from electrical resistance gauges and Optotrak at the base of the repair is provided in Figure 4.50 through Figure 4.53. The left plot of each figure shows the strain from an electrical resistance gage just below the footing interface while the right plot provides the average calculated strain of the two exposed repair bars on each face using Optotrak data just above the footing interface. The average of two bars was used in place of that from a single bar in attempt to smooth the plot out since measurements of very low

levels of strain are not as precise using Optotrak as they are from traditional strain gauges. Gage 2 was used in place of Gage 1 for the Optotrak data, as much of the data from Gage 1 was incomplete. Also, Optotrak Gage 2 and Strain Gauge 2 were each located approximately 3" above and below the footing respectively and therefore should correspond to equal levels of strain. It can be seen that this is roughly the case for each of the plots shown. The levels of strain reported from both sources indicate that the repair bars did in fact remain below the elastic limit as intended. Furthermore, it seems that the use of the electrical resistance strain gauges on the longitudinal repair bars may be preferable to Optotrak since the data obtained is much more precise.

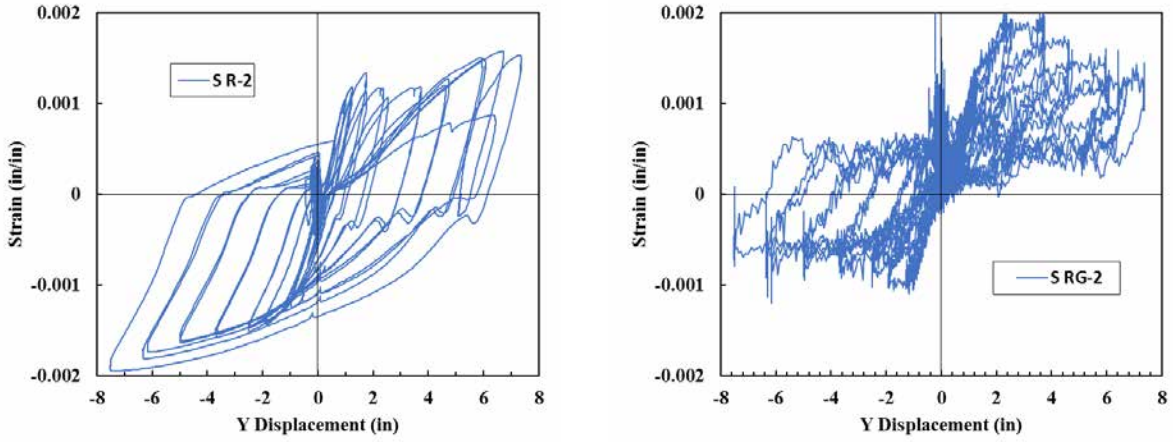

(a) **(b)**

Figure 4.50: Repair #4 Strain in South repair bars vs Y- Displacement from (a) SG2-RS; (b) Optotrak gage 2.

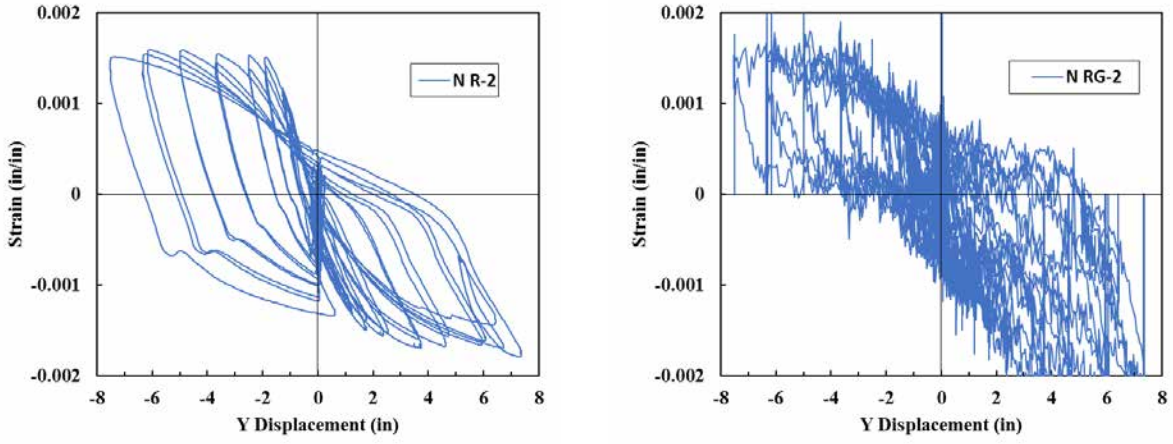

(a) **(b)**

Figure 4.51: Repair #4 Strain in North repair bars vs Y- Displacement from (a) SG2-RN; (b) Optotrak gage 2.

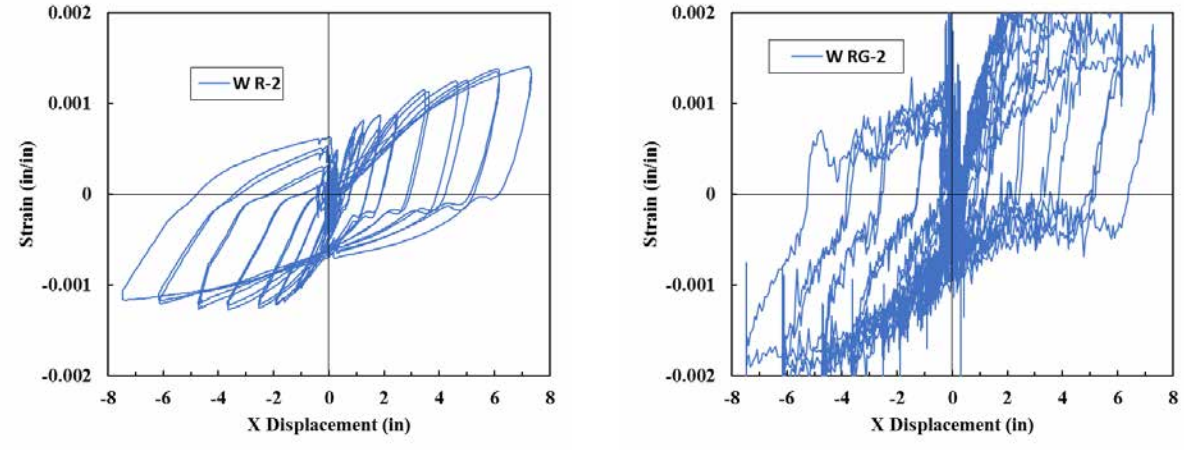

(a) **(b)**

Figure 4.52: Repair #4 Strain in West repair bars vs X- Displacement from (a) SG2-RWS; (b) Optotrak gage 2.

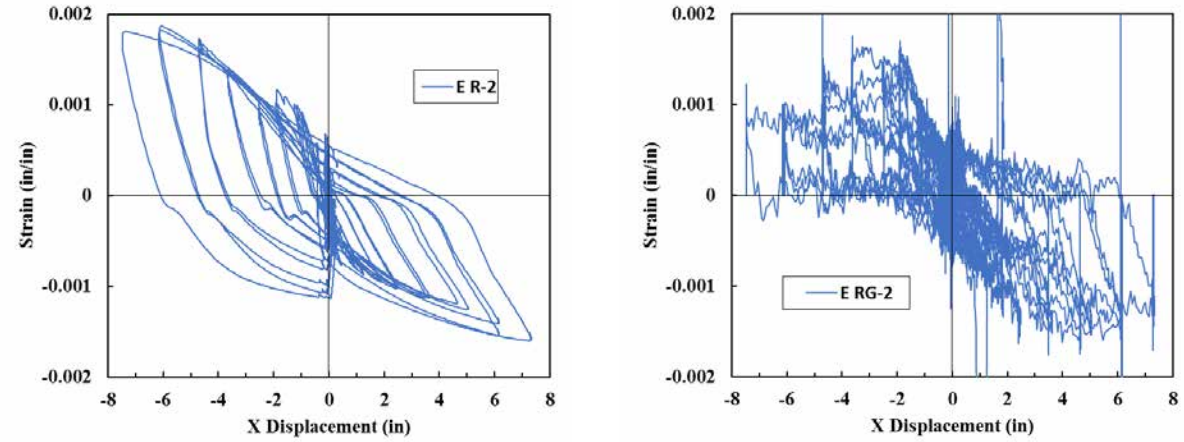

(a) **(b)**

Figure 4.53: Repair #4 Strain in East repair bars vs X-Displacement from (a) SG2-RE; (b) Optotrak gage 2.

4.5 Repair #5

4.5.1 Summary of Repair Considerations

The fifth repair test aimed to investigate specific means of bond development for fractured reinforcing steel, as well as the impact of residual deformation on the performance of the repaired structure. Two specific methods were employed in an attempt to develop the fractured bars: 1) chipping out existing concrete from the full perimeter of the bar along the height of the repair prior to installing repair concrete as shown in Figure 4.54 (a), and 2) installing a mechanically fastened headed stud to the base of the fractured bar as shown in Figure 4.54 (b).

(a) **(b)**

Figure 4.54: Repair #5 fractured bar anchorage mechanisms considered.

The intent of removing the concrete from the perimeter of the fractured bar is to provide clearance for complete bonding of the repair material to both the bar and the concrete substrate. This method is recommended in the ACI Guide to Concrete Repair (ACI Committee 546, 2014) when preparing a surface to receive new repair materials. By removing the deteriorated concrete from the full perimeter of the reinforcing steel and replacing it with freshly placed concrete or grout, it is assumed that the bond conditions will improve and potentially provide sufficient development of the fractured bars. Although it is recognized that the repair considered in this research is beyond the scope of a typical surface repair, the general principles still apply. This method was applied to the ENE and W longitudinal bars.

Alternatively, the mechanical headed stud aims to provide anchorage at the base of the fractured bar inside the repair instead of just improving the bond development conditions of the bar itself. The product used is the Dayton Superior D252L Bar Lock® End Anchor, which is

commercially available and easily installed to the end of the fractured bar. Prior to installation, however, a significant amount of cleanout of core concrete and cutting of transverse steel was required to make room for the device. It was also necessary to cut the bottom portion of the longitudinal bar to remove the buckled section to provide a straight section on which to install the anchor. The initial state of the column section can be seen in Figure 4.55 (a) and the final installation in Figure 4.54 (b). The anchor was installed on the E reinforcing bar.

(a) **(b)**

Figure 4.55: Repair #5 (a) Initial state of damage prior to headed anchor installation; (b) Dayton Superior D252L Bar Lock ® End Anchor.

An additional parameter considered during this test was an imposed residual drift on the column. For each of the specimens considered to this point, the column has been brought back to plumb (or very close to it) at the conclusion of the initial test and then the repair installed and tested. This is an unlikely case for a structure that has sustained levels of damage requiring a repair of this extent, thus it is of interest to investigate any impact on the physical behavior of the system or constructability of the repair in a residual deformation state.

Upon review of the literature, it was determined that a residual drift of approximately 1% to 1.75% would be an upper bound of what would be considered "repairable damage" by today's standards (FEMA, 2012; Kawashima, MacRae, Hoshikuma, & Nagaya, 1998; Lee & Billington, 2010; Lehman & Moehle, 2000; Pampanin, Christopoulos, & Priestley, 2002). A drift of 1.5% (Δ_R = 1.64in) was imposed on the column before beginning the construction process of the repair. Since the direction of residual deformation would likely align with the direction of maximum damage, the drift was imposed in the direction of the fractured longitudinal bars, which in this case was the X-direction. The ENE bar was fractured during this loading cycle unintentionally and was

treated with the same consideration for bond development as the W bar on the opposite face. The residual drift was applied to the column by imposing a displacement in the direction of the desired drift and then cutting off the actuator force, allowing the specimen to come to rest. The final position of the column is shown in Figure 4.56 along with a plot of the force vs. displacement history from imposing the residual drift in Figure 4.57.

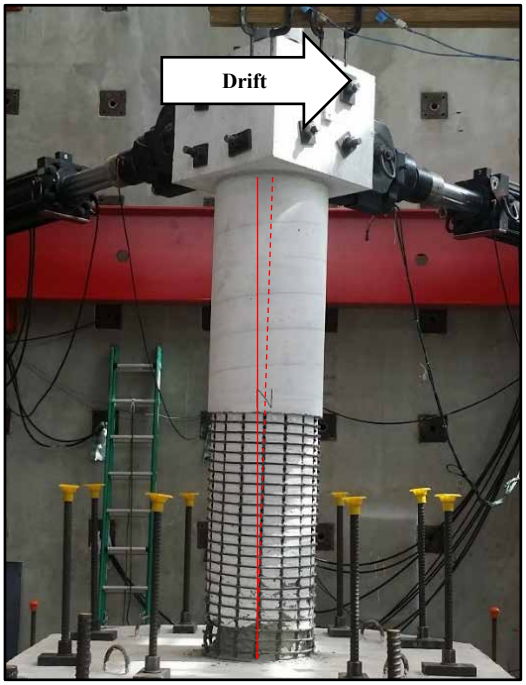

Figure 4.56: Repair #5 column with 1.5% residual drift.

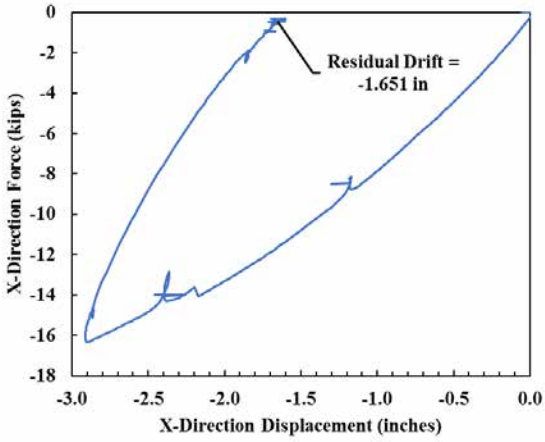

Figure 4.57: Repair #5 Force vs. Displacement plot of imposing residual drift.

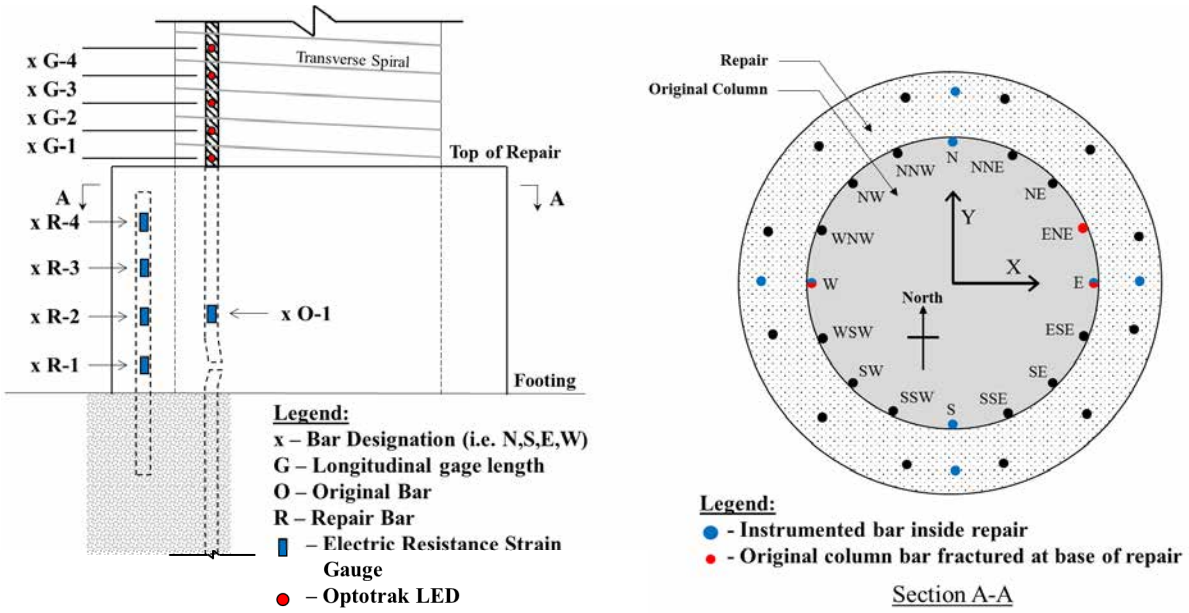

Figure 4.58: Repair #5 Instrumentation labels and repair cross section layout.

Table 4.7: Repair #5 summary of values of interest.

Original Column Properties	
Load History	Scaled Bidirectional Megathrust
Column Geometry	L = 9 *ft*, D = 24 *in*, (L/D = 4.56)
Longitudinal Steel Detailing	16 #6 for $\rho_l = A_{st} / A_g$ = 1.6%
Longitudinal Steel Properties	f_y = 70.33 *ksi*, f_u = 98.68 *ksi*, ε_y = 0.00283
Transverse Steel Detailing	#3 @ 2 *in for* $\rho_s = 4A_{sp} / D'$ *s* = 1.0%
Transverse Steel Properties	f_y = 63.89 *ksi*, f_u = 93.64 *ksi*, ε_y = 0.00418
Column Concrete Strength	f'_c = 6.11 *ksi*
Footing Concrete Strength	f'_c = 6.45 *ksi*
Equivalent Yield Displacement	Δ_y = 1.22 *in*
Damage State	Buckling of all longitudinal bars, fracture of E, ENE and W bars. Imposed residual drift of 1.65" (1.5%) in the West Direction.
Repair Properties	
Load History	Symmetric Two Cycle Set
Repair Geometry	H = 22 *in*, D = 32 *in*
Longitudinal Steel Detailing	16 #7 *A706 gr80*
Longitudinal Steel Properties	f_y = 83.2 *ksi*, f_u = 109.5 *ksi*, ε_y = 0.0033
Transverse Steel Detailing	11ga A36 steel sheet $\rho_s = 4t_j / D'$ = 1.5%
Transverse Steel Properties	f_y = 48.2 *ksi*, f_u = 56.7 *ksi*, ε_y = 0.00154
Repair Concrete Strength	f'_c = 3.84 *ksi* (Pea Gravel Concrete Mix)

4.5.2 Discussion of test results

The repaired specimen performed well early on, however a failure in the weld of the sleeve caused the test to be terminated early following the first cycle of displacement ductility 4. This is two full ductility levels lower than the Repair #4, however this reduced capacity is attributed to the quality of the weld itself and not the mechanism of the repair, which has been shown to be effective in the previous tests. A further discussion of the weld failure is provided in Section 3.3.3 along with specific considerations that should be made to avoid such outcomes in the future. Prior to the weld failure, the specimen performed as intended with deformation concentrating above the annular ring. Regardless of the early termination, there was still a large amount of data collected from which we can draw conclusions, as will be discussed in the following sections.

4.5.2.1 Summary of Events

As mentioned above, this test was not able to reach the full displacement capacity of the repaired cross section due to a failure in the weld of the sleeve. However, it was evident up until this point that the plastic hinge was forming above the repair as it had done in the previous tests. Small cracks began to form on the tension side of the repair during the first yield cycle, consistent with previous tests, with larger cracks forming during $\mu_{\Delta 1}$. Figure 4.59 shows the initial formation of the crack on top of the repair as the column begins to rotate about the relocated hinge. Crushing of the core concrete above the repair began during $\mu_{\Delta 3}$ as shown in Figure 4.60 (a).

During the second cycle of ductility 3, an audible cracking noise was observed when pulling in the -Y direction. It was at this point that the separation of the weld on the North face was noticed. Despite the damage, the test was still able to carry on through the remaining cycles of $\mu_{\Delta 3}$ followed by a full set of $\mu_{\Delta 4}$. The weld on the North face of the column separated completely during the $\mu_{\Delta 4}^{-2y}$ cycle, at which point the test was stopped.

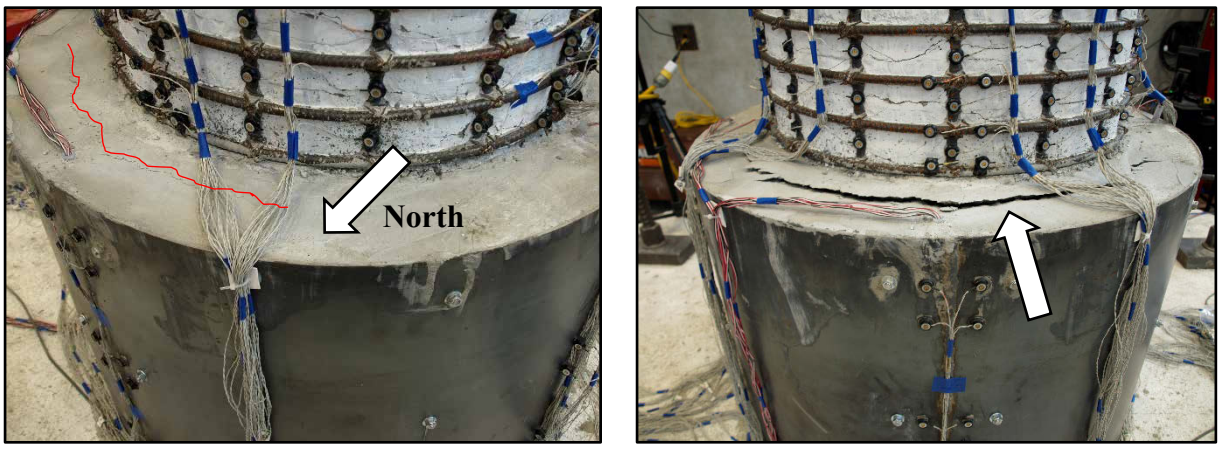

(a) (b)

Figure 4.59: Repair #5 (a) Cracking at the top of the repair during cycle $\mu_{\Delta 1}^{-y}$; (b) Progression of crack opening on North Face during cycle $\mu_{\Delta 2}^{-y}$.

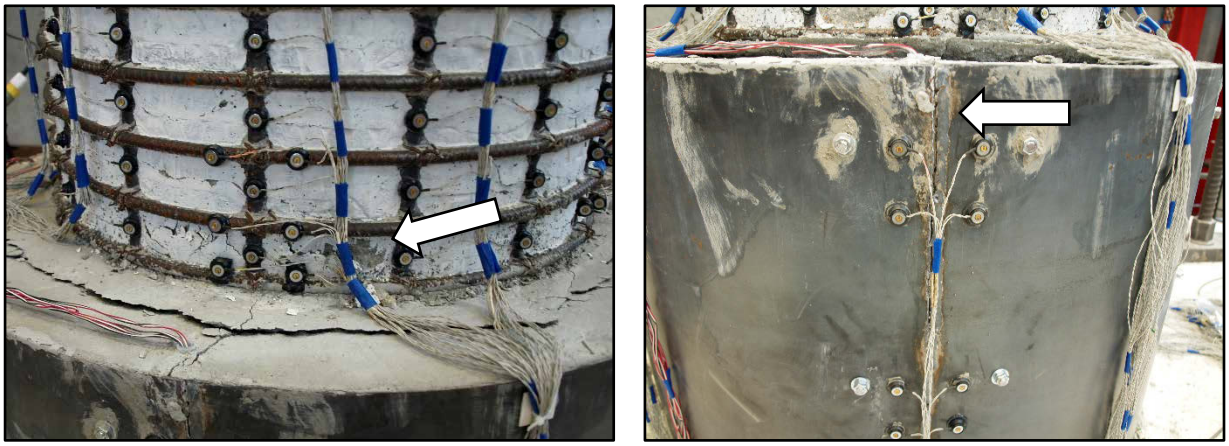

(a) (b)

Figure 4.60: Repair #5 (a) Onset of core crushing during cycle $\mu_{\Delta 3}^{+y}$; (b) Initiation of weld failure on North Face during cycle $\mu_{\Delta 3}^{-2y}$.

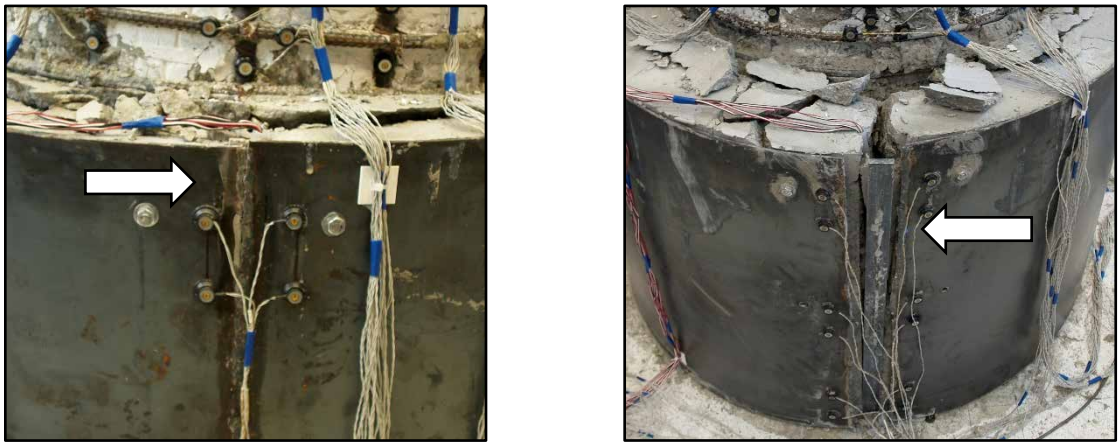

(a) (b)

Figure 4.61: Repair #5 (a) Initiation of weld failure on South Face during cycle $\mu_{\Delta 3}^{2x}$; (b) Complete weld failure on North Face during $\mu_{\Delta 4}^{-2y}$.

4.5.2.2 Global Column Response

The global Force vs Displacement hysteresis response is plotted in Figure 4.62 and Figure 4.63 below for the Y and X directions respectively, along with a comparison to Load Path Study Test 8 which investigated a nominally identical specimen, under the same two-cycle set loading protocol. Although the repair test was terminated early, it can be seen that until that point the response matched with what was expected from previous tests. As with Repair #4, both the initial stiffness and the unloading curves followed that of the original response very closely. It is interesting to note that even though the compressive strength of the repair concrete was lower than intended (f'_c = 3.84 ksi), the stiffness of the repair was still much higher than what was observed with the neat grout mixtures in Repairs #1-3.

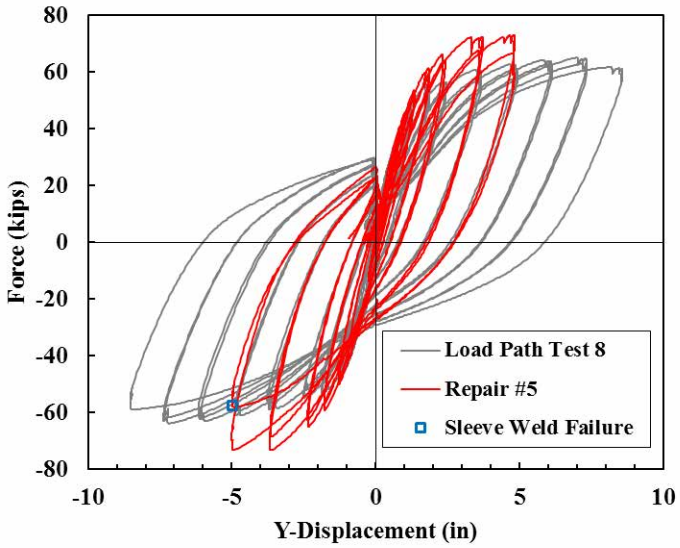

Figure 4.62: Repair #5 Y-Direction Force vs. Displacement.

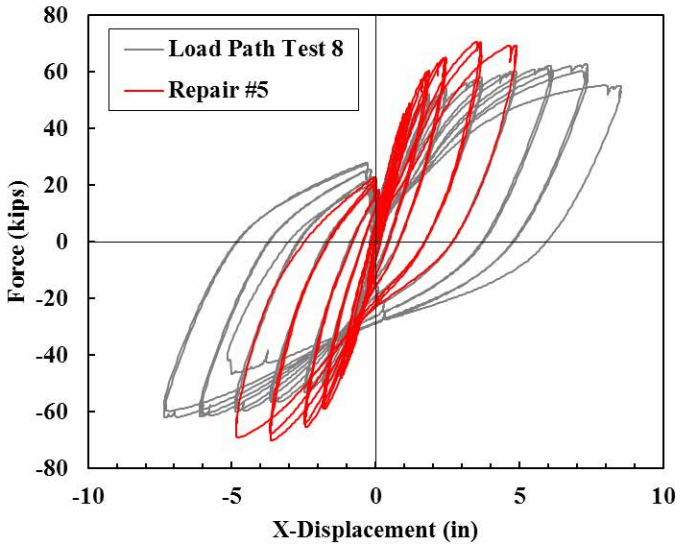

Figure 4.63: Repair #5 X-Direction Force vs. Displacement.

4.5.2.3 Performance of Anchorage Mechanisms

Figure 4.64 compares the strains of the longitudinal bars in the relocated plastic hinge to the top of column displacements for the 'W' and 'ENE' bars. These correspond to the bars that were fractured at the base during the previous test, but had concrete removed completely from their perimeter prior to the repair concrete placement. These plots indicate a loss of bond development occurred during the $\mu_{\Delta 3}$ cycles, exactly as it had during Repair #2 and Repair #4. Thus, it can be concluded that this consideration alone has no effect on the bond development of the reinforcing bars within the repair.

Figure 4.65 compares the same parameters for the 'E' bar, which was repaired using the mechanical headed coupler. This plot shows no significant drop off in strain, which indicates that the bar remained anchored inside of the repair. Although it does appear that the strain begins to drop off slightly during the $\mu\Delta 4$ cycle, this is attributed to the loss of strength in the overall member, as opposed to loss of bond development of the bar. Figure 4.81 (b) compares the strain in this bar to the force applied to the top of the column and shows that the bar continued to deform consistently with the amount of applied loading which would confirm that anchorage was maintained.

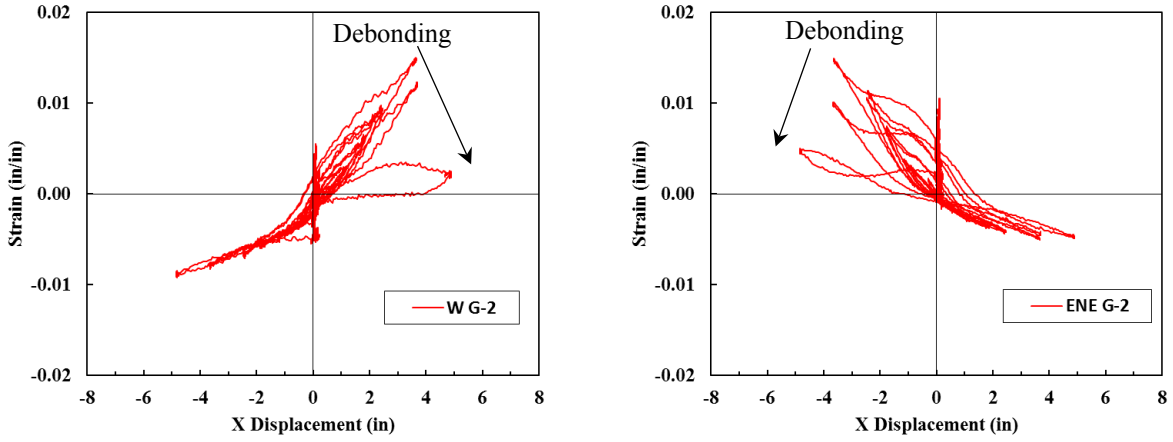

(a) **(b)**

Figure 4.64: Repair #5 strain in longitudinal bars vs X- Displacement on (a) W Bar; (b) ENE Bar.

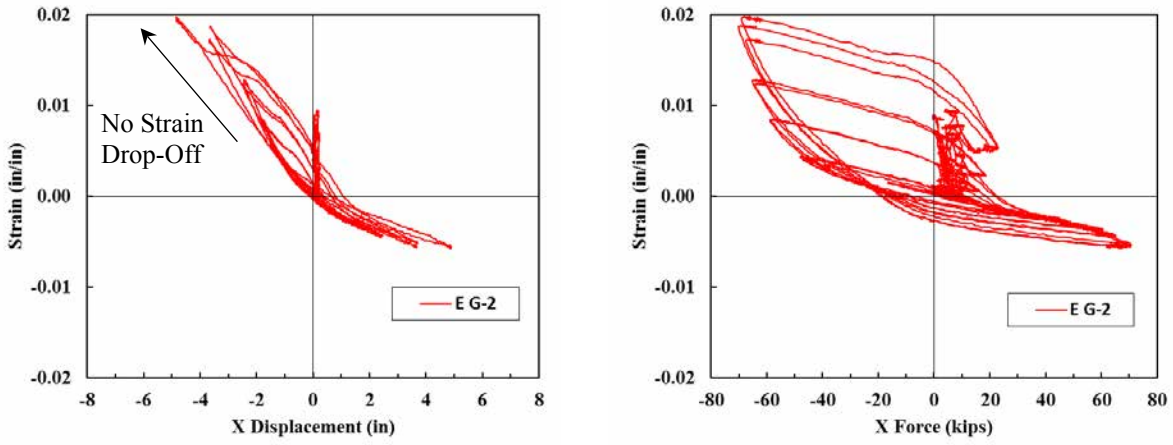

(a) **(b)**

Figure 4.65: Repair #5 (a) Strain in longitudinal bars vs X- Displacement on East bar with Mechanical Headed Stud; (b) Strain vs. X-Force on East bar.

4.5.2.4 Effects of Residual Drift

Although the repair was not able to reach failure through buckling and fracture of the longitudinal steel in the relocated hinge, some conclusions can be drawn from the strain data that was gathered with regards to the effects of residual drift on the overall performance. Recall that the residual drift of the column was imposed in the negative X direction, therefore the East bars would have residual tension while the West bars would be in compression. One of the primary questions entering this test was whether this residual deformation would have any impact on the performance of the repaired column.

A comparison of the strain histories between tests #4 and #5 in the 'WSW' and 'ESE' bars is shown in Figure 4.66 (a) and (b) respectively. Neither of these bars were fractured in either test

and had the same nominal properties therefore they should provide a suitable comparison. Although Test #5 was terminated earlier than Test #4, notice that the peak strains in each bar are nearly identical for a given displacement between the two tests. Note that the strain data that is presented does not account for residual strain between tests (i.e. the strain at the start of each test is taken to be zero on these plots), however the majority of residual strain accumulation would have been at the base of the column where the previous plastic hinge was located. Thus, the difference in total strain between these two bars at this location would be negligible.

It has been shown that buckling and fracture limit states in longitudinal reinforcement can be accurately predicted based on strains and transverse steel detailing (Goodnight et al., 2015) (in addition to other parameters such as axial load, but those have remained constant for each of the tests). Given that the transverse steel spacing in Repair #5 was closer than that of Repair #4, it can be assumed that the onset of bar buckling, and subsequent fracture, would have taken place at an equal or greater displacement demand in Repair #5 than it did during Repair #4. While P-Delta effects will certainly impact the overall demand on the column with significant residual drift, it appears that the capacity of the repaired section is not affected. The impacts of residual drift on the performance of an actual bridge structure subjected to dynamic loading will be addressed in greater detail in Chapter 7.

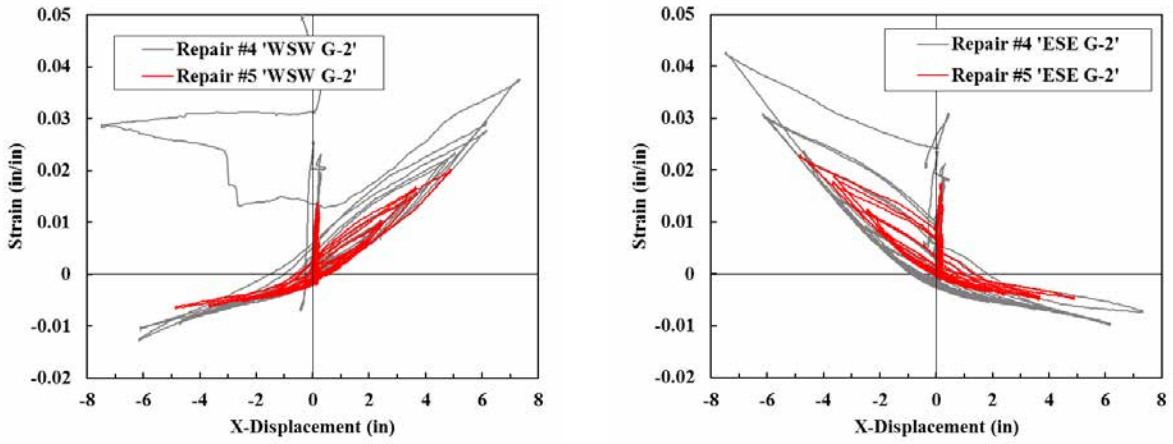

(a) **(b)**

Figure 4.66: Comparison of strain history between Repair #4 and Repair #5 in the (a) WSW bars and; (b) ESE bars.

4.6 Repair #6

4.6.1 Summary of Repair Considerations

Repair #6 again aimed to investigate specific means of bond development for fractured longitudinal bars inside of the repair; however, a different method was utilized than either of those in Repair #5. To describe the mechanism utilized in this repair, it is helpful to first consider the force transfer mechanism that is assumed within the repair region. Figure 4.67 (a) illustrates an idealization of this mechanism as described by (Lehman et al., 2001). This diagram shows compression struts developing between the flexural tension bars in the original cross section and the longitudinal and transverse steel in the jacket. This results in two components of force, one vertical and one horizontal. The vertical is resolved by tension in the repair longitudinal bar and the horizontal component is resisted by the transverse steel (discrete hoops were used in the Lehman, et. al. study, however this would correspond to the steel sleeve in Repair #6). This mechanism relies on fully composite behavior through flexure to develop, however Figure 4.67 (b) shows the formation of a gap between the repair and the original column observed in Repair #1. With the presence of this gap, there is no pathway for the compression struts on the flexural tension side of the column to form and develop the mechanism as illustrated in Figure 4.67 (a), therefore further consideration is needed.

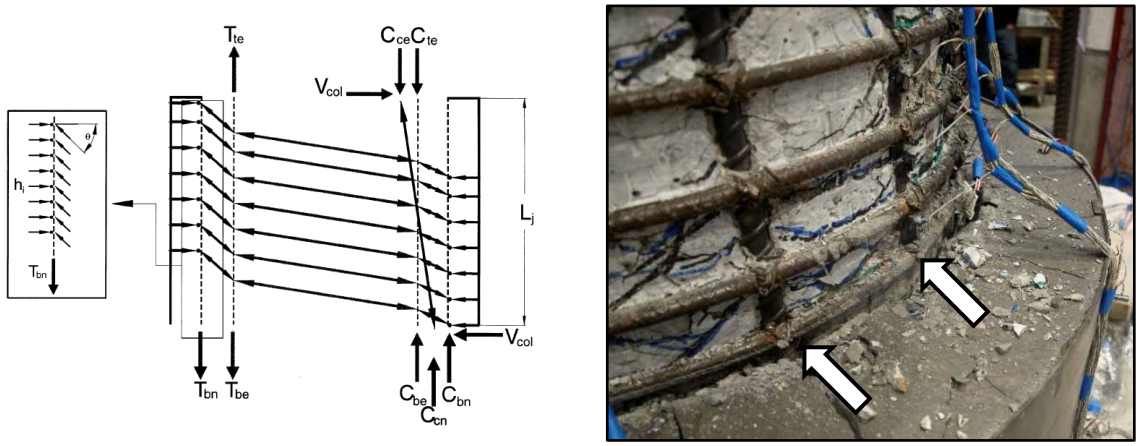

Figure 4.67: (a) Idealized force-transfer mechanism in repair region, as described by Lehman, et. al. (2001); (b) Separation of repair and original column on flexural-tension side of column in Repair #1.

For non-fractured bars, this issue is not of concern since they are not developing their capacity over the relatively short length of the repair region, but are instead still continuous into

the footing. Fractured column bars, however, need to develop their tensile capacity over the length of the repair to be considered in strength calculations for the repaired column. Repair #5 addressed this for individual bars using two different methods: 1) by utilizing a mechanically fastened headed stud to the base of a single fractured bar in order to provide direct anchorage, and 2) by improving bond conditions by fully exposing the fractured bar within the repair region prior installing the repair material, as recommended in (ACI 546, 2014). Following the test of Repair #5 it was seen that the headed stud performed as intended with the fractured bar continuing to develop force through the end of the test, however the bars that were only exposed and fully encased with fresh concrete saw little change in performance.

Repair #6 utilizes a different method to develop these bars, the aim of which is to provide a mechanism through which the flexural behavior assumed in Figure 4.67 (a) can develop. By doing so, it is assumed that the compression struts will bear against the fractured bars, therefore increasing friction and improving the bond conditions. In the previous tests, it was noted that the performance of the repair seemed to more closely match that of a socket than an enlarged flexural cross-section. Upon investigation of the behavior of column-socket connections, it was found that precast column connections have been shown to exhibit very close to monolithic flexural behavior when provided a rough interface through which to develop these forces (Canha, Debs, De Borja Jaguaribe, & De Cresce El Debs, 2009). This rough interface was provided via a shear key detail that is illustrated, along with the modified force transfer mechanism, in Figure 4.68.

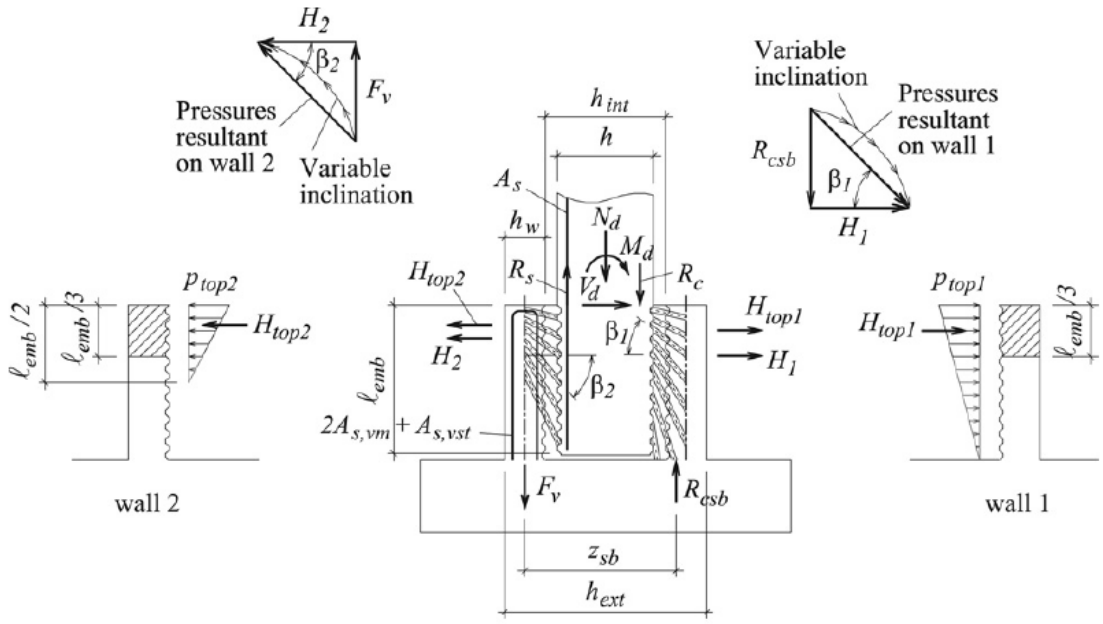

Figure 4.68: Transfer of force resultants from precast column to socket base with roughened interface (Canha, de Borja Jaguaribe, de Cresce El Debs, & El Debs, 2009).

Although the above figure specifically relates to a precast column which is placed into a socket and grouted in place, the condition of a fractured longitudinal bar resembles that which is shown. However, since in the case of the repair the column is already in place and the socket is installed afterwards, the shear key mechanism cannot simply be formed into the column and socket prior to installation. To simulate the shear key in the repair, an inner sleeve made of 16ga Aluminized ASTM A-929 corrugated steel drainage pipe was placed between the existing column and the repair longitudinal bars. The installation sequence is described in Section 3.3.2.

The corrugated inner sleeve is meant to deform with the original column as it is affixed via the grout. As the column deforms, the textured profile of the corrugated steel sleeve will act as a mechanical shear key which will bear on the outer concrete and transfer forces to the longitudinal repair bars and outer steel confining jacket. This reaction should, in turn, provide increased friction force on the fractured bar, therefore improving bond conditions inside the repair as discussed above. An illustration of this mechanism is shown in Figure 4.69 below.

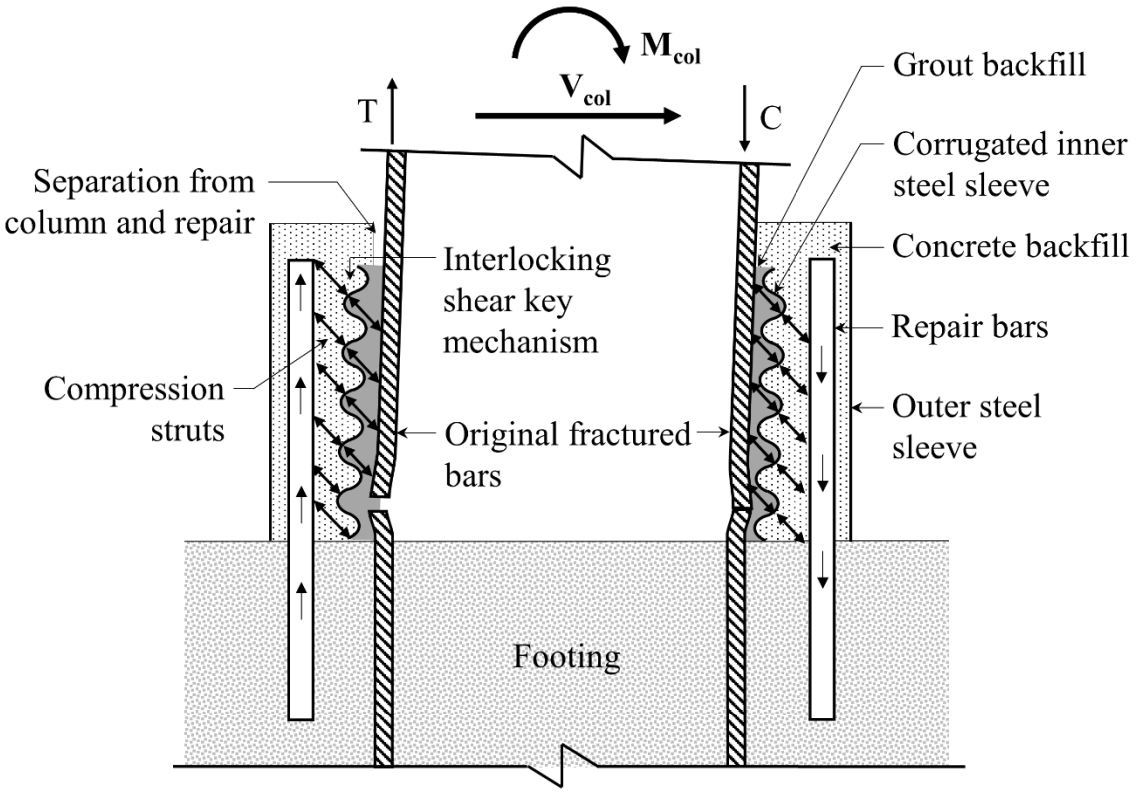

Figure 4.69: Illustration of corrugated steel sleeve shear key mechanism.

The existing column bars and repair bars resemble the condition of a non-contact lap splice, where the forces in the fractured column bars are transferred completely to those of the repair bars via the compression strut mechanism. A model to calculate the non-contact splice length of Grade 60 reinforcement subjected to repeated loading was developed by (Sagan, Gergely, & White, 1991). This model assumes a plane truss analogy with the rebar acting as the tension chords and the concrete providing compression struts inclined at 50º. Transverse steel is also required for equilibrium of the horizontal force component. Figure 4.70 illustrates this mechanism, and the calculation of the total required splice length is given in Equation 4-1 and Equation 4-2. Assuming a 3" spacing between the original column longitudinal steel and the repair bars and compressive strength of 9000 psi for the grout, the total splice length to develop the fractured #7 column bars would be 18". With the bar fracture location at roughly 3" above the footing and 1" of cover above the top of the repair bar, this corresponds to the 22" repair height that was used.

$$l_{eff} = \frac{3100 d_b}{\sqrt{f_c'}\left(1.5 + 0.2 s_p / d_b\right)} \qquad \textit{Equation 4-1}$$

$$l_s = l_{eff} + 1.2 s_p$$ *Equation 4-2*

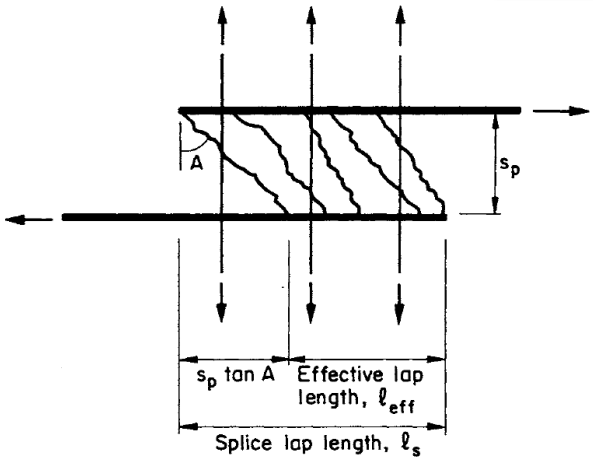

Figure 4.70: Inclined truss mechanism and effective length of non-contact lap splice (Sagan et al., 1991).

In addition to the corrugated steel sleeve that was discussed above, the damage state of the column was imposed such that it matched that of Repair #2. This includes 3 fractured longitudinal bars on the North and South faces for a total of 6 fractured bars. The North face bars were also exposed similar to those in Repair #5 to investigate whether this has any added benefit with the corrugated sleeve. The South face bars did not receive any additional consideration aside from the corrugated steel sleeve. Figure 4.71 below shows the damage state of the North and South faces prior to installation of the repair. A summary of the original and repaired column properties is provided in Table 4.8 along with a layout of the repaired cross section and definitions of the instrumentation tags referenced later in the section in Figure 4.72.

(a) **(b)**

Figure 4.71: Damage state of column (a) North face with concrete stripped from fractured bars; (b) South face with original column concrete.

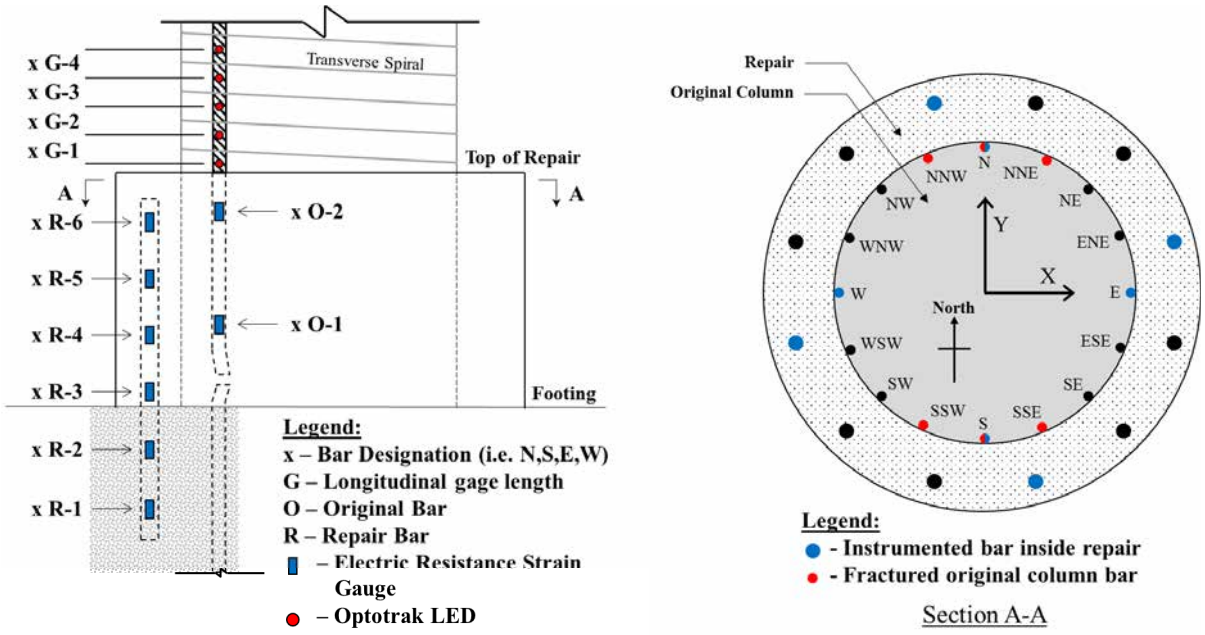

Figure 4.72: Repair #6 Instrumentation labels and repair cross section layout.

Table 4.8: Summary of Repair #6 values of interest.

Original Column Properties	
Load History	Symmetric Two Cycle Set
Column Geometry	L = 9 *ft*, D = 24 *in*, (L/D = 4.56)
Longitudinal Steel Detailing	16 #7 for $\rho_l = A_{st} / A_g$ = 2.1%
Longitudinal Steel Properties	f_y = 69.63 *ksi*, f_u = 96.66 *ksi*, ε_y = 0.0027
Transverse Steel Detailing	#3 @ 1.5 *in for* $\rho_s = 4A_{sp} / D' s$ = 1.3%
Transverse Steel Properties	f_y = 63.89 *ksi*, f_u = 93.64 *ksi*, ε_y = 0.00418
Column Concrete Strength	f'_c = 6.13 *ksi*
Footing Concrete Strength	f'_c = 7.52 *ksi*
Equivalent Yield Displacement	Δ_y = 1.36 *in*
Damage State	Buckling of all longitudinal bars, fracture of NNE, N, NNW, SSW, S and SSE bars.
Repair Properties	
Load History	Symmetric Two Cycle Set
Repair Geometry	H = 22 *in*, D = 32 *in*
Longitudinal Steel Detailing	12 #10 *A706 gr80*
Longitudinal Steel Properties	f_y = 83.6 *ksi*, f_u = 114.9 *ksi*, ε_y = 0.0030
Transverse Steel Detailing	11ga A36 steel sheet $\rho_s = 4t_j / D'$ = 1.5%
Transverse Steel Properties	f_y = 48.2 *ksi*, f_u = 56.7 *ksi*, ε_y = 0.00154
Repair Concrete Strength	f'_c = 4.86 *ksi* (Pea Gravel Concrete Mix)
Repair Grout Strength	f'_c = 11.33 *ksi* (BASF MasterFlow® 928)

4.6.2 Discussion of test results

4.6.2.1 Summary of Events

Overall, the repair performed as intended with the plastic hinge visibly relocating above the repair. The test began with a single cycle of ½ yield followed by a single cycle of first yield displacement, as was determined in the first column test. As with the previous repairs, these cycles were mostly uneventful, however cracking on the top of the repair was observed during the first yield cycle as shown in Figure 4.73 (a). These cracks progressed through ductility 2 growing progressively larger as Figure 4.73 (b) shows.

Core crushing of the original column above the repair was observed during the first cycle of ductility 3. Figure 4.74 (a) shows the South face of the column during the first cycle of ductility 3 in the -y direction. This damage continued through sets of ductility 4 and 5 with the top of the repair and interior core of the original column further degrading. Larger chunks of concrete were removed from the top of the repair as they became free to protect the instrumentation. Visible onset of bar buckling occurred during the first -y cycle of ductility 6 on the SE corner bar, as shown in Figure 4.75 (a). The test continued through two complete cycles at ductility 6 with several other bars buckling. The SE bar fractured during the first +y cycle of ductility 6.5 at a displacement of 8.95", shown in Figure 4.75 (b), at which point the test was terminated.

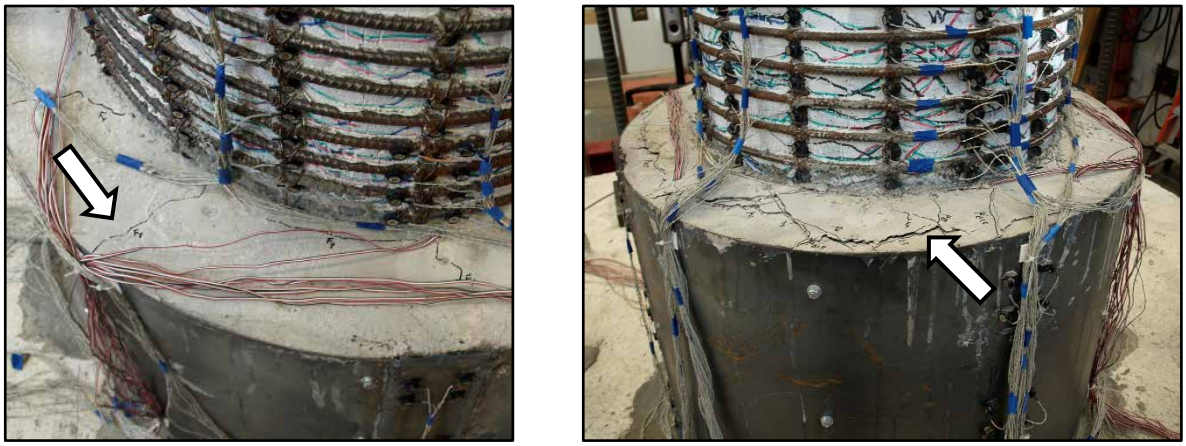

(a) **(b)**

Figure 4.73: Repair #6 (a) Cracking at the South side top of the repair during cycle F_y^{+y}; (b) Progression of crack opening on West face during cycle $\mu_{\Delta 2}^{+x}$.

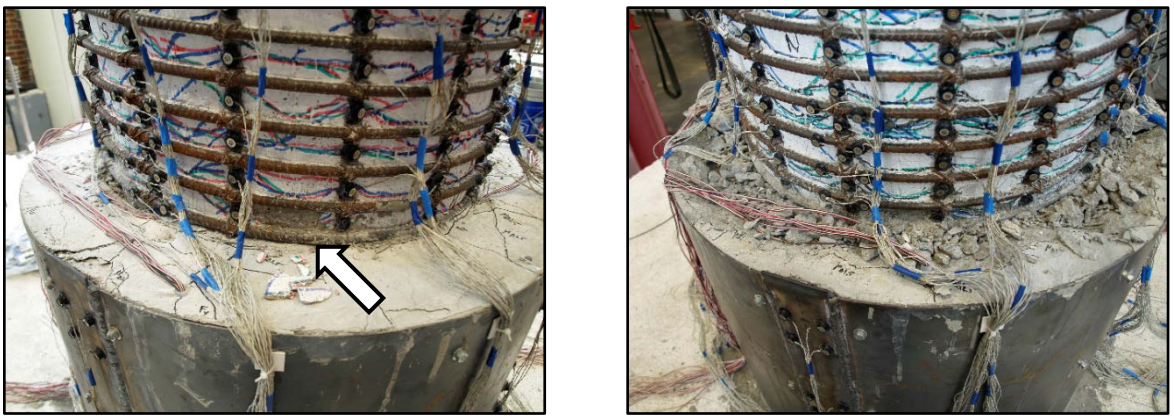

(a) **(b)**

Figure 4.74: Repair #6 (a) Onset of core crushing during cycle $\mu_{\Delta 3}^{-y}$; (b) Progression of damage on North Face during cycle $\mu_{\Delta 5}^{+1y}$.

(a) **(b)**

Figure 4.75: Repair #6 (a) Initiation of visible buckling of SE bar during cycle $\mu_{\Delta 6}^{-1y}$; (b) Fracture of SE bar during $\mu_{\Delta 6.5}^{+1y}$.

4.6.2.2 Global Column Response

A global Force vs Displacement hysteresis response is plotted in Figure 4.76 and Figure 4.77 below for the Y and X directions respectively. These figures provide a comparison of the response of Test 10 of the load path study, which corresponds to the same column that was repaired and tested for Repair #6. It is observed that both the global Y direction and global X direction provide substantial increases in peak strength while maintaining similar initial stiffness. The unloading curves for the repaired Y direction response begin to exhibit pinching behavior during the ductility 4 cycle, which would likely indicate the onset of the fractured bars debonding. Despite this, the repaired specimen was capable of reaching the same level of displacement as the original column, as they both failed through bar fracture at displacement ductility 6.5.

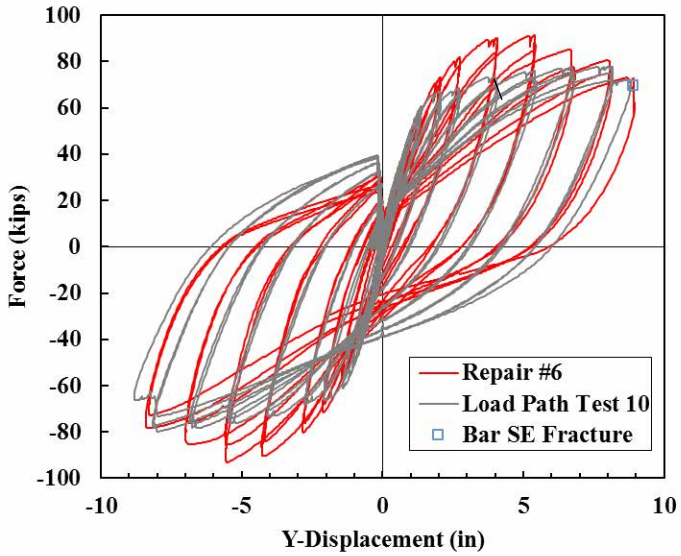

Figure 4.76: Repair #6 Y-Direction Force vs. Displacement compared to Load Path Test #10.

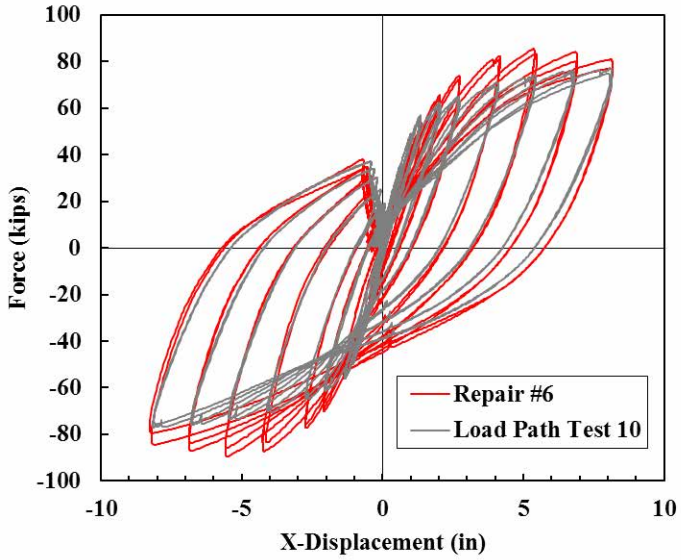

Figure 4.77: Repair #6 X-Direction Force vs. Displacement compared to Load Path Test #10.

Figure 4.78 and Figure 4.79 below provide a comparison between Repair #6 and Repair #2. Repair #2 corresponded to the same level of damage as that of Repair #6 with 3 of the bars on the North and South faces fractured. The response in the X-direction is remarkably similar between the two tests with the curves overlapping almost entirely. This is to be expected as there were no fractured bars in this direction of loading. The Y-direction response also matches very closely, however there is a noticeable increase in strength for Repair #6. This is more apparent in the negative Y direction, which would correspond to tension in the bars that were fully exposed on the

North face prior to installation of the repair. This behavior is also apparent in analysis of the individual bar strains which is discussed in the following section.

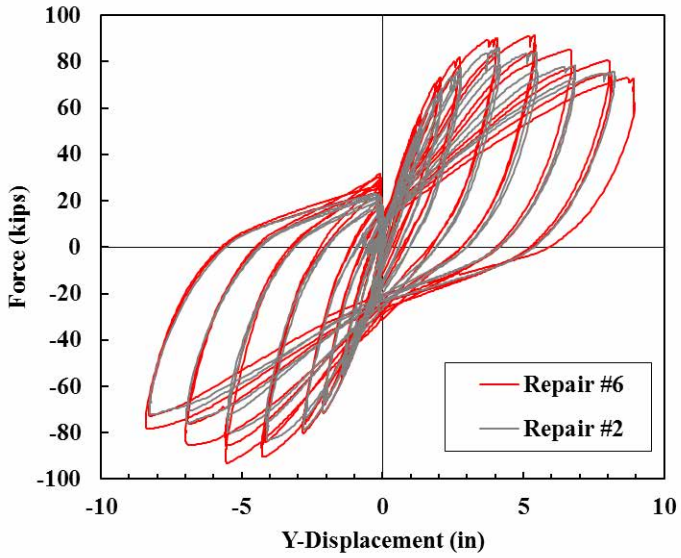

Figure 4.78: Repair #6 Y-Direction Force vs. Displacement compared to Repair #2.

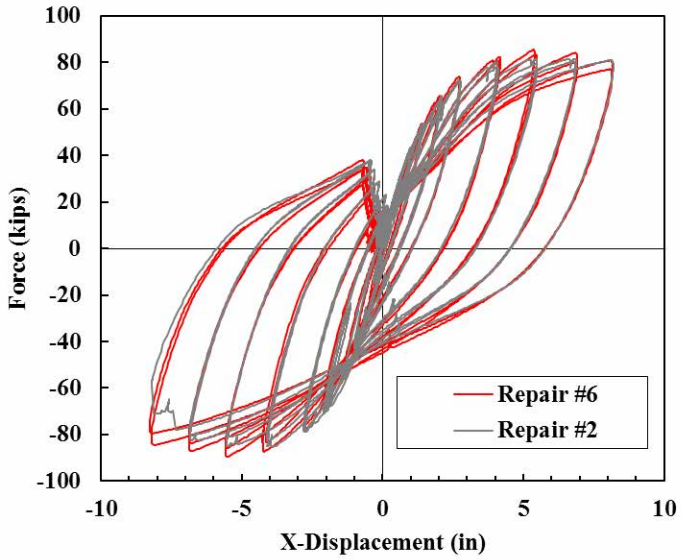

Figure 4.79: Repair #6 X-Direction Force vs. Displacement compared to Repair #2.

4.6.2.3 Local Behavior

The following plots compare the strains in the longitudinal bars above the repair to the top of column displacement. These correspond to the strains calculated from the red Optotrak gage lengths indicated in Figure 4.72. Gage 2 was used for each of the plots, except for that of the East bar in Repair #2 where there was not sufficient data. Gage 3 was used instead for this bar.

Figure 4.80 illustrates the strains on the North and South faces of the columns, which correspond to the fractured bars. In each of these plots the strains begin to drop off once displacement reaches a certain level, which would indicate that the bars have lost their bond and are no longer contributing to the response of the column. If we compare the results from Repair #6 to those of Repair #2, however, we can see that this behavior is delayed significantly. Figure 4.80 (a) shows the strains of the North bar in the two repairs. Recall that the North face in Repair #6 had all of the existing concrete removed and replaced with fresh grout around the full perimeter of the fractured bars in addition to the corrugated sleeve. While the bars in each repair did eventually debond prior to the end of the test, the debonding of Repair #6 was delayed until the ductility 4 cycle, whereas that of Repair #2 occurred by ductility 2. Additionally, the peak strains observed in this bar for Repair #6 were around 0.02, whereas those of Repair #2 only reached 0.007. This indicates a significant improvement in performance and delays the increased demand on adjacent bars. The South face of Repair #6 did not have any additional considerations beyond the corrugated sleeve. Figure 4.80 (b) compares the strains of the two repairs on this face and while there is some improvement, it is not as noticeable as that of the North face. Onset of debonding is not significantly delayed, however the peak strains do increase from roughly 0.01 to 0.014 in Repair #6.

Figure 4.81 compares the strains in the East and West directions for Repair #2 and Repair #6. Neither contained fractured bars in these directions, and the plots indicate that the strain behavior in both repairs was nearly identical. As such, it would seem that there is no real benefit to providing the corrugated sleeve in cases where there are no fractured bars as the performance remains the same.

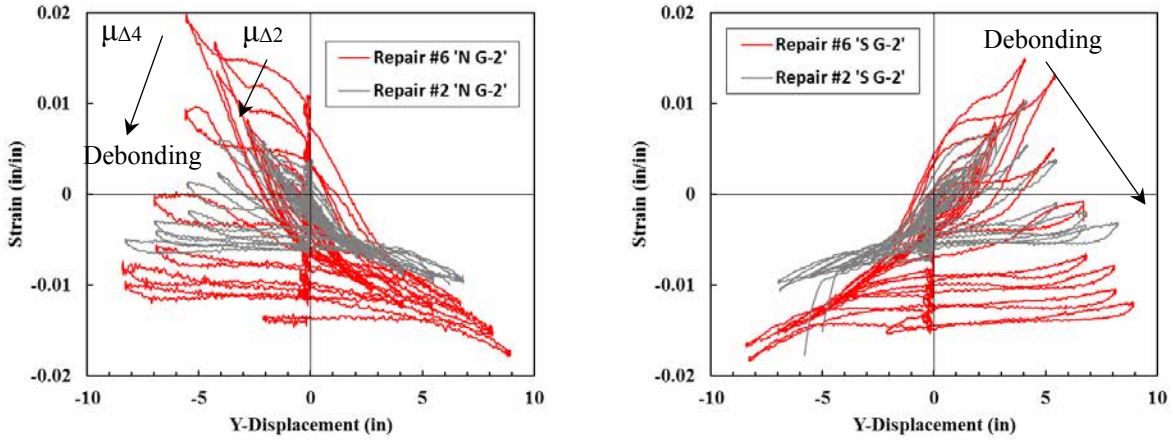

(a) **(b)**

Figure 4.80: Strain in longitudinal bars vs Y- Displacement on (a) North Bar; (b) South Bar.

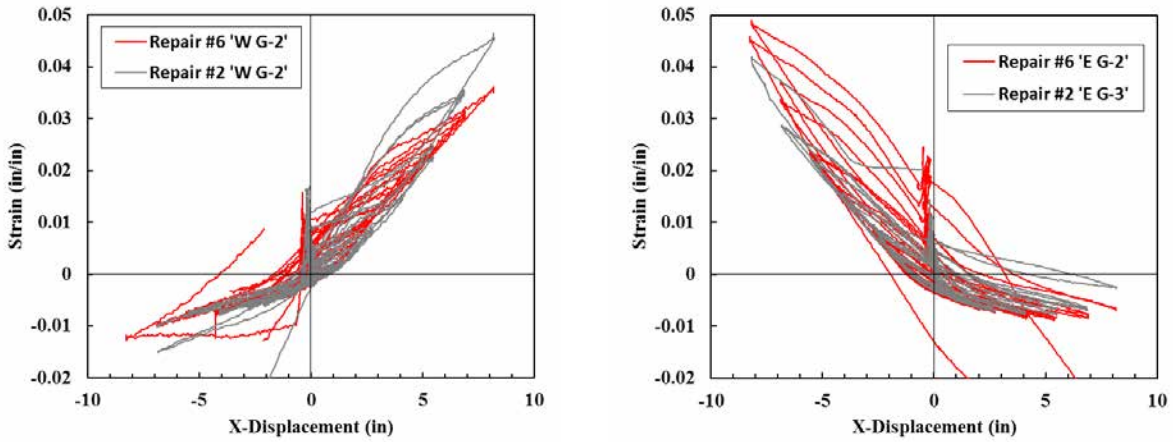

(a) **(b)**

Figure 4.81: Strain in longitudinal bars vs X- Displacement on (a) West Bar; (b) East Bar.

Strains in the repair region were measured using electrical resistance strain gauges. The peak strains, and most reliable data, in each direction were observed in the gauges located just below the surface of the footing. These gauges correspond to 'x R-2' in Figure 4.72, where the 'x' indicates the column face on which the instrumented bar is located. Each of the plots indicate the strains remaining well below yield, as they have in previous tests, with a peak strain of approximately 0.0017 occurring in the South bar.

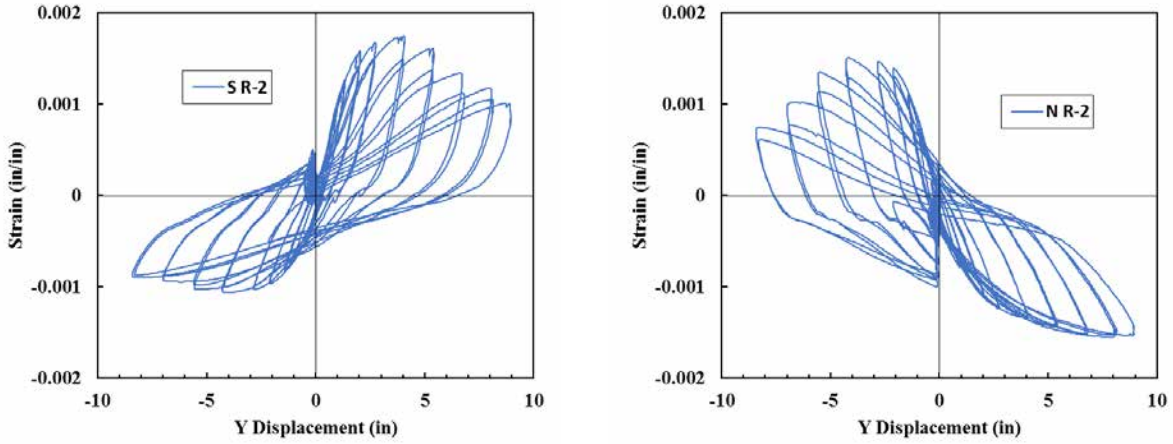

(a) **(b)**

Figure 4.82: Strain vs Y- Displacement in (a) South repair bar; (b) North repair bar.

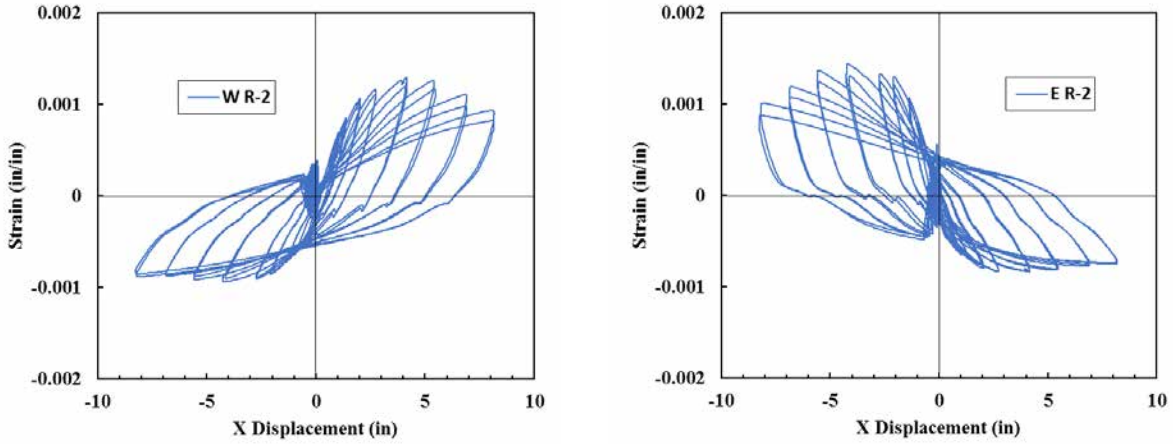

(a) **(b)**

Figure 4.83: Strain vs X- Displacement in (a) West repair bar; (b) East repair bar.

Chapter 5: Analytical Design Model

This chapter discusses methods by which to account for all modes of deformation within the repaired system, and how to design the repair itself. A performance-based design approach is adopted with specific limit state criteria.

5.1 Components of Deformation

The top of column displacements measured during each test represent the sum of many individual components of deformation. The list below provides an exhaustive account of each potential source of deformation, with a visualization of each illustrated in Figure 5.1. Of those listed, foundation translation and rotation are explicitly removed from the reported displacements for each test as they do not provide any useful information with regards to the performance of the repaired column. Therefore, the displacements reported in Chapter 4 consist of the sums of components 3 through 8.

1. Foundation Translation
2. Foundation Rotation
3. Repair Shear
4. Repair Flexure
5. Column Shear
6. Column Flexure
7. Rigid Repair Rotation
8. Column Base Rotation

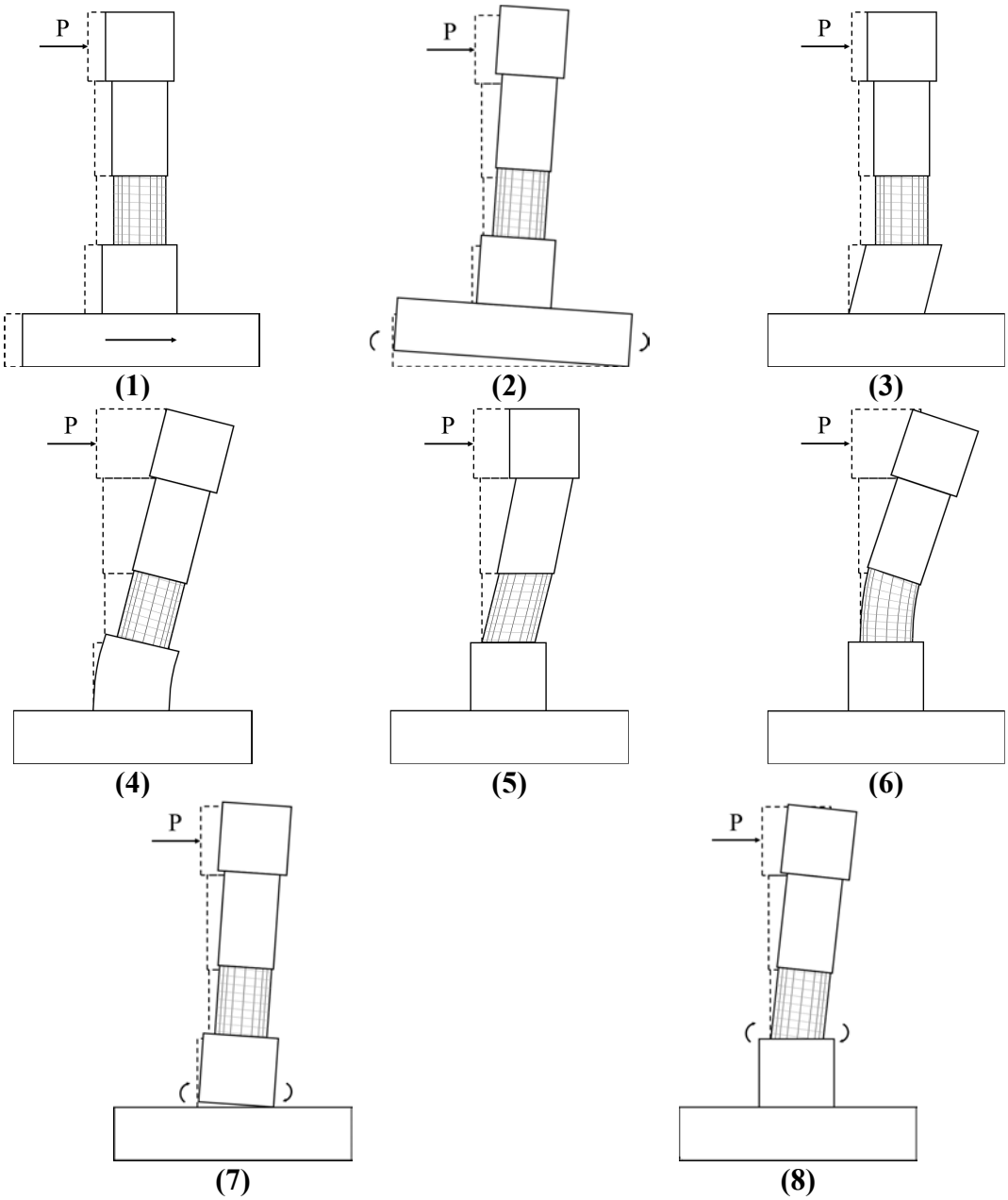

Figure 5.1: Visualization of the components of lateral column displacements.

Of the above listed components, column flexure (6), rigid repair rotation (7), and column base rotation (8) account for the overwhelming majority of deformations in the test specimens. Figure 5.2 through Figure 5.6 illustrate the contributions of each component to the overall measured displacement of the columns. Each bar represents the average contribution during peak displacement response for the ductility cycles listed (i.e. the average response in the positive and negative directions for each of the two cycles), and each plot is meant to show the general trends during the tests. The methods for calculating each component of deformation are detailed in

Section 3.5. Repair #5 is explicitly omitted from the figures below, as the weld failure of the sleeve changes the boundary conditions and resulting response of the column in a way that is not meaningful to the development of this repair method.

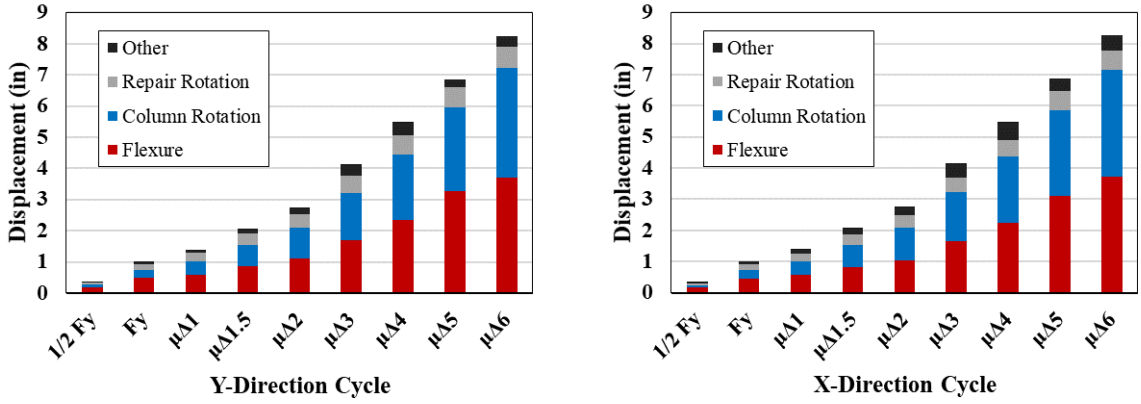

Figure 5.2: Repair #1 average components of deformation.

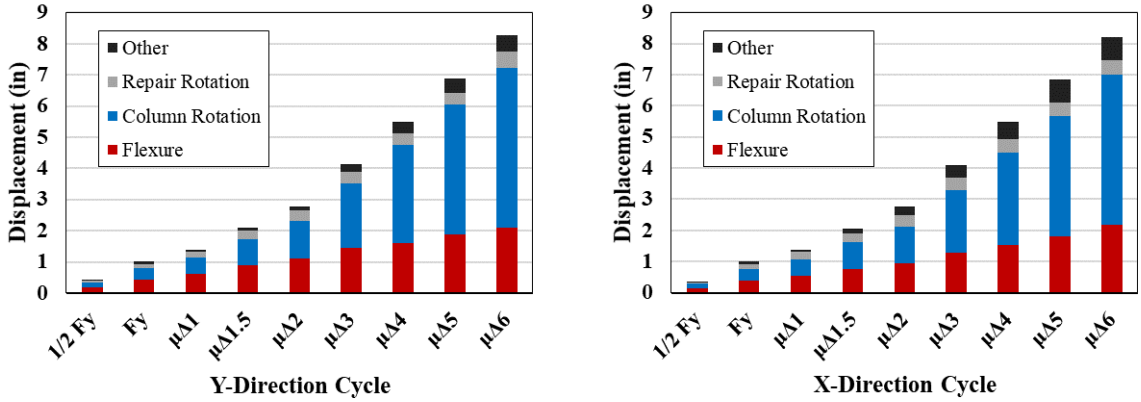

Figure 5.3: Repair #2 average components of deformation.

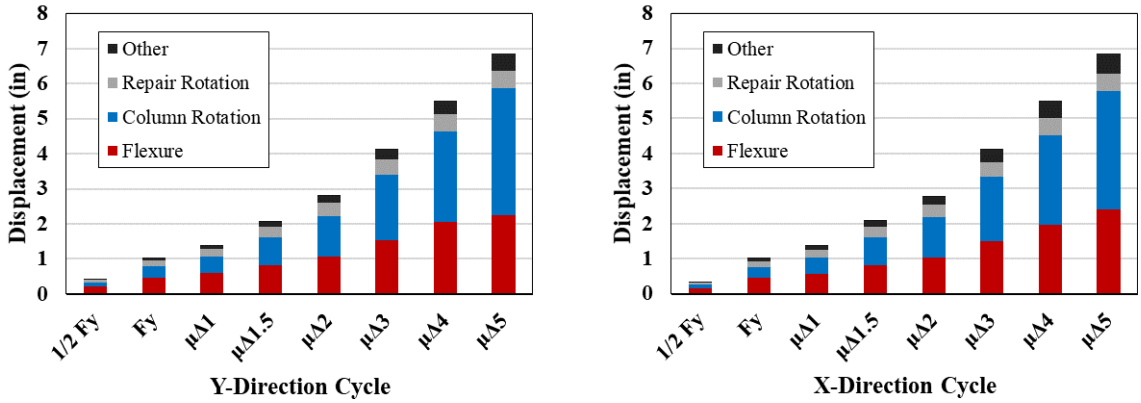

Figure 5.4: Repair #3 average components of deformation.

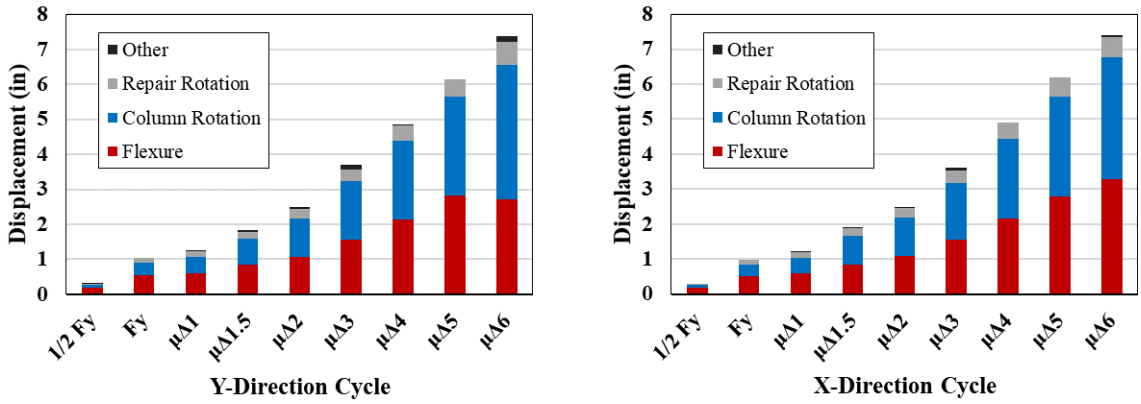

Figure 5.5: Repair #4 average components of deformation.

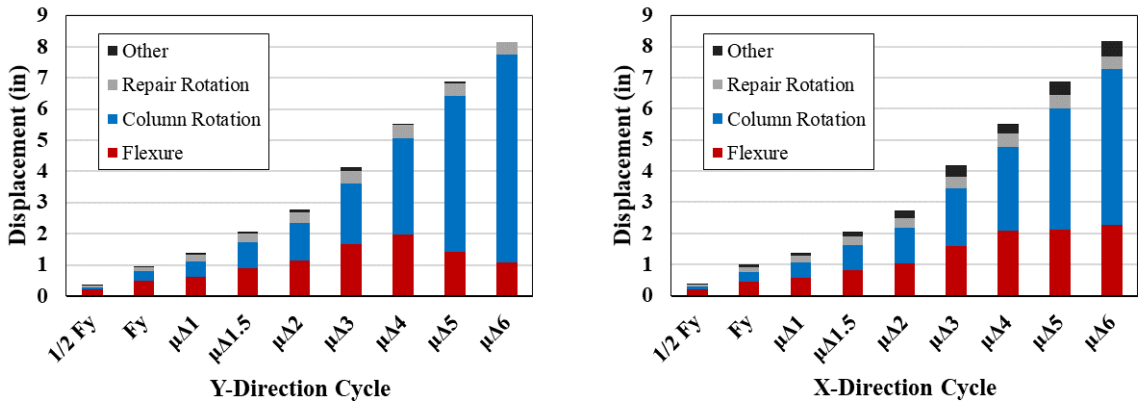

Figure 5.6: Repair #6 average components of deformation.

In each test, column rotation due to strain penetration into the repair accounts for a very large proportion of deformation, especially in Repairs #2 and #6 which had multiple bars fractured on the extreme faces in the Y-direction. This contrasts with a typical RC column test, where column flexure accounts for a majority of the overall deformation, and base rotation due to strain penetration is smaller, although not insignificant. For example, consider Figure 5.7 which compares the response of Repair #1 to that of load path test #6, which is the same column prior to installation of the repair.

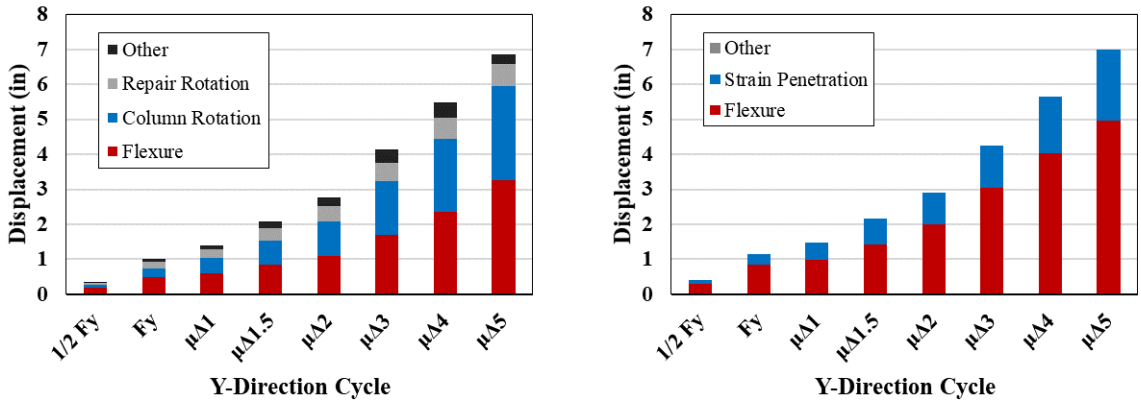

Figure 5.7: Comparison of average components of deformation between (a) Repair #1 and (b) Load path test #6.

5.2 Displacement Response Prediction

Performance based design of RC bridges requires that the designer understands how the structure behaves during an earthquake and can accurately predict key modes of failure. In most RC bridges, the primary mode of failure is through ductile plastic hinges in the columns which dissipate energy through non-linear deformation. While damage to buildings is often described by the state of its contents following a seismic event, which can be related to peak inter-story drift, bridges are typically limited only by the damage to the structure itself, which is more commonly related to local strains within the plastic hinge. Thus, it is of interest to describe the global force-displacement response of the bridge with respect to the local strains in the plastic hinge region. Furthermore, it will be shown that by describing the deformation of the repaired system through fundamental principles, the necessary quantities for the design of the repair can be directly and easily obtained.

5.2.1 Typical Reinforced Concrete Bridge Columns

Calculation of the non-linear force-displacement response of typical RC bridge columns normally follows the well-established principles laid out by Priestley, Calvi, and Kowalsky (2007). This method divides the overall column response into elastic and plastic components, which are summed together, along with the effects of strain penetration into the adjacent member, to obtain the total inelastic column deformation. Column shear also contributes to the overall deformation; however, plastic hinge forming members are typically flexure dominant with shear accounting for very little of the total displacement and it is therefore typically neglected. While not directly

applicable to the solution of the repaired system, the following section summarizes the procedures associated with this method as the general concept will form the basis of the proposed model.

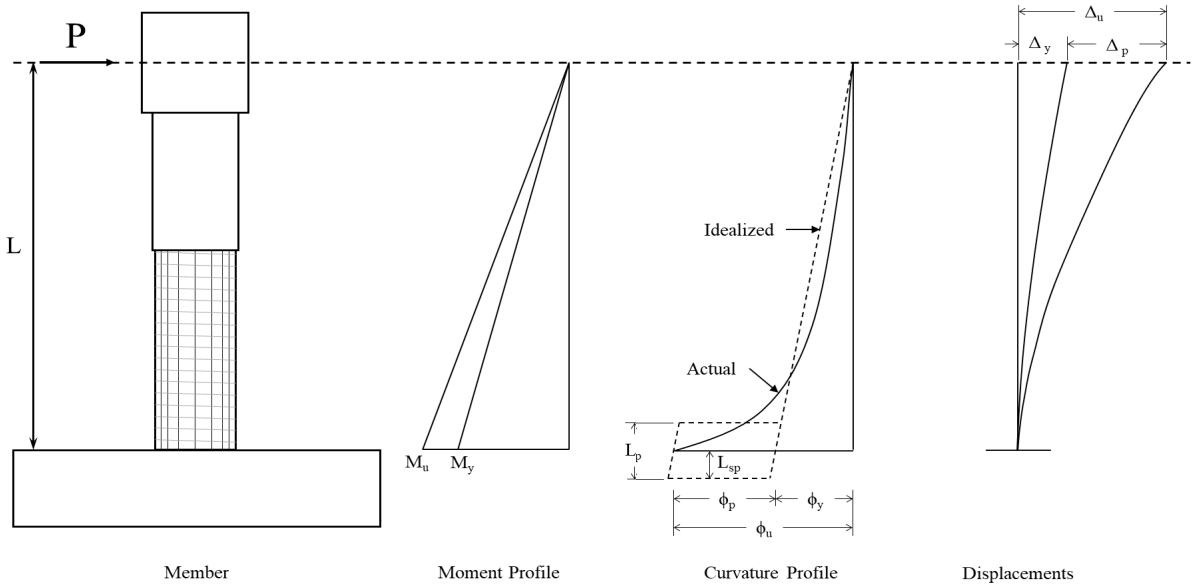

Figure 5.8: Force and deformation profile for typical single bending column, adapted from (Priestley et al., 2007).

For a system of known geometry and cross section profile, the calculation of the force-displacement response is relatively straight forward. First, a moment-curvature analysis is performed on the column cross-section in which nonlinear steel and concrete material models are defined throughout the cross-section accounting for reinforcement layout, confinement effects, and strain hardening. From this analysis, the nominal and yield moments (M_N and M_y respectively) are obtained, along with their corresponding curvatures (ϕ_u and ϕ'_y), at the points when specified strain limits are reached. This resulting section response is then translated to member response. While the actual distribution of deformation at the member level is quite complex, an idealization method using a "plastic hinge" is used to simplify the analysis. An illustration of the actual and idealized curvatures over the length of a single-bending column is shown in Figure 5.8 along with the resulting top of column displacements. The calculation of total displacements using actual curvature distributions requires an integration of the non-linear curvature profile over the entire length of the member, which requires extensive computational effort. However, the plastic hinge method requires only the application of the moment-area method for a single triangular and rectangular region by approximating the elastic deformation as linear over the entire length of the column and the plastic deformation as the result of a constant curvature distributed over a specified

distance referred to as the "plastic hinge length" (L_p), which is calculated using Equation 5-1 through Equation 5-3.

$$L_p = kL_c + L_{sp} \geq 2L_{sp} \qquad \textit{Equation 5-1}$$

$$k = 0.2\left(\frac{f_u}{f_y} - 1\right) \leq 0.08 \qquad \textit{Equation 5-2}$$

$$L_{sp} = \begin{cases} 0.022\, f_{ye} d_{bl} & (MPa) \\ 0.15\, f_{ye} d_{bl} & (ksi) \end{cases} \qquad \textit{Equation 5-3}$$

Equation 5-2 defines the coefficient *'k'* that accounts for moment gradient, while Equation 5-3 represents the strain penetration length, L_{sp}, into the adjacent member. The strain penetration length accounts for the fact that the strains in the longitudinal bars do not immediately drop to zero at the adjoining member interface, but instead decrease over some distance and therefore result in additional rotation at the column joint which translates to additional displacement over the length of the member. The elastic and plastic displacements are then calculated using Equation 5-4 and Equation 5-6 respectively and the total ultimate displacement is simply the sum of these values, as represented in Equation 5-7. Note that Equation 5-6 is only exact when $L_p = 2L_{sp}$; however, more accurate results can be obtained by multiplying the plastic rotation by the distance between the top of column and the centroid of the hinge region (Priestley et al., 2007).

$$\Delta_e = \frac{\phi_y \left(L_c + L_{sp}\right)^2}{3} \qquad \textit{Equation 5-4}$$

$$\phi_y = \frac{M_N}{M_y}\phi_y' \qquad \textit{Equation 5-5}$$

$$\Delta_p = \left(\phi_u - \phi_y\right) L_p L_c \qquad \textit{Equation 5-6}$$

$$\Delta_u = \Delta_e + \Delta_p \qquad \textit{Equation 5-7}$$

It is important to note that the plastic hinge length obtained by this method does not represent the actual extent of plasticity in the member; but instead is only a mathematical convenience to relate global top-of-column displacements to local section response at the adjoining member interface. However, this limitation is sufficient for design since only the extreme value strains and displacements are required.

Traditionally, this single plastic hinge length equation has been used to predict global column response as a result of any strain limit state in the plastic hinge region. However, a recent study demonstrates that the plastic hinge length is sensitive to whether the global column response is estimated from a tension or compression limit state (Goodnight et al., 2015). Goodnight defines a modified plastic hinge method in which separate plastic hinge lengths are defined for strain-displacement predictions based on either tension or compression strain limits. The original study is based only on unidirectional column tests, but was later updated to include the influence of bidirectional load histories (Goodnight et al., 2017). The resulting plastic hinge length equations are shown in Equation 5-8 and Equation 5-9 for compression and tension respectively. The compression plastic hinge length remains identical to that recommended by (Priestley et al., 2007), but the tension plastic hinge length increases to include the effect of tension shift.

$$L_{pc} = kL_c + L_{sp} \geq 2L_{sp} \qquad \textit{Equation 5-8}$$

$$L_{pt} = L_{pc} + \gamma D \ \textit{where} \ \gamma = \begin{cases} 0.33 & \textit{bidirectional} \\ 0.4 & \textit{unidirectional} \end{cases} \qquad \textit{Equation 5-9}$$

While the (Priestley et al., 2007) method is widely accepted for the design and response prediction of RC bridge columns, it assumes behavior based on columns connected to members with a much larger relative stiffness, such as a footing or cap-beam, which offer greater confinement and bond development to the longitudinal bars than a more flexible adjoining member. As a result, a column with a plastic hinge forming away from the footing, such as that of the repair discussed in this report, will have a longer plastic hinge length due to a greater amount of strain penetration. This is evident in the figures presented in Section 5.1 and must be accounted for in the displacement response of the repaired column.

5.2.2 Reinforced Concrete Bridge Columns with Relocated Plastic Hinges

A modification to the plastic hinge length derivation discussed above for newly designed members with plastic hinges located away from the footing is presented in a research report by Hose et al (1997) and later more completely in the dissertation of Hose (2001). As stated above, these columns can no longer rely on the confinement of the rigid supporting member and therefore demonstrate a larger spread of plasticity which must be accounted for in the equivalent plastic hinge length. In the study conducted by Hose, the plastic hinges of circular RC bridge columns are relocated by providing an additional internal longitudinal steel cage at the footing interface which terminates some distance above the footing in a staggered pattern. This results in a weakened cross section above the inner reinforcing cage, thus forcing the plastic hinge to occur in this location. Figure 5.9 below illustrates the general reinforcement layout described along with the parameters assumed to influence the plastic hinge length.

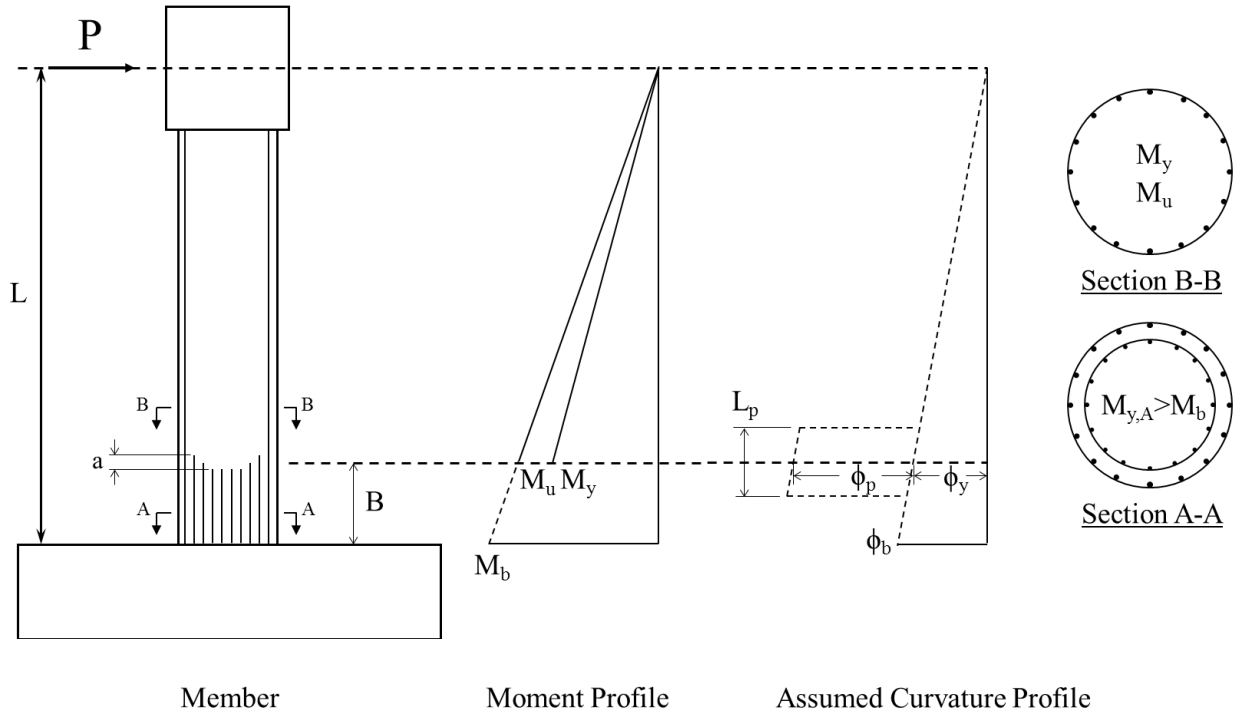

Figure 5.9: Assumptions for derivation of plastic hinge length equation by Hose et al (1997).

Hose's model assumes the center of plastic rotation develops a distance *'B'* away from the footing and defines *'a'* to be the length over which the reinforcement termination is staggered. The effective shear span of the column, L_{eff} is assumed to be the difference in overall column height, L, and the distance B between the footing and plastic hinge. The ultimate displacement is then

calculated using Equation 5-10 and the plastic rotation is defined by Equation 5-11. Substituting θ_p into Equation 5-10 and solving for L_p results in Equation 5-12 in which the plastic hinge length could be calculated from test data.

$$\Delta_u = \Delta_y + \theta_p L_{eff} \qquad \textit{Equation 5-10}$$

$$\theta_p = \left(\phi_u - \phi_y\right) L_p \qquad \textit{Equation 5-11}$$

$$L_{p,ex} = \frac{\Delta_u - \Delta_y}{\left(\phi_u - \phi_y\right) L_{eff}} \qquad \textit{Equation 5-12}$$

An empirical parametric study was then performed using the available test data to devise a correlation between the observed plastic hinge length and the parameters shown in Figure 5.9. The general form of the empirical equation is shown in Equation 5-13. The first and third terms of this equation are of the same form as the two terms presented in Equation 5-1 for the plastic hinge length in typical columns, while the second term represents the parameters specific to relocation of the plastic hinge. Therefore, γ is taken as 0.022 or 0.15 for MPa and ksi respectively so that the strain penetration term would equal that of the original equation. With all other values known, the parameters χ and ω were determined such that the error between the plastic hinge length calculated from Equation 5-12 and that found using Equation 5-13 is minimized.

$$L_p = 0.08 L_{eff} + \chi\left(a + B^{\omega}\right) + \gamma f_y d_{bl} \qquad \textit{Equation 5-13}$$

The resulting equation is shown in Equation 5-14

$$\begin{aligned} L_p &= 0.08 L_{eff} + 1.5\left(a + B^{0.1}\right) + 0.15 f_y d_{bl} \quad (ksi) \\ L_p &= 0.08 L_{eff} + 1.5\left(a + B^{0.1}\right) + 0.022 f_y d_{bl} \quad (MPa) \end{aligned} \qquad \textit{Equation 5-14}$$

The equation is then further simplified on the basis that the $B^{0.1}$ term is relatively insignificant to the overall result. The final form of the modified plastic hinge length proposed by Hose is presented in Equation 5-15 below.

$$L_p = 0.08L_{eff} + 1.85a + 0.15 f_y d_{bl} \quad (ksi)$$
$$L_p = 0.08L_{eff} + 1.85a + 0.022 f_y d_{bl} \quad (MPa)$$

Equation 5-15

While this equation provides a good fit to the data presented in the research study in which it was derived, it should be noted that the only source of increased plasticity in Equation 5-15 results from the length over which the termination of the internal reinforcing cage is staggered. When applied to the configuration of the repair presented in this report, this indicates that no additional plasticity should be expected as *'a'* is equal to zero; however, this is shown not to be the case. Equation 5-14 also results in only a minimal increase of plasticity which does not account for that observed in the tests either. From these results, it is clear that none of the available plastic hinge length equations are suitable to predict the behavior of a column repaired using the technique presented in this report. Therefore, a new method must be developed, which is discussed in the following section.

5.2.3 Calculation of Repaired Column Response

A key requirement of the modified plastic hinge length derivation described above is the continuous flexural development of the plastic hinge forming member. In other words, when the plastic moment develops at the relocated position in the member, dimension *B* in Figure 5.9, the extrapolated base moment, M_b, is resisted entirely by the strengthened cross section, Section A-A, at the member-footing interface. The inner cage bars develop within the column cross section over the length *B* and the base cross section is designed using conventional sectional analysis assuming a linear variation in strain across the member. From the discussion of experimental results of Repair #1 in Section 4.1.2, this assumption is not valid with the repair presented in this report, as the strains in the interior column bars far exceed those of the outer repair bars. Therefore, the forces in the repaired system do not transfer through flexure between the column and repair as originally assumed.

The basis of the proposed model recognizes and addresses this through a unique application of the existing plastic hinge method summarized in Section 5.2.1. First, to illustrate the conceptual framework in which this method is derived, consider the series of structural systems depicted in Figure 5.10. System (a) is a simply supported column with a single point load applied at the center of the span. The deformation, moment, and elastic curvature profiles are shown, along with a

plastic curvature profile that develops if the moment exceeds the yield capacity of the member. Recognizing this as a symmetrical system allows for reduction of the model to that shown in system (b), where the midspan is free to translate, but rotation is restrained to zero. The force and deformation profiles of system (b) are identical to that of the cantilever column shown in system (c). Finally, system (d) moves the fixed reaction of system (c) down a distance L_r from the midspan; but provides a flexible reaction at the previous support location with stiffness such that the rotation at this point, θ_{repair}, is equal to that which results at a point L_r from the midspan of system (a). A rigid link supported by a rotational spring provides the flexible reaction to the member and represents the repair applied to the base of the column. The force transferred at this reaction, V_r, and resulting moment in the rotational spring, $M_{b,r}$, represent the design shear force and base moment of the repair respectively. Furthermore, the total rotation at the top of the repair, θ_{repair}, represents the sum of contributions from rotation of the column inside the repair, strain penetration of the column into the footing, and rigid body rotation of the repair, thus accounting for each of the unknown components of deformation discussed in Section 5.1. Note also that the sum of the repair moment, $M_{b,r}$, and the base column moment, $M_{b,c}$, equal the total extrapolated column moment. Calculation of these quantities using the proposed model is discussed in the following sections.

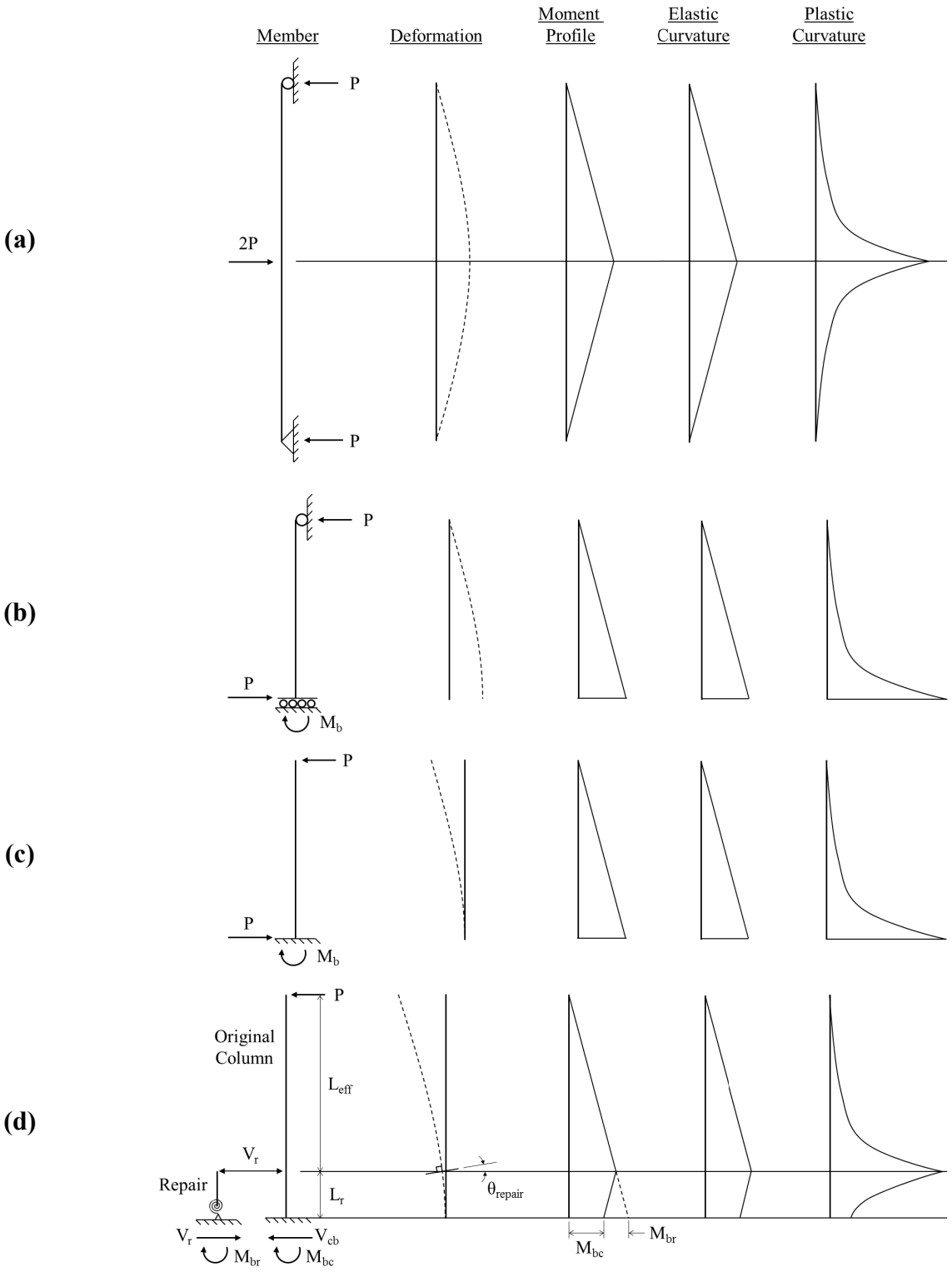

Figure 5.10: Derivation of mirrored plasticity model through symmetry of simply supported beam system.

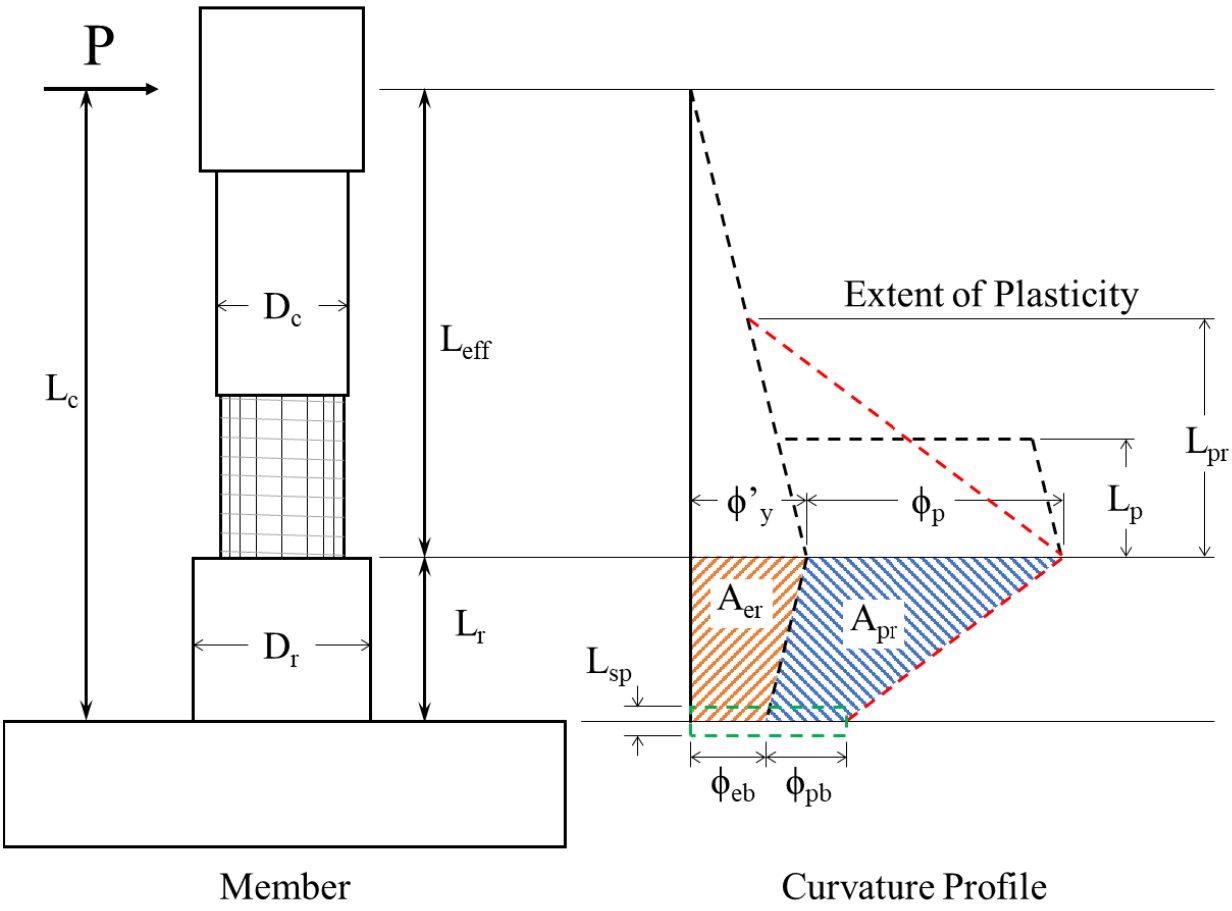

Figure 5.11: Idealization of repaired column curvature distribution with mirrored plasticity.

The displacement response of the column is found through application of the moment-area method to the idealized curvature distribution illustrated in Figure 5.11. To describe this approach, it is convenient to break the member into discrete sections of deformation: 1) flexure above the repair, 2) rotation within the repair, and 3) rotation due to column strain penetration into the footing. An additional contribution to the overall displacement response arises from rigid rotation of the repair, which is determined separately from the column response. Derivation of the displacement response from each component is outlined in the following sections.

5.2.3.1 Displacement due to column flexure above the repair

This component of deformation accounts for flexure above the column-repair interface and is calculated using the (Priestley et al., 2007) method with plastic hinge length modifications developed by Goodnight et al (2017). For the purposes of calculating this response, the rectangular plastic hinge length is sufficient and therefore used for the sake of simplicity. Equation 5-16

through Equation 5-18 outline the calculations necessary to determine the equivalent plastic hinge lengths. Note that the strain penetration length component, L_{sp}, has been removed as it is accounted for directly later on. It is recommended to use the tension plastic hinge length, L_{pt}, since the primary failure limit state of each repair was bar buckling which is shown to be most closely related to maximum tension strains during previous cycles (Goodnight et al., 2013); however, both hinge length equations are provided.

$$L_{pc} = kL_c \qquad \textit{Equation 5-16}$$

$$k = 0.2\left(\frac{f_u}{f_y} - 1\right) \leq 0.08 \qquad \textit{Equation 5-17}$$

$$L_{pt} = L_{pc} + \gamma D \qquad \textit{Equation 5-18}$$

Where,

$$\gamma = \begin{cases} 0.33 & \textit{bidirectional} \\ 0.4 & \textit{unidirectional} \end{cases}$$

Next, the yield and ultimate curvatures are found from a moment-curvature analysis of the original column cross section. When conducting this analysis, the elastic modulus of the steel should be reduced by a factor of 0.5 to account for softening of the material during the previous inelastic loading, as recommended by Vosooghi and Saiidi (2013). This factor can be adjusted considering the damage level at the new hinge location; however, the value of 0.5 produced good results when compared to the experimental tests, as shown later in the report. The curvature at first yield, $\phi_y^{'}$, and corresponding yield moment, M_y, are those at which the tension strain in the extreme fiber reinforcing bar reaches yield, noting that this value will be double that of its typical quantity due to the reduced modulus. The ultimate curvature, ϕ_u, and ultimate moment, M_u, are those at which the desired limit state strain is reached. The moment area method is then applied to obtain the resulting member displacements, as described in Equation 5-19 and Equation 5-20, where L_p corresponds to either the tension or compression hinge length depending on which strain limit was

used to calculate ϕ_u. Note that these equations traditionally use an equivalent yield curvature; however, the first yield curvature has been used here. This is intended to account for the increased first yield curvature obtained from the softened steel material. Also, the yield point of the repaired system is somewhat arbitrary given that the member has already yielded prior to this analysis and that displacement ductilities are based on initial member properties.

$$\Delta_{y,c} = \frac{\phi'_y L_{eff}^2}{3} \qquad \textit{Equation 5-19}$$

$$\Delta_{u,c} = \Delta_{y,c} + \left(\phi_u - \phi'_y\right) L_p \left(L_{eff} - 0.5L_p\right) \qquad \textit{Equation 5-20}$$

Calculation of the above quantities, $\Delta_{e,c}$ and $\Delta_{p,c}$, provides the elastic and plastic flexural components of deformation respectively and independently from each other. The column shear force is then obtained from statics, as shown in Equation 5-21.

$$F_u = \frac{M_u}{L_{eff}} \qquad \textit{Equation 5-21}$$

5.2.3.2 Displacement due to column rotation within the repair

This component of deformation accounts for the net rotation of the column over the distance between the top of footing and the top of the repair resulting from the downward spread of plasticity from the relocated hinge. As explained in Section 5.2.2, this is different than the effect of strain penetration due to the fact that the repair provides a different boundary condition than that of a comparatively rigid footing or cap beam. In this case, the original column bears against the repair in a manner that is assumed to behave as a flexible reaction resulting in a distribution of curvature mirroring that of the column above. Although the deformation profiles are symmetric above and below the repair, it is likely that the total spread of plasticity below the top of the repair is greater than the length of the repair. Thus, the resulting rotations derived through the areas of curvature should account for this truncation of plasticity.

As with the above flexural displacements, these deformations are separated into elastic and plastic components. The elastic and plastic rotations are represented in Figure 5.11 by the trapezoidal areas A_{er} and A_{pr} respectively and are calculated by Equation 5-22 and Equation 5-23

below. Note that L_{pr} is simply double the rectangular plastic hinge length calculated using Equation 5-16 or Equation 5-18.

$$A_{er} = \theta_{er} = \frac{\phi'_y}{2}\left(1 + \frac{L_{eff} - L_r}{L_{eff}}\right)L_r \qquad \textit{Equation 5-22}$$

$$A_{pr} = \theta_{pr} = \frac{\left(\phi_u - \phi'_y\right)}{2}\left(1 + \frac{L_{pr} - L_r}{L_{pr}}\right)L_r \;\; if \;\; L_{pr} > L_r \qquad \textit{Equation 5-23}$$

Otherwise,

$$A_{pr} = \theta_{pr} = \left(\phi_u - \phi'_y\right)L_{pr}$$

The net rotations are then applied over their effective moment arm to determine the top of column displacement. However, since the translational deformation of the column is restrained within the repair, this moment arm is not to the centroid of each area but instead to the location at which the column is free to translate (i.e. the top of the repair). Thus, the yield and ultimate displacements due to rotation of the column inside the repair are described by Equation 5-24 and Equation 5-25 respectively.

$$\Delta_{y,r} = \theta_{er} L_{eff} \qquad \textit{Equation 5-24}$$

$$\Delta_{u,r} = \Delta_{y,r} + \theta_{pr} L_{eff} \qquad \textit{Equation 5-25}$$

5.2.3.3 Displacement due to column strain penetration

Recall that the contribution of strain penetration was removed from the plastic hinge equations derived for the displacement due to column flexure above the repair. This was done to account for the fact that while the strain penetration length, L_{sp}, at the column-footing interface is the same as that calculated using Equation 5-3 (reprinted as Equation 5-26 below for convenience), the curvature on which it acts is different from that applied to L_p. Instead, the strain penetration length applies to curvatures ϕ_{yb} and ϕ_{ub} at the base of the column to obtain the elastic and plastic components of rotation due to strain penetration into the footing. As with the column rotation

inside the repair, the displacement from this rotation is propagated only from the top of the repair and not the location of the strain penetration itself. The calculations of ϕ_{yb} and ϕ_{ub} are carried out using Equation 5-27 and Equation 5-28 respectively, where L_{pr} is the triangular plastic hinge length described in the previous section.

$$L_{sp,c} = \begin{cases} 0.022\, f_{ye} d_{bl} & (MPa) \\ 0.15\, f_{ye} d_{bl} & (ksi) \end{cases} \qquad \textit{Equation 5-26}$$

$$\phi_{yb} = \phi'_{y} \left(\frac{L_{eff} - L_r}{L_{eff}} \right) \qquad \textit{Equation 5-27}$$

$$\phi_{ub} = \left(\phi_u - \phi'_{y} \right) \left(\frac{L_{pr} - L_r}{L_{pr}} \right) \; if \; L_{pr} > L_r \qquad \textit{Equation 5-28}$$

Otherwise,

$$\phi_{ub} = 0$$

$$\Delta_{y,sp} = \phi_{yb} L_{sp} L_{eff} \qquad \textit{Equation 5-29}$$

$$\Delta_{u,sp} = \Delta_{y,c} + \phi_{ub} L_{sp} L_{eff} \qquad \textit{Equation 5-30}$$

5.2.3.4 Displacement due to rigid repair rotation

The final component of deformation is that from the rigid rotation of the repair. Consider the idealization of the repair in Figure 5.10 (d) as a rigid member supported by a rotational spring element. To relate this to the physical system at hand, the rigid member represents the large relative stiffness of the repair to that of the column, and the rotational spring support represents the flexural stiffness of the repair cross section at the repair-footing interface. When the column deforms, it imparts a lateral force into the repair which then translates to a moment at its base, $M_{b,r}$, as illustrated in Figure 5.12. This moment can be directly calculated from the moment profile

illustrated in Figure 5.13 below, which derives from the assumed system behavior outlined in Figure 5.10.

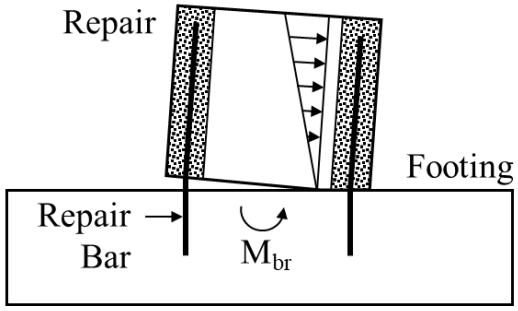

Figure 5.12: Illustration of repair rigid body rotation restrained by base moment $M_{b,r}$.

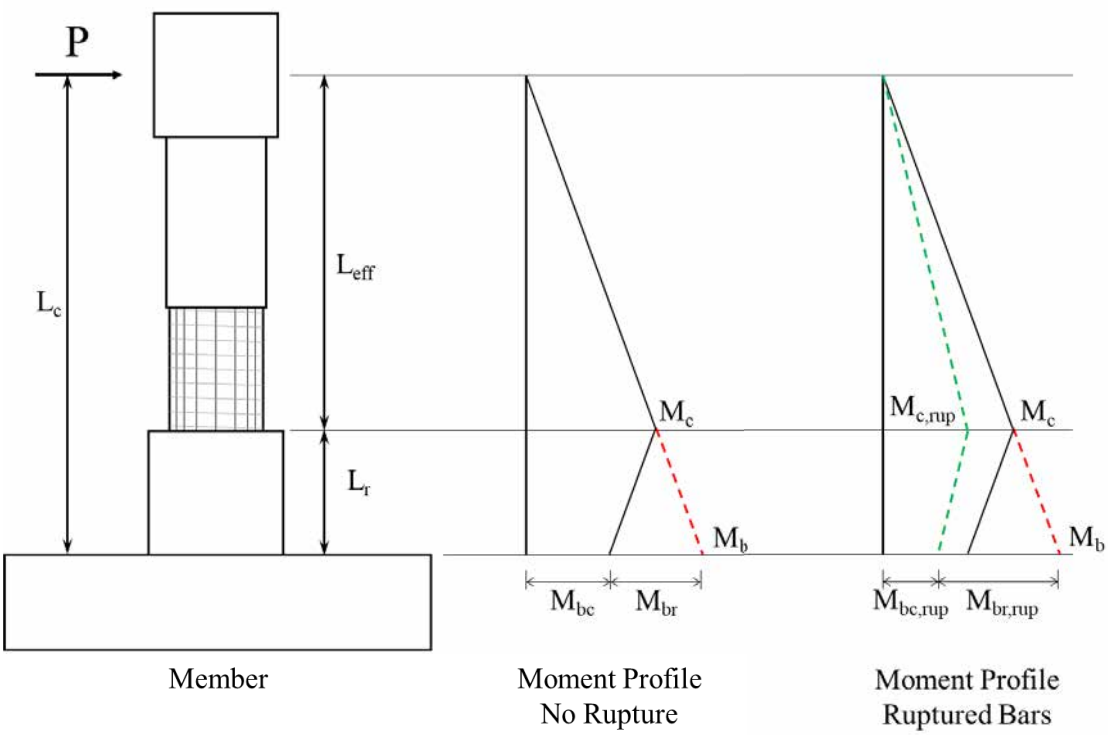

Figure 5.13: Repaired column assumed moment distribution

Note that the distribution of moments between the repair and column base varies depending on whether the column contains ruptured bars. When there are no ruptured bars, the moment in the column follows that of the solid black line in the left profile of Figure 5.13. The maximum column moment, M_c, develops at the top of the repair, and the total base moment, M_b, is extrapolated to the footing per the dashed red line and calculated using Equation 5-31. The proportion of M_b carried by the column and repair can then be described by Equation 5-32 and Equation 5-33 respectively.

$$M_b = M_c \left(\frac{L_c}{L_{eff}} \right)$$ *Equation 5-31*

$$M_{bc} = M_c \left(\frac{L_{eff} - L_r}{L_{eff}} \right)$$ *Equation 5-32*

$$M_{br} = M_b - M_{bc}$$ *Equation 5-33*

In the case where some of the longitudinal bars are ruptured, the column moment capacity at the footing reduces to some value $M_{bc,rup}$. However, assuming these bars develop over the length of the repair, they will still contribute to the flexural strength of the column, M_c, at the top of the repair, thus the total base moment, M_b, remains the same. The difference between M_{bc} and $M_{bc,rup}$ must therefore be carried by the repair as shown in the right profile of Figure 5.13.

The process to determine $M_{bc,rup}$ requires another moment-curvature analyses of the column cross section which omits the ruptured bars. The value for $M_{c,rup}$ then corresponds to the moment developed in the second analysis at the same curvature that results in M_c in the original analysis conducted earlier in this section. Note that the moment-curvature analysis to obtain $M_{c,rup}$ should consider the most severe orientation, with the ruptured bars located in the extreme tension location. The tool selected for analysis should also be capable of modeling individual bar locations and should not consider the longitudinal reinforcement as a smeared average, as this would not capture the full reduction in strength from the fractured bars and result in under prediction of repair forces. Once $M_{c,rup}$ has been found, the extrapolated base moment, M_b, remains the same as that found from Equation 5-31; however, the proportions of this moment carried by the column and repair, $M_{bc,rup}$ and $M_{rc,rup}$, are calculated from Equation 5-34 and Equation 5-35 respectively.

$$M_{bc,rup} = M_{c,rup} \left(\frac{L_{eff} - L_r}{L_{eff}} \right)$$ *Equation 5-34*

$$M_{br,rup} = M_b - M_{bc,rup}$$ *Equation 5-35*

Now, with knowledge of the base moment resisted by the repair, all that remains is relating this moment to the rigid body rotation of the repair and resulting column displacement. Since it is

designed to remain elastic, the flexural stiffness of the repair can be estimated from effective section properties. According to Priestley et al (1996) the effective stiffness depends on the axial load ratio and longitudinal reinforcement ratio and can range from 35 to 60% of the gross section stiffness. Since there is no axial load present in the repair and the longitudinal reinforcement ratio is expected to be low, it is reasonable to estimate the effective flexural stiffness using a lower bound of 35% of the gross section stiffness. The gross moment of inertia is calculated from the annular section geometry of the repair, which is given by Equation 5-36 for a circular column. The modulus of elasticity of the repair backfill material can also be estimated using ACI code equations for grout (ACI 530/530.1, 2013) and concrete (ACI 318, 2014) shown in Equation 5-37 and Equation 5-38 respectively. The corresponding curvature is then calculated from Equation 5-39.

These estimates are meant to be rough calculations for the purpose of design; however, EI_{eff} can be taken directly from a moment-curvature analysis of the repair cross section if more detailed results are desired. In the overall response, this rotation contributes only a small (although not insignificant) amount to the total displacement and the estimated properties produced reasonable results when compared to experimental values.

$$I_g = \frac{\pi\left(D_r^{\,4} - D_c^{\,4}\right)}{64} \qquad \textit{Equation 5-36}$$

$$E_{grout} = 500 f'_c \qquad \textit{Equation 5-37}$$

$$E_{conc} = \begin{cases} 57,000\sqrt{f'_c} & (psi) \\ 4,700\sqrt{f'_c} & (MPa) \end{cases} \qquad \textit{Equation 5-38}$$

$$\phi_{br} = \frac{M_{br}}{0.35EI_g} \qquad \textit{Equation 5-39}$$

This curvature can then be integrated over some length to obtain the rigid rotation of the repair, which is assumed to rotate about a single crack located at the interface between the base of the repair and the top of the footing, as illustrated in Figure 5.12. The resulting rotation is a product of the section curvature calculated above and strain penetration of the longitudinal repair bars. While the strain penetration length from Equation 5-26 still applies, it is recognized that these bars

are developing both into the footing and into the repair. Thus, the strain penetration length of the repair should be doubled to account for this, as shown in Equation 5-40.

$$L_{sp,r} = \begin{cases} 0.044 f_{ye,r} d_{bl,r} & (MPa) \\ 0.30 f_{ye,r} d_{bl,r} & (ksi) \end{cases} \qquad \textit{Equation 5-40}$$

Finally, the top of column displacement due to rigid body rotation of the repair can be obtained from Equation 5-41. Note that, unlike the column deformations, the repair remains elastic and therefore the displacement equation is the same regardless of whether the relocated hinge has formed.

$$\Delta_{rr} = \phi_{br} L_{sp,r} L_c \qquad \textit{Equation 5-41}$$

5.2.3.5 Total column displacement

Once each component of deformation has been accounted for, the total column displacement is simply the sum of each part, as shown in Equation 5-42 and Equation 5-43 for yield displacement and ultimate displacement respectively. Note that Δ_{rr} should be calculated independently in each equation for the yield and ultimate moments.

$$\Delta'_y = \Delta_{y,c} + \Delta_{y,r} + \Delta_{y,sp} + \Delta_{rr} \qquad \textit{Equation 5-42}$$

$$\Delta_u = \Delta_{u,c} + \Delta_{u,r} + \Delta_{u,sp} + \Delta_{rr} \qquad \textit{Equation 5-43}$$

5.3 Test Comparisons

The following sections illustrate the application of the mirrored plasticity model as applied to the experimental tests conducted in this report. First, the responses of Repair #1 and Repair #3 are analyzed, which contained no fractured bars, followed by analysis of Repairs #2, #4 and #6 which each contained at least one fractured bar. Repair #5 is again omitted from comparison, since the failure of the weld in the steel sleeve results in deformations not representative of the assumptions in this model.

5.3.1 No Ruptured Bars

The first step in obtaining the repaired column response is to perform a moment-curvature analysis of the column cross section at the relocated plastic hinge location. Repairs #1 and #3 both have identical longitudinal and transverse steel detailing and similar concrete strengths; however, Repair #3 considers a reduced cross section strength above the repair. Figure 5.14 illustrates the discretization of the column-cross sections used and Table 5.1 summarizes the properties of each analysis. The moment-curvature analysis was conducted in OpenSEES (McKenna, Fenves, & Scott, 2000) using a simple bi-linear model to describe the stress-strain behavior of the steel, and the concrete01 material model with zero tension capacity to define the concrete behavior. Only the concrete core was modeled, considering the effects of confinement by the steel spiral.

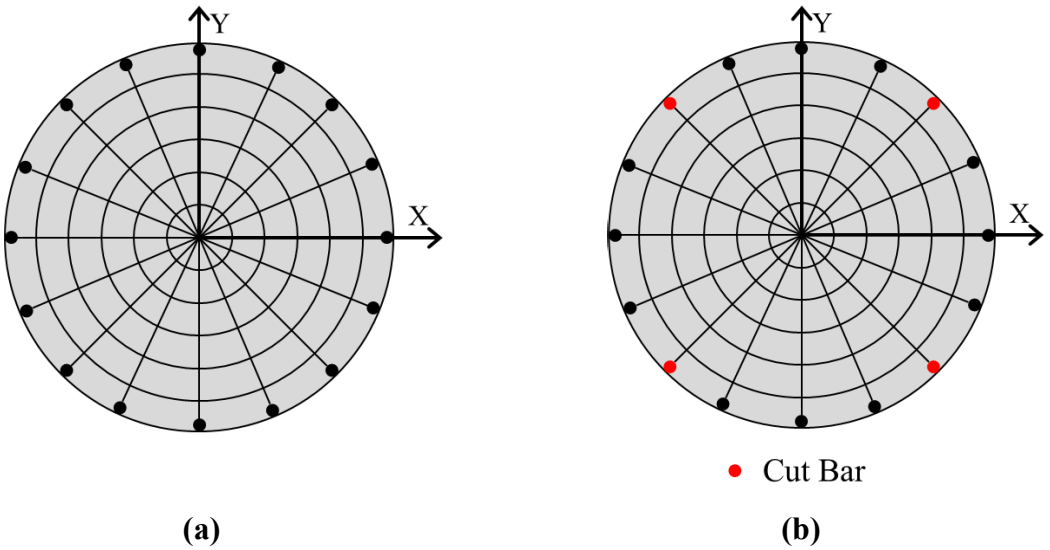

Figure 5.14: Discretization of column cross section for moment-curvature analysis (a) Repair #1; (b) Repair #3.

Table 5.1: Repair #1 and #3 column properties used for moment-curvature analysis.

	Repair #1	Repair #3
f'_c (ksi)	7.81	7.6
f_y (ksi)	71.2	71.2
f_u (ksi)	97.9	97.9
ε_y (in/in)	0.0051	0.0051
d_{bl} (in)	0.875	0.875
A_{sl} (in^2)	0.6	0.6
f_{yv} (ksi)	67.6	67.6
ρ_v (%)	1.0	1.0
Number of Long Bars	16	12
Axial Load (kips)	191	191
D_{col} (in)	24	24
Cover (in)	0.5	0.5

The strains considered for first yield and ultimate limit states are presented in Table 5.2. Note that the yield strain corresponds to double that of the tested yield strain due to the softening of the material during prior loading. The ultimate limit state strain is determined from Equation 5-44 below, which was developed by (Goodnight et al., 2015) and represents the maximum longitudinal steel tension strain before bar buckling is expected on the subsequent cycle. Since bar buckling was observed as the primary failure mode in each of repaired specimens, prior to eventual rupture, this is taken as a reasonable limit of column strain capacity.

$$\varepsilon_{bb} = 0.03 + 700\rho_s \frac{f_{yve}}{E_s} - 0.1\frac{P}{f'_{ce} A_g} \qquad \textit{Equation 5-44}$$

Table 5.2: Repair #1 and #3 strain limits for moment-curvature analysis.

	First Yield	Ultimate
Repair #1	$\varepsilon_s = 0.0051$	$\varepsilon_{bb} = 0.041$
Repair #3	$\varepsilon_s = 0.0051$	$\varepsilon_{bb} = 0.041$

Running the moment-curvature analysis considering each of the factors listed above results in the critical values listed in Table 5.3. Note that the column forces are taken as the force required to generate the respective moment over a distance L_{eff}, corresponding to the clear span of the column above the repair.

Table 5.3: Repair #1 and #3 limit state moments and curvatures.

	First Yield			Ultimate		
	ϕ'_y (1/in)	M_y (kip-in)	F_y (kips)	ϕ_u (1/in)	M_u (kip-in)	F_u (kips)
Repair #1	0.00034	5716	66.4	0.00243	8227	95.7
Repair #3	0.00034	4718	54.9	0.00239	6863	79.8

The information from Table 5.3, along with the known properties of the column, provide all that is required to predict the full response of the repaired system and design the repair itself, as outlined in the following sections.

5.3.1.1 Force vs. Displacement Response

A full displacement response curve for the repaired system can be developed using the above methodology. A summary of the calculation process to obtain the yield and ultimate components of displacement for Repair #1 is presented below.

Displacement due to column flexure above the repair:

Parameter	Description	Value	Corresponding Equation
L_{pt}	Plastic Hinge Length	16.05 in	Equation 5-18
$\Delta_{y,c}$	Displacement due to elastic column flexure above the repair	0.838 in	Equation 5-19
$\Delta_{u,c}$	Displacement due to plastic flexure of relocated hinge	2.62 in	Equation 5-20

Displacement due to column rotation within the repair:

Parameter	Description	Value	Corresponding Equation
θ_{er}	Elastic rotation due to column strains within the repair region	0.0065	Equation 5-22
θ_{pr}	Plastic rotation due to column strains within the repair region	0.030	Equation 5-23
$\Delta_{y,r}$	Displacement due to elastic rotation of column within the repair region	0.561 in	Equation 5-24
$\Delta_{u,r}$	Displacement due to plastic rotation of column within the repair region	2.58 in	Equation 5-25

Displacement due to column strain penetration into the footing:

Parameter	Description	Value	Corresponding Equation
L_{sp}	Column strain penetration length	9.35 in	Equation 5-26
ϕ_{yb}	Elastic component of curvature in column at footing interface	0.00025 1/in	Equation 5-27
ϕ_{ub}	Plastic component of curvature in column at footing interface	0.00066 1/in	Equation 5-28
$\Delta_{y,sp}$	Displacement due to elastic component of column strain penetration	0.203 in	Equation 5-29
$\Delta_{u,sp}$	Displacement due to plastic component of column strain penetration	0.482 in	Equation 5-30

Displacement due rigid rotation of the repair:

Parameter	Description	Value	Corresponding Equation
$M_{b,y}$	Total column base moment at yield	7,178 kip-in	Equation 5-31
$M_{bc,y}$	Component of base moment carried by column at yield	4,256 kip-in	Equation 5-32
$M_{br,y}$	Component of base moment carried by repair at yield	2,922 kip-in	Equation 5-33
$M_{b,u}$	Total column base moment at ultimate	10,331 kip-in	Equation 5-31
$M_{bc,u}$	Component of base moment carried by column at ultimate	6,122 kip-in	Equation 5-32
$M_{br,u}$	Component of base moment carried by repair at ultimate	4,209 kip-in	Equation 5-33
$I_{g,repair}$	Gross moment of inertia of annular repair section	35,186 in^4	Equation 5-36
E_{grout}	Modulus of elasticity of repair grout (f'_c = 8.2ksi)	4100 ksi	Equation 5-37
$\phi_{br,y}$	Curvature at base of repair at yield	5.79e-5 1/in	Equation 5-39
$\phi_{br,u}$	Curvature at base of repair at ultimate	8.33e-5 1/in	Equation 5-39
$L_{sp,r}$	Strain penetration length of repair bars into footing and repair	31.85 in	Equation 5-40

$\Delta_{rr,y}$	Displacement due to rigid repair rotation at yield	0.20 in	Equation 5-41
$\Delta_{rr,u}$	Displacement due to rigid repair rotation at ultimate	0.286 in	Equation 5-41

Total displacement response:

Parameter	Description	Value	Corresponding Equation
Δ'_y	Total member displacement at first yield	1.80 in	Equation 5-42
Δ_u	Total displacement capacity of member at ultimate limit state	7.57 in	Equation 5-43

Figure 5.15 below illustrates the accuracy of the Mirrored Plasticity Method (MPM) in predicting the overall system response of Repair #1. Note that only the positive response in each direction is shown for clarity, as the total response is symmetric about either axis. The red line represents the continuous curve developed over the entire moment-curvature data set while the dashed blue line indicates the bilinear approximation formed by connecting only the yield and ultimate data points. Each plot terminates at the predicted displacement for the onset of bar buckling which corresponds to $\Delta_u = 7.60$in for Repair #1. This falls directly between $\mu_{\Delta 5}$ and $\mu_{\Delta 6}$ of the experiment, and buckling was observed during $\mu_{\Delta 6} = 8.22$. Furthermore, the model also accurately captures the initial stiffness of the repaired system and the overall shape of the force-displacement response. Figure 5.16 shows the same plots for Repair #3 which demonstrate equally promising results in prediction of the overall response. The model did over predict the ultimate displacement in this repair; however, recall that the strains observed in the longitudinal bars during this experiment were higher than expected due to the reduction in steel area above the repair.

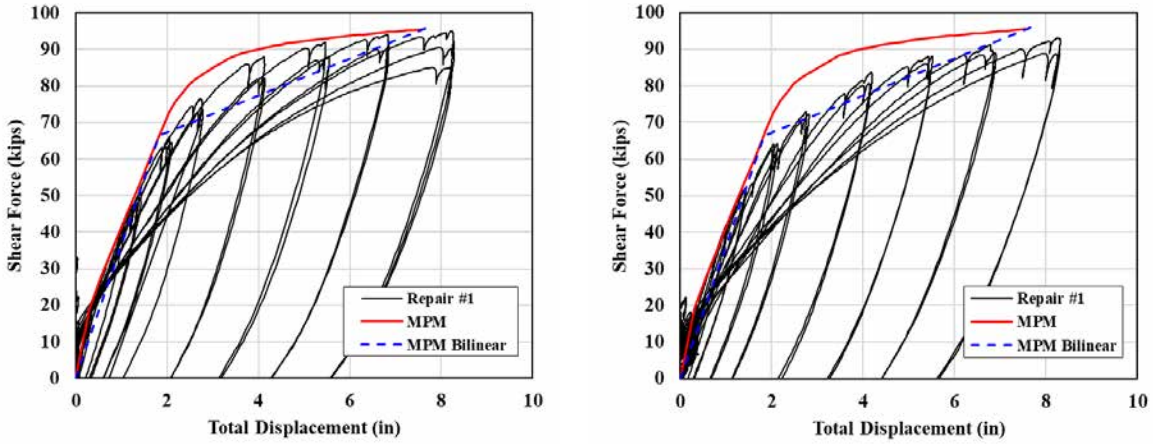

Figure 5.15: Repair #1 Force vs. Displacement response with comparison to MPM prediction in the (a) Y-direction; and (b) X-direction.

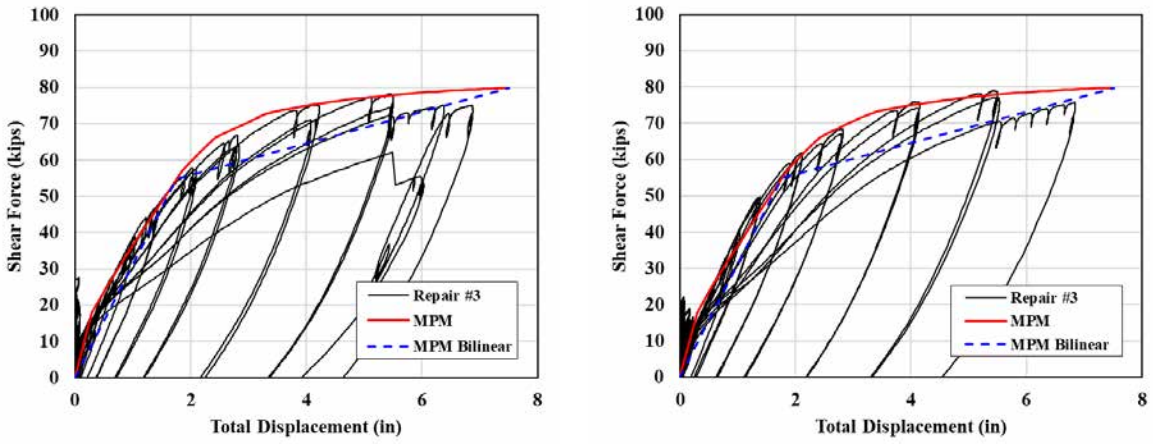

Figure 5.16: Repair #3 Force vs. Displacement response with comparison to MPM prediction in the (a) Y-direction; and (b) X-direction.

5.3.1.2 Local Plastic Hinge Strain Response

One of the many benefits of using this method, is that the global member response is obtained as a direct result of the local hinge strains and can therefore be compared directly to test data. Figure 5.17 and Figure 5.18 below show the strain vs. displacement response of the extreme fiber tension bars in the Y and X directions for Repair #1 and #3 respectively. Note that the predictions for Repair #1 match very closely with those observed in the test and that the mirrored plasticity method conservatively slightly over-predicts the strains at a given displacement which is desirable for design. Also note that the max tension strain prior to bar buckling, calculated from

Equation 5-44, matched very closely with that observed during the test, as shown in Figure 5.17 (a).

The strain predictions of Repair #3 did not coincide as closely with the observed experimental results; however, the strain distributions in the longitudinal bars of this test were much greater than expected. Figure 5.18 (a) demonstrates this variation where the strains in the 'SSW' bar exceed those of the 'S' bar, despite the 'S' bar being at the extreme fiber. Although the strain predictions of the model are not off by an excessive margin, it should be noted that they do not represent a conservative estimate when applied to the case where the relocated hinge section has been modified to reduce moment capacity, which is likely due to the non-uniform distribution of longitudinal steel around the cross section created by cutting several bars. However, the predicted max tension strain prior to bar buckling again proved to be accurate, as shown in Figure 5.18 (a). Nonetheless, the effect of removing steel from the plastic hinge cross section should be further investigated prior to implementation.

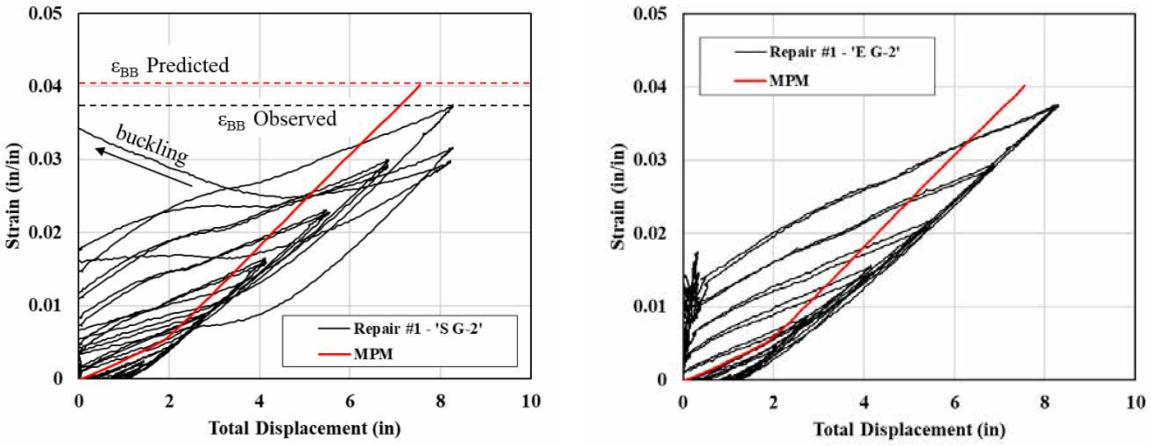

Figure 5.17: Repair #1 relocated hinge strain vs. displacement response with comparison to MPM prediction in the (a) Y-direction; and (b) X-direction.

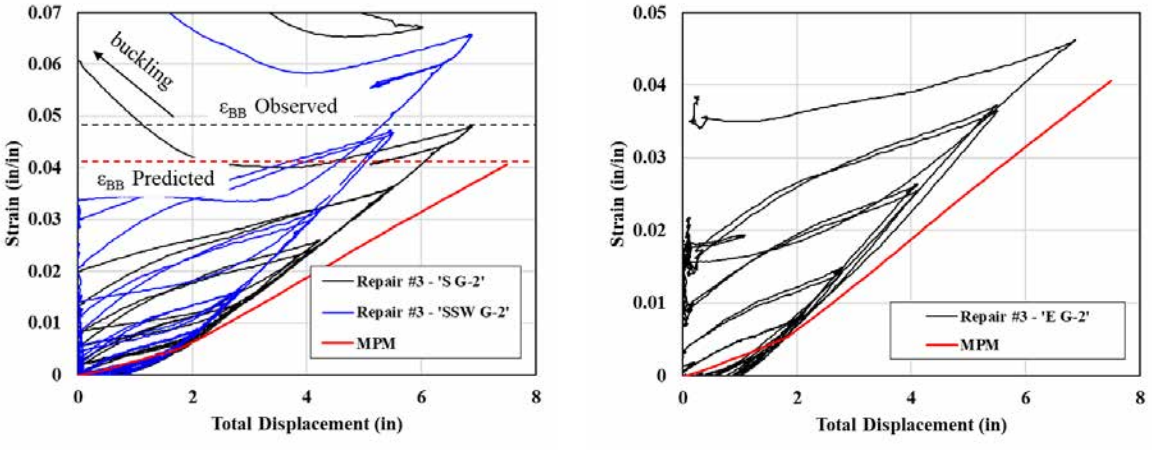

(a) **(b)**

Figure 5.18: Repair #3 relocated hinge strain vs. displacement response with comparison to MPM prediction in the (a) Y-direction; and (b) X-direction.

5.3.1.3 Local Repair Strain Response

Once the repair cross section has been designed, the strains in the longitudinal steel repair bars can be extracted from a moment-curvature analysis of the annular section. Recall that estimated values are used in the prediction of the displacement contribution from rigid rotation of the repair; however, the proportion of the total base moment transferred to the repair, M_{br}, is known from either Equation 5-33 or Equation 5-35. Therefore strains corresponding to this moment can be predicted for any point of response. The same analysis was performed on these sections as was done on the original column cross sections, also using OpenSEES (McKenna et al., 2000). Examples of the discretization of the cross sections used for each repair are shown in Figure 5.19.

The resulting strain predictions, as compared to the experimental results, are presented in Figure 5.20 and Figure 5.21 for Repair #1 and #3 respectively. Note that the observed strains in each slightly exceed that which was predicted by the model, but overall the fit is very close for each. Furthermore, the moment-curvature analysis used actual tested material properties, therefore these predicted strains fall well within the margin which would be considered through overstrength demand considerations employed in capacity protected design.

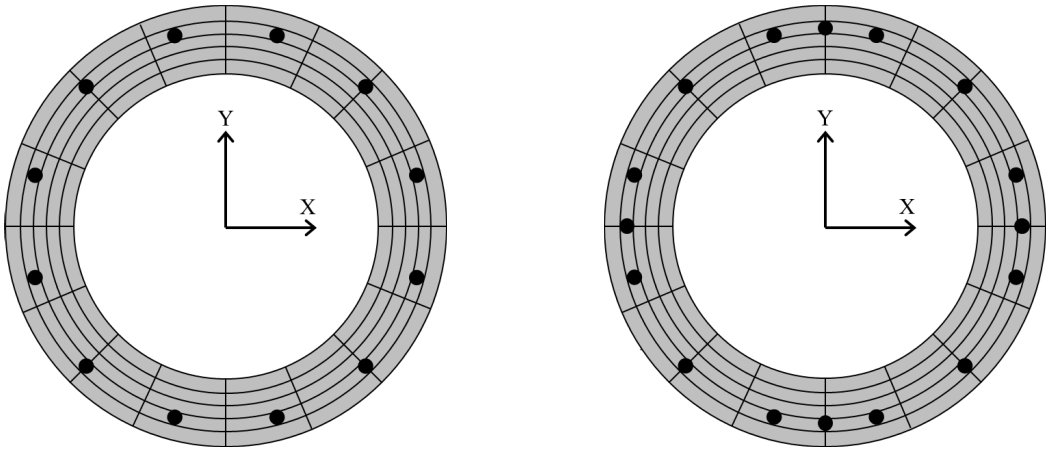

(a) **(b)**

Figure 5.19: Discretization of repair cross section for moment-curvature analysis (a) Repair #1; (b) Repair #3.

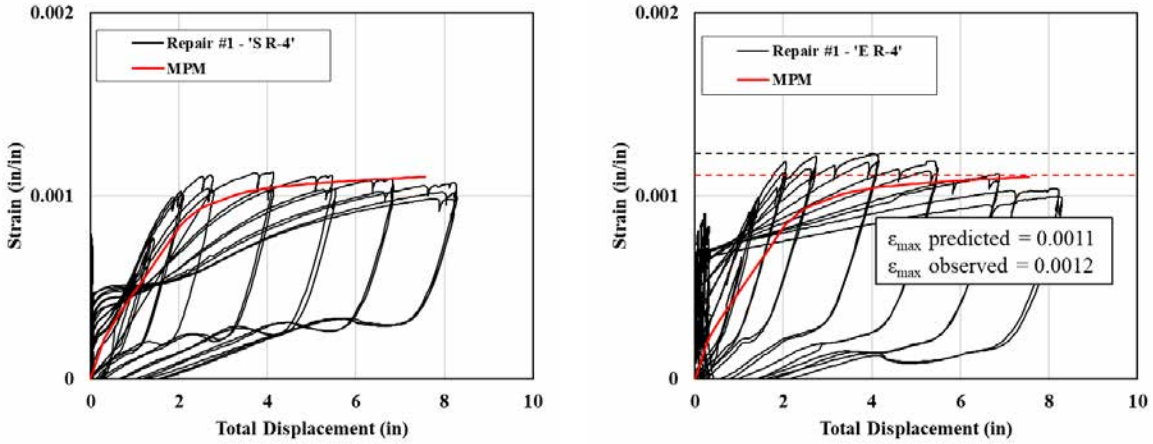

(a) **(b)**

Figure 5.20: Repair #1 repair bar strain vs. displacement response with comparison to MPM prediction in the (a) Y-direction; and (b) X-direction.

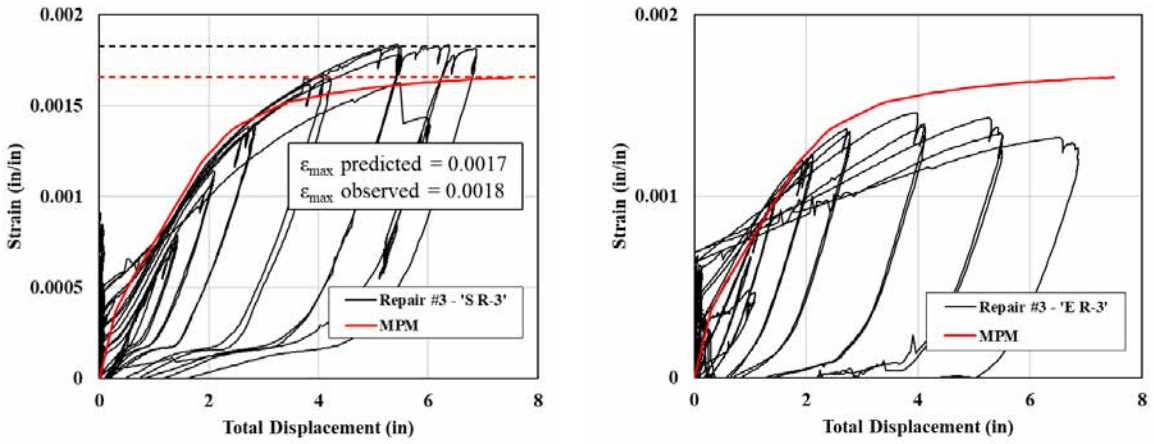

Figure 5.21: Repair #3 repair bar strain vs. displacement response with comparison to MPM prediction in the (a) Y-direction; and (b) X-direction.

From each section above, the mirrored plasticity model, when applied to a member without fractured bars, provides accurate predictions of the global system behavior, the local strain behavior at the critical relocated hinge section, and the local demands and deformations of the installed repair. The following section focuses on the same parameters, but for tests that contained ruptured reinforcing steel prior to repair.

5.3.2 Ruptured Bars

The process for obtaining the repaired column response for a column with ruptured bars is similar to that of a column without ruptured bars, but requires a second moment-curvature analysis of the ruptured base cross section. The first analysis consists of the full available cross section at the relocated plastic hinge location, considering the effect of the bars ruptured at the base. The second analysis considers only the non-fractured bars at the base cross section and omits any effect from the fractured bars. Figure 5.22 illustrates the discretization of each cross section used for analysis of the tested repairs, where (a) corresponds to the full cross section in each, (b) corresponds to the fractured bar configuration of Repairs #2 and #6, and (c) corresponds to the fractured bar configuration of Repair #4. Table 5.4 summarizes the properties used in each analysis.

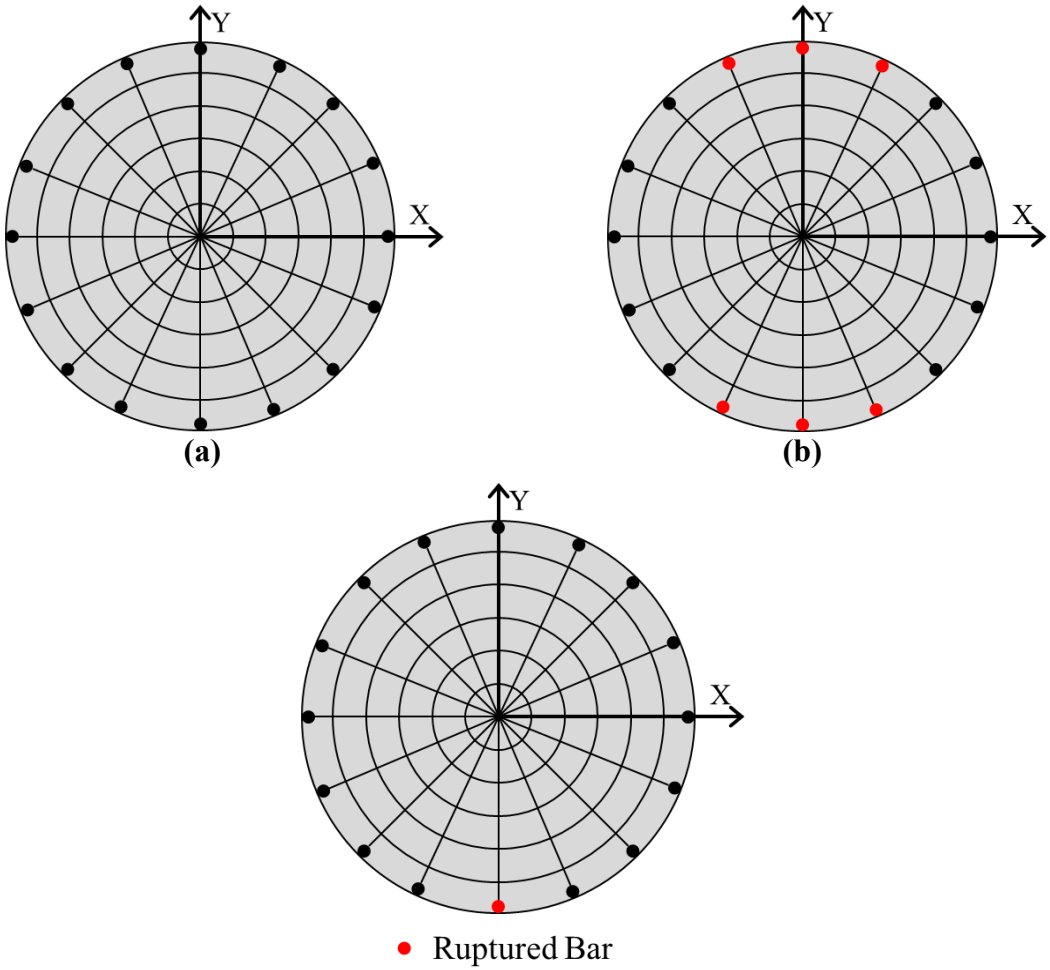

Figure 5.22: Discretization of column cross section used in moment-curvature analysis for (a) full cross section; (b) fractured base of Repair #2 and #6; and (c) fractured base of Repair #4.

Table 5.4: Repair #2, #4 and #6 column properties used for moment-curvature analysis.

	Repair #2	Repair #4	Repair #6
f'_c (ksi)	7.68	6.23	6.13
f_y (ksi)	71.2	70.3	69.6
f_u (ksi)	97.9	98.7	96.7
ε_y (in/in)	0.0051	0.0057	0.0054
d_{bl} (in)	0.875	0.75	0.875
A_{sl} (in^2)	0.6	0.44	0.6
f_{yv} (ksi)	67.6	63.9	69.6
ρ_v (%)	1.0	0.7	1.3
Number of Long Bars	16	16	16
Axial Load (kips)	191	191	191
D_{col} (in)	24	24	24
Cover (in)	0.5	0.5	0.5

Again, the yield strain and corresponding initial modulus of the longitudinal bars are modified to account for softening of the material. The ultimate limit state strains are determined through the same process as they were previously and are presented in Table 5.5, along with the resulting yield and ultimate moments and curvatures in Table 5.6 which correspond to those values obtained from the full section analysis. Note that two additional values for each repair are also calculated, $M_{y,rup}$ and $M_{u,rup}$, which correspond to the resulting moments in the ruptured cross section analysis at ϕ'_y and ϕ_u. These will be used to calculate the increased proportion of base moment from the column to the repair due to the reduced column moment capacity at the base.

Table 5.5: Repair #2, #4 and #6 strain limits for moment-curvature analysis.

	First Yield	Ultimate
Repair #2	$\varepsilon_s = 0.0051$	$\varepsilon_{bb} = 0.041$
Repair #4	$\varepsilon_s = 0.0057$	$\varepsilon_{bb} = 0.034$
Repair #6	$\varepsilon_s = 0.0054$	$\varepsilon_{bb} = 0.043$

Table 5.6: Repair #2, #4 and #6 limit state moments and curvatures.

	First Yield				Ultimate			
	ϕ'_y (1/in)	M_y (kip-in)	$M_{y,rup}$ (kip-in)	F_y (kips)	ϕ_u (1/in)	M_u (kip-in)	$M_{u,rup}$ (kip-in)	F_u (kips)
Repair #2	0.00034	5,722	3,749	66.5	0.00243	8,234	5,684	95.7
Repair #4	0.00038	4,567	4,706	53.1	0.00203	6,281	5,706	73.0
Repair #6	0.00038	5,458	3,597	63.5	0.00260	8,048	5,673	93.6

This information again provides all that is required for to predict the full response of the repaired system and obtain design demand values for the repair. The following sections outline this process, highlighting the key considerations for columns with fractured longitudinal bars.

5.3.2.1 Force vs. Displacement Response

A summary of the calculations for Repair #2 is presented below to illustrate the process for a member with ruptured longitudinal bars. Note that the general layout and geometry of Repair #2 was almost identical to that of Repair #1, therefore the process is similar to that presented previously for members without fractured bars. However, there are key differences which have been highlighted in grey.

Displacement due to column flexure above the repair:

Parameter	Description	Value	Corresponding Equation
L_{pt}	Plastic Hinge Length	16.05 in	Equation 5-18
$\Delta_{y.c}$	Displacement due to elastic column flexure above the repair	0.838 in	Equation 5-19
$\Delta_{u,c}$	Displacement due to plastic flexure of relocated hinge	2.62 in	Equation 5-20

Displacement due to column rotation within the repair

Parameter	Description	Value	Corresponding Equation
θ_{er}	Elastic rotation due to column strains within the repair region	0.0065	Equation 5-22
θ_{pr}	Plastic rotation due to column strains within the repair region	0.030	Equation 5-23

$\Delta_{y,r}$	Displacement due to elastic rotation of column within the repair region	0.561 in	Equation 5-24
$\Delta_{u,r}$	Displacement due to plastic rotation of column within the repair region	2.58 in	Equation 5-25

Displacement due to column strain penetration into the footing:

Parameter	Description	Value	Corresponding Equation
L_{sp}	Column strain penetration length	9.35 in	Equation 5-26
ϕ_{yb}	Elastic component of curvature in column at footing interface	0.00025 1/in	Equation 5-27
ϕ_{ub}	Plastic component of curvature in column at footing interface	0.00066 1/in	Equation 5-28
$\Delta_{y,sp}$	Displacement due to elastic component of column strain penetration	0.203 in	Equation 5-29
$\Delta_{u,sp}$	Displacement due to plastic component of column strain penetration	0.482 in	Equation 5-30

Displacement due rigid rotation of the repair:

Parameter	Description	Value	Corresponding Equation
$M_{b,y}$	Total column base moment at yield	7,178 kip-in	Equation 5-31
$M_{bc,y}$	Component of base moment carried by column at yield	2,790 kip-in	Equation 5-34
$M_{br,y}$	Component of base moment carried by repair at yield	4,388 kip-in	Equation 5-35
$M_{b,u}$	Total column base moment at ultimate	10,331 kip-in	Equation 5-31
$M_{bc,u}$	Component of base moment carried by column at ultimate	4,230 kip-in	Equation 5-34
$M_{br,u}$	Component of base moment carried by repair at ultimate	6,101 kip-in	Equation 5-35
$I_{g,repair}$	Gross moment of inertia of annular repair section	35,186 in^4	Equation 5-36
E_{grout}	Modulus of elasticity of repair grout (f'_c = 7.2ksi)	3600 ksi	Equation 5-37

$\phi_{br,y}$	Curvature at base of repair at yield	9.89e -5 1/in	Equation 5-39
$\phi_{br,u}$	Curvature at base of repair at ultimate	1.38e -4 1/in	Equation 5-39
$L_{sp,r}$	Strain penetration length of repair bars into footing and repair	31.85 in	Equation 5-40
$\Delta_{rr,y}$	Displacement due to rigid repair rotation at yield	0.340 in	Equation 5-41
$\Delta_{rr,p}$	Displacement due to rigid repair rotation at ultimate	0.473 in	Equation 5-41

Total displacement response

Parameter	Description	Value	Corresponding Equation
Δ'_y	Total member displacement at first yield	1.94 in	Equation 5-42
Δ_u	Total displacement capacity of member at ultimate limit state	7.76 in	Equation 5-43

The final calculated response of the repaired system matches closely with that of Repair #1 which had no ruptured bars. The main difference lies in the transfer of forces from the original column into the repair which did not occur in the specimen with no ruptured bars resulting in additional force carried by the annular section of the repair, as shown in the calculations of M_{bc} and M_{br} above. Secondly, the consideration the global force vs. displacement response is described by an envelope of two individual curves. The first, shown in red in Figure 5.23 through Figure 5.25, corresponds to the curve developed using the full cross section analysis (i.e. Figure 5.29 (a)). This curve assumes that all of the ruptured bars have remained bonded within the repair and contribute to the overall force response of the member. Thus, this curve is used to obtain the peak predicted force of the repaired system. The second, shown as a blue dashed line, corresponds to the curve developed using the reduced cross section (i.e. Figure 5.29 (b) or (c)), which assumes complete debonding and zero contribution from the ruptured bars. Note that the calculations presented from above represent those of the solid red line, and a second set would be carried out from the response of the debonded system with the minimum ultimate displacement capacity from each representing that of the system. The ultimate response is considered that where the extreme fiber reaches the ultimate limit strain, where on the debonded system this would correspond to the extreme *non-ruptured* fiber.

The system response is assumed to first follow the red line until the ruptured bars begin to debond from within the repair, at which point the response will reduce and approach that of the blue dashed line. The exact strain at which the bars debonded varied between tests and between individual bars within each test; however, the overall trend matched that of the envelope created by the two curves described above very well. The ruptured bars in Repair #2 began to debond at approximately $\varepsilon_s = 0.01$, at which point the force in the system dropped dramatically over the following cycles. This trend matches that shown in Figure 5.23 (a) where the force from the ruptured bars is initially realized, but tails off around $\Delta_y = 4$ in and begins to approach that of the debonded system through failure. The debonded system in the X-direction is calculated similar to that of the Y-direction, except the moment-curvature analysis is conducted with rotation about the orthogonal direction.

Repair #4 contained only a single fractured bar on the South face, therefore the bonded and debonded curves create a much narrower solution envelope. The same trend from Repair #2 is still present with the force initially matching that of the red curve until debonding of the ruptured bar occurs resulting in a drop of force approaching that of the blue dashed line.

Finally, Repair #6 demonstrated an increased strain at debonding of the ruptured bars which is illustrated in Figure 5.25 (a) with the response following that of the red curve longer before abruptly dropping to approach that of the reduced capacity system.

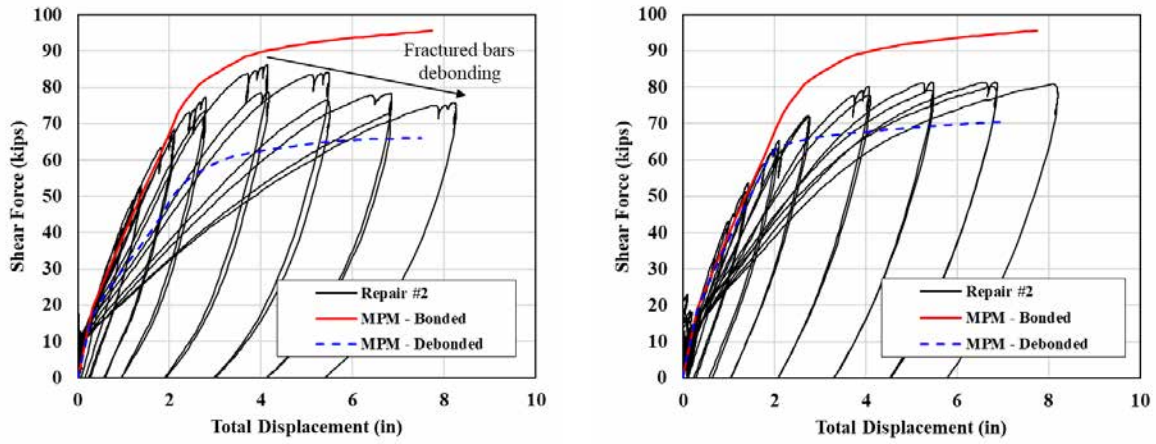

Figure 5.23: Repair #2 Force vs. Displacement response with comparison to MPM prediction in the (a) Y-direction; and (b) X-direction.

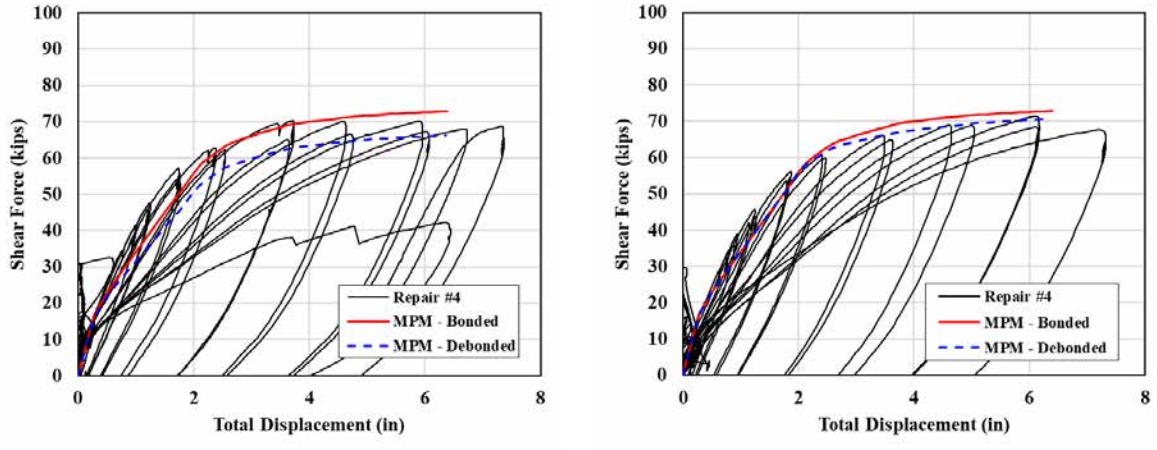

Figure 5.24: Repair #4 Force vs. Displacement response with comparison to MPM prediction in the (a) Y-direction; and (b) X-direction.

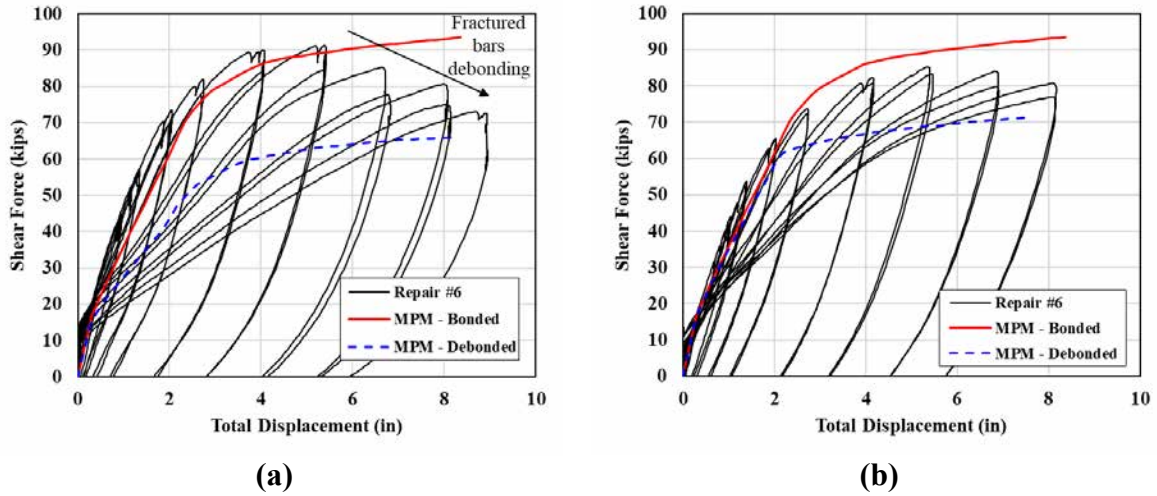

Figure 5.25: Repair #6 Force vs. Displacement response with comparison to MPM prediction in the (a) Y-direction; and (b) X-direction.

5.3.2.2 Local Plastic Hinge Strain Response

Figure 5.26 through Figure 5.28 below outline the strain predictions of the mirrored plasticity method as compared to those observed during each test. Recall that the extreme fiber bars on the South and North faces of Repair #2 were ruptured and debonded early on the test, as illustrated in Figure 5.26 (a). However, the opposite face extreme fiber bars were intact and the response of the East bar is shown in Figure 5.26 (b). Similar to the global response of the member, the response of these bars are predicted within an envelope between the bonded and unbonded response. For design, the conservative deformation response would again be taken as that considering debonded ruptured bars.

The same response is shown for Repairs #4 and #6 in Figure 5.27 and Figure 5.28 respectively. The North bar is shown for the Y-direction response of Repair #4 as this bar was not ruptured. Again, since only a single bar is ruptured in this test, the bonded and debonded predictions are very similar. Figure 5.29 (b) illustrates more clearly how the strains in the bars begin along the red line and then trend more towards the blue dashed line once the ruptured bars debond from the within the repair.

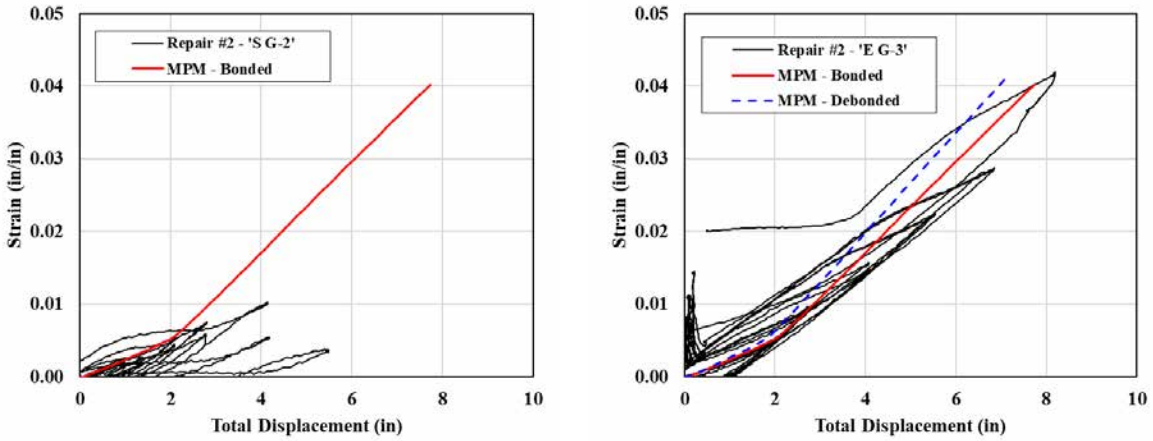

(a) **(b)**

Figure 5.26: Repair #2 relocated hinge strain vs. displacement response with comparison to MPM prediction in the (a) Y-direction; and (b) X-direction.

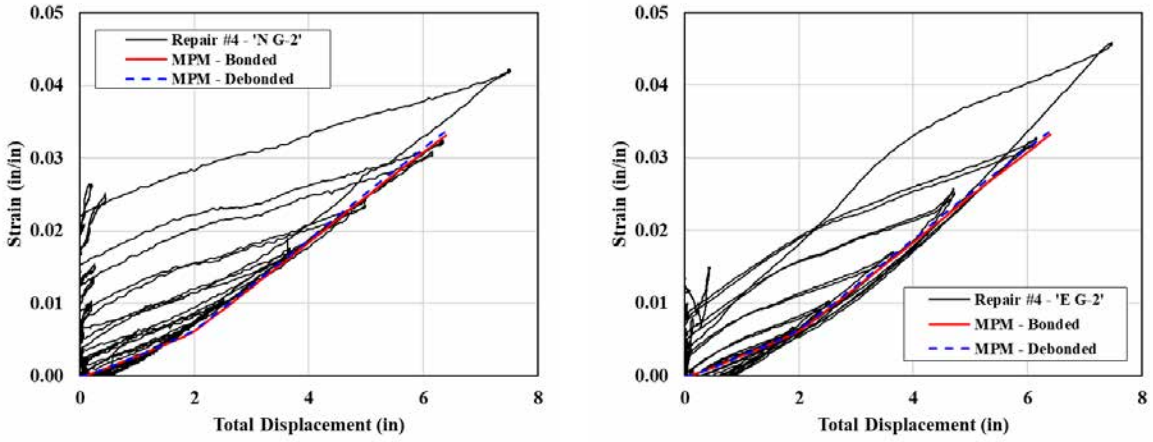

(a) **(b)**

Figure 5.27: Repair #4 relocated hinge strain vs. displacement response with comparison to MPM prediction in the (a) Y-direction; and (b) X-direction.

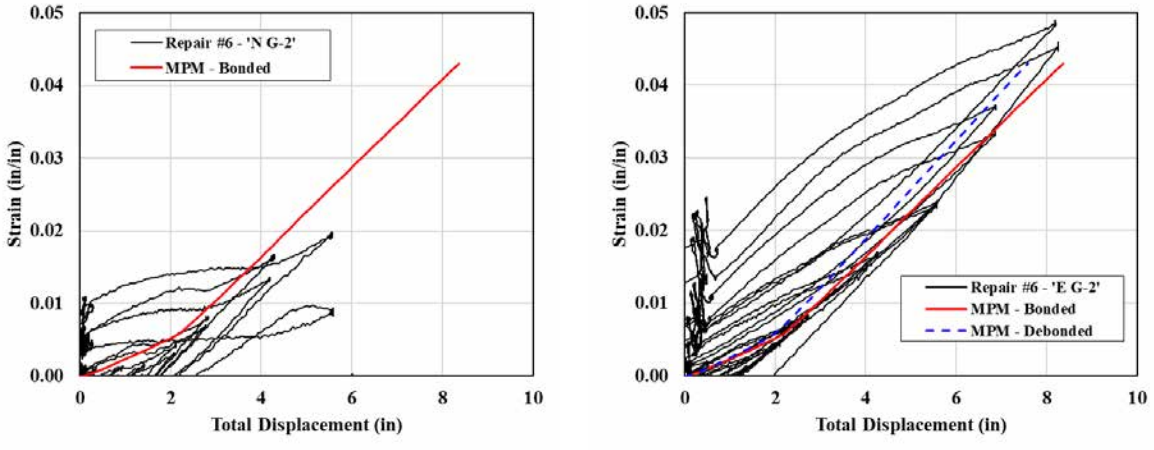

Figure 5.28: Repair #6 relocated hinge strain vs. displacement response with comparison to MPM prediction in the (a) Y-direction; and (b) X-direction.

5.3.2.3 Local Repair Strain Response

The strains of the longitudinal repair bars also agree well with this predicted values from the mirrored plasticity method. A moment curvature analysis of each repair provides strain information in the longitudinal bars corresponding the moment which results from the bonded and debonded systems. While the ruptured bars are bonded, their forces are transferred directly to the repair, resulting in increased demand. Once the ruptured bars debond, this force is no longer transferred and therefore the demand in the repair drops off to approach the demand from that of the debonded analysis, similar to that of the force vs. displacement response. Figure 5.29 illustrates the section discretization used for Repairs #2, #4 and #6 and Figure 5.30 through Figure 5.32 show the strain vs. displacement response predictions of each test compared to that which was observed.

Note that for each repair the strains tend to initially follow that of the bonded system and drop off to approach that of the debonded system as the ruptured bars lose bond. For design, the expected strains would be from that of the bonded system. The model tends to underestimate the initial strains in the Y-direction for Repair #6; however, recall that this repair employed the shear key mechanism in an attempt to transfer more of the column forces via flexure. Thus, it would appear that this technique succeeded in doing so, and therefore a more conservative design approach when using this is design would be that of a fully composite cross section.

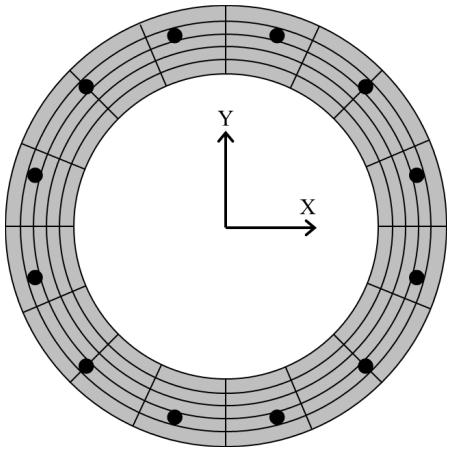

Figure 5.29: Discretization of repair cross section for moment-curvature analysis in Repairs # 2, 4 and 6.

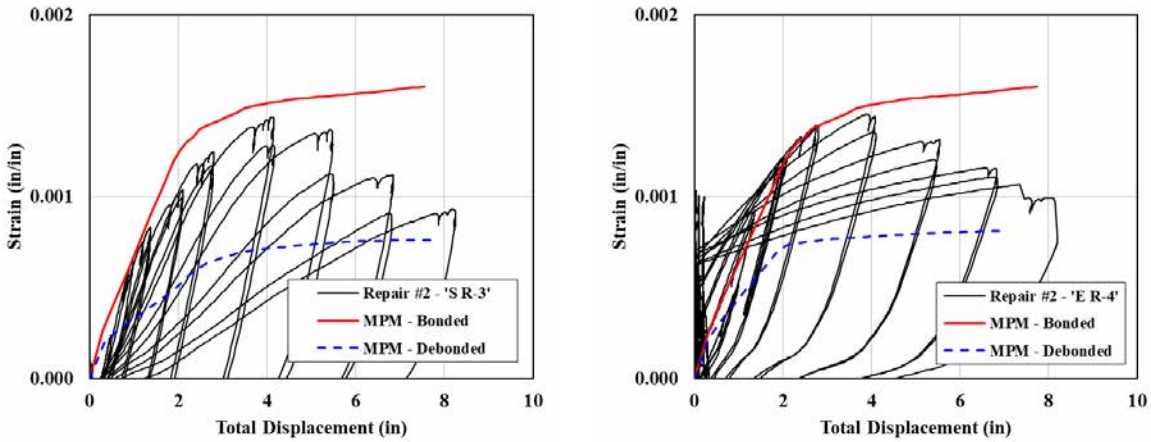

(a) **(b)**

Figure 5.30: Repair #2 repair bar strain vs. displacement response with comparison to MPM prediction in the (a) Y-direction; and (b) X-direction.

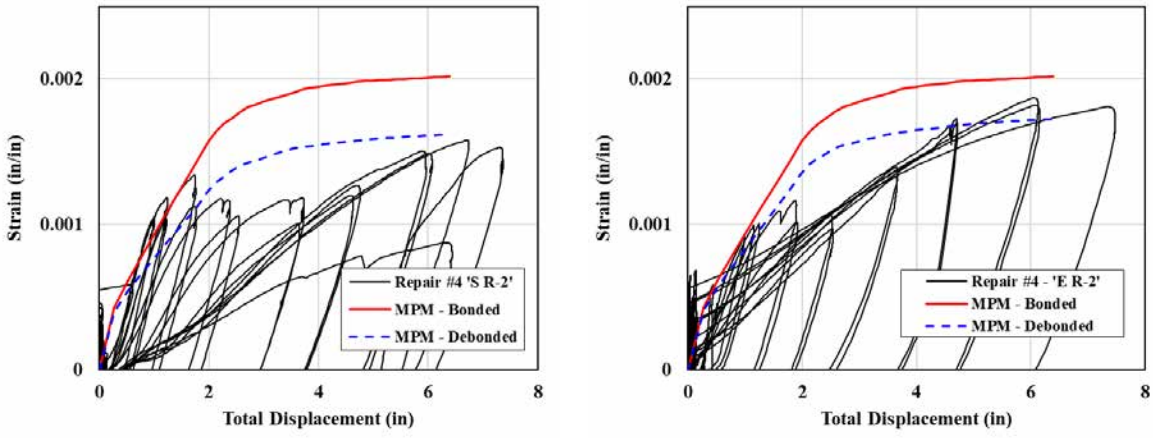

(a) **(b)**

Figure 5.31: Repair #4 repair bar strain vs. displacement response with comparison to MPM prediction in the (a) Y-direction; and (b) X-direction.

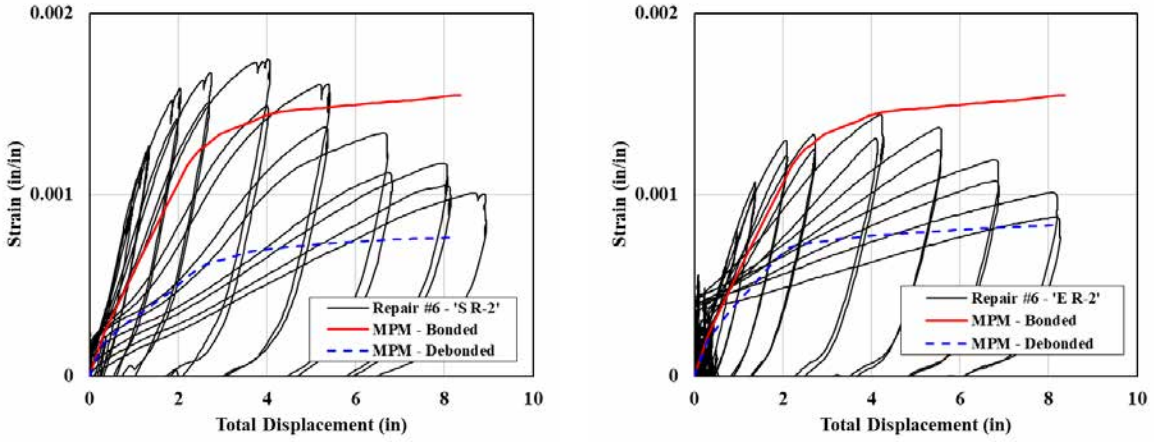

Figure 5.32: Repair #6 repair bar strain vs. displacement response with comparison to MPM prediction in the (a) Y-direction; and (b) X-direction.

5.3.3 Summary of results

From the results presented above, the mirrored plasticity method derived earlier in this section appears to provide accurate and reliable results for the response prediction of a member repaired using the plastic hinge relocation technique presented in this report. The method provides a sound basis for prediction of the global member response, local strain behavior at the relocated plastic hinge, and local force demands and strain behavior of the repair itself. Furthermore, the analytical design model relies only on engineering principles and techniques already widely used in performance based engineering of RC bridge columns, and can therefore can be easily implemented into design practice. The tables below summarize the results presented in the previous sections, outlining the performance of the model in predicting the global and local strain behavior of each test. Table 5.7 includes the max displacement capacity of each test as well as the displacement at which bar buckling was observed, which corresponds to the ultimate limit state used in the analytical model. For each test, the model was successful in conservatively predicting the ultimate displacement of the repaired column, except for Repair #3 which considered reduced longitudinal steel in the relocated hinge. If designing for this case, it is recommended to reduce the calculated displacement capacity by an amount equal to a full displacement ductility of the original column.

Table 5.7: Summary of global performance predictions compared to experimental results.

	Predicted		Observed		
	F_u (kips)	Δ_u (in)	F_u (kips)	Δ_{bb} (in)	Δ_u (in)
Repair #1	96	7.68	95.1	8.22	8.31
Repair #2	96	7.61	86.2	8.22	8.28
Repair #3	80	7.51	80.6	6.85	6.88
Repair #4	73	6.50	75.4	6.10	7.51
Repair #6	94	8.19	93.1	8.22	8.95

Table 5.8 below provides a summary of the predicted maximum tension strains in each repair compared to those observed in each test. These values demonstrate that the proposed analytical model can not only conservatively estimate design forces, but can accurately capture how these forces are distributed given the state of the original column and geometry of the selected repair. Thus it is concluded that this model is suitable for use in the design of the repair itself and for use in predicting the behavior of the repaired system as a whole.

Table 5.8: Summary of max tension repair strain predictions compared to experimental results.

	Predicted $\varepsilon_{t,repair}$ (in/in)	Observed $\varepsilon_{t,repair}$ (in/in)
Repair #1	0.0011	0.0012
Repair #2	0.0016	0.0016
Repair #3	0.0017	0.0018
Repair #4	0.0020	0.0019
Repair #6	0.0015	0.0017

5.4 Design Limit States

A major benefit of using the mirrored plasticity method derived in the previous section is that the deformation of the system is tied directly to the local strain behavior of the critical cross section at the relocated plastic hinge. Therefore, any previously established strain limit can be applied. The values presented in Table 5.9 outline those recommended for use in typical performance based design of reinforced concrete bridge columns. The serviceability limit states correspond to the compression strain at which concrete cover begins to crush and the peak tension

strain which results in residual crack widths of approximately 1 mm. These limits are generally accepted as nominal limit states for RC members. The compression limit state for damage control is defined by Equation 5-45, which refers to the compression strain in the confined concrete at which fracture of the transverse reinforcement confining the core occurs (Priestley et al., 2007). This equation is obtain via a strain-energy balance between that absorbed by the confined core concrete and the capacity of the confining steel. Although this strain limit is theoretically applicable, this failure mode was not observed during any of the experimental tests. Therefore, it is recommended to define the ultimate capacity on that of the tension strain limit presented previously in Equation 5-44. This equation demonstrated accurate predictions of the onset of bar buckling in the repaired specimens, and most systems displayed reserve displacement capacity beyond that of the onset of this limit state prior to bar fracture and eventual member failure.

$$\varepsilon_{c,dc} = 0.004 + 1.4\frac{\rho_v f_{yh}\varepsilon_{su}}{f'_{cc}} \qquad \textit{Equation 5-45}$$

Table 5.9: Recommended strain limit states for repaired member design.

	ε_c (in/in)	ε_t (in/in)
Servicability	0.004	0.015
Damage Control	Equation 5-45	Equation 5-44

5.5 Repair Design

The design of the repair can be carried out directly considering the base moment demand, M_{br}, obtained from the analytical model. When designing the repair for an actual structure, the moment-curvature analysis should consider overstrength material properties of the system to ensure the design strength of the repair annulus is sufficient to remain elastic. Recommendations for the typical values to be used for material properties in the initial moment-curvature analysis are presented in Figure 5.33 below.

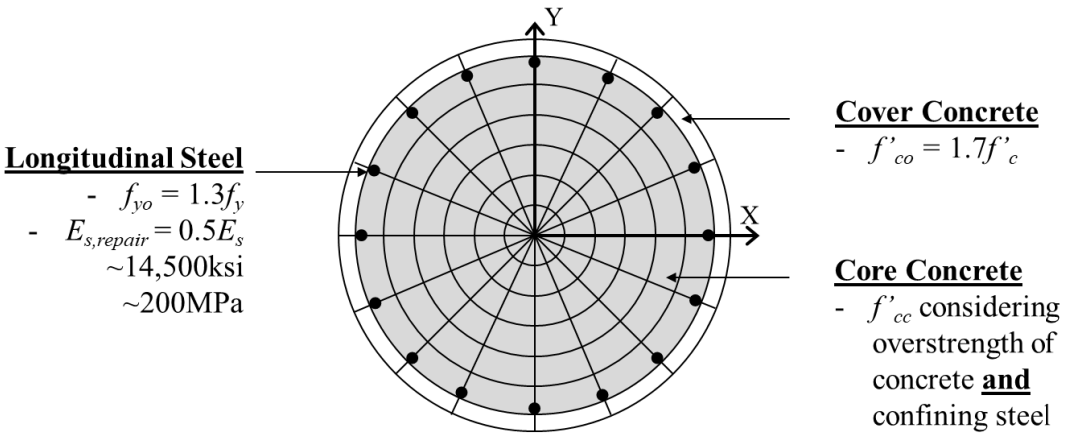

Figure 5.33: Typical moment-curvature material property considerations for repair analysis.

5.5.1 Repair Height

The designer must first determine the height of the repair as all other design values depend on it. The height of the repair should be minimized so as to reduce the demand on the remaining system due to the increased shear forces that arise from the relocated plastic hinge. The greatest of the following three criteria should be taken as the design repair length, L_r, for the column, each of which will be discussed:

1. Column Geometry
2. Damage at new hinge location
3. Development length of the longitudinal repair bars within the repair

5.5.1.1 Column geometry

Based on prior research, the general rule for the height of a plastic hinge relocation repair is approximately equal to the diameter of the original column (Lehman et al., 2001; Parks et al., 2016; Rutledge et al., 2014). The tests conducted in this report actually utilized a repair slightly less than the gross column diameter. Therefore, given the available literature and the repair tests conducted in this report, a lower bound of repair length for design purposes is recommended to be that calculated by Equation 5-46.

$$L_{r,\min} = 0.9D_c \qquad \textit{Equation 5-46}$$

5.5.1.2 Damage at new hinge location

To ensure that the new hinge is located in a region of sufficiently low damage, it is recommended that the peak prior tension strain in the relocated hinge region be limited to $\varepsilon_t = 0.02$. This was accomplished during the experimental tests by directly checking the strain distribution in longitudinal bars to ensure this limit was not exceeded above where the repair was installed, as illustrated in Figure 5.34. This is obviously not practical or feasible for actual bridge columns, therefore another method is required.

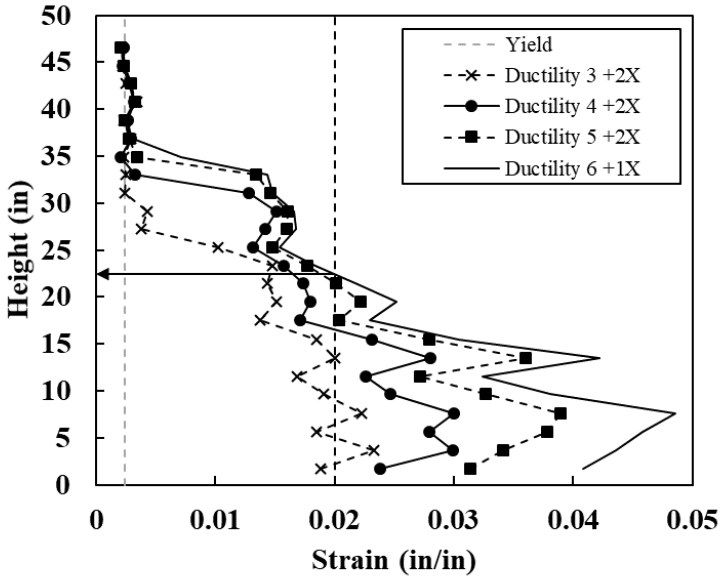

Figure 5.34: Tension strain distribution of Load Path Test 4 corresponding to Repair #1 (Goodnight et al., 2017).

The triangular plastic hinge length developed by Goodnight et al (2015) is meant to describe the extent of plasticity within the hinge region of the column, and can therefore be used as a basis to determine the previous strain history at the relocated hinge region. Assuming a peak tension strain, ε_{max}, at the base of the column, this relationship is determined through similar triangles as shown in Equation 5-47 below. From observations of peak tension strains during tests, a conservative estimate of ε_{max} would be 125% of the ultimate tension strain limit used for moment-curvature analysis.

$$L_{r,\varepsilon} = L_{prt}\left(1 - \frac{0.02}{\varepsilon_{\max}}\right) \qquad \textit{Equation 5-47}$$

Where,

$L_{prt} = 2L_{pt}$ *from Equation 5-18*

5.5.1.3 Repair bar development length

The final criteria to be met when determining the height of the repair is to ensure the longitudinal repair bars have sufficient length over which to develop their yield strength. As previously discussed in Section 3.2.4, the repair annulus can be considered analogous to a grouted pocket connection utilized in accelerated bridge construction. A report prepared by Matsumoto et al (2001) defines a development length equation for reinforcing bars extending into these connections as presented in Equation 5-48. This equation considers the improved bond conditions provided by the well confined repair region as compared to that of a traditional lap splice of a reinforcing bar. The recommended cover in this application is no less than 3 in above the top of the reinforcing bars.

$$L_{r,dev} = \frac{0.022 d_b f_y}{\sqrt{f'_c}} + cover \qquad (psi) \qquad \textit{Equation 5-48}$$

5.5.2 Repair Cross Section

The repair cross section is designed to resist the maximum base moment applied to the repair, as determined from either Equation 5-33 or Equation 5-35. This demand should be determined from overstrength material properties, as discussed at the beginning of this section. Design of the repair annulus can be carried out via a moment-curvature analysis where the longitudinal steel is linear elastic and the repair concrete or grout is considered fully confined by the outer steel sleeve. The design should ensure that the longitudinal steel remains below yield to ensure the repair is capacity protected.

5.5.3 Repair Shear

Finally, the shear demand on the repair can be calculated from the design base moment. While it is assumed that the repair acts as a reaction support with the original column bearing against its top, the distribution of forces resulting from the column bearing against the inner wall of the annulus is assumed to resemble that of Figure 5.35. The column applies a triangular distribution of load over the height of the repair, with a maximum at the repair top and tapering to zero at the base. Thus, a resultant shear force, V_{repair}, can be determined at the centroid of the distributed load. The repair shear demand can then be calculated from Equation 5-49.

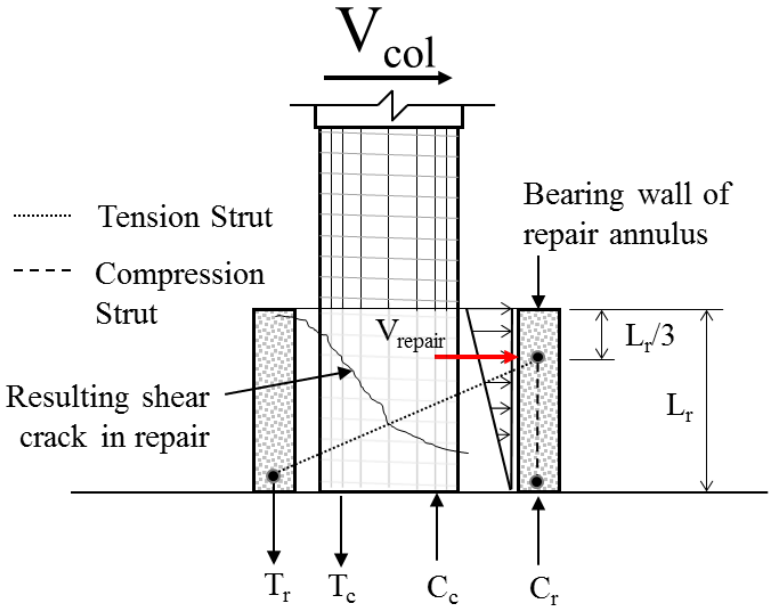

Figure 5.35: Assumed bearing force distribution between column and repair.

$$V_r = \frac{3M_{br}}{2L_r}$$ *Equation 5-49*

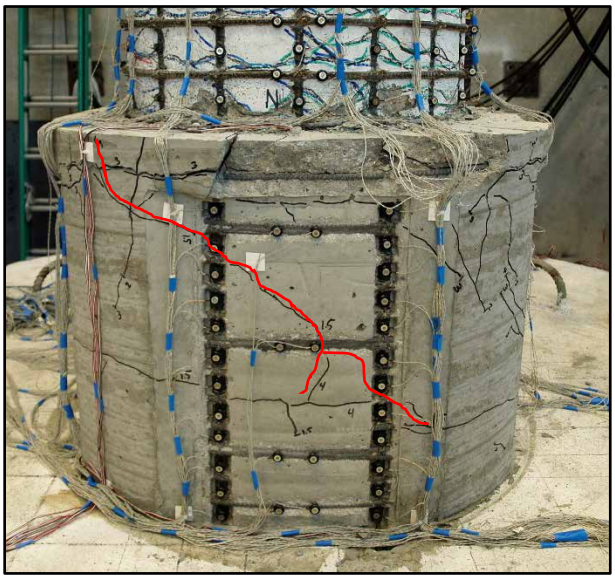

Figure 5.36: Shear crack development in Repair #4.

The assumed crack angle illustrated in Figure 5.35 can be seen in the concrete jacket of Repair #4, as shown in Figure 5.36, since the steel sleeve is not used in this test. Therefore, this crack opening engages the steel truss mechanism developed by the rebar hoops, or an equivalent mechanism created by the steel sleeve. This is the same mechanism on which the modified UCSD shear model is based (Priestley et al., 1996), and it is therefore assumed to be applicable in this case for design. The equations for design are outlined in Equation 5-50 through Equation 5-53 below:

$$V_r = \phi_s V_{cap} = \phi_s \left(V_C + V_S + V_P\right)$$ *Equation 5-50*

The concrete shear resisting mechanism, V_C, should be calculated using design values as opposed to assessment values. Also, considering the repair is to remain elastic, inelastic ductility factors do not need to be considered. V_C is calculated by Equation 5-51 below, where A_g is the gross area of the annular section and ρ_l is the ratio of longitudinal steel in the repair to A_g.

$$V_C = \alpha\beta\gamma\sqrt{f'_c} \cdot \left(0.8A_g\right)$$ *Equation 5-51*

Where,

$$1.0 \le \alpha = 3 - \frac{L_r}{D_r} \le 1.5$$

$$\beta = 0.5 + 20\rho_l \le 1.0$$

$$\gamma = 0.25 \ \textit{(MPa) or} \ \gamma = 3.0 \ \textit{(psi)}$$

The steel strength component is taken from Equation 5-52 below, which applies to circular sections only. The values A_h, s, and c refer to the area of a single transverse reinforcement bar, the spacing of transverse reinforcement and the cover to the centroid of the transverse steel respectively. Where a steel jacket is used, the steel area can be taken as that of a unit length (i.e. the thickness of the material) and the spacing as 1.0. Note that since there is no axial load in the repair, the neutral axis depth has been assumed to be equal to 20% of the section diameter. Also, the absence of axial load also results in the axial load component of shear strength equaling zero, as shown in Equation 5-53.

$$V_S = \frac{\pi}{2} \cdot \frac{A_h f_{yh} \left(0.8D_r - c_o\right) \cdot \cot\left(35\right)}{s} \qquad \textit{Equation 5-52}$$

$$V_P = 0 \qquad \textit{Equation 5-53}$$

5.6 Conclusions

This chapter examines the physical behavior of the repaired system and provides an analytical model solution by which the repair can be designed, and the repaired system performance can be evaluated. The analytical model modifies existing methods which are familiar to design engineers and uses first principles to define the behavior and force distribution of the system. It assumes that there is no bond interface between the original column and the interior surface of the repair, and that the repair acts as a rigid support creating a distribution of plasticity that is mirrored about the top plane of the repair. Furthermore, the model is capable of accurately capturing the global column behavior, local plastic hinge strains, and the demand on the repair

through a simple set of calculations, as demonstrated through comparison with experimental tests. The following chapter uses the principles defined in the analytical model to develop a computational design model which can be used to further evaluate the repaired system behavior through computer simulation.

Chapter 6: Computational Model

The analytical model described in the previous chapter provides the engineer with the tools necessary to design and assess the performance of a repair for any single bridge column of arbitrary configuration. This chapter discusses the development of a computational model in which the same principles are applied to develop a computer model for further analysis of the repaired structure. The resulting product is a simple extension of the existing Beam with Hinges fiber element available in OpenSEES (2000) which allows the user to easily model the effects of the plastic hinge relocation repair on the applied element. Deformation due to strain penetration into the repair is modeled using a single zero-length section element with modified material properties to achieve the equivalent rotations observed in the experiments. A second zero-length element with elastic properties is also used to represent the deformation due to rigid body rotation of the repair. The resulting model can then be substituted into a full bridge model or investigated independently at relatively low computational cost as compared to more involved finite element models.

6.1 Background

Analysis of repaired reinforced concrete structures poses many complications in addition to those already present in non-linear modeling when considering earthquakes. A list of necessary considerations is provided by Vecchio and Bucci (1999) as follows: (1) consideration of changing structural configuration; (2) superposition of previously loaded or damaged portions of a structure with newly-added unstressed elements; (3) proper constitutive modeling of the repair materials; (4) inclusion of residual stress and strain differentials across repair interfaces; (5) and correct account of the chronology of the loading, damage, and repair sequences.

He et al (2015) reports that two different general procedures have been presented in the literature to model repaired RC columns. The first is what is referred to as the two-phase method in which the original and repaired systems are both considered within the same model. The initial phase of the analysis consists of only the original member elements and, once the first analysis

concludes, elements and boundary conditions are added and/or removed representing the installed repair. At this point the model is then reloaded to obtain the response of the repaired system. This method has the obvious advantage of directly considering the accumulation of damage in the original system prior to "installing" the repair, and strain histories associated with the initial loading can be carried directly into the repaired analysis. A study by Vecchio and Bucci (1999) utilizes this approach through modification of a finite element software in which they implement the ability to engage and disengage elements at any time throughout a loading history through use of what is called the plastic offset approach. Their method maintains overall strain compatibility of initially disengaged elements but holds the elastic component of their deformation to zero, therefore they do not contribute to the strength or stiffness of the structure during initial loading. Once activated, these elements begin to deform from a state of zero elastic strain and behave as they would under initial loading. Damaged elements that are removed no longer make any contribution to the stiffness matrix. Lee et al (2011) developed a similar method for fiber element models using the *ZeusNL* software package (now referred to as SeismoStruct). This study considered effects not only of individual members, but also of the repaired member's effects on an overall structure. Fiber elements were used in this case for their ease of implementation into a larger stick model. Regardless of complexity, both studies showed good fit when compared to experimental results.

The second approach available to model repaired systems is referred to as the damage index method, in which the damaged/repaired condition is considered as the initial state of the model. Damage is considered through modification of material parameters or cross sectional properties to simulate the expected response and the repair is directly modeled into the system with corresponding material properties and boundary conditions. This method does not directly capture the previous load history of the system and resulting damage; however, the computational expense and modeling effort can be drastically reduced by only considering the post-repair system as opposed to modeling and analyzing both the pre and post-repair systems in the two-phase approach. Furthermore, through careful modification of material response properties and repair interaction, it is possible to achieve very good results that closely match those of experimental tests as shown by (Duarte, Correia, Ferreira, Nunes, & Arruda, 2014; Ashkan Vosooghi & Saiidi, 2013).

6.2 Model Configuration

Both the damage-index and two-phase methods were considered for use in this report. Initially, it was assumed that the two-phase method would be ideal since this would directly capture the accumulation of damage during the first test and the repair elements could be added to the model prior to the second analysis. While the software used, OpenSEES (2000), is capable of carrying out this progressive analysis, it was found that it is not possible to accurately represent the complex interaction between the repair and original column using only beam elements as intended. This is due to the fact that the introduction of the repair results in a sharp modification of boundary condition to the original column producing a disturbed region which does not follow beam theory principles. More refined finite element analysis has been shown to be capable of capturing this interface reaction when investigating column-socket behavior (Canha, Ebeling, De Cresce El Debs, & El Debs, 2009); however, the intent of the model created herein is to minimize complexity while still accurately capturing the global and local member behavior. Therefore, a simplified approach using the damage-index method was chosen over a more complex finite element analysis.

The layout of the model used to describe the repaired system is illustrated in Figure 6.1. A total of four elements are distributed between five nodes. The following sections describe the contribution of each element as it pertains to the overall member behavior, along with the constituent material models considered for each. Each section focuses specifically on the development of the model within the OpenSEES framework; however, the general principles apply to any software package that supports fiber element analysis.

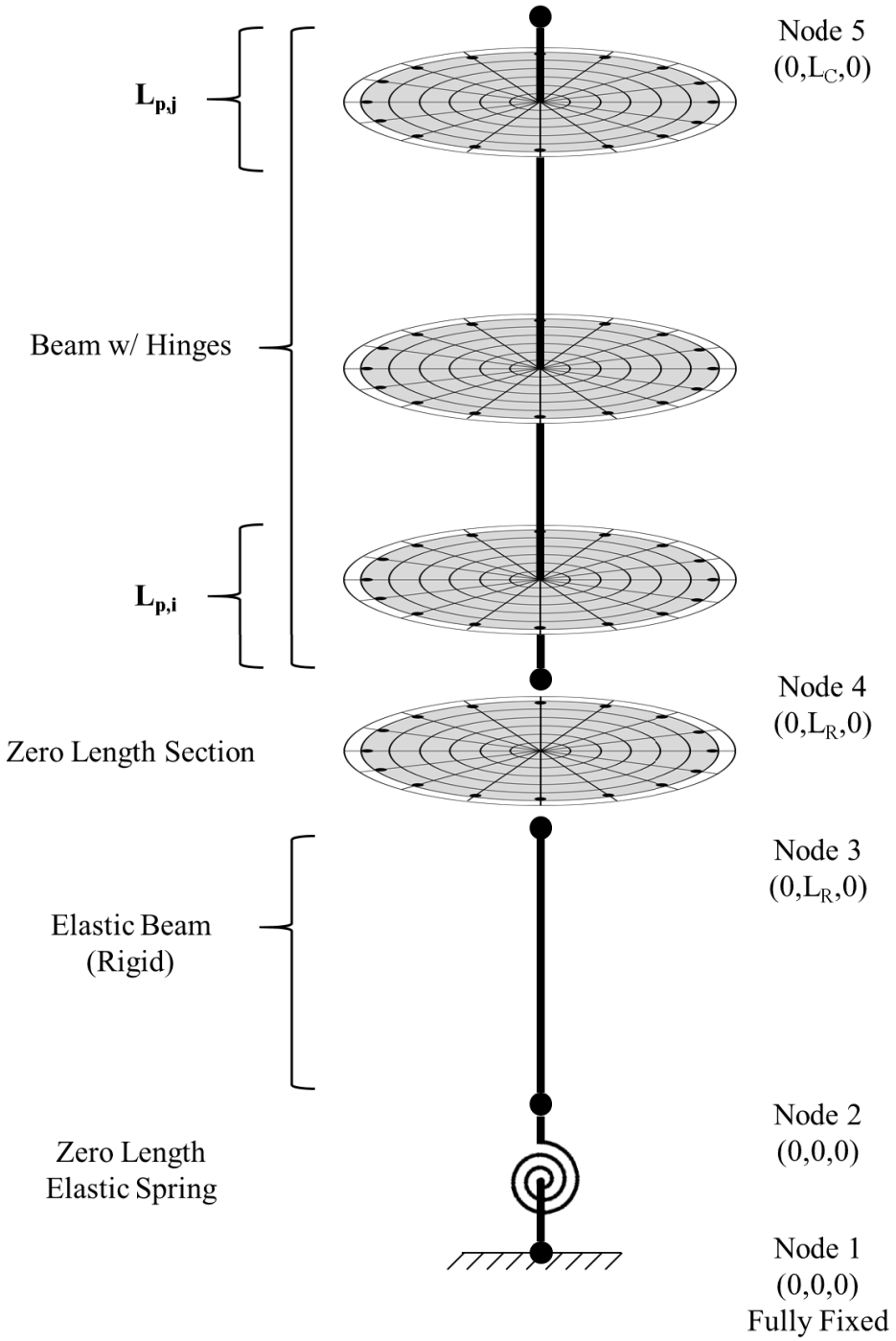

Figure 6.1: Computational model schematic diagram.

6.2.1 Column section above repair

The column above the repair is modeled assuming it behaves as any other typical reinforced concrete column. This is based on the principle defined in the previous chapter where the flexural component of deformation of the column above the repair is described using the traditional plastic

hinge method outlined in Equation 5-16 through Equation 5-18. The *forceBeamColumn* element is used with two-point Gauss-Radau integration applied in the hinge regions and two-point Gauss integration applied on the element interior for a total of six integration points (Scott & Fenves, 2006). The force based formulation requires only a single element to accurately represent the full nonlinear deformation of the member and the integration scheme selected prevents the loss of objectivity during softening response while also providing integration points at the member ends (Calabrese, Almeida, & Pinho, 2010; Scott & Fenves, 2006). The element requires the length of plasticity be defined at each end of the member, for which the tension based rectangular plastic hinge length calculated by Equation 5-18 is recommended. Furthermore, the two-point Gauss-Radau integration is applied such that the end node integrations are weighted equal to the specified plastic hinge length, as illustrated in Figure 6.2. Therefore, strains recorded at the end sections represent accurate values even in the case where deformation localizes to the ends from strain softening behavior. For the case of the cantilever column considered in this report, only one hinge length is defined, and the opposite end is given an arbitrary unit length.

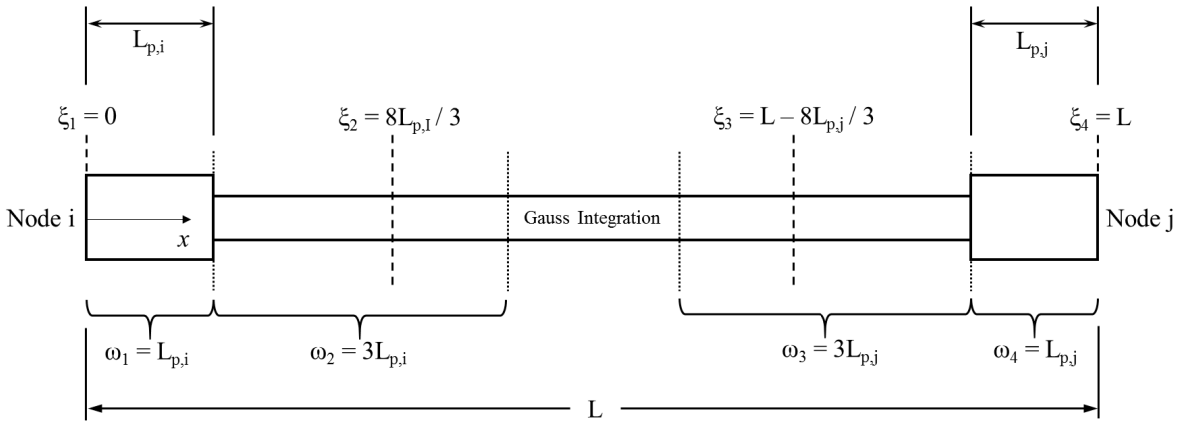

Figure 6.2: Modified two-point Gauss-Radau integration scheme used in member above repair, reproduced from (Scott & Fenves, 2006).

Two different sections are defined for use at the integration points within the element. Both sections are discretized with concrete and steel material fibers representing the geometry of the section. Concrete fibers are modeled using the Concrete01 material, modified for confined material strength based on the Mander confined concrete model (Mander, Priestley, & Park, 1988) where applicable. The Steel02 material, based on the Giuffre-Menegotto-Pinto model (Filippou, Popov, & Bertero, 1983), is used for the longitudinal reinforcement with recommended parameters (b = 0.01, R0 = 20, cR1 = 0.925, cR2 = 0.15). As discussed in Section 5.2.3, the modulus of the steel in the section assigned to the relocated plastic hinge is reduced by 50% to represent the softening

of the material due to prior strain as recommended by Vosooghi & Saiidi (2010). As a consequence, the strain hardening ratio, *b*, in these sections is increased by a factor of two to ensure the post yield behavior remains that of the initial material. All sections located outside of the plastic hinge region use the original material properties at their full values. Figure 6.3 illustrates the material properties assigned to each region of the column in the model.

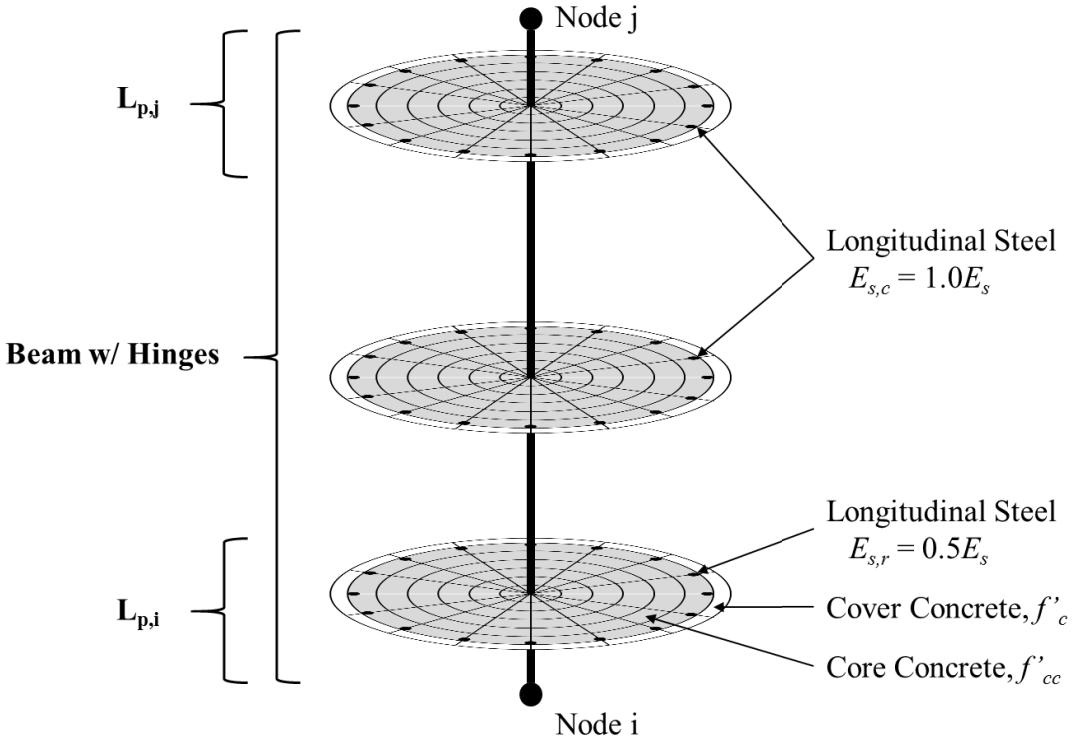

Figure 6.3: Definition of column section material properties within repaired member.

6.2.2 Zero-length section strain penetration element

The next major component to be considered in the model is the strain penetration into the repair. As mentioned previously, modeling of a new beam element within the repair results in a sharp discontinuity at the repair interface which does not accurately capture the member behavior. Therefore, instead of modeling the entire region, the *zeroLengthSection* element is used to capture the effects of the rotations due to strain penetration into the repair. While this method does not provide direct information on the distribution of strains within the repair, it does result in accurate predictions of the strain penetration contribution to overall member deformation. Also, it has been shown previously in this report that failure limit states of the repaired column are best predicted by strains above the repair and do not depend on precise knowledge of the strain magnitudes within the repair. Therefore, the intent of this element is only to modify the member stiffness such that

the calculated strains in the end section of the adjacent beam-column are accurate for a given deformation.

The formulation of this element assumes that the moment-curvature relationship of the zero-length section is identical to that of the plastic hinge section defined in the adjacent column element as described in the previous section. The resulting curvature is then integrated over a specified strain penetration length to obtain the equivalent rotation that results at the top of the repair due to strain penetration of the column into the repair. This is consistent with the methodology discussed in the previous chapter when considering the deformation due to column rotation inside of the repair. Thus the equivalent strain penetration length can be taken from Equation 5-22, Equation 5-23, Equation 5-27, and Equation 5-28 as the component which combines with the section curvature to produce the corresponding rotation. Note, however, that the strain penetration length is different for elastic and plastic components. The resulting strain penetration length equations for the elastic, $L_{sp,e}$, and plastic, $L_{sp,p}$, components are presented in Equation 6-1 and Equation 6-2 respectively, where $L_{sp,c}$ is the strain penetration length of the reinforcement bars into the footing, as displayed in Equation 5-26.

$$L_{sp,e} = \frac{L_r}{2}\left(1 + \frac{L_{eff} - L_r}{L_{eff}}\right) + L_{sp,c}\left(\frac{L_{eff} - L_r}{L_{eff}}\right) \qquad \textit{Equation 6-1}$$

$$L_{sp,p} = \frac{L_r}{2}\left(1 + \frac{L_{prt} - L_r}{L_{prt}}\right) + L_{sp,c}\left(\frac{L_{prt} - L_r}{L_{prt}}\right) \qquad \textit{Equation 6-2}$$

These factors are then used to modify the constituent material properties of the element to scale the resulting deformations as desired. Zero-length elements assume a unit length, meaning that section deformation is equal to element deformation. In other words, if a zero-length section is defined using typical stress-strain values, the element rotation would be exactly equal to the curvature of that section under the given moment demand. However, if the stress component is left alone, but the strains are scaled by some value, the resulting rotation under the same moment would also be scaled by that same value. Figure 6.4 illustrates this concept, where the strain values are multiplied by a factor, L_{sp}, which results in the total section deformation equaling that of a similar section with typical assigned strain values which has been integrated over a length L_{sp}.

Furthermore, by implementing this scaling at the material level, it is also possible to modify the elastic and plastic components separately.

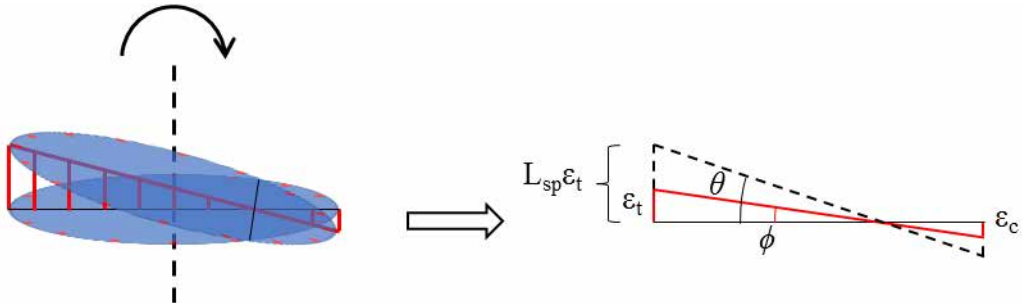

Figure 6.4: Scaled strain properties in zero-length sections.

The process for modifying each material property varies slightly depending on what values are specified to define the material. For example, the Concrete01 material is defined on the following values:

f'_{cc} = peak compressive strength (confined)

f'_{cu} = compressive strength at ultimate

ε_{cc} = strain at peak stress

ε_{cu} = strain at ultimate

Each of these values can be obtained either directly from tests or calculated. When modifying the material properties, f'_{cc} and f'_{cu} remain the same; however, the strain values are such that the resulting curve resembles that shown in Figure 6.5, where $\varepsilon_{cc,pr}$ and $\varepsilon_{cu,pr}$ represent the scaled elastic and plastic components of strain respectively and are obtained from Equation 6-3 and Equation 6-4. Note that when modifying the plastic component of strain, it is necessary to remove the elastic portion prior to applying the factor and then add back to the scaled elastic strain.

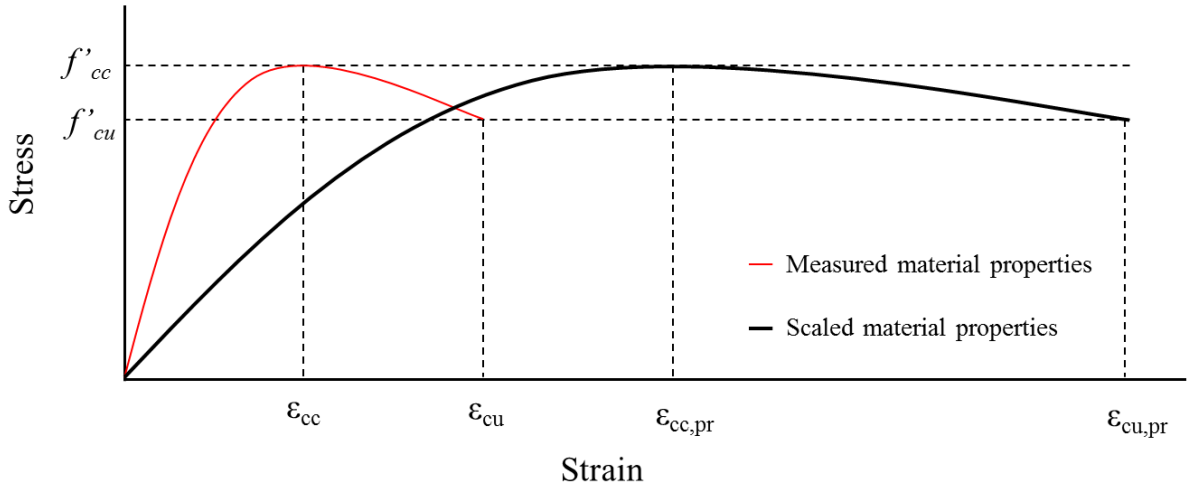

Figure 6.5: Scaled concrete material properties for Concrete01 material type.

$$\varepsilon_{cc,pr} = L_{sp,e}\varepsilon_{cc} \qquad \textit{Equation 6-3}$$

$$\varepsilon_{cu,pr} = L_{sp,p}\left(\varepsilon_{cu} - \varepsilon_{cc}\right) + \varepsilon_{cc,pr} \qquad \textit{Equation 6-4}$$

Modification of the steel material requires a different approach since the material is defined based on initial and post yield stiffness rather than directly by strains. The Steel02 material model is defined based on the following properties:

f_y = Yield strength

E_s = Initial steel modulus

b = Strain hardening ratio

Many other parameters are available to fine tune the material; however, these three are responsible for defining the overall backbone curve and the others adjust based on how these are defined. As with the concrete material, the yield strength remains the same since the same force response is desired. The elastic modulus is then reduced such that the resulting strains scale accordingly, as defined in Equation 6-5. The post yield stiffness is calculated as a percentage of the initial stiffness as defined by b, which must be modified by the ratio of $L_{sp,e}$ to $L_{sp,p}$, as shown in Equation 6-6. This accounts for the shift in strain penetration length post yield. Also, the initial material modulus, E_s, should represent that which is used in the plastic hinge section of the column. In the case of the element described in the previous section, this is half of the original material modulus.

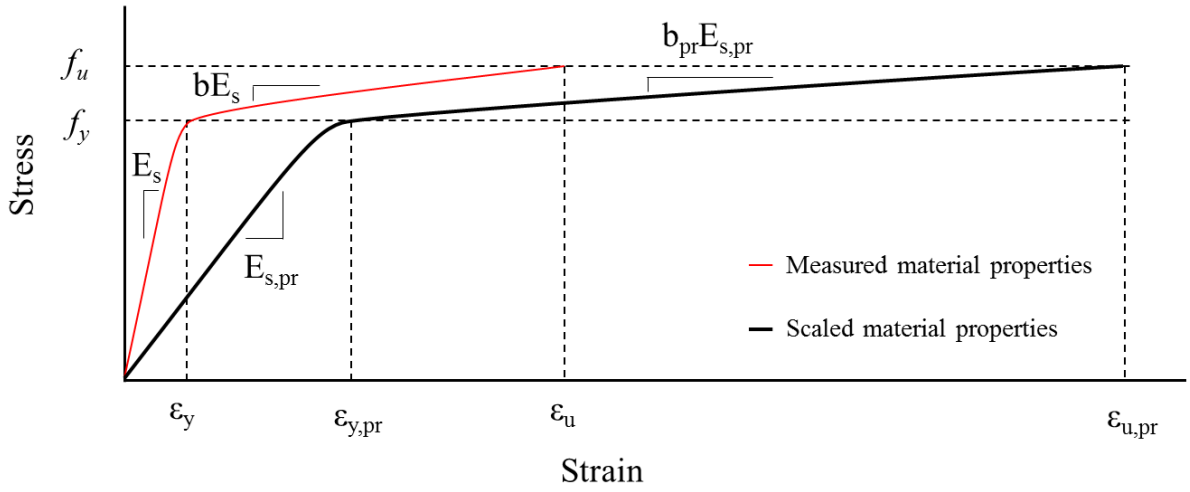

Figure 6.6: Scaled steel material properties for Steel02 material type.

$$E_{s,pr} = \frac{E_s}{L_{sp,e}} \qquad \textit{Equation 6-5}$$

$$b_{pr} = b\left(\frac{L_{sp,e}}{L_{sp,p}}\right) \qquad \textit{Equation 6-6}$$

Once the material properties of the zero-length section have been modified according to the above criteria, the moment demand at the column-repair interface results in the corresponding rotations which were described in the previous chapter. These rotations represent all of the original column deformation below the column-repair interface. This element essentially behaves as a concentrated plastic hinge that retains all of the sectional and hysteretic properties of the column as it rotates within the repair.

6.2.3 Rigid elastic member

The *elasticBeamColumn* element with very large stiffness properties is used to translate the top of repair forces to the base of the repair. This element is used in place of a rigid link element, as the rigid link was found to be unstable within the model. The following member properties to simulate a rigid link:

A = Cross-sectional Area = 1.e10

E = Elastic Modulus = 1.e10

G = Shear Modulus = 1.e10

J = Torsional Moment of Inertia = 1.e10

Iz = Iy = Rotational Moment of Inertia = 1.e10

6.2.4 Repair base rotation spring

The deformation due to rigid rotation of the repair is considered by a second zero-length rotational spring at the base of the model. Since this element is to remain elastic, it can be modeled as a simple spring, with elastic section properties assigned as calculated from Equation 5-36 through Equation 5-38, using the *zeroLength* element available in OpenSEES. This *zeroLength* element also assumes a unit length, therefore the resulting section curvature must be scaled by the repair strain penetration length, $L_{sp,r}$, found using Equation 5-40. Furthermore, the total base moment acting on the section in the analysis does not represent the actual moment demand on the repair. A portion of this base moment is carried by the original column at the footing interface, whose deformations are accounted for in the zero-length section above the repair. Therefore, the spring stiffness must be again modified such that the resulting deformations reflect that of the reduced moment demand, as opposed to the full moment resulting at the base of the model. Shear deformation of the repair contributes negligibly to the overall member deformation, therefore the shear and torsional stiffness of the zero-length section are set to very large values such that they are effectively rigid. For repairs considering only buckled bars, the rotational spring stiffness is calculated from Equation 6-7.

$$k_{\theta,rr} = \frac{0.35EI_g}{L_{sp,r}}\left(\frac{L_c}{2L_r}\right) \qquad \textit{Equation 6-7}$$

For columns with ruptured bars, the base moment distribution is more complex. Assuming that each of the fractured bars are fully anchored inside the repair, the moment-curvature relation at the column-repair interface considers the full cross section of steel, whereas that at the footing considers only the non-fractured bars. Therefore sectional analysis of each location is required to determine the relative strength of each cross section. A parameter, β, is taken as the ratio of the strength of the reduced section to that of the full cross section. This ratio is not constant for all curvatures, but a reasonable estimate can be obtained. The resulting rotational stiffness of the repair then becomes that shown in Equation 6-8. Note that β will always be less than one, and in the case where $\beta = 1$, Equation 6-8 collapses back to be Equation 6-7.

$$k_{\theta,rr,rup} = \frac{0.35EI_g}{L_{sp,r}}\left(\frac{L_c}{L_c - \beta\left(L_{eff} - L_r\right)}\right) \qquad \textit{Equation 6-8}$$

This model assumes either continuous longitudinal steel, or that fractured bars have been sufficiently anchored in the repair such that they do not debond. In the case where fractured bars are *not* sufficiently anchored to prevent debonding, the model should conservatively assume that the bars will debond and should not be considered in the analysis. In this case, the fractured bars are excluded in all cross sections definitions and Equation 6-7 is used to define the repair rotational stiffness.

6.3 Comparison of model to experimental results

The plots shown below in Figure 6.7 through Figure 6.12 compare the numerical model performance response prediction to that which was observed in experimental tests. Comparisons are provided for the global force vs. displacement response as well as the local strain response within the plastic hinge. Repairs #2 and #6 are omitted since they contain a significant number of fractured bars that debonded during the tests, which this model is not capable of capturing, and Repair #5 was omitted due the premature fracture of the welded sleeve. Although Repair #4 did contain a single fractured bar that debonded, it did not have as dramatic of an effect on the global behavior as did those in Repairs #2 and #6 and was therefore included in the comparisons. Each plot also contains a comparison of the backbone curves developed using the analytical model described in the previous chapter to the results of the numerical model developed here.

Each of the global force vs. displacement plots displays a good match with experimental data overall. The envelope backbone curve of each model corresponds very closely with that of the experiments and from the analytical model. Some overestimation of initial stiffness is observed in Repairs #1 and #3; however, the response at large ductilities tends to converge to the observed values. The unloading stiffness of each model does show some significant deviation from the experimental results. This is likely attributed to the concrete material model, as it assumes zero force contribution from the concrete until the strain reaches the point at which tension forces were first observed. This implies that cracks close perfectly onto the planes at which they formed, which is not the case. Material models are available to address this (Lee & Billington, 2010); however, convergence issues were observed when attempting to use them. Furthermore, the reloading

stiffness is considered less of a concern than capturing the peak forces within the system, which the model is currently capable.

In addition to the global response accuracy, the strains within the plastic hinge of the numerical model match exactly with those of the analytical model and provide good estimates of experimental results. When performing computational analysis, it is critical to have reliable estimates of strain, as many limit states are directly related to local strain behavior. Since the tension based plastic hinge was used in the formulation of the model, damage states such as excessive residual crack widths and bar buckling can be reliably predicted with this model to a reasonable degree of accuracy.

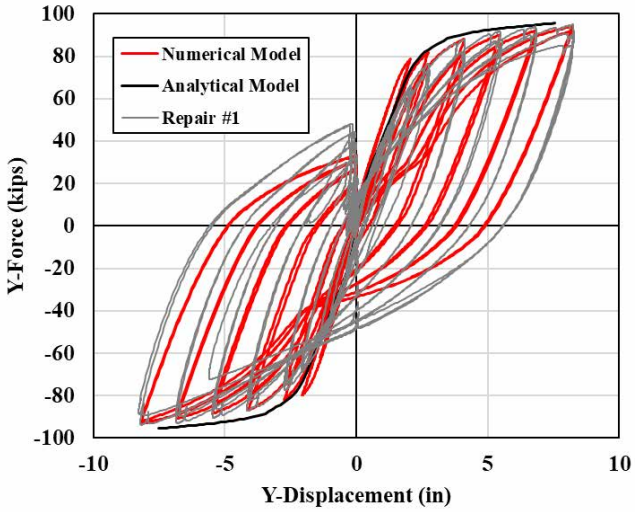

Figure 6.7: Repair #1 force vs. displacement comparison of numerical model to experimental results.

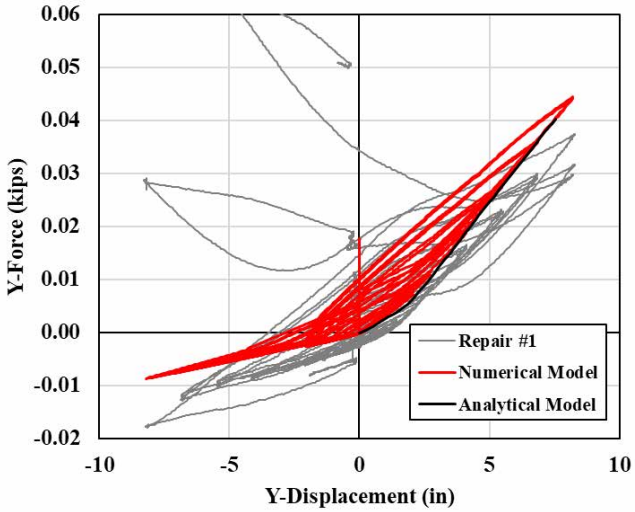

Figure 6.8: Repair #1 strain vs. displacement comparison of extreme fiber bars in numerical model to experimental results.

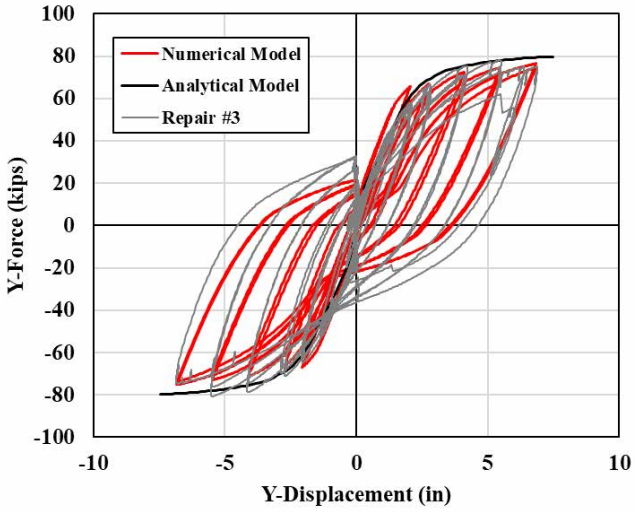

Figure 6.9: Repair #3 force vs. displacement comparison of numerical model to experimental results.

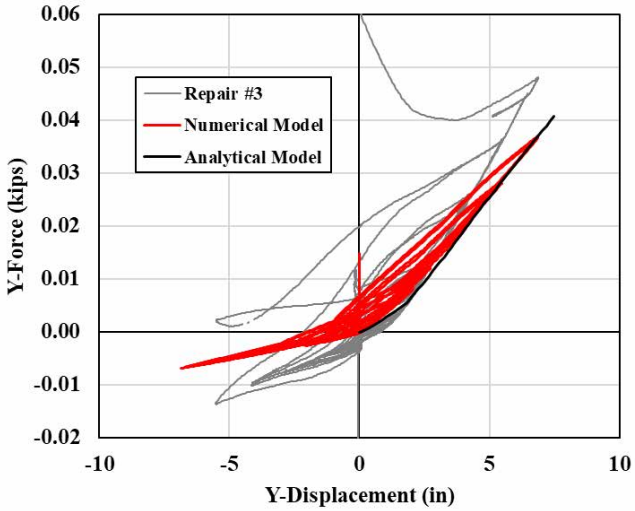

Figure 6.10: Repair #3 strain vs. displacement comparison of extreme fiber bars in numerical model to experimental results.

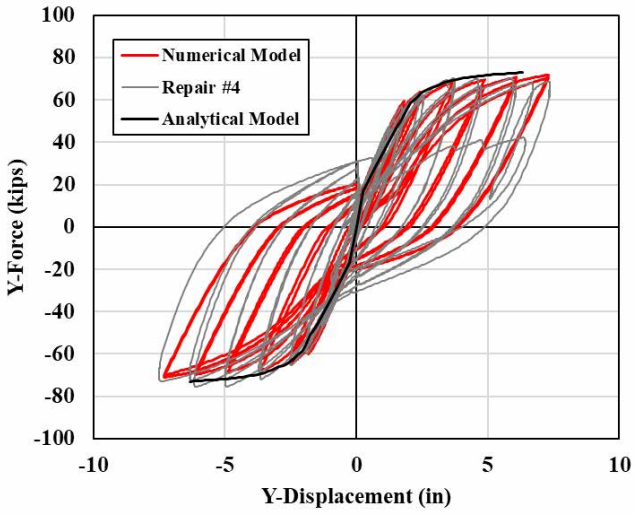

Figure 6.11: Repair #4 force vs. displacement comparison of numerical model to experimental results.

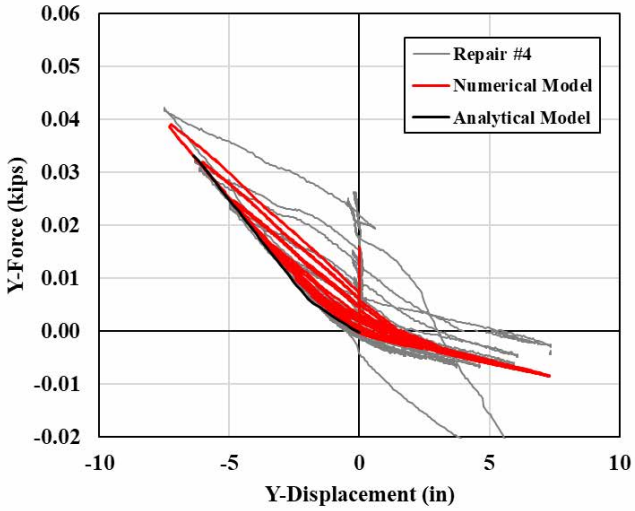

Figure 6.12: Repair #4 strain vs. displacement comparison of extreme fiber bars in numerical model to experimental results.

In addition to the individual quantities measured above, the contribution of each component of deformation to the overall system response is compared in Figure 6.13 through Figure 6.15 below. The plots on the left represent the average components of deformation observed experimentally, while those on the right show the components of deformation calculated from the numerical model. Here it is evident that each individual element is contributing to the overall behavior as intended.

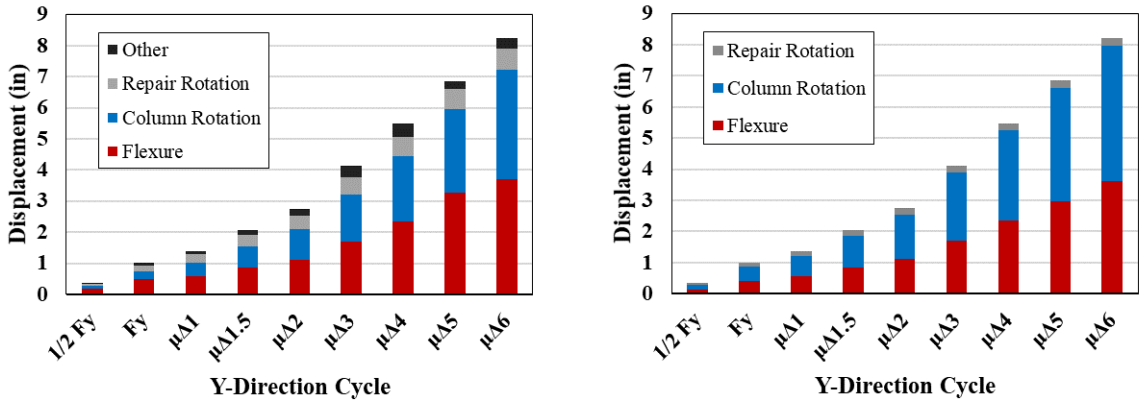

(a) **(b)**

Figure 6.13: Repair #1 components of deformation from (a) experimental, and (b) numerical model.

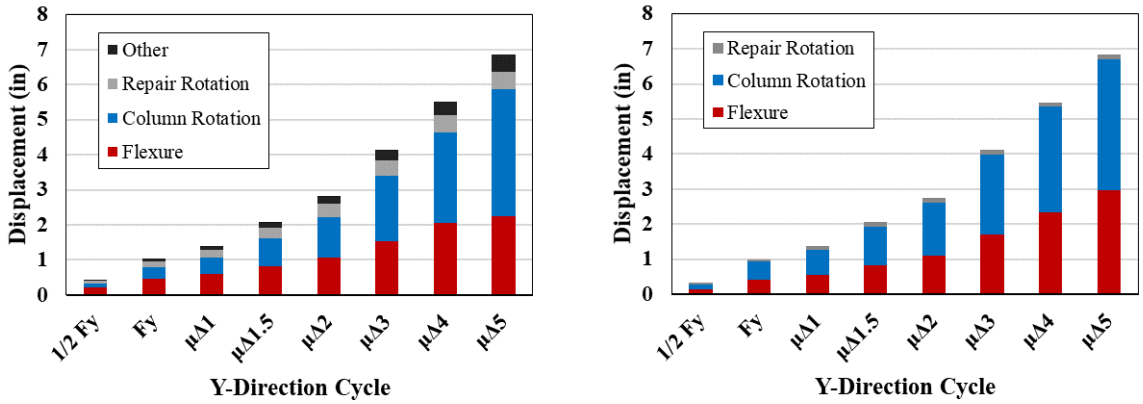

(a) **(b)**

Figure 6.14: Repair #3 components of deformation from (a) experimental, and (b) numerical model.

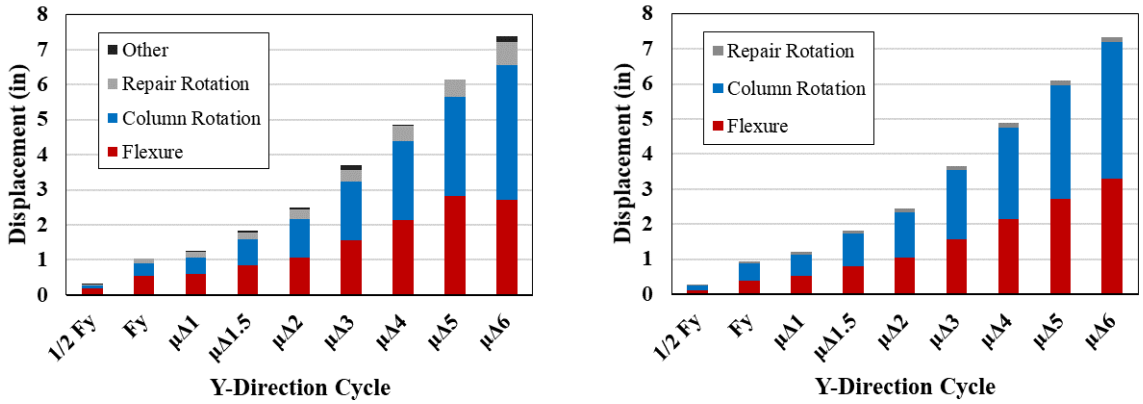

(a) **(b)**

Figure 6.15: Repair #4 components of deformation from (a) experimental, and (b) numerical model.

6.4 Conclusions

This chapter discusses the development of a computational model which accurately captures the behavior of a circular reinforced concrete column which has been repaired using the plastic hinge relocation technique described in this report. The proposed model has been shown to predict both the global force vs. displacement response of the member as well as the local strains within the relocated plastic hinge when compared to experimental results. These parameters provide sufficient information to investigate the performance of the repaired member using strain or drift-based limit states, and to understand the potential effects of using this type of repair on the overall structure in question. The following chapter outlines an application of the model to investigate the impact of residual drift when considering the use of this repair method.

Chapter 7: Impact of Residual Drift on Repaired System Performance

One of the key goals of this research is to determine the limits of repairability of RC bridge columns after being subjected to an earthquake. To this point, it has been experimentally demonstrated that columns exhibiting buckled and fractured longitudinal steel, fractured transverse spirals, and crushed cored concrete can be restored to their initial capacities using the plastic hinge relocation technique described herein. With this said, it is reasonable to assume that any level of localized damage within the plastic hinge region of the column can be considered repairable given that the structure remains vertical and capable of carrying load. Consequently, the question of what defines the limit of repairable damage remains unanswered; aside from total collapse, which does not provide a very satisfying conclusion.

Since local damage states do not provide a clear basis on which to define the limits of repairability, the global state of the structure serves as the next logical approach. The bridge is assumed to be designed using capacity protection principles within the scope of this research, therefore failure through other undesirable mechanisms (i.e. brittle shear failure, unseating of spans, abutment failure, etc.) are not considered as relevant measures. However, since large displacements during the initial earthquake are likely the cause of the damage, it is reasonable to assume that some residual displacement will be present afterwards. Residual displacements are typically not explicitly limited in capacity design procedures, and therefore could potentially be very large. This chapter aims to address the impact of residual drift on the performance of a structure which has been repaired using the plastic hinge relocation method through development of a rational, probabilistic approach.

7.1 Background

Upon reaching inelastic deformations associated with the levels of damage considered for the repair described in this report, it is likely that some residual displacement will remain once the structure comes to rest. Consider the structural response illustrated in Figure 7.1 below, which has been reproduced from (Pampanin et al., 2002). If the column is pushed to some maximum displacement, d_{max}, and then released, it will return to a maximum residual displacement, rd_{max}; however, in an earthquake the structure is likely to continue shaking through further nonlinear cycles resulting in a final residual displacement, rd, which is some fraction of rd_{max}. Whereas rd_{max} is simply a function of the structure's unloading stiffness, the final resting position following an earthquake, rd, is dependent on the following: 1) magnitude of peak transient inelastic drifts (i.e. d_{max}), 2) lateral strength of the structure relative to earthquake demand, 3) inelastic post-yield stiffness, 4) cyclic unloading response, 5) pulses in ground motions, and 6) duration of ground shaking (FEMA, 2012).

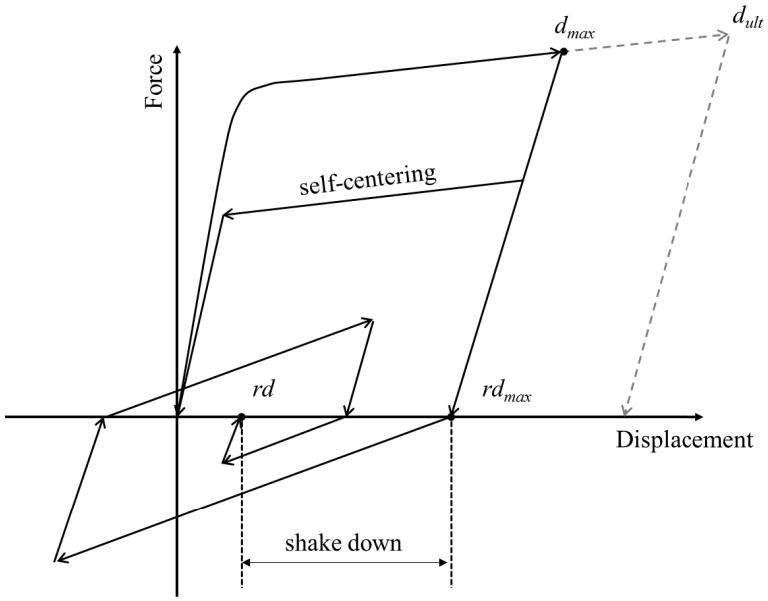

Figure 7.1: Characteristics of residual deformation; reproduced from (Pampanin et al., 2002).

Although great strides have been made in the modeling and prediction of peak structural response, residual displacements remain a challenge when it comes to design. This is largely due to the high variability in relevant parameters listed above, especially those related to ground motions, as well as sensitivity of the analysis results to modeling assumptions. Regardless, attempts have been made to quantify residual drift as a function of ground motion intensity and in turn use that measure as a performance metric in design (Kawashima et al., 1998; Pampanin et al.,

2002; Pettinga, Pampanin, Christopoulos, & Priestley, 2007). Each of these studies demonstrate wide scatter in results and reiterate the need to rationally define performance limit states for residual drift which can be related to damage. Other research has aimed to address the issue by eliminating residual drift altogether through development of self-centering systems such as that proposed by Lee & Billington (2011). While each of these approaches are suitable as an attempt to limit residual drift during initial design of a structure, they do not address the question of what to do when faced with a traditional RC column that has a measurable, definite level of residual drift.

As it currently stands, residual displacement remains more of an inconvenient fact of a structure's post-earthquake condition. However, it is also one of the few directly measurable effects of an earthquake on an actual structure and is therefore one of the most widely used measures of functionality and safety when considering whether to allow access following a major seismic event. Despite this fact, there is relatively little guidance on what is considered an allowable limit to residual deformation when it comes to making these decisions (FEMA, 2012; Lee & Billington, 2011; Mackie & Stojadinovic, 2004). Furthermore, the criteria that are available are largely based on engineering judgement or prior precedent. For example, approximately 100 of the RC columns that did not collapse in the Kobe earthquake were demolished and rebuilt simply due to residual drift exceeding an arbitrary limit of 1.75% (Kawashima et al., 1998). The Seismic Performance Assessment of Buildings (FEMA, 2012) proposes slightly more refined limit state criteria, presented in Table 7.1; however, these are still largely prescriptive in nature and come with the caveat that they too are based primarily on engineering judgement.

Table 7.1: Damage States for Residual Story Drift; reproduced from (FEMA, 2012).

Damage State	Description	Residual Story Drift Ratio $\Delta / h^{(1)}$
DS1	No structural realignment is necessary for structural stability; however, the building may require adjustment and repairs to nonstructural and mechanical components that are sensitive to building alignment (e.g., elevator rails, curtain walls, and doors).	0.2% (equal to the maximum out-of-plumb tolerance typically permitted in new construction)
DS2	Realignment of structural frame and related structural repairs required to maintain permissible drift limits for nonstructural and mechanical components and to limit degradation in structural stability (i.e., collapse safety)	0.5%
DS3	Major structural realignment is required to restore margin of safety for lateral stability; however, the required realignment and repair of the structure may not be economically and practically feasible (i.e., the structure might be at total economic loss).	1%
DS4	Residual drift is sufficiently large that the structure is in danger of collapse from earthquake aftershocks (note: this performance point might be considered as equal to collapse, but with greater uncertainty).	High Ductility Systems $4\% < 0.5V_{design}/W$
		Moderate Ductility Systems $2\% < 0.5V_{design}/W$
		Limited Ductility Systems $1\% < 0.5V_{design}/W$

Notes: (1) h is the story height.

A study by Mackie and Stojadinovic (Mackie & Stojadinovic, 2004) highlights the need for a more quantitative and systematic method for decision making by engineers, owners, and operators when assessing the post-earthquake functionality of a bridge. Their investigation uses the performance based design probabilistic framework developed by the Pacific Earthquake Engineering Research Center (PEER) (Moehle & Deierlein, 2004) to quantify the deterioration of load carrying capacity of the structure as a direct function of the residual drift. The approach first subjects structural models to a range of dynamic time history analyses representing an array of intensity measures. Following the mainshock analysis, static push-over and push-under tests are run to assess the loss in both horizontal and vertical load carrying capacities respectively. A push-under analysis is described as analogous to a push-over; however, the load is applied downward and vertical displacements are monitored.

The result of this analysis is the development of fragility curves describing the probability of exceeding specified limit states as a function of measured residual displacement, as shown in Figure 7.2. This information could then be used in conjunction with the criteria defined in Table 7.2 to make decisions on whether a bridge should remain open to traffic, limited to some reduced capacity, or closed altogether.

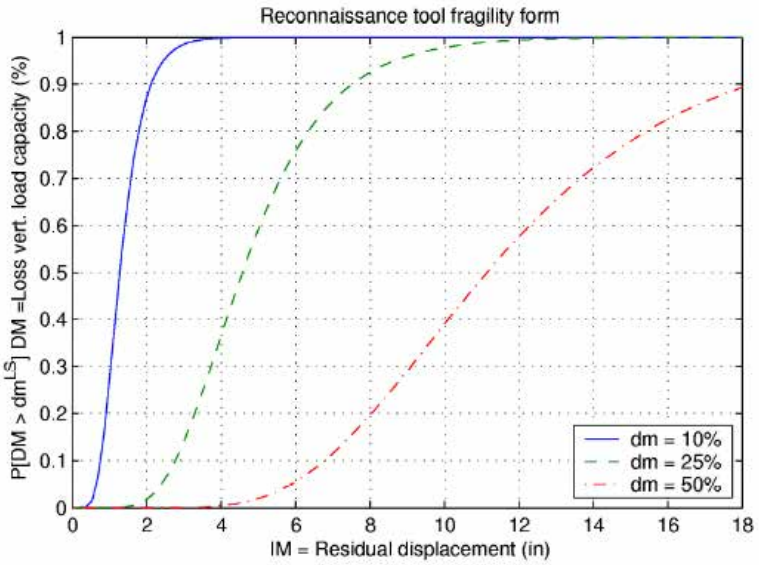

Figure 7.2: Residual drift fragility tool; reproduced from (Mackie & Stojadinovic, 2004).

Table 7.2: Example performance levels using expected residual capacity; reproduced from (Mackie & Stojadinovic, 2004).

Objective name	Traffic capacity remaining (volume)	Loss of lateral load carrying capacity	Loss of vertical load carrying capacity
Immediate access	100%	< 2%	< 5%
Weight restriction	75%	< 2%	< 10%
One lane open only	50%	< 5%	< 25%
Emergency access only	25%	< 20%	< 50%
Closed	0%	> 20%	> 50%

This approach certainly provides a more rational method by which to make decisions in the immediate aftermath of a major earthquake; however, there are still many problems to be addressed when establishing true residual drift limits. First, the residual drifts resulting from the initial dynamic analysis are still highly sensitive to the modeling assumptions selected. Thus, the fragility functions defining the loss of capacity associated with these values are also subject to this sensitivity. This may be less of an issue in the vertical direction; however, the loss of lateral strength is highly dependent on peak lateral displacement which may or may not be represented by the residual drift, but instead by other physically observable damage such as spalling, bar

buckling, and bar fracture. Secondly, this method only provides information on what to do immediately following an event and does not provide any insight on whether the bridge should be repaired moving forward. When deciding whether to repair a structure, it is necessary to understand the performance of the final repaired state and not that of the initially damaged column. For extensively damaged columns requiring plastic hinge relocation, it is assumed that the damage state will be at or above that requiring closure of the bridge initially. Lastly, since a repair is intended to restore functionality of the structure, the performance should be tied to future potential earthquake hazards and not just the ability to carry vertical traffic loads.

The remaining sections of this chapter describe the development of such a tool for use when deciding whether it is safe to implement a plastic hinge relocation repair on a bridge with permanent deformation. The aim is to use a similar approach to that of Mackie and Stojadinovic (Mackie & Stojadinovic, 2004), while addressing the limitations described above.

7.2 Analysis Approach

The framework methodology in which the proposed model is developed utilizes a probabilistic approach, as described by Moehle & Deierlein (2004). The procedure integrates earthquake hazard, structural response, corresponding damage measures, and resulting decision variables to inform stakeholders of potential risks and their associated costs. The probability of each event occurring is combined using the theorem of total probability, and its general form is outlined in Equation 7-1 below.

$$v(DV) = \iiint G\langle DV \,|\, DM \rangle \cdot \left| dG\langle DM \,|\, EDP \rangle \right| \cdot \left| dG\langle EDP \,|\, IM \rangle \right| \cdot \left| d\lambda(IM) \right| \qquad \textit{Equation 7-1}$$

Equation 7-1 defines the mean annual probability of exceeding a certain Decision Variable (DV) as a function of Intensity Measures (IM), Engineering Demand Parameters (EDP), and Damage Measures (DM). While this generalized form represents the framework in which the overall concept is applied, the aim of the analysis presented herein is to describe the likelihood of a repaired structure exhibiting residual drift reaching some EDP when exposed to various levels of earthquake hazard. This relationship is established by means of a probabilistic risk assessment using the results of dynamic nonlinear time history analyses conducted on a structural model representing a bridge column which has been repaired using plastic hinge relocation. The aim of these results is to provide rational means by which to determine the expected performance for a

given structure and hazard, which can then be related to existing damage relationships and, in turn, inform the decision-making process on whether a structure should be repaired using this method. The following sections outline the methods and assumptions made throughout this process.

7.2.1 Engineering Demand Parameters (EDP)

Selection of an EDP should consider the parameter's ability to describe damage of the structure as well as the model's ability to accurately predict the chosen parameter. Each of these factors is necessary to develop a reliable relationship between a given earthquake hazard and the probability of reaching some specified damage limit state. It has been shown that tension strain limits are reliable indicators of structural damage (Goodnight et al., 2015), and the structural model has been shown to accurately predict peak tension strains within the relocated plastic hinge. Therefore, tension strains within the relocated plastic hinge section are selected as the EDP of this study.

7.2.2 Hazard Analysis (IM)

7.2.2.1 Selection of ground motions

Ground motions were selected from the PEER NGA West2 database (https://ngawest2.berkeley.edu) with the intention of representing a wide variety of ground motion intensities. When initially selecting the ground motions, site PGA was used as the primary selection criteria between levels of ground motion, selected at increments of 0.1g ranging from 0.1g to 1.4g. Following the structural analysis, a correlation study was then conducted to determine the most reliable IM to relate to the desired EDP, as discussed in the following section. A full list of the ground motions considered in this study are presented in Appendix A. Note that each ground motion was unscaled when used in analysis and the range of input intensity measure comes only from the variety of ground motions selected. Further discussion of the dynamic analysis procedure is provided in Section 7.3.

A total of 99 ground motions were selected for analysis, resulting in 198 horizontal acceleration records. Furthermore, since the structural model is asymmetric due to the residual drift, each record was analyzed in the positive and negative direction resulting in a total of 396 nonlinear time-history analyses for each structural configuration. Ideally, additional orientations would be included; however, this would further increase the already enormous computational

effort. Additional discussion on the consideration of ground motion directionality is provided in Section 7.2.2.3.

7.2.2.2 Selection of optimal IM

When relating ground motions to structural response parameters, it is crucial to select appropriate quantities that accurately capture their relationship. An extensive discussion of the selection of such intensity measures is provided by Mackie and Stojadinovic (2003), where the authors provide an exhaustive comparison of the suitability of individual IMs to predict various EDPs. In this report, they conclude that the first mode spectral displacement, $Sd(T_1)$, is the optimal IM to predict most EDPs: including local, intermediate, and global parameters (i.e. material stress, moment, and displacement respectively). In this same report, the authors also conclude that strain is a poor EDP on which to predict performance due to large dispersions in the analysis data sets. However, since publication there have been advances in the modeling of plastic hinge forming members to more accurately relate strains to the intermediate and global parameters (i.e. the "Beam with Hinges" element used in the analysis presented here). Therefore, strains are considered adequate performance measures and will be used as the primary EDP in this report.

Figure 7.3 illustrates the correlation between $Sd(T_1)$ and the observed peak tensile strain within each test. Note that this correlation is dependent on the calculation of the first mode period and two such examples are shown (a full procedure for estimating the first mode period is provided in Section 7.2.2.4). The first considers the column length to be the full clear span above the footing ($L = L_C$), whereas the second considers only the effective length above the repair ($L = L_{eff}$). A stronger correlation is shown when $Sd(T_1)$ is calculated from the period considering the full column clear span as opposed to the effective span. While this at first seems counterintuitive, recall that there is a large amount of strain penetration into the repair which serves to soften the structural response, thus lengthening the period.

Figure 7.4 and Figure 7.5 illustrate the correlation of peak tensile strain to other IMs which were considered: maximum spectral displacement (Sd_{max}) and peak ground acceleration (PGA) respectively. While each of these parameters are period independent, and therefore more broadly applicable, they do not correlate as closely with observed damage. Sd_{max} tends to improve in the longer period range, which makes sense as this would more closely align with $Sd(T_1)$; however, PGA remains a very poor predictor of damage universally. Consequently, $Sd(T_1)$ will be used as

the sole ground motion intensity parameter to which damage is related in the remainder of this report.

Note that Figure 7.3 through Figure 7.5 exclude records with observed strains exceeding 0.05, as these structures would be considered "collapsed" within the criteria of this study. In other words, strains greater than 0.05 produce the same binomial result as those equal to 0.05. Furthermore, the collapsed structures exhibited irrationally large strains which disproportionately skewed the results.

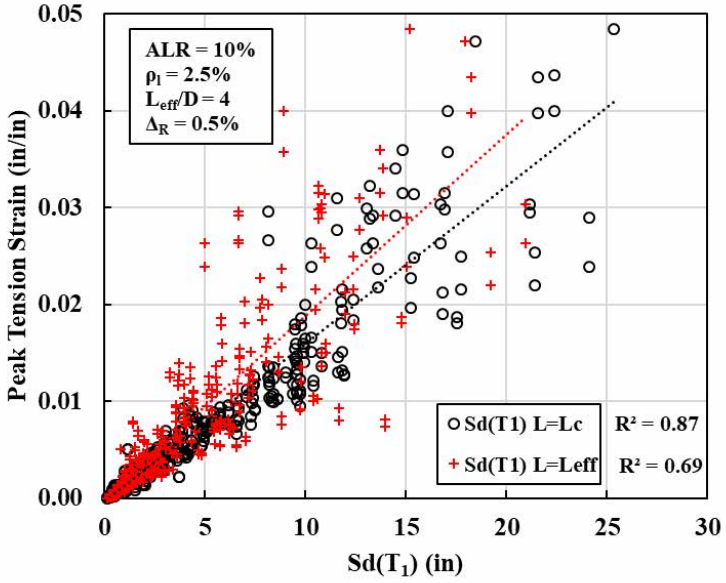

Figure 7.3: Correlation of first mode spectral displacement, $Sd(T_1)$, to peak tensile strain.

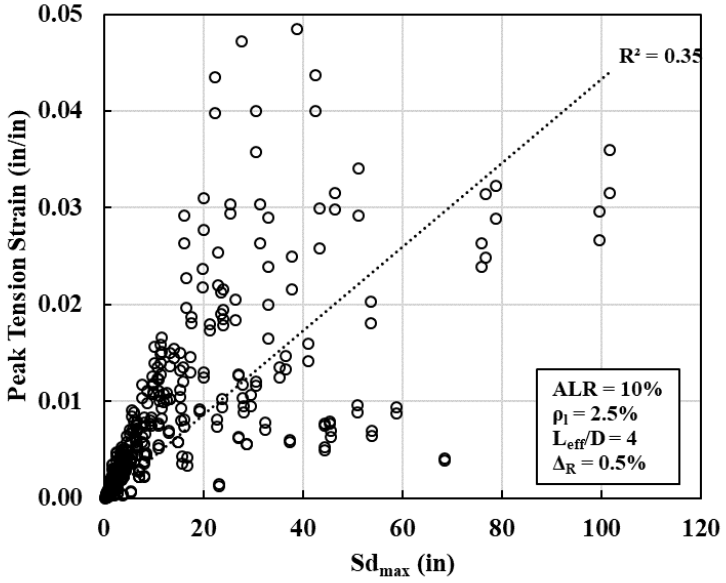

Figure 7.4: Correlation of maximum spectral displacement, Sd_{max}, to peak tensile strain.

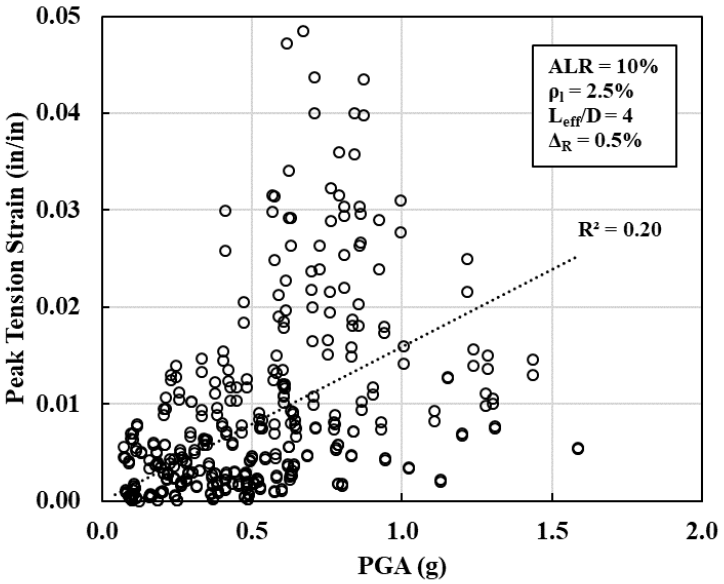

Figure 7.5: Correlation of peak ground acceleration (PGA) to peak tensile strain.

7.2.2.3 Hazard Directionality

The structural model considered in this study is inherently asymmetric due to the residual drift component. Therefore, a given load applied in one direction will not produce the same result if it is applied in the opposite direction. Consider the displacement time histories presented in Figure 7.6 below. Each analysis represents the exact same acceleration record applied to the exact same structure, except with the directions reversed. As a result, an identical hazard results in two different EDPs. In the case shown, the resulting values are: $\varepsilon_{t,max} = 0.039$ when the loading is applied in the negative direction, and $\varepsilon_{t,max} = 0.049$ when applied in the positive direction. Thus, the positive acceleration record triggers a "collapse" of the $\varepsilon_{t,LS} = 0.04$ limit state, but the negative record does not.

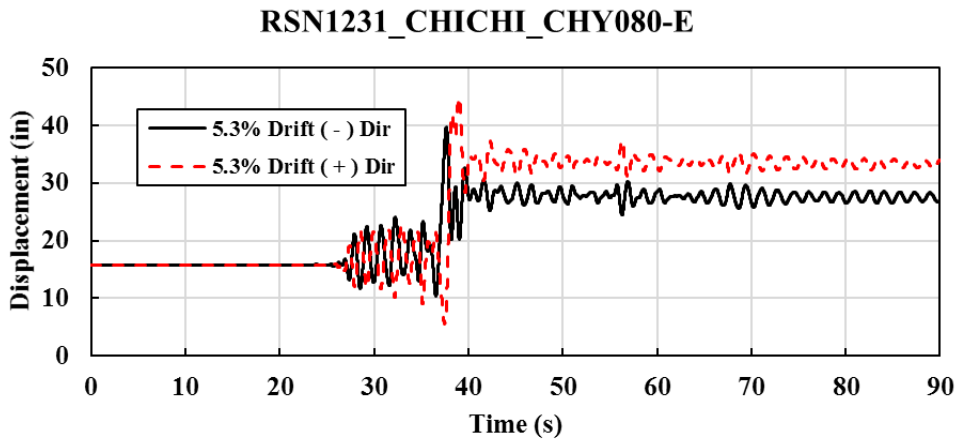

Figure 7.6: Displacement time history comparison between ground motion directionality; L/D = 4, ρ_l = 2.5%, ALR = 10%.

This raises an interesting question when considering how to best relate the analysis results to the anticipated design hazards for which they will be used. It is expected that an IM would be extracted from a code-based design hazard curve, which would then be used to determine the probability of collapse for a given structural configuration and limit state. However, codes are often formulated using different criteria; such as the ASCE7-16 (ASCE, 2016) building design code which is based on the RotD100 spectrum (or maximum site response) and the AASHTO bridge design code (AASHTO, 2017) which is based on the RotD50 spectrum (or mean site response). Therefore, the hazards associated with the ASCE7-16 code are based on the worst-case scenario, whereas those associated with the AASHTO code are based on the mean expected hazard for a given site.

Considering this, it is logical that a fragility function which is developed on the basis of individual record IMs, with the anticipation of relating to hazards defined by a RotD100 based spectrum, should associate the IM only to the *maximum* of the observed EDPs. Alternatively, if relating to hazards of a RotD50 spectrum, the fragility function should relate the IM to the *mean* of the observed EDPs. Otherwise, the resulting fragilities are incompatible with the assumptions of the hazard. To illustrate the impact this can have, consider Figure 7.7 below. Each curve is developed using identical analysis results, with the only difference being whether all EDPs are considered for a given IM (mean case) or if only the maximum value is considered (max case). The result is two distinctly different fragility curves representing different levels of risk.

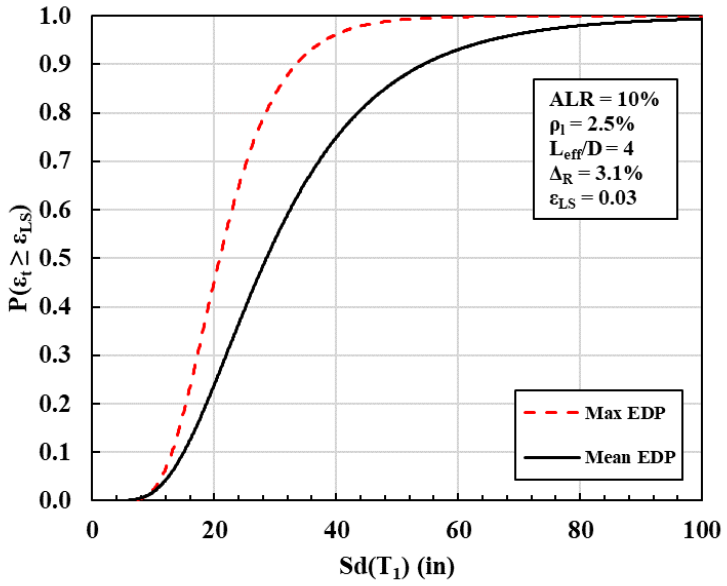

Figure 7.7: Comparison of fragility functions considering max and mean EDP.

Note that this discussion is relevant only to ground motions related to a specific site. Therefore, if two unrelated ground motions share the same IM their resulting EDPs would be considered independently. However, in the case presented here, the only variable is the directionality of the ground motion itself. Arguably, each pair of site ground motions should be considered across a range of combined directions with each resulting IM and EDP combination representing the true range of possible outcomes. Each record would have a corresponding negative counterpart (i.e. 0º and 180º, 45º and 225º, etc) with identical frequency and intensity content, and a resulting pair of EDPs (in the case of asymmetric response).

In this case, it is argued that some determination must be made on how to appropriately represent the associated risk to best reflect that of the assumed design hazard. Priestley et. al. (2007) suggests that when considering the results of both positive and negative directionality of a given ground motion on an asymmetric structure (i.e. that presented here), the average of all EDPs should be taken when considering a design hazard that is based on the average intensity. Therefore, it is established that the fragility functions presented in this chapter consider the mean effect of a ground motion since the expected design hazard will be that of the AASHTO design curve, which is based on the RotD50 site response hazard. This is considered the best course of action given the available literature; however, it is noted that further investigation into the relationship between hazard and fragility definitions is warranted in future research.

7.2.2.4 Estimation of Effective First Mode Period

When using $Sd(T_1)$ as the IM to relate to our EDP, it is first necessary to estimate T_1, and then extract the spectral displacement demand from the design hazard curve. Note that the effective fundamental period should account for the softening of the structure due to the initial loading, as well as the reduction in stiffness due to the geometric nonlinearity introduced by the residual drift. Since the intent of this study is to provide a rapid assessment procedure by which to assess the performance of a bridge which has been repaired using plastic hinge relocation, it is of interest to quickly estimate the first mode period of that structure. This should ideally be done with simple hand calculations as opposed to rigorous structural modeling and modal analysis. The simplified approach proposed in this study is outlined in the following steps.

First, determine the effective stiffness of the column considering the repaired state using Equation 7-2, where: E_c is the elastic modulus of concrete, as calculated in Equation 7-3. I_{eff} represents the effective moment of inertia as determined using the elastic stiffness ratio defined in Figure 7.8 or by any other rational means, and L_c is the total height of the column above the footing. L_c is used instead of L_{eff} to account for the significant strain penetration into the repair. Note that the section stiffness is reduced by half to account for the softening of the steel due to the previous strain history. An additional factor, λ, is included to consider the influence of residual drift on the initial period of the structure as calculated from Equation 7-4. This term assumes that the initial stiffness is reduced by the ratio of the P-Delta moment to the total moment capacity of the column cross section. The yield strain of the steel is also taken to reflect that of the reduced modulus discussed previously.

$$k_{eff} = \lambda \frac{3\left(0.5E_c I_{eff}\right)}{L_c^{\,3}} \qquad \textit{Equation 7-2}$$

$$E_c = \begin{cases} 57{,}000\sqrt{f'_c} & (psi) \\ 4{,}700\sqrt{f'_c} & (MPa) \end{cases} \qquad \textit{Equation 7-3}$$

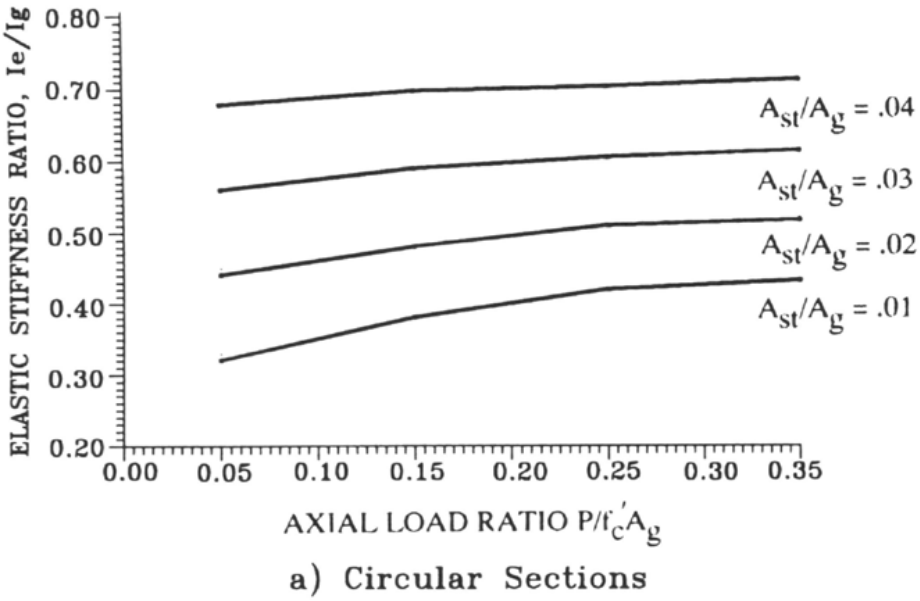

Figure 7.8: Elastic stiffness of cracked reinforced concrete sections; reproduced from (Priestley et al., 1996).

$$\lambda = 1 - \frac{P\Delta_r}{\left(0.5E_cI_{eff}\right)\phi_y} \qquad \textit{Equation 7-4}$$

$$\phi_y = \frac{2.25\varepsilon_y}{D_{col}} \quad \textit{Where:} \quad \varepsilon_y = 0.004 \qquad \textit{Equation 7-5}$$

Once the repaired column stiffness has been calculated, the resulting elastic first mode period is found using Equation 7-6, where *P* is the axial load on the column and *g* is the acceleration due to gravity. While the described method is applicable to SDOF systems, it could be extended in practice to apply to MDOF structures when considering the response of an entire bridge. The stiffness of bents with repaired columns would be described using this method, while undamaged bents would be calculated using traditional means.

$$T_1 = 2\pi\sqrt{\frac{P/g}{k_{eff}}} \qquad \textit{Equation 7-6}$$

7.2.3 Structural Analysis

The structural analysis model described in Chapter 6 was used as the basis of the model for this study. The scope of this study is limited to two-dimensional analysis of a single bending

column; however, multiple configurations are considered, as will be discussed in Section 7.2.3.1. The following sections outline the specific modeling considerations for this study, and the selected structural parameters to be investigated. All structural modeling is carried out using the OpenSEES platform (McKenna et al., 2000).

7.2.3.1 Analysis Matrix

To establish a meaningful set of data which can be used in a general sense, it is necessary to understand the impact of residual drift for a wide variety of structures. The parameters assumed to have the largest impact on a structure's performance when considering residual drift are: 1) L/D ratio, 2) longitudinal steel ratio (ρ_l), and 3) Axial Load Ratio (ALR). Table 7.3 outlines the values considered for each parameter, along with the increments of residual drift that were analyzed. Other parameters held constant during each analysis included: 1) D_{col} = 60in, 2) D_{rep} = 80in, 3) $L_{rep} = D_{col}$, 4) f'_{ce} = 5.2 ksi, 5) f_{ye} = 66 ksi, and ρ_v = 1.1%. The dimensions of the repair were calculated to provide similar height and proportion of repair annulus area to gross column area as considered in experimental tests. Also, note that the L/D ratio is calculated from the repaired effective length of the column (L_{eff}) from the top of the repair to center of superstructure mass, as opposed to the original column height.

Each combination of structural parameters was considered, for a total of 48 unique cases. Every increment of residual drift was then analyzed for each structure, resulting in a total of 480 cases for each acceleration record. With a total of 99 ground motions, each considered in 4 directions, this comes to a total of 190,080 NLTH analysis runs required.

Table 7.3: Structural analysis parameter matrix.

Δ_r (%)	0.5, 1.0, 1.5, 2.0, 2.5, 3.0, 3.5, 4.0, 4.5, 5.0
L/D Ratio	2, 4, 6, 8
ρ_l (%)	0.01, 0.025, 0.04
ALR ($P / f'_{ce}A_g$)	0.05, 0.1, 0.15, 0.2

7.2.3.2 Structural Model

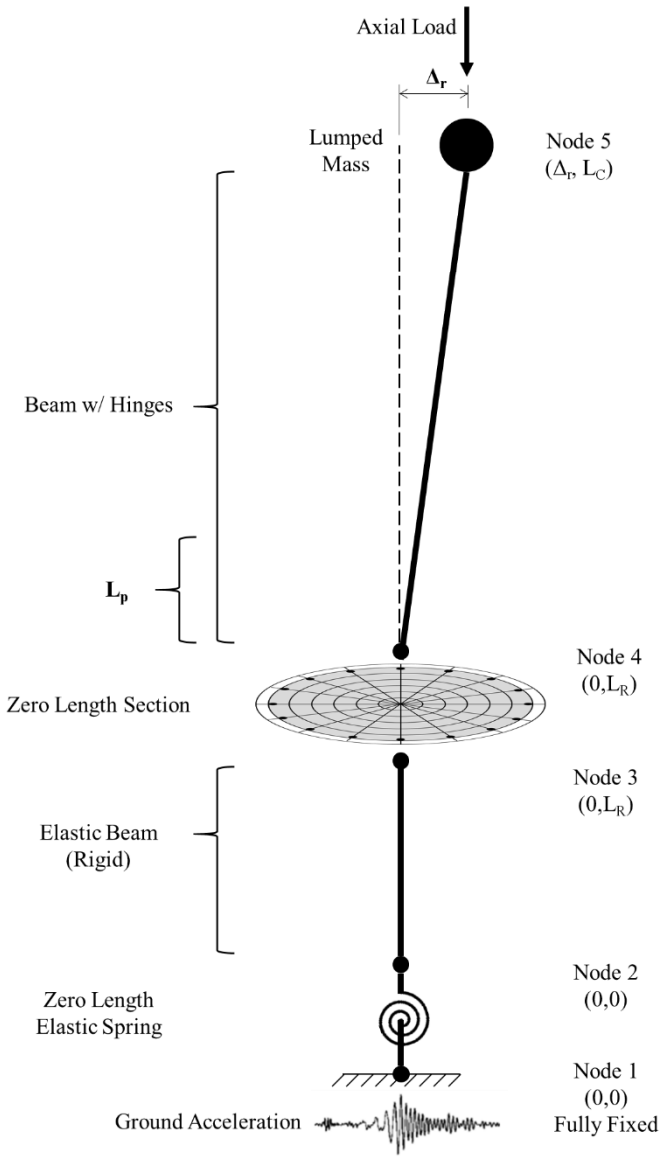

Figure 7.9: Schematic of structural analysis model used in residual drift study.

The basic schematic of the model used in this study is illustrated in Figure 7.9 above. The general configuration is the same as that presented in the previous chapter, with some

modifications to account for the specifics of this study. First, the model described in the previous chapter was based on a pseudo-static loading procedure to match the experimental tests, which did not consider inertial or P-delta effects. The superstructure mass is lumped at the top node and axial load is applied as an external static force in the negative Y-direction prior to beginning the dynamic analysis. P-delta effects are considered in the analysis, as these are assumed to be a key factor in capturing the effects of excessive residual drift on the response of the system. Also, the geometric nonlinearity associated with the residual drift is initially modeled into the system by offsetting the top node as shown in the figure. This is a requirement of the modeling approach since the repair is not "activated" following an initial analysis, as discussed in the previous chapter. Furthermore, by directly modeling the residual drift, the initial conditions are not dependent on the variability associated with capturing residual drift with nonlinear analysis, as discussed earlier in this chapter.

One drawback to this approach is that the initial strain condition at the new plastic hinge is not directly known. The softening of the steel due to prior yielding is accounted for through modification of the material model, as described in the previous chapter; however, there is also the potential for residual strain from the prior loading as well. While this is not directly accounted for, it is assumed that any residual strain would be negligible as they would tend to concentrate within the original plastic hinge. Additionally, the initial application of axial load does impart some flexural strain from P-delta effects which are likely on the order of what would be expected in the new hinge location. It should also be noted that this initial application of load results in some lateral deflection due to the offset of the top node, which varies for different structural configurations. Therefore, the final lateral displacement reached upon application of the axial load is considered the "true" residual drift of the system.

To illustrate the model's capability of capturing the effects of residual drift, consider Figure 7.10 through Figure 7.12 below. Each figure compares different response quantities of a column with L/D = 4, ρ_l = 2.5%, ALR = 10% for varying residual drifts. Figure 7.10 shows the displacement time history response for the column at 0%, 3.1%, and 5.3% residual drift. Note that at 0% residual drift, the final structure comes to rest with a negative displacement, whereas for the columns at 3.1% and 5.3% the ground motion pushes the column further in the positive direction of the initial residual drift with increasing ratcheting effect for larger residual drifts.

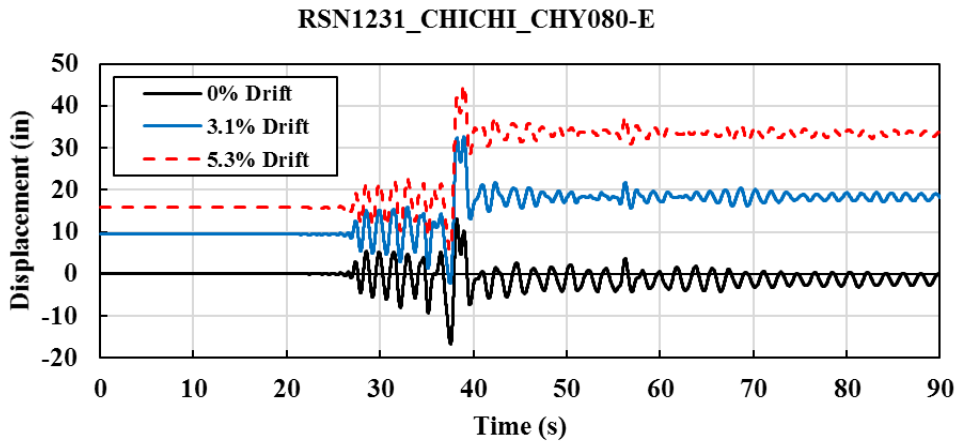

Figure 7.10: Displacement time history comparison for different residual drifts; L/D = 4, ρ_l = 2.5%, ALR = 10%.

Figure 7.11 shows the global force vs. displacement response of the same columns. Note the effect of the P-delta force on the overall structural response of each column. As the residual drift increases, the effective strength and stiffness of the column decreases. Eventually, this strength loss leads to instability and collapse of the structure which is captured by irrationally large displacements in the data output.

Figure 7.12 illustrates the effect of residual drift on the strain demand within the new plastic hinge. As the residual drift increases, the strain demand in the plastic hinge also generally increases for the same ground motion due to the reduced effective stiffness of the column from P-delta effects. This results in reaching strain limit states earlier for columns with larger residual drifts, as would be expected. However, while this is generally the case, there were instances in which greater residual drift actually resulted in less strain demand within the column. This is likely due to the dynamic nature of the analysis and the structural period's dependence on residual drift. As a result, the softened structure could push the response to a lower intensity frequency of the ground motion and result in less demand.

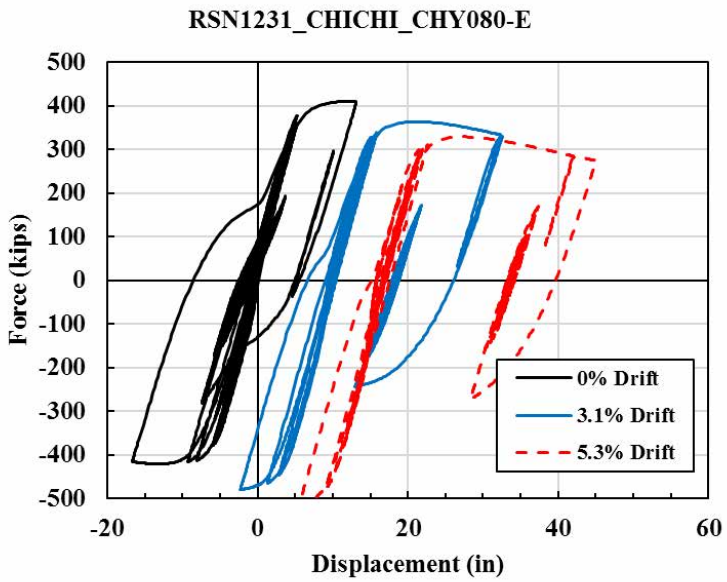

Figure 7.11: Force vs. displacement hysteresis comparison for different residual drifts; L/D = 4, ρ_l = 2.5%, ALR = 10%.

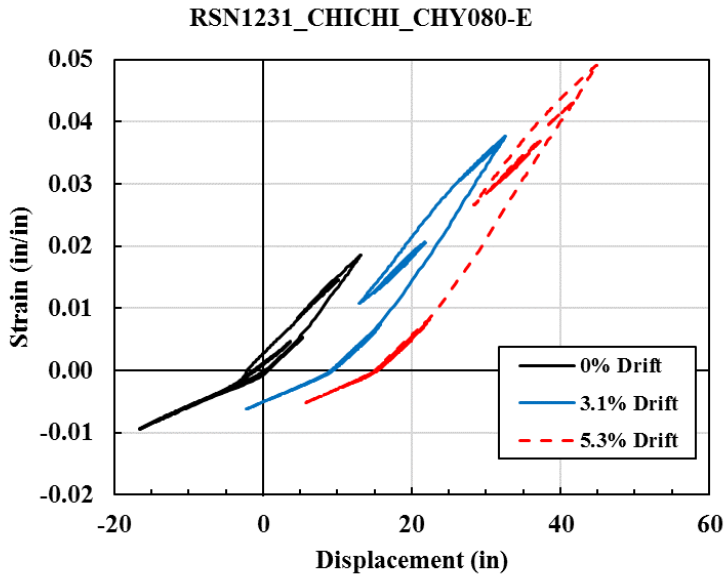

Figure 7.12: Strain vs. displacement comparison for different residual drifts; L/D = 4, ρ_l = 2.5%, ALR = 10%.

7.3 Development of Fragility Functions

Once the analysis is complete, the data is then post processed to determine the resulting fragilities. A multiple stripes analysis (MSA) procedure was used to fit fragility curves to the raw data, as described by Baker (2015). A summary of this procedure is provided as follows: At each intensity level, x_j, the probability, P, of observing z_j collapses in n_j observations is given by the

binomial distribution, as shown in Equation 7-7, where p_j is the probability of a single ground motion with $IM = x_j$ to cause collapse of the structure.

$$P = \binom{n_j}{z_j} p_j^{z_j} \left(1 - p_j\right)^{n_j - z_j} \qquad \textit{Equation 7-7}$$

Note that "collapse" of the structure does not necessarily mean collapse in a traditional sense, but just that a specified limit state has been exceeded. To consider the overall likelihood of observing multiple instances of this distribution across multiple IM levels, the product of this distribution is taken for each IM level considered, as shown in Equation 7-8.

$$Likelihood = \prod_{j=1}^{m} \binom{n_j}{z_j} p_j^{z_j} \left(1 - p_j\right)^{n_j - z_j} \qquad \textit{Equation 7-8}$$

A lognormal cumulative distribution function (CDF) is used to define the fragility function and is substituted for p_j. This explicitly states the fragility function parameters within the function; in this case the median of the fragility function, θ, and the standard deviation of *ln(IM)*, β (also referred to as the dispersion of IM). Furthermore, the solution is simplified by taking the natural log of each side, thus reducing the product formulation to a summation which is computationally more efficient. The resulting function is that described by Equation 7-9.

$$\left\{\hat{\theta}, \hat{\beta}\right\} = \arg\max_{\theta,\beta} \sum_{j=1}^{m} \left\{ \ln\binom{n_j}{z_j} + z_j \ln\Phi\left(\frac{\ln\left(x_j/\theta\right)}{\beta}\right) + \left(n_j - z_j\right)\ln\left[1 - \Phi\left(\frac{\ln\left(x_j/\theta\right)}{\beta}\right)\right]\right\}$$

Equation 7-9

In this final equation, n_j, z_j, and x_j are all defined via the analysis results, and θ and β are the only unknowns. These two unknown parameters are then optimized using numerical solution techniques to find the values that produce the highest probability of observing the analysis results. Several analysis tools for conducting this optimization, including Excel spreadsheets and Matlab codes, are provided in the appendices of the paper by Baker (2015) and were used to produce the analysis results presented in this study.

The MSA procedure was selected over traditional incremental dynamic analysis (IDA) primarily because unscaled ground motions were used in the analysis. The MSA procedure is particularly well suited for this type of analysis because each IM level does not require multiple observations (i.e. n_j can be equal to one). In this case, each record is considered individually and

either does or does not cause a collapse. An example of curves fit to the analysis data for the limit states of ε_t = 0.02 and 0.04 is shown in Figure 7.13 for a structure with 0.5% residual drift, ALR = 10%, L/D = 4, and ρ_l = 2.5%.

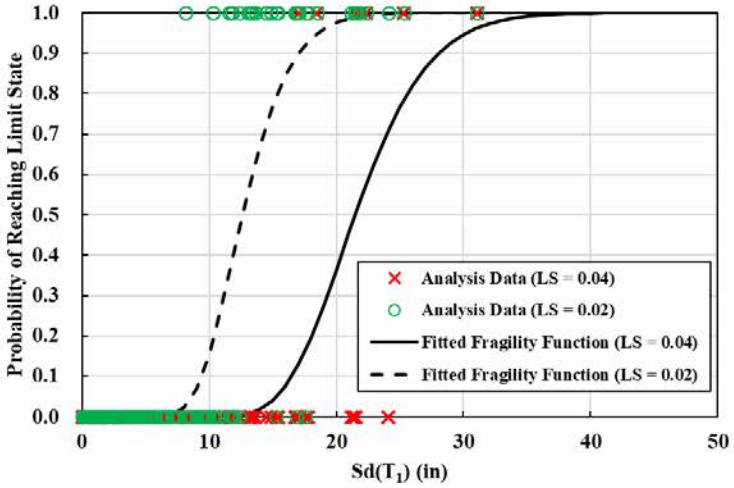

Figure 7.13: Example of fragility fitting to analysis data using MSA procedure.

7.4 Analysis Results

In general, columns with large L/D ratios were shown to be the most sensitive to residual drift when compared to those with small L/D ratios. This intuitively makes sense, as an equal percentage of drift for a longer column results in a larger P-Delta moment, and thus more disproportionately affects the relative strength and stiffness of the member. Consider the plots in Figure 7.14. Each shows the fragility functions calculated for a limit state of 3% strain and columns of equal ρ_l and ALR, but varying L/D ratios and residual drifts ranging from 0.5% to 5% (Note each plot shows a slight different range of residual drift due to the initial increase from axial load application. The "true" residual drift is shown, which represents the state after axial load is applied, but before the dynamic analysis is performed). As L/D increases, the spread between each fragility function also increases, indicating a greater influence of residual drift. For example, a column of L/D = 2 shows almost no difference in performance regardless of residual drift. However, if that same column had an L/D of 8 the difference in performance could be as great as 95% between columns with residual drift of 0.6% and 6.2%.

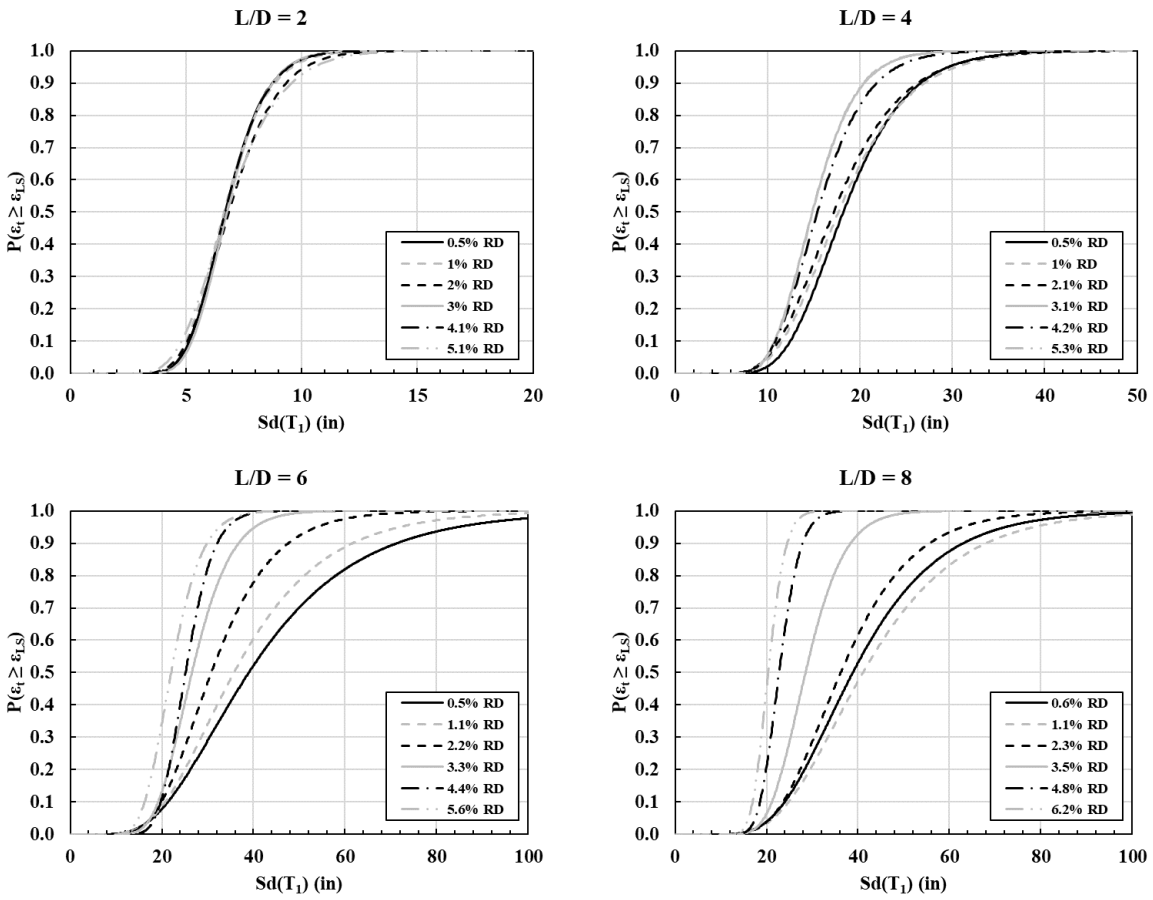

Figure 7.14: Influence of L/D on residual drift sensitivity for ε_{LS} = 0.03, ALR = 10%, ρ_l = 2.5%.

Increasing ALR tended to have a similar effect to that of L/D in that a larger axial load increased the dependence on residual drift, as shown in Figure 7.15. Note also that increasing the mass for a given column stiffness will serve to also increase the period, and thus increase the spectral displacement demand. Therefore, the hazard demand for a structure of larger mass will be further to the right on the x-axis; however, as the mass increases there is also a noticeable shift of the fragility functions towards the left. Thus, additional mass not only increases the hazard demand, but also reduces the capacity of the structure to resist that demand.

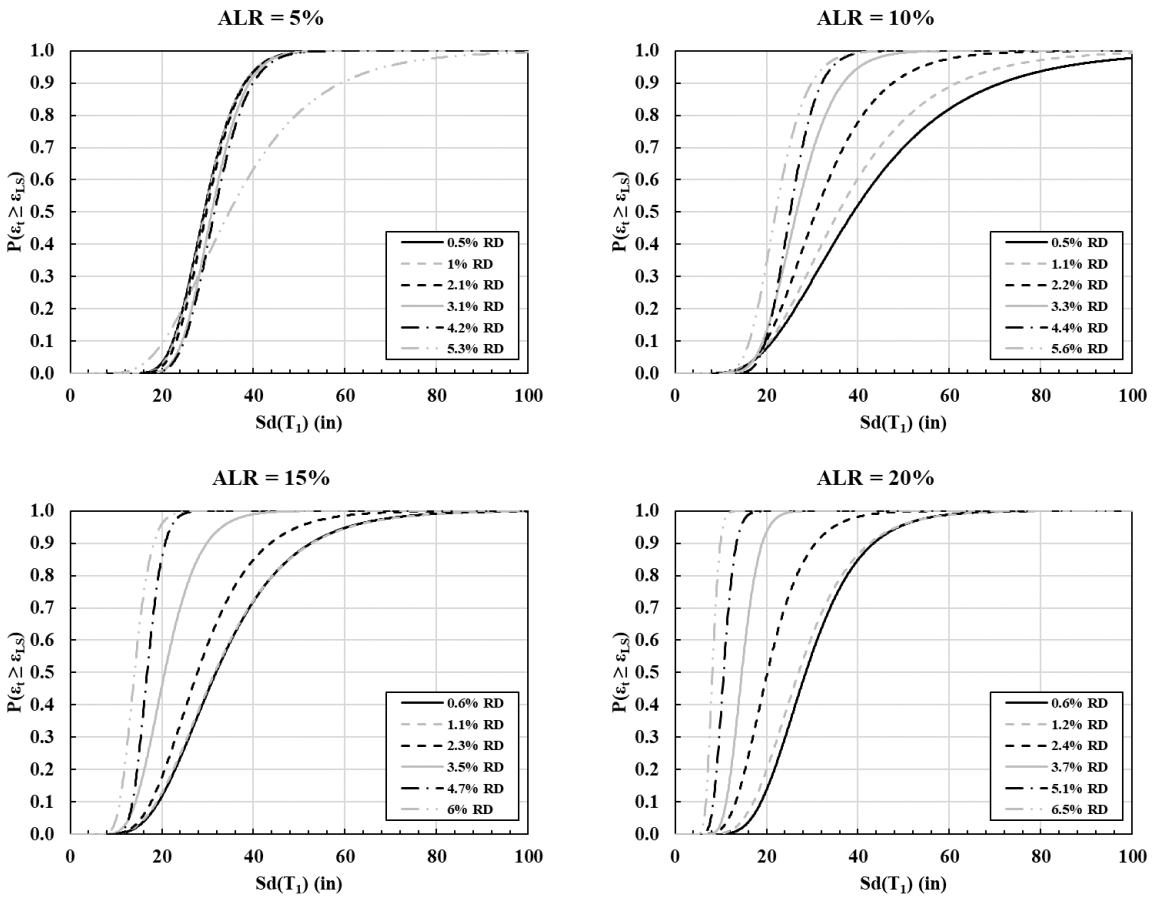

Figure 7.15: Influence of ALR on residual drift sensitivity for ε_{LS} = 0.03, L/D = 6, ρ_l = 2.5%.

Lastly, Figure 7.16 demonstrates the impact of ρ_l on the fragility of each system. This parameter does not much affect the sensitivity of residual drift on the performance of the structure, but instead serves to shift the curves along the hazard axis. This, again, makes intuitive sense as additional steel will add strength to the cross section, and thus reduce the likelihood of exceeding a given strain demand for a given hazard. Furthermore, additional steel has the opposite effect of additional mass, as it will increase the stiffness and therefore reduce the period. Thus, with more steel, the fragility curve will shift to the right, but the hazard demand will also likely decrease to the left.

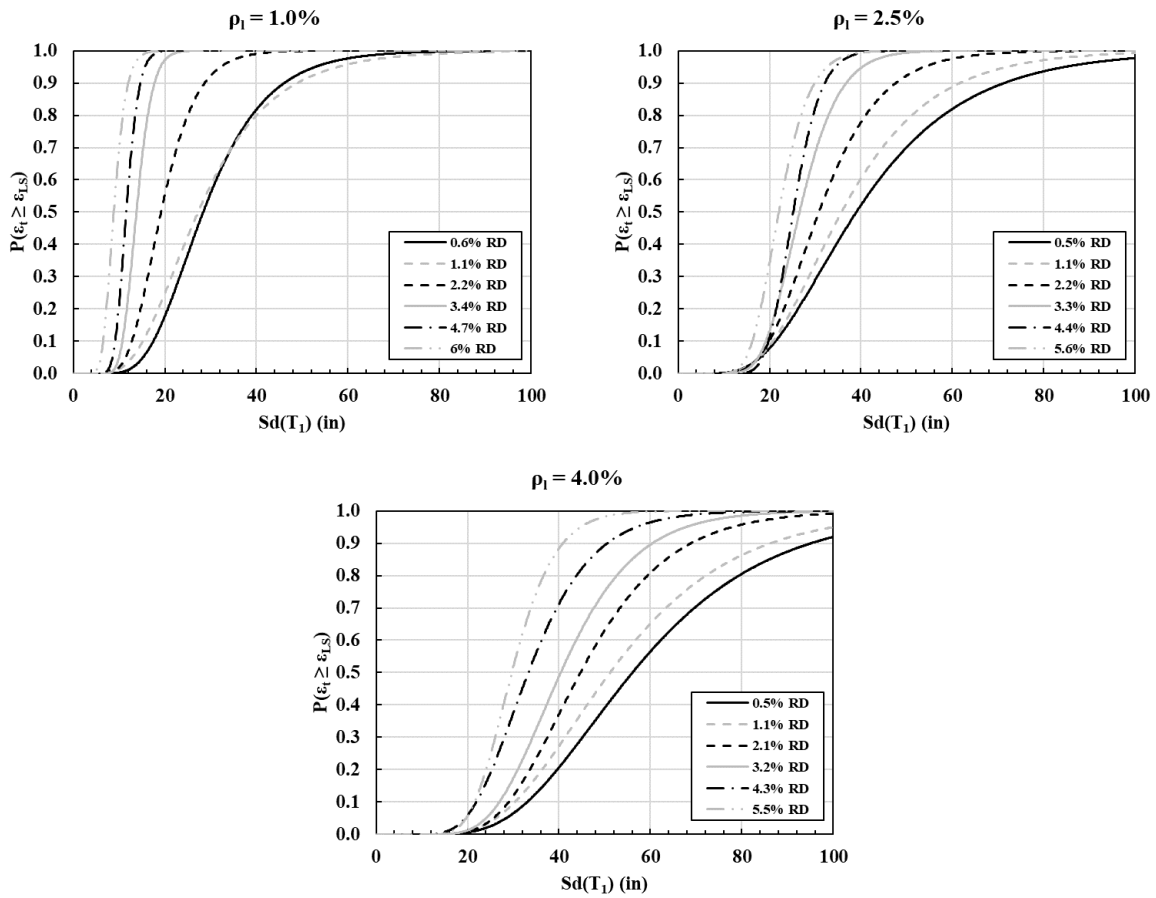

Figure 7.16: Influence of ρ_l on residual drift sensitivity for ε_{LS} = 0.03, L/D = 6, ALR = 10%.

The results presented in this section are intended to provide an overview of the analysis conducted and discuss the impact of the parameters considered. A full presentation of the analysis results for all parameter combinations and limit state considerations is provided in Appendix B.

7.5 Application Example

To demonstrate how the information provided by this analysis is useful, consider the following scenario. A bridge located in Aleknagik, AK has been damaged from an earthquake and is presented to a design engineer with the information outlined in Figure 7.17. The engineer must make the decision as to whether it is safe to repair the bridge considering there is a 3% residual displacement in the column. For the sake of this example, we will only consider the single column and not the effect of the entire structure.

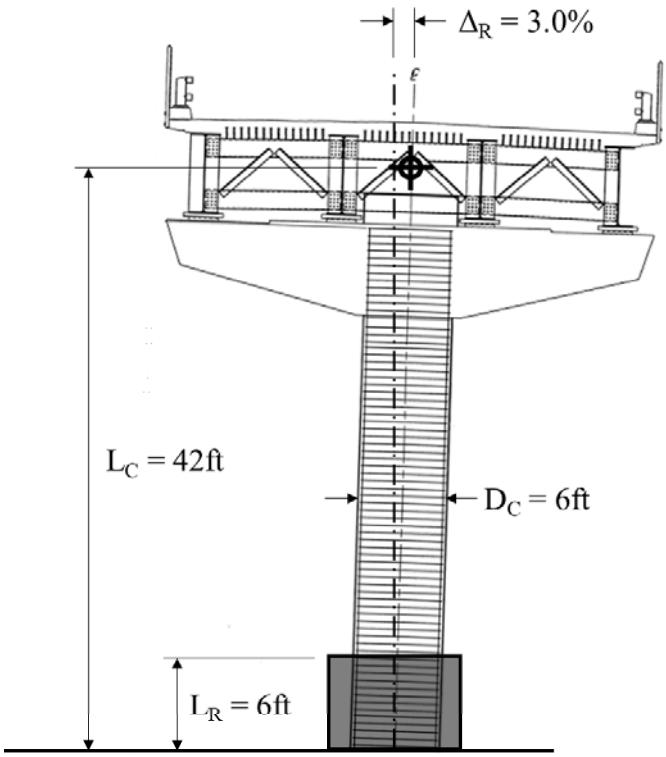

Structural Parameters:

ALR = 10%

ρ_l = 1.4%

L/D = 6

Site Hazard (AASHTO):

PGA = 0.08g

S_s = 0.17g

S_1 = 0.09g

T_0 = 0.103s

T_S = 0.515s

Figure 7.17: Example damaged bridge structural and hazard parameters.

First, we must calculate the effective period of the structure. The associated calculations are carried out in Equation 7-10 through Equation 7-17

$$\frac{I_{eff}}{I_g} = 0.39 \qquad \textit{Equation 7-10}$$

$$I_{eff} = 0.39\frac{\pi D_c^4}{64} = 510{,}000 in^4 \qquad \textit{Equation 7-11}$$

$$E_c = 57{,}000\sqrt{f'_c} = 57{,}000\sqrt{1.3 \cdot 4{,}000} = 4{,}100 ksi \qquad \textit{Equation 7-12}$$

$$P = ALR \cdot f'_c A_g = 0.1\left(1.3 \cdot 4{,}000\right)\left(\frac{\pi D_C^2}{4}\right) = 2{,}100 kips \qquad \textit{Equation 7-13}$$

$$\phi_y = \frac{2.25\varepsilon_y}{D_C} = \frac{2.25(0.004 \cdot 1.1)}{72} = 0.00014\frac{1}{in} \qquad \textit{Equation 7-14}$$

$$\lambda = 1 - \frac{P\Delta_r}{(0.5E_c I_{eff})\phi_y} = 1 - \frac{(2{,}100)(0.03 \cdot 42 \cdot 12)}{0.5(4{,}100)(510{,}000)(0.00014)} = 0.78 \qquad \textit{Equation 7-15}$$

$$k_{eff} = \lambda \frac{3(0.5E_c I_{eff})}{L_c^{\,3}} = 0.78\left(\frac{3(0.5)(4{,}100)(510{,}000)}{(42 \cdot 12)^3}\right) = 19.1\frac{kip}{in} \qquad \textit{Equation 7-16}$$

$$T_1 = 2\pi\sqrt{\frac{P/g}{k_{eff}}} = 2\pi\sqrt{\frac{2{,}100/386}{19.1}} = 3.4s \qquad \textit{Equation 7-17}$$

With this period, we can then determine the site spectral acceleration demand for the first mode period of the repaired structure, which comes to a value of 0.027g. Since most codes use acceleration response spectra to define the hazard curve, we must convert this value to a spectral displacement. This can be done using the relationship defined in Equation 7-18. This results in a spectral displacement demand of approximately $Sd(T_1) = 10.5in$.

$$S_d = \frac{S_a}{\omega^2} = \frac{S_a T^2}{4\pi^2} \qquad \textit{Equation 7-18}$$

With the site hazard established, we can now use the fragility plots to determine what the probability of collapse in a future design level earthquake is if we repair the column using plastic hinge relocation. Since the exact curves for 1.4% steel and 3% residual drift are not available, we will conservatively use the 1% and 3.4% curves respectively. Interpolation between bounding plots is also an option but is not shown here for simplicity. Figure 7.18 shows the fragility curves for this system. Here it can be seen that for the hazard in Aleknagik, AK there is approximately 90% chance of exceeding $\varepsilon_t = 0.01$ in a future design level earthquake, but less than 10% chance of exceeding $\varepsilon_t = 0.03$. However, if the same bridge was located in Juneau, AK the resulting $Sd(T_1)$ would be approximately 24.5in and the bridge would be almost certain to exceed all of the strain limit states.

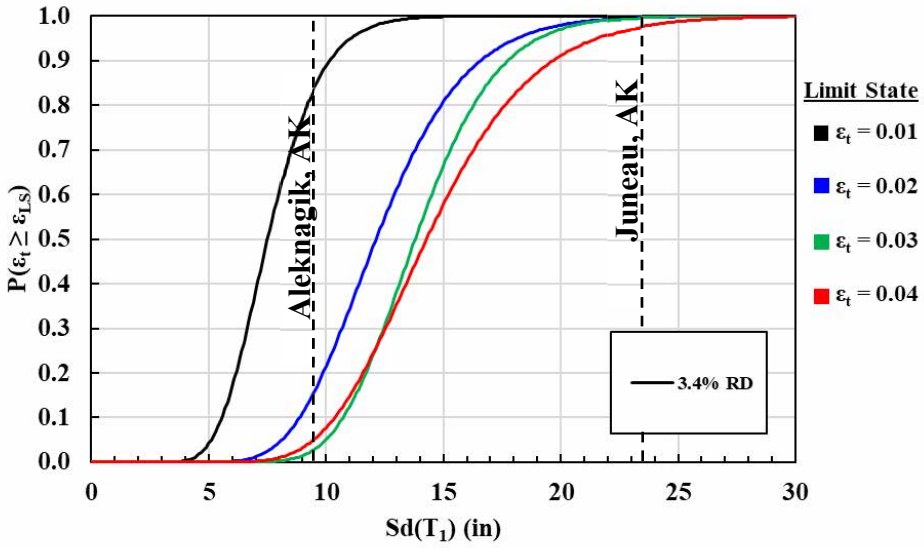

Figure 7.18: Limit state fragility curves for columns with 3.4% residual drift, ρ_l = 1.0%, ALR = 10%, and L/D = 6.

Now consider the same bridge, but if it were to have only a 1.1% residual drift. This would reduce the first mode period to 3.20s and the *Sd(T1)* of Aleknagik and Juneau would become 9in and 22in respectively. We would then use the curves presented in Figure 7.19 to determine the fragility of the system with the reduced residual drift. In this case, the structure in Aleknagik has reduced its probability of exceeding ε_t = 0.01 to approximately 25%. Furthermore, the same bridge in Juneau now only has a 30% probability of exceeding ε_t = 0.03.

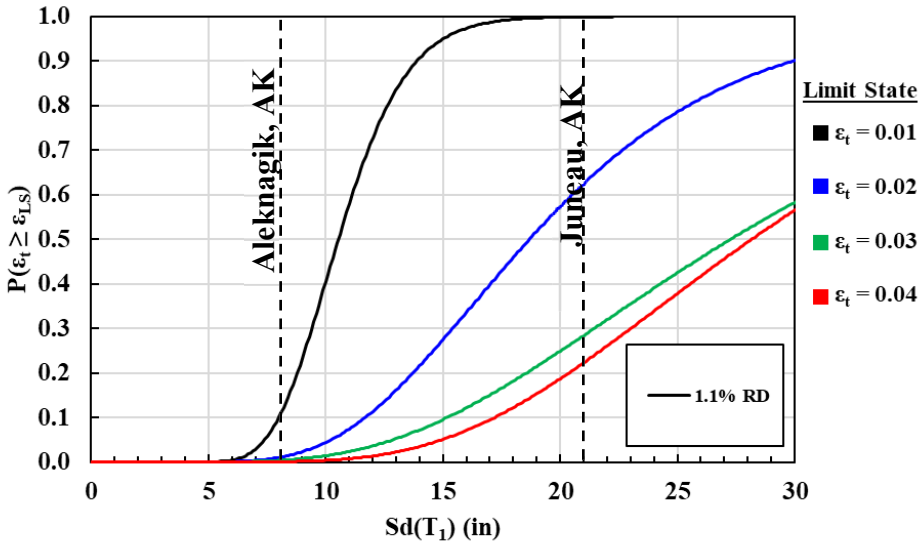

Figure 7.19: Limit state fragility curves for columns with 1.1% residual drift, ρ_l = 1.0%, ALR = 10%, and L/D = 6.

7.6 Conclusions

This chapter presents the development of a tool which engineers can use to assess the potential performance of a repaired RC column considering there is residual displacement due to the initial earthquake loading. The intent of this tool is to provide a rational means by which to decide whether a structure is beyond the scope of repair given its global damage state. Detailed discussion is provided on the development of probabilistic fragility functions which can be used for various structural configurations, site hazards, and levels of residual drift to determine the probability of exceeding a given limit state in a future design level earthquake. It is shown that for a given structure, the potential risk of repair can vary a great deal between site hazards and levels of residual drift, but the use of this method provides a quantifiable basis on which to make repair decisions in a post-earthquake environment. The analysis presented in this chapter is limited to consideration of a plastic hinge relocation repair and should also be limited to columns with buckled bars, unless specific measures are taken to ensure anchorage of fractured bars.

Chapter 8: Conclusions and Future Work

The research described in this report has aimed to develop a rapid repair solution for extensively damaged reinforced concrete bridge columns via a method called plastic hinge relocation. An experimental program was conducted in which six large scale RC bridge columns were subjected to varying levels of damage and repaired using this method. An analytical design model was then developed based on the outcomes of these experimental tests, which was also extended to a computational model using the open source structural software OpenSEES (McKenna et al, 2000). Finally, a numerical study was completed in which the influence of residual drift on the performance of a repaired column was investigated. The following sections summarize each phase of this research and highlight key observations made throughout. The final section outlines recommendations for future research related to this topic.

8.1 Experimental Program

The experimental study consisted of the repair of six large-scale reinforced concrete bridge columns using the plastic hinge relocation method. The repair strategy addressed in this report specifically considers the use of traditional RC materials such as steel rebar, flat plate steel sleeves, commercially available two-part epoxy and prepackaged grout, and ready-mix concrete. The intent is to provide a solution which could be rapidly implemented with materials that most transportation departments have broad experience with and would have readily available. The original columns were constructed and initially tested as part of a previous research program which investigated the influence of bidirectional load histories on the development of strain limit states and plastic hinge length equations for circular RC columns (Goodnight et al, 2017). Table 8.1 summarizes the parameters and performance of each repair test.

Table 8.1: Summary experimental test matrix and results.

	Repair #:	1	2	3	4	5	6
Original Column	Long. Steel ρ_l	(16) #7 2.1%	(16) #7 2.1%	(16) #7 2.1%	(16) #6 1.6%	(16) #6 1.6%	(16) #7 2.1%
	Trans. Steel ρ_v	#3 @ 2in.	#3 @ 2in.	#3 @ 2in.	#3 @ 2.75 in.	#3 @ 2in.	#3 @ 1.5in.
	Δ_{max} (in.)	8.24.	8.25	8.24	7.35	8.57	8.83
	F_{max} (kips)	79.9	78.0	77.7	62.4	64.2	79.9
	$\mu_{\Delta,max}$	6	6	6	6	7	6.5
	Damage State	All long. bars buckled	3 extreme fiber bars on N & S faces fractured, all other bars buckled	All long. bars buckled, spiral fracture, initial torsional deformation	Extreme fiber bar on S face fractured, all other bars buckled	2 bars on E face and 1 on W face fractured, all others buckled, 1.5% residual drift in W direction	3 extreme fiber bars on N & S faces fractured, all other bars buckled
Repair	Repair Configuration	(12) #10; 11ga A36 steel sleeve; Grout	(12) #10; 11ga A36 steel sleeve; Grout	(16) #7; 11ga A36 steel sleeve; Grout	(12) #7; #3 @ 1.5in; Concrete	(16) #7; 11ga A36 steel sleeve; Concrete & bar anchors	(12) #10; 11ga A36 steel sleeve; Concrete & shear key mechanism
	Δ_{max} (in.)	8.31	8.28	6.88	7.51	5.0	8.9
	F_{max} (kips)	95.1	86.2	80.6	75.4	73.2	93.1
	$\mu_{\Delta,max}$	6	6	5	6	4	6.5

The following items highlight key observations made over the course of the experimental program:

1. The first, and most readily apparent, conclusion is that the repair does relocate the plastic hinge as intended in columns with extreme levels of damage. This was observed visibly in each repair test, as the original column deformed and eventually failed through bar buckling and fracture of the longitudinal steel above the top plane of the repair. Figure 8.1 illustrates the typical damage progression observed for each test.

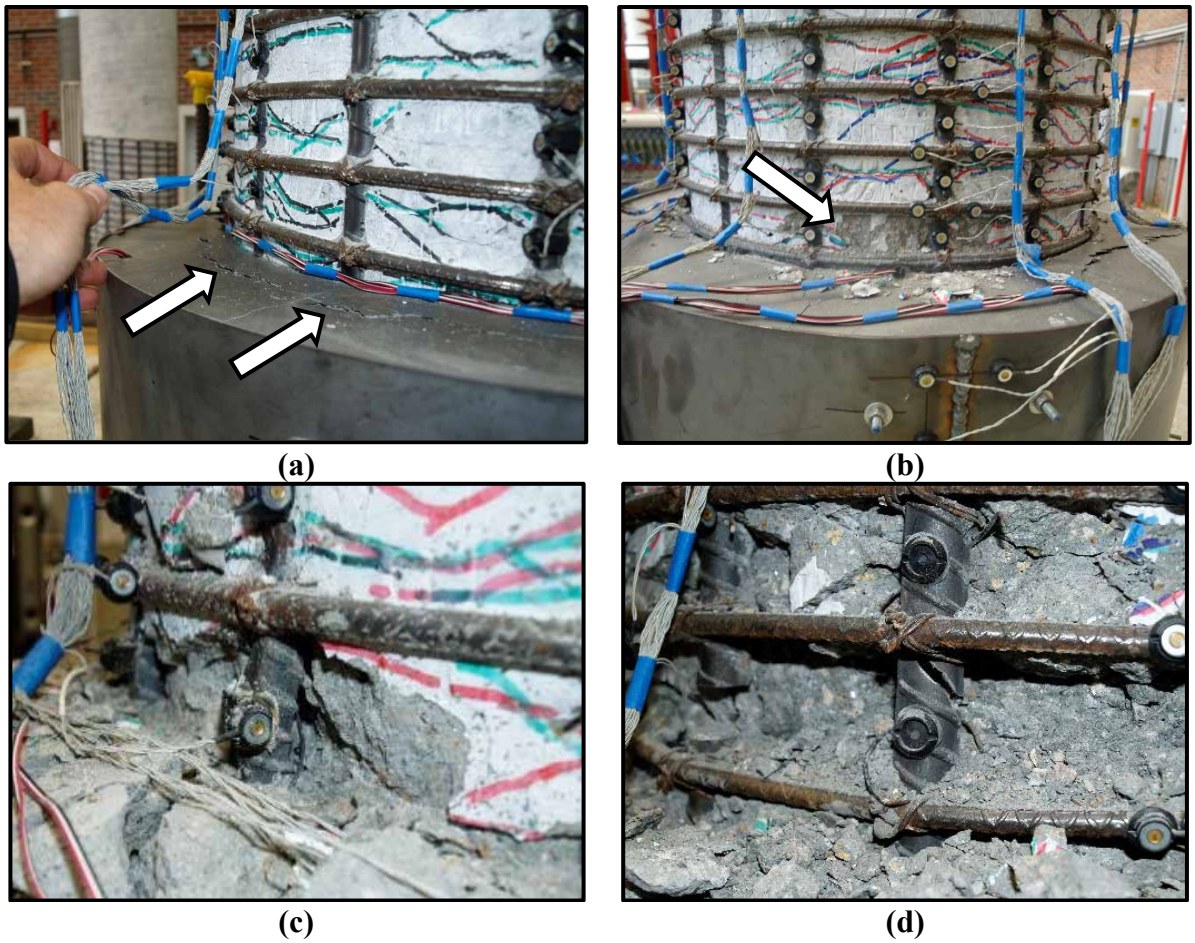

Figure 8.1: Typical damage progression of column with relocated plastic hinge: (a) Initial cracking, (b) core crushing, (c) bar buckling, and (d) bar fracture.

2. One of the primary design assumptions when first implementing this repair was that the enlarged cross section would respond in flexure, and thus traditional moment-curvature analysis could be used to predict the demand on the repair bars. However, this was not the case as evident from the analysis of Repair #1 strain data. Instead, the original column bars were found to have far greater strains than the repair bars despite their location closer to the neutral axis. An example of this is shown in Figure 8.2 where the strains in the original column bars (S O-1) are much larger than those in the repair bars (S R-4) at the same cross section plane. While this is good in the sense that it results in a lower demand on the repair, and thus less steel, it poses a problem that the basic design assumption is not correct. However, this issue is thoroughly addressed and accounted for in the development of the analytical design model.

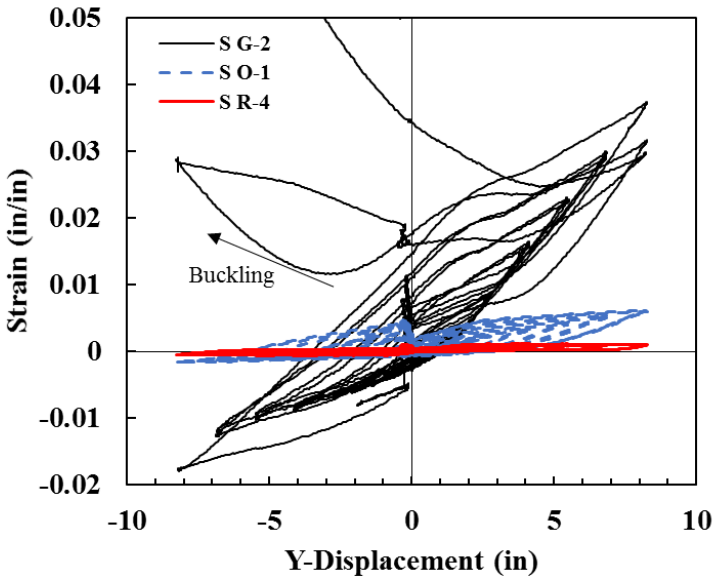

Figure 8.2: Strain vs. displacement profiles of longitudinal bars in relocated hinge (S G-2), original bars at footing interface (S O-1), and repair bars at footing interface (S R-4).

3. The repair performed well for both buckled and fractured longitudinal bars in the damaged section; however, it was observed that fractured bars tended to debond from within the repair as the test progressed to larger ductilities. This resulted in the softening response and pinching behavior observed in Figure 8.3 (b), whereas columns with only buckled reinforcement tended to gain strength until eventual failure, as shown in Figure 8.3 (a). Considerations for this behavior were made in Repairs #5 and #6, where the bars were specifically treated to improve bond conditions. Examples of these methods include fully stripping the surrounding concrete from the fractured bar, as recommended by (ACI Committee 546, 2014), and application of a mechanical headed stud to fully anchor the bar inside the repair. These methods are illustrated in Figure 8.4 (a) and (b) respectively.

   It is recommended that only the mechanical headed stud be considered if the strength of the fractured bar is required, as this was the only method that reliably developed the strength of the fractured bar. With that said, it is also noted that it may be more economical to simply leave fractured bars untreated and allow them to debond in the event of future lateral loading, assuming they only account for a relatively small percentage of the overall longitudinal steel. This would reduce the overall force demand on the system, which will already be larger due to the reduced effective shear span, and it did not have a negative impact on the displacement

capacity of the repaired column. However, if this course of action is considered, it is critical to ensure that the capacity of the repaired column is sufficient to achieve the intended design strength and displacement demands.

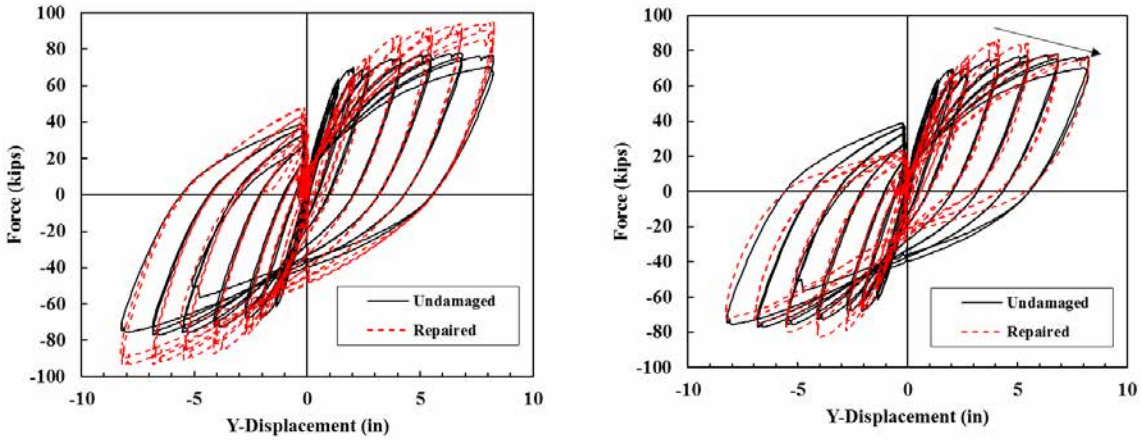

Figure 8.3: Force vs. displacement response of repaired column with (a) only buckled steel, and (b) fractured steel.

Figure 8.4: Examples of fractured bar anchorage mechanisms considered.

4. Each repair restored, or came very close to restoring, the original displacement capacity of the undamaged column test. This was surprising, as it was expected that the repaired column would have a reduced displacement capacity due to the shortened span, which would, in turn, result in a larger rotation and strain demand on the plastic hinge. However, it was observed that the relationship between top of column displacement and strains in the plastic hinge were almost identical between original and repaired columns. This discrepancy is attributed to much larger strain

penetration into the repair than initially anticipated. This is considered in the development of the analytical design model and therefore accounted for in the final design recommendations.

The one exception to this observation, aside from Repair #5 in which weld of the sleeve failed, was Repair #3 which involved cutting bars *above* the repair to reduce the force demand on the repaired system. As a result, this practice is not recommended unless there is a direct need to do so to maintain capacity protection of the system.

5. Finally, the testing of Repair #5 highlighted the importance of ensuring the weld of the steel sleeve is adequate to resist the force demand on the repair. It was determined that the likely cause of weld failure was due to a combination of heat affected zone (HAZ) effects at the welded edge, improper edge preparation, and inadequate welding process. As such, the following recommendations are made to ensure sound welding of the repair sleeve:
    - The welded edge should be properly prepared with clean surfaces and straight edges.
    - Ensure all welding is conducted by a certified welder and supervised by a certified weld inspector.
    - Plasma cutting of thin gauge metal (< ¼") that is intended to be welded should be avoided as it has been shown to reduce the welded capacity of the connection.

8.2 Analytical Design Model

An analytical design model is proposed that recognizes and addresses the inconsistencies of the original design assumptions, as described in the previous section. The key assumption of the proposed method is that the repair does not act to strengthen the damaged column, but instead changes the support boundary conditions resulting in a redistribution of forces and deformations within the original member. The force-displacement response is determined through a unique application of the existing plastic hinge method, as described by (Priestley et al., 2007) and later modified by (Goodnight et al., 2015), and the force demand on the repair is found through statics. The procedure for this analysis is briefly outlined below.

The flexural displacement of the column above the repair is found using the traditional plastic hinge length with modifications to account for tension-based strain limits. Equation 8-1 through Equation 8-4 summarize the procedure for calculating the yield and ultimate displacements; denoted by $\Delta_{y,c,}$ and $\Delta_{u,c}$ respectively. Note that ϕ'_y and ϕ_u refer to the first yield and ultimate curvatures of the original column cross section respectively and consider softened material response due to prior loading. L_{eff} refers to the reduced effective shear span of the column, as measured from the top of the repair.

$$L_{pt} = kL_c + \gamma D_c \qquad \textit{Equation 8-1}$$

$$k = 0.2\left(\frac{f_u}{f_y} - 1\right) \leq 0.08 \qquad \textit{Equation 8-2}$$

Where,

$$\gamma = \begin{cases} 0.33 & \textit{bidirectional} \\ 0.4 & \textit{unidirectional} \end{cases}$$

$$\Delta_{y,c} = \frac{\phi'_y L_{eff}^2}{3} \qquad \textit{Equation 8-3}$$

$$\Delta_{u,c} = \Delta_{y,c} + \left(\phi_u - \phi'_y\right) L_{pt}\left(L_{eff} - 0.5L_{pt}\right) \qquad \textit{Equation 8-4}$$

Additional displacement is accounted for through strain penetration of the relocated plastic hinge into the repair and into the footing or adjoining member. These components are separated into elastic and plastic contributions as well and presented in Equation 8-5 and Equation 8-6 respectively. Note that the full derivation of the model accounts for strain penetration into the repair separately from that into the adjacent footing; however, these factors have been combined in these equations for simplicity. Also note that these equations are dependent solely on the geometry of the repaired system and do not rely on any empirically derived factors, other than those present in the strain penetration length equation which is already broadly accepted for use in design.

$$\Delta_{y,sp} = \left[\frac{1}{2}\left(1+\frac{L_{eff}-L_r}{L_{eff}}\right)L_r + \left(\frac{L_{eff}-L_r}{L_{eff}}\right)L_{sp}\right]\phi'_y\, L_{eff} \qquad \textit{Equation 8-5}$$

$$\Delta_{u,sp} = \Delta_{y,sp} + \left[\frac{1}{2}\left(1+\frac{L_{pr}-L_r}{L_{pr}}\right)L_r + \left(\frac{L_{pr}-L_r}{L_{pr}}\right)L_{sp}\right]\left(\phi_u - \phi'_y\right)L_{eff} \qquad \textit{Equation 8-6}$$

$$\textit{if } L_{pt} > L_r \textit{, else}$$

$$\Delta_{u,sp} = \Delta_{y,sp} + \left(\phi_u - \phi'_y\right)L_{pt}L_{eff}$$

$$L_{sp} = \begin{cases} 0.022\, f_{ye} d_{bl} & (MPa) \\ 0.15\, f_{ye} d_{bl} & (ksi) \end{cases} \qquad \textit{Equation 8-7}$$

The final deformation component is that of rigid rotation of the repair, which is assumed to rotate about a single crack at the interface of the repair and the top of the footing. This is calculated assuming elastic response of the repair bars and effective section stiffness. Therefore, the deformation is directly related to the moment demand at the base of the repair, which is calculated from either Equation 8-8 or Equation 8-9 depending on whether the damaged cross section contains fractured bars. M_c is the moment in the original column at the relocated plastic hinge location considering all longitudinal bars are active and $M_{c,rup}$ is the same, except the contribution of fractured bars to the moment response is removed. The resulting curvature at the base of the repair is then calculated using Equation 8-10 and assumed constant over the strain penetration length derived in Equation 8-11. Note that this is the same strain penetration length defined in Equation 8-7 except doubled to account for the penetration into the repair and into the adjacent footing. The resulting product of these values is a rotation angle which, when multiplied by the distance to the top of column, yields the total contribution of repair rotation to the total column displacement as shown in Equation 8-12.

$$M_{br} = M_c\left(\frac{2L_r}{L_{eff}}\right) \textit{ if no bars ruptured} \qquad \textit{Equation 8-8}$$

$$M_{br} = M_c\left(\frac{L_c}{L_{eff}}\right) - M_{c,rup}\left(\frac{L_{eff}-L_r}{L_{eff}}\right) \text{ if bars ruptured} \qquad \textit{Equation 8-9}$$

$$\phi_{br} = \frac{M_{br}}{0.35EI_g} \qquad \textit{Equation 8-10}$$

$$L_{sp,r} = \begin{cases} 0.044\, f_{ye,r} d_{bl,r} & (MPa) \\ 0.30\, f_{ye,r} d_{bl,r} & (ksi) \end{cases} \qquad \textit{Equation 8-11}$$

$$\Delta_{rr} = \phi_{br} L_{sp,r} L_c \qquad \textit{Equation 8-12}$$

The total displacement is then represented by the sum of each component defined above, as presented in Equation 8-13 and Equation 8-14 for yield and ultimate displacements respectively, where Δ_{rr} is calculated for the yield and ultimate column moments.

$$\Delta_y = \Delta_{y,c} + \Delta_{y,sp} + \Delta_{rr} \qquad \textit{Equation 8-13}$$

$$\Delta_u = \Delta_{u,c} + \Delta_{u,sp} + \Delta_{rr} \qquad \textit{Equation 8-14}$$

When designing the repair, it is recommended to minimize the height of the repair, such that there is a minimal increase in overall force demand on the system. However, the minimum height should consider prior strain in the column, development length of the repair bars, and relative geometry of the repair to the original column. Equation 8-15 defines the minimum recommended repair height, although a value of $L_r = D_c$ has been cited in the literature and should fall within the bounds of this equation for most systems.

$$L_r = L_{prt}\left(1 - \frac{0.02}{\varepsilon_{\max}}\right) \geq \frac{0.022 d_b f_y}{\sqrt{f'_c}} + cover \geq 0.9 D_c \qquad \textit{Equation 8-15}$$

The repair cross section is designed such that it can elastically resist the base repair moment demand, as calculated by Equation 8-8 or Equation 8-9. This can be accomplished via any analysis approach, but a moment-curvature analysis of the repair annulus section was used in this report.

Note that, although an annular section is used, the repair concrete is considered confined on both sides as it is restrained by the outer repair sleeve and the original column.

Finally, the repair is designed for shear assuming the column bearing against it results in the activation of a truss mechanism across the transverse steel sleeve. This truss is then anchored by the tension force in the longitudinal repair bars which are in turn anchored to the footing. The design shear force is calculated assuming a triangular distribution of loading from the bearing of the original column onto the inner surface of the repair annulus and is presented in Equation 8-16. The repair is designed to resist this force using the modified UCSD shear model, assuming zero axial load contribution, and a ductility of one.

$$V_r = \frac{3M_{br}}{2L_r} \qquad \textit{Equation 8-16}$$

8.3 Numerical Study on Residual Drift

Upon review of the experimental results presented in the report, it was concluded that localized damage within the plastic hinge (i.e. buckled and fractured bars, crushed concrete, fractured transverse steel, etc.) was not a sufficient measure by which to define a limit to repairability. The repairs conducted throughout this research considered up to 37.5% loss of longitudinal steel, at which point it would be questionable as to whether the damaged structure would still be standing. Thus, it is assumed that the next logical measure an engineer would utilize to make such a decision would be the residual deformation of the system. Therefore, a numerical study was conducted to assess the influence of residual drift on the performance of a column which has been repaired using the plastic hinge relocation methodology.

A structural model, based on the underlying assumptions of the analytical design model, was developed for use in this study. The structural model consisted of four elements in total: a force-based beam with hinges element to represent the column above the repair, a zero-length section element to represent the column strain penetration into the repair and footing, a rigid elastic beam-column to translate column forces to the footing-repair interface, and an elastic rotational spring to represent the rigid rotation of the repair. Prior to use in the numerical study, the model was shown to reliably predict the global force-displacement response and local strain behavior in the relocated plastic hinge when compared to experimental results. Furthermore, the relative

simplicity of this stick model, as opposed to a more rigorous finite element approach, allowed for much quicker analysis runs without sacrificing accuracy of the targeted output parameters.

The analysis within the numerical study consisted of subjecting repaired structures of varying combinations of longitudinal steel content (ρ_l), axial load ratio (ALR), L/D ratio, and residual drift to a suite of unscaled acceleration records with varying intensities. Upon completion of the analysis, the peak tension strain observed in each run was selected as an engineering demand parameter (EDP) and paired with the input intensity measure (IM) of the earthquake that produced it. The resulting data was then assembled to produce fragility functions relating the probability of exceeding a given tension strain limit state at a specified hazard intensity for the range of structural parameters considered.

The final product of the study is a tool which engineers can use to assess the potential performance of a repaired RC column considering there is residual displacement due to an initial earthquake loading. The intent of this tool is to provide a rational means by which to decide whether a structure is beyond the scope of repair given its global damage state. This contrasts with the presently ill-defined residual drift limits which are based on prescriptive values and do not take structural configuration, performance of proposed repair, or future hazard into consideration. The results from the study show that for a given structure, the potential risk of repair can vary a great deal between site hazards and levels of residual drift and demonstrate that this method provides a quantifiable basis on which to make repair decisions in a post-earthquake environment. The scope of this study considers only a plastic hinge relocation repair and should also be limited to columns with buckled bars, unless specific measures are taken to ensure anchorage of fractured bars. Also, while the results presented herein are likely insufficient on their own for immediate implementation, they do establish a conceptual framework which can be expanded upon in future research to develop rational residual lift limits.

8.4 Future Work

The research presented in this report serves as the basis of developing the plastic hinge relocation method as a rapid repair solution for modern, well designed RC bridge columns. Although multiple experimental tests were conducted with a variety of different considerations, many other possible configurations and parameters were identified as potential candidates for investigation in addition to those presented here. Examples of such variations include:

1. Mechanical rebar couplers as an alternative to splice welding when discrete rebar hoops are used for transverse reinforcement. This could provide a useful alternative when welding is not a viable option.
2. Pre-embedded bars that are anchored into the footing the expectation of their use for coupling to future repair bars.
3. Pre-formed holes for insertion of repair bars, thus facilitating the placement of repair bars.
4. Circumferentially pre-stressed repair sleeve to increase bond friction for the development of fractured longitudinal steel. This would also likely have the effect of engaging flexural force transfer between the original column and repair by improving conditions for shear transfer across the column-repair interface.
5. Further investigation on the impact of various steel sleeve thicknesses.
6. Variation of steel sleeve connection and preparation (i.e. plasma cutting, shear cutting, welding, bolting).
7. Further investigation on durability of ready-mix concrete backfill.
8. Further experimental investigation of residual drift.
9. Investigation of additional connection types (i.e. column-to-oversized shaft, column-to-cap beam, etc.)

While the tests conducted during this research are sufficient to support the proposed design methods, it is recommended that additional research be done to consider these, and other, configurations as it would work towards building confidence in the repair and broadening the range of possible solutions available to the design engineer.

Further investigation is also recommended to expand the applicability of the residual drift study. The current study presents only a single case of a cantilever column. Additional configurations including, but not limited to, columns in double bending, multi-column bents, additional connection types, and full structure interaction should be considered.

REFERENCES

AASHTO. (2017). *AASHTO LRFD Bridge Design Specifications, 8th Edition*. Washington, DC: American Association of State Highway and Transportation Officials.

Abdel-Fatteh, B., & Wight, J. (1987). Study of Moving Beam Plastic Hinging Zones for Earthquake-Resistant Design of Reinforced Concrete Buildings. *Structural Journal*, **84**(1), 31-39.

ACI Committee 318. (2014). *Building Code Requirements for Structural Concrete; and Commentary.* (ACI 318-14 & ACI 318R-14). Farmington Hills, MI: American Concrete Institute.

ACI Committee 530. (2013). *Building Code Requirements and Specification for Masonry Structures and Companion Commentaries.* (ACI 530/530.1-13). Farmington Hills, MI: American Concrete Institute.

ACI Committee 341, (2007). *Seismic Evaluation and Retrofit Techniques for Concrete Bridges.* (ACI 341.3R-07). Farmington Hills, MI: American Concrete Institute.

ACI Committee 546, (2014). *Guide to Concrete Repair.* (ACI 546R-14). Farmington Hills, MI: American Concrete Institute.

Al-Haddad, M. S., & Wight, J. (1988). Relocating Beam Plastic Hinging Zones for Earthquake Resistant Design of Reinforced Concrete Buildings. *Structural Journal*, **85**(2), 123–133.

ASCE. (2016). *Minimum Design Loads for Buildings and Other Structures.* (ASCE7-16). Reston, VA: American Society of Civil Engineers.

ASTM A370. (2015). *Standard Test Methods and Definitions for Mechanical Testing of Steel Products*, West Conshohocken, PA: ASTM International.

ATC. (1996). *Seismic Evaluation and retrofit of concrete buildings (Volume 1 & 2)*. (ATC-40). Redwood City, CA: Applied Technology Council.

Baker, J. W. (2015). *Efficient analytical fragility function fitting using dynamic structural analysis*. Earthquake Spectra, **31**(1), 579–599.

Burtz, J. (2003). *Behavior and Design of Grouted Anchors Loaded in Tension Including Edge and Group Effects and Qualification of Engineered Grout Products*. Masters Thesis, University of Florida, Tallahassee, FL. Retrieved from: http://etd.fcla.edu/UF/UFE0000854/burtz_j.pdf

Calabrese, A., Almeida, J. P., & Pinho, R. (2010). Numerical issues in distributed inelasticity modeling of RC frame elements for seismic analysis. *Journal of Earthquake Engineering* **14**(Supp. 1), 38-68.

Caltrans. (2009). *Bridge Design Details: Section 18 - Bridge Seismic Retrofit and Strengthening*. Sacramento, CA: California Department of Transportation.

Canha, R. M. F., de Borja Jaguaribe, K., de Cresce El Debs, A. L. H., & El Debs, M. K. (2009). Analysis of the behavior of transverse walls of socket base connections. *Engineering Structures*, **31**(3), 788–798.

Canha, R. M. F., El Debs, M. K. El, de Borja Jaguaribe, K., & De Cresce El Debs, A. L. H. (2009). Behavior of socket base connections emphasizing pedestal walls. *ACI Structural Journal*, **106**(3), 268–278.

Canha, R. M. F., Ebeling, E. B., de Cresce El Debs, A. L. H., & El Debs, M. K. (2009). Analysing the base of precast column in socket foundations with smooth interfaces. *Materials and Structures/Materiaux et Constructions*, **42**(6), 725–737.

Duarte, P., Correia, J. R., Ferreira, J. G., Nunes, F., & Arruda, M. R. T. (2014). Experimental and numerical study on the effect of repairing reinforced concrete cracked beams strengthened with carbon fibre reinforced polymer laminates. *Canadian Journal of Civil Engineering*, **41**(3), 222–231.

FEMA. (1997). *Guidelines for the seismic rehabilitation of buildings*. (FEMA-273). Washington, DC: Federal Emergency Management Agency.

FEMA. (2012). *Seismic Performance Assessment of Buildings – Methodology (Vol. 1)*. (FEMA P-58-1). Washington, DC: Federal Emergency Management Agency.

FHWA. (2006). *Seismic Retrofitting Manual for Highway Structures : Part 1 – Bridges*. (Report No. FHWA-HRT-06-032). McLean, VA: Federal highway Administration

Filippou, F. C., Popov, E. P., & Bertero, V. V. (1983). Effects of Bond Deterioration on Hysteretic Behavior of Reinforced Concrete Joints, *NSF Report No. NSF/CEE-83032*, Earthquake Engineering Research Center, University of California, Berkeley.

Fulmer, S. J., Kowalsky, M. J., & Nau, J. M. (2015). Grouted shear stud connection for steel bridge substructures. *Journal of Constructional Steel Research*, **109**, 72–86.

Goodnight, J., Kowalsky, M., & Nau, J. (2013). Effect of Load History on Performance Limit States of Circular Bridge Columns. *Journal of Bridge Engineering*, **18**(12), 1383–1396.

Goodnight, J. C., Kowalsky, M. J., & Nau, J. M. (2015). The Effects of Load History and Design Variables on Performance Limit Stats of Circular Bridge Columns, *AKDOT Report No. 4000(072)*, Department of Civil Engineering, North Carolina State University, Raleigh, NC.

Goodnight, J. C., Kowalsky, M. J., & Nau, J. M. (2017). Seismic Load Path Effects in Reinforced Concrete Bridge Columns and Wall Piers, Volume 1: Strain Limit States for RC Bridge Columns, *AKDOT Report No. 4000(134)*, Department of Civil Engineering, North Carolina State University, Raleigh, NC.

He, R., Yang, Y., & Sneed, L. H. (2015). Seismic repair of reinforced concrete bridge columns: review of research findings. *Journal of Bridge Engineering*, **20**(12), 04015015.

Hose, Y. D. (2001). *Seismic Performance and Failure Behavior of Plastic Hinge Regions in Flexural Bridge Columns*. PhD Dissertation. University of California, San Diego, CA.

Hose, Y. D., Priestley, M. J. N., Seible, F. (1997). Strategic Relocation of Plastic Hinges in Bridge Columns, *Caltrans Report No. SSRP-97/05*, Division of Structural Engineering, University of California, San Diego, La Jolla, CA.

Kawashima, K., MacRae, G. A., Hoshikuma, J. I., & Nagaya, K. (1998). Residual displacement response spectrum. *Journal of Structural Engineering*, **124**(5), 523–530.

Lee, W. K., & Billington, S. L. (2010). Modeling Residual Displacements of Concrete Bridge Columns under Earthquake Loads Using Fiber Elements. *Journal of Bridge Engineering*, **15**(3), 240–249.

Lee, W. K., & Billington, S. L. (2011). Performance-based earthquake engineering assessment of a self-centering, post-tensioned concrete bridge system. *Earthquake Engineering & Structural Dynamics*, **40**(8), 887–902.

Lehman, D. E., Gookin, S. E., Nacamull, A. M. and Moehle, J. P., (2001). Repair of earthquake-damaged bridge columns, *ACI Structural Journal* **98**(2), 233–242.

Lehman, D. E., & Moehle, J. P. (2000). Seismic performance of well-confined concrete bridge columns. *PEER Report No. 98/01,* Pacific Earthquake Engineering Research Center, University of California, Berkeley.

Mackie B., K. & Stojadinovic, B. (2003). Seismic demands for performance-based design of bridges. *PEER Report 2003/16*, Pacific Earthquake Engineering Research Center, University of California, Berkeley.

Mackie, K., & Stojadinovic, B. (2004). Residual displacement and post-earthquake capacity of highway bridges. *Proceedings of the Thirteenth World Conference on Earthquake Engineering*, Vancouver, Canada.

Mahini, S. S., & Ronagh, H. R. (2011). Web-bonded frps for relocation of plastic hinges away from the column face in exterior RC joints. *Composite Structures*, **93**(10), 2460–2472.

Mander, J. B., Priestley, M. J. N., & Park, R. (1988). Theoretical Stress-Strain Model for Confined Concrete. *Journal of Structural Engineering*, **114**(8), 1804–1826.

Matsumoto, E. E., Waggoner, M. C., Sumen, G., Kreger, M. E., Wood, S. L., and Breen, J. E. (2001). Development of a Precast Bent Cap System, *FHWA Report No. TX-0-1748-2*, Center for Transportation Research, The University of Texas, Austin, TX.

McKenna, F., Fenves, G. L., & Scott, M. H. (2000). Open System for Earthquake Engineering Simulation (OpenSEES). Available from: http://opensees.berkeley.edu/

Moehle, J., & Deierlein, G. G. (2004). A framework methodology for performance-based earthquake engineering. *Proceedings of the 13th World Conference on Earthquake Engineering*, Vancouver, Canada.

Overby, D., Kowalsky, M., & Seracino, R. (2017). Stress-strain response of A706 grade 80 reinforcing steel. *Construction and Building Materials*, **145**, 292–302.

Pampanin, S., Christopoulos, C., & Priestley, M. J. N. (2002). *Residual Deformations in the Performance-Based Seismic Assessment of Frame Structures*. Pavia, Italy: IUSS Press.

Parks, J. E., Brown, D. N., Ameli, M. J. and Pantelides, C. P. (2016). Seismic repair of severely damaged precast reinforced concrete bridge columns connected with grouted splice sleeves, *ACI Structural Journal*, **113**(3), 615–626.

Paulay, T. and Priestley, M. J. N. (1992). *Seismic Design of Reinforced Concrete and Masonry Buildings*, John Wiley & Sons, Inc., New York, NY.

Pettinga, J. D., Pampanin, S., Christopoulos, C., & Priestley, M. J. N. (2007). *Developments in the Prediction and Mitigation of Residual Deformations due to Seismic Demand, including Asymmetric Structural Response*. Pavia, Italy: IUSS Press.

Priestley, M. J. N., Calvi, G. M., Kowalsky, M. J. (2007). *Displacement Based Seismic Design of Structures*. IUSS Press, Pavia, Italy.

Priestley, M. J. N., Seible, F. and Calvi, G. M. (1996). *Seismic Design and Retrofit of Bridges*, John Wiley & Sons, Inc., New York, NY.

Rutledge, S. T., Kowalsky, M. J., Seracino, R. and Nau, J. M. (2014). Repair of reinforced concrete bridge columns containing buckled and fractured reinforcement by plastic hinge relocation, *Journal of Bridge Engineering.* **19**(8), A4013001.

Sagan, V. E., Gergely, P., & White, R. N. (1991). Behavior and design of noncontact lap splices subjected to repeated inelastic tensile loading. *ACI Structural Journal*, **88**(4), 420–431.

Scott, M. H., & Fenves, G. L. (2006). Plastic Hinge Integration Methods for Force-Based Beam–Column Elements. *Journal of Structural Engineering*, **132**(2), 244–252.

SEAOC. (2003). *Revised Interim Guidelines for Performance-Based Seismic Engineering*. Sacramento, CA: Structural Engineer's Association of California.

Shafaei, J., Hosseini, A., & Marefat, M. S. (2014). Rehabilitation of earthquake damaged external RC beam-column joints by joint enlargement using prestressed steel angles. *Engineering Structures*, **81**, 265–288.

U.S. Army Corps of Engineers. (1995). *Evaluation and Repair of Concrete Structures*, Manual No. 1110-2-2002). Washington, DC: U.S. Army Corps of Engineers.

Vecchio, F., & Bucci, F. (1999). Analysis of repaired reinforced concrete structures. *Journal of Structural Engineering*, **125**(6), 644–652.

Vosooghi, A. and Saiidi, M. S. (2010). Seismic Damage States and Response Parameters for Bridge Columns, *American Concrete Institute – Special Publication 271*, 29-46.

Vosooghi, A., & Saiidi, M. S. (2013). Design Guidelines for Rapid Repair of Earthquake-Damaged Circular RC Bridge Columns Using CFRP. *Journal of Bridge Engineering*, **18**(9), 120725052316002.

APPENDIX A:

GROUND MOTIONS FOR RESIDUAL DRIFT STUDY

The below listed ground-motions were obtained from the NGA West 2 database provided by the Pacific Earthquake Engineering Research Center (PEER). Acceleration records can be retrieved from https://ngawest2.berkeley.edu/ using the Record Sequence Number (RSN) as a reference.

Record Sequence Number	Earthquake Name	Earthquake Magnitude	EpiD (km)	PGA RotD50 (g)	PGD RotD50 (cm)
77	San Fernando	6.61	11.87	1.22	27.96
126	Gazli, USSR	6.80	12.81	0.70	24.08
140	Tabas, Iran	7.35	117.66	0.10	3.31
143	Tabas, Iran	7.35	55.24	0.81	72.01
154	Coyote Lake	5.74	23.24	0.10	1.44
173	Imperial Valley-06	6.53	28.79	0.20	31.42
180	Imperial Valley-06	6.53	27.80	0.41	62.49
183	Imperial Valley-06	6.53	28.09	0.53	41.44
223	Livermore-02	5.42	16.57	0.20	2.49
235	Mammoth Lakes-02	5.69	3.49	0.42	3.65
240	Mammoth Lakes-04	5.70	2.75	0.48	2.27
247	Mammoth Lakes-06	5.94	19.97	0.10	1.48
248	Mammoth Lakes-06	5.94	12.03	0.31	2.80
250	Mammoth Lakes-06	5.94	14.04	0.72	5.38
251	Mammoth Lakes-07	4.73	4.04	0.10	0.72
258	Mammoth Lakes-08	4.80	6.02	0.20	0.41
265	Victoria, Mexico	6.33	33.73	0.61	4.68
288	Irpinia, Italy-01	6.90	46.16	0.20	2.29
319	Westmorland	5.90	7.02	0.41	13.09
335	Coalinga-01	6.36	41.42	0.10	5.23
368	Coalinga-01	6.36	9.98	0.52	15.77
373	Coalinga-02	5.09	3.38	0.48	1.23
400	Coalinga-04	5.18	7.73	0.10	0.39
413	Coalinga-05	5.77	9.99	0.31	2.66

Record Sequence Number	Earthquake Name	Earthquake Magnitude	EpiD (km)	PGA RotD50 (g)	PGD RotD50 (cm)
415	Coalinga-05	5.77	5.99	0.84	7.60
451	Morgan Hill	6.19	24.55	0.94	13.48
485	Bishop (Rnd Val)	5.82	21.93	0.10	0.09
495	Nahanni, Canada	6.76	6.80	1.16	8.43
496	Nahanni, Canada	6.76	6.52	0.40	4.54
514	N. Palm Springs	6.06	18.30	0.21	2.39
540	N. Palm Springs	6.06	4.24	0.60	4.88
558	Chalfant Valley-02	6.19	14.33	0.42	8.21
566	Kalamata, Greece-02	5.40	7.12	0.21	2.82
568	San Salvador	5.80	7.93	0.58	12.86
569	San Salvador	5.80	9.54	0.49	16.06
578	Taiwan SMART1(45)	7.30	77.57	0.20	9.79
585	Baja California	5.50	3.69	1.14	13.46
727	Superstition Hills-02	6.54	7.50	0.73	3.76
753	Loma Prieta	6.93	7.17	0.50	11.39
779	Loma Prieta	6.93	18.46	0.59	30.45
803	Loma Prieta	6.93	27.05	0.30	30.07
879	Landers	7.28	44.02	0.73	80.77
901	Big Bear-01	6.46	10.15	0.52	4.28
982	Northridge-01	6.69	12.97	0.52	33.83
983	Northridge-01	6.69	13.00	0.76	31.61
1004	Northridge-01	6.69	8.48	0.75	17.19
1044	Northridge-01	6.69	20.27	0.65	25.79
1050	Northridge-01	6.69	20.36	0.42	5.18
1051	Northridge-01	6.69	20.36	1.39	16.18
1063	Northridge-01	6.69	10.91	0.71	30.74
1084	Northridge-01	6.69	13.11	0.70	33.75
1086	Northridge-01	6.69	16.77	0.64	24.16
1106	Kobe, Japan	6.90	18.27	0.78	19.74
1119	Kobe, Japan	6.90	38.60	0.65	24.39

Record Sequence Number	Earthquake Name	Earthquake Magnitude	EpiD (km)	PGA RotD50 (g)	PGD RotD50 (cm)
1120	Kobe, Japan	6.90	13.12	0.67	34.25
1197	Chi-Chi, Taiwan	7.62	32.67	0.77	23.99
1201	Chi-Chi, Taiwan	7.62	46.13	0.30	14.73
1205	Chi-Chi, Taiwan	7.62	51.15	0.50	8.58
1231	Chi-Chi, Taiwan	7.62	31.65	0.83	27.41
1492	Chi-Chi, Taiwan	7.62	39.58	0.40	221.20
1503	Chi-Chi, Taiwan	7.62	26.67	0.69	81.78
1510	Chi-Chi, Taiwan	7.62	20.67	0.30	70.59
1511	Chi-Chi, Taiwan	7.62	16.03	0.40	38.62
1520	Chi-Chi, Taiwan	7.62	57.63	0.52	22.52
1531	Chi-Chi, Taiwan	7.62	49.28	0.10	46.29
1540	Chi-Chi, Taiwan	7.62	37.70	0.10	30.55
1549	Chi-Chi, Taiwan	7.62	14.16	0.75	49.03
1551	Chi-Chi, Taiwan	7.62	24.22	0.21	31.18
2049	Yorba Linda	4.27	8.01	0.10	0.27
3474	Chi-Chi, Taiwan-06	6.30	12.26	0.70	6.37
3682	Taiwan SMART1(45)	7.30	75.70	0.10	8.29
3968	Tottori, Japan	6.61	6.56	0.84	25.25
4040	Bam, Iran	6.6	12.59	0.74	27.18
4066	Parkfield-02, CA	6.00	15.12	0.41	3.01
4070	Parkfield-02, CA	6.00	14.96	0.56	4.21
4071	Parkfield-02, CA	6.00	19.64	0.31	8.37
4083	Parkfield-02, CA	6.00	6.82	0.20	1.76
4097	Parkfield-02, CA	6.00	31.53	0.31	7.50
4099	Parkfield-02, CA	6.00	12.06	0.48	2.40
4101	Parkfield-02, CA	6.00	11.87	0.65	2.80
4102	Parkfield-02, CA	6.00	12.17	0.41	6.16
4107	Parkfield-02, CA	6.00	8.40	0.64	10.83
4110	Parkfield-02, CA	6.00	6.82	0.21	3.61
4112	Parkfield-02, CA	6.00	6.94	0.48	2.25

Record Sequence Number	Earthquake Name	Earthquake Magnitude	EpiD (km)	PGA RotD50 (g)	PGD RotD50 (cm)
4114	Parkfield-02, CA	6.00	9.28	0.83	1.87
4116	Parkfield-02, CA	6.00	8.68	1.04	13.46
4119	Parkfield-02, CA	6.00	3.27	0.21	0.60
4122	Parkfield-02, CA	6.00	4.76	0.60	3.51
4123	Parkfield-02, CA	6.00	7.97	0.40	1.94
4126	Parkfield-02, CA	6.00	7.17	0.72	4.74
4128	Parkfield-02, CA	6.00	8.75	0.20	2.10
4129	Parkfield-02, CA	6.00	21.65	0.10	1.07
4130	Parkfield-02, CA	6.00	18.76	0.30	7.57
4134	Parkfield-02, CA	6.00	19.20	0.31	5.54
4141	Parkfield-02, CA	6.00	12.48	0.30	3.47
4337	Umbria Marche (foreshock), Italy	5.7	2.73	0.30	4.01
5657	Iwate	6.90	2.52	1.35	29.18
6906	Darfield, New Zealand	7.00	4.42	0.73	77.59
12261	40199209	4.20	6.02	0.31	0.87

APPENDIX B:

RESIDUAL DRIFT STUDY FRAGILITY FUNCTIONS

L/D Ratio = 2

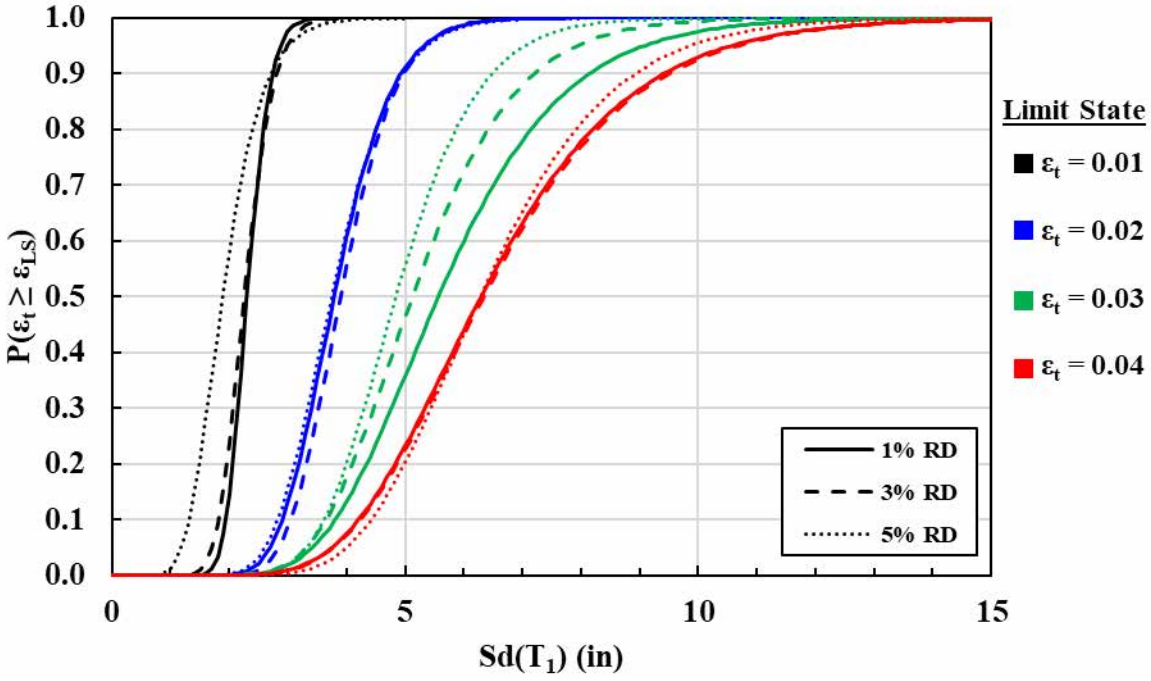

Figure B. 1: Limit state fragilities L/D = 2, ρ_l = 1.0%, ALR = 5%.

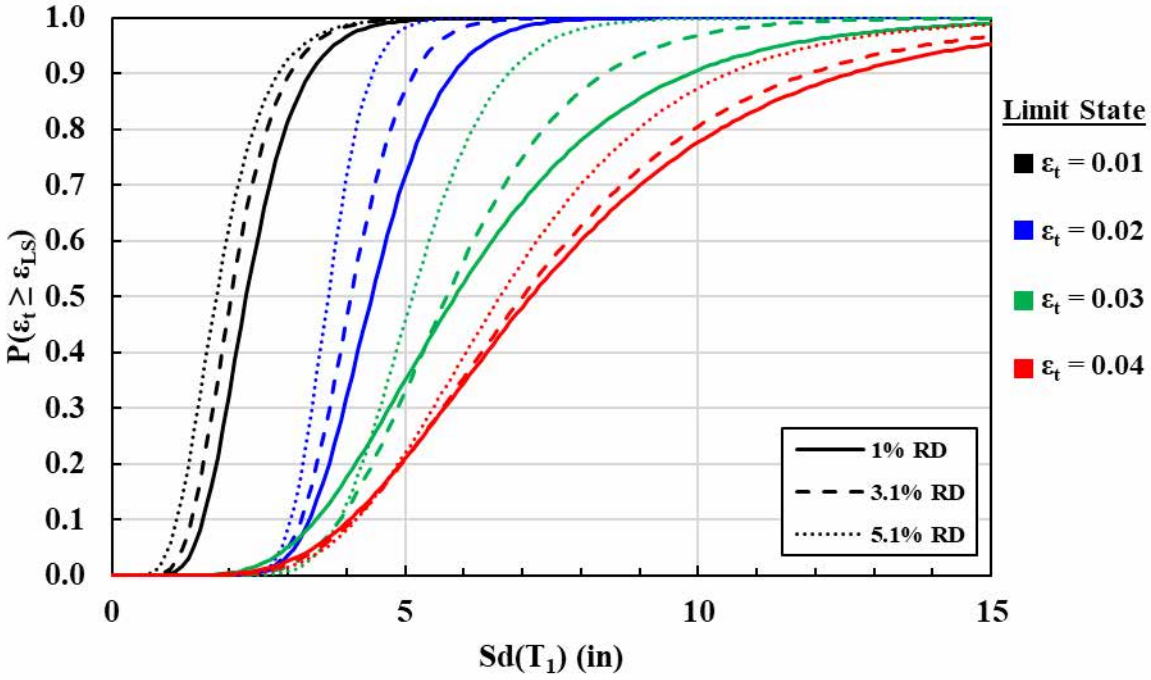

Figure B. 2: Limit state fragilities L/D = 2, ρ_l = 1.0%, ALR = 10%.

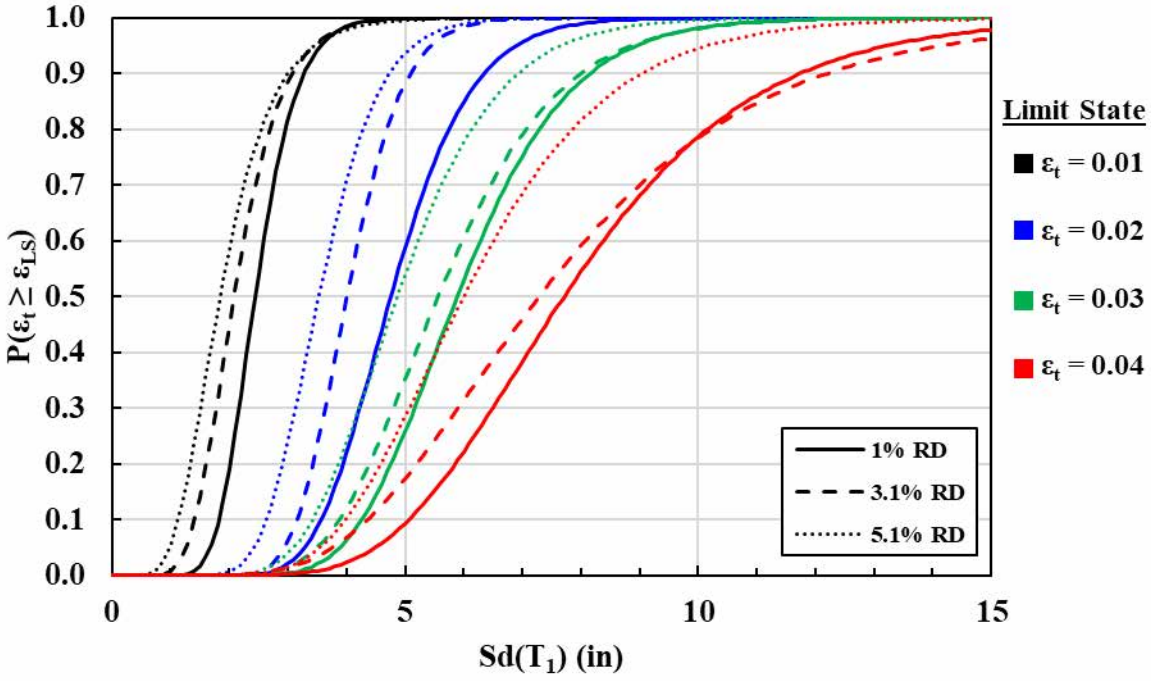

Figure B. 3: Limit state fragilities L/D = 2, ρ_l = 1.0%, ALR = 15%.

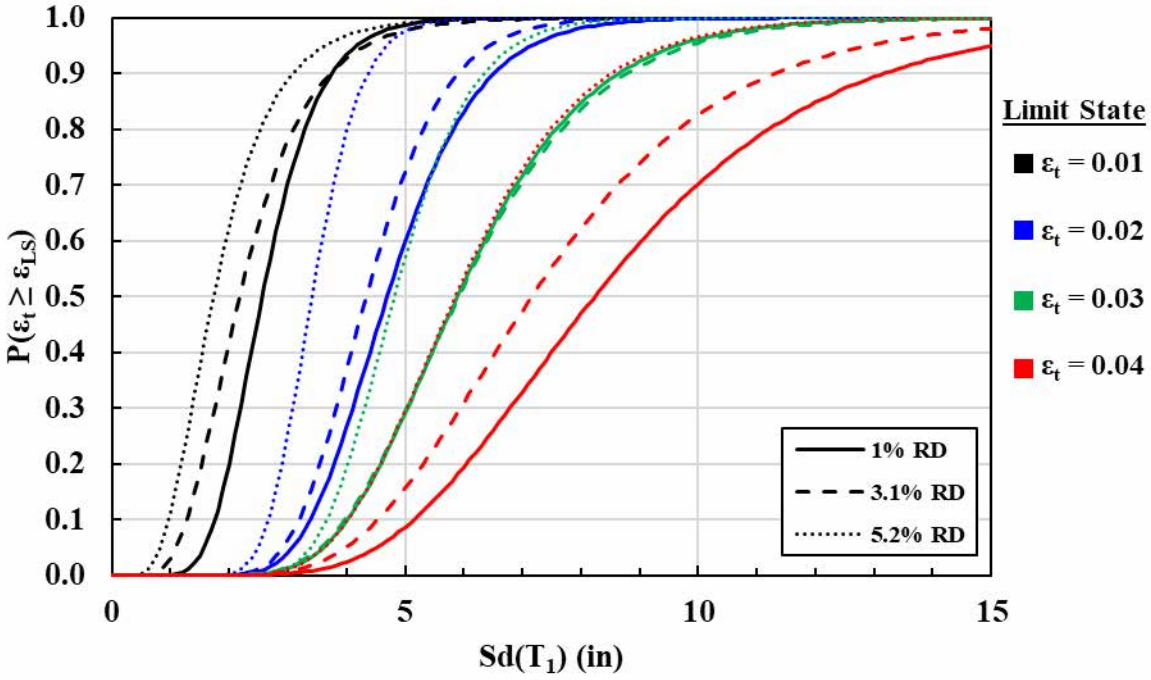

Figure B. 4: Limit state fragilities L/D = 2, ρ_l = 1.0%, ALR = 20%.

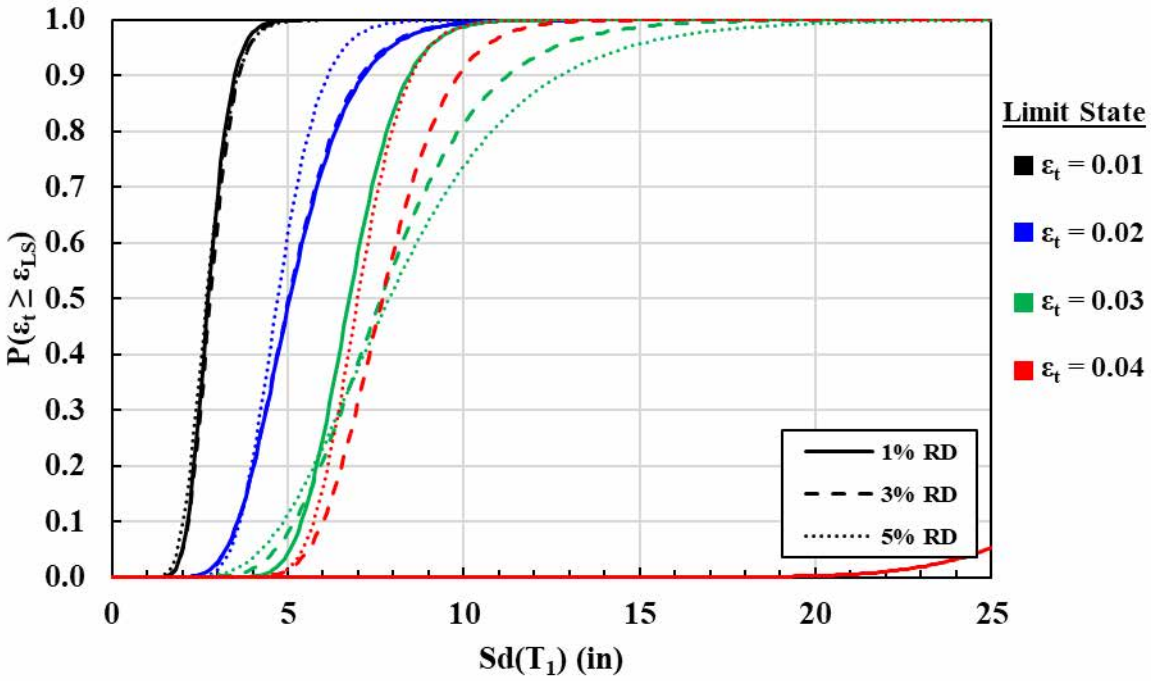

Figure B. 5: Limit state fragilities L/D = 2, ρ_l = 2.5%, ALR = 5%.

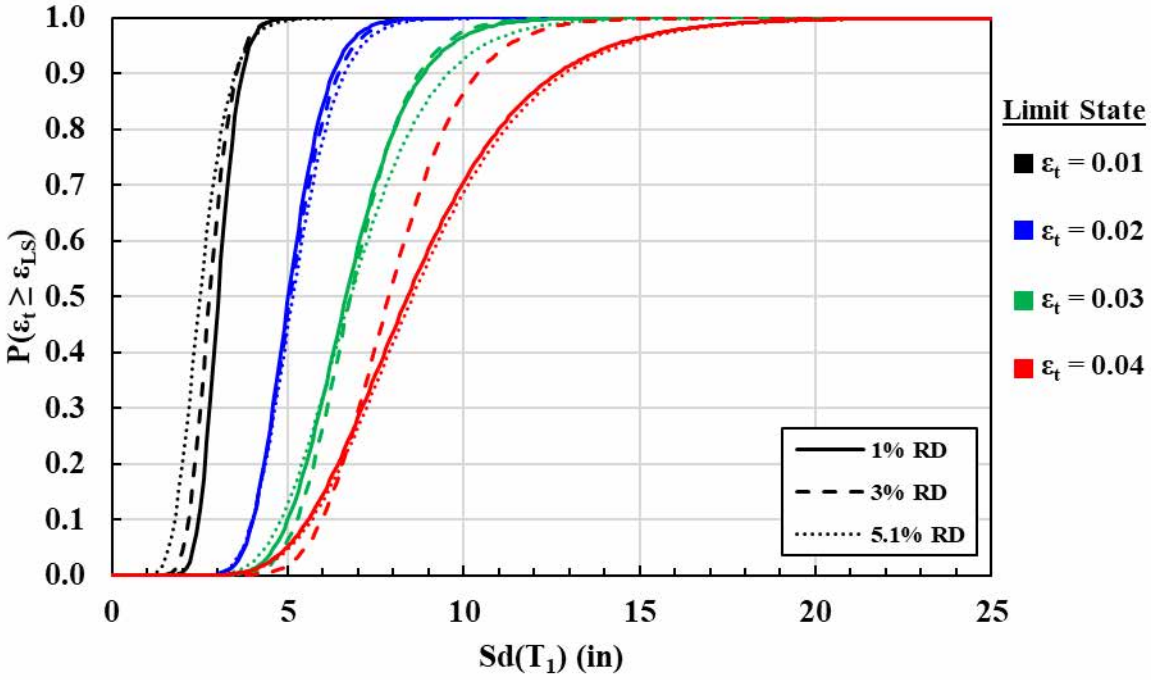

Figure B. 6: Limit state fragilities L/D = 2, ρ_l = 2.5%, ALR = 10%.

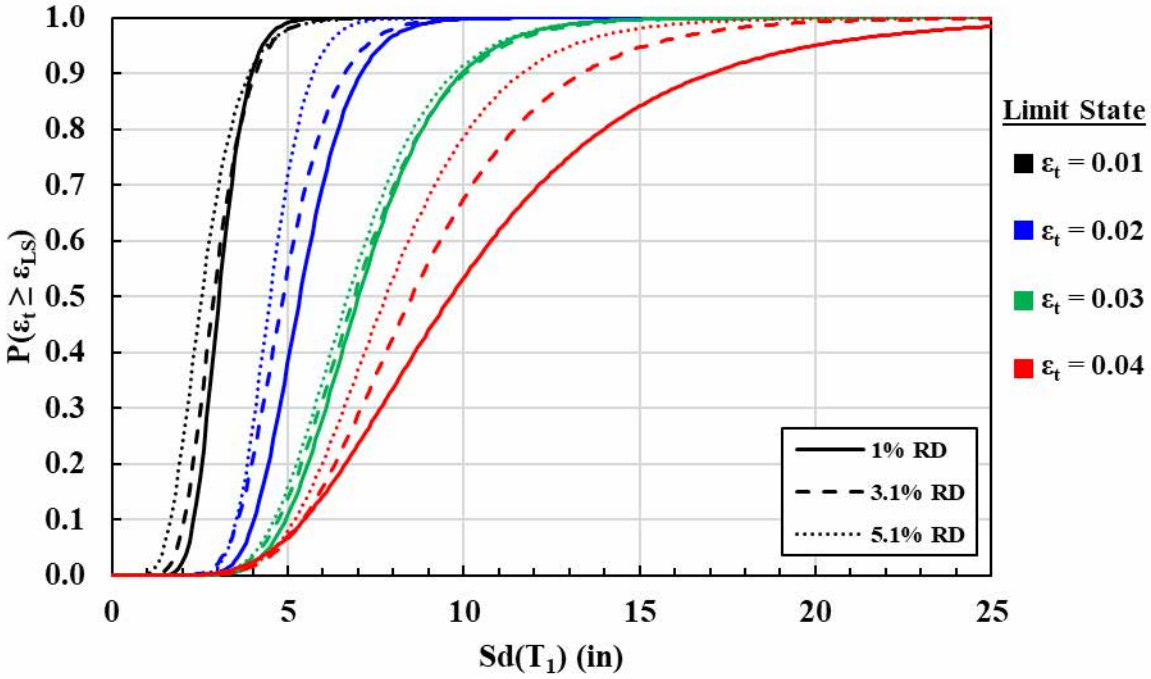

Figure B. 7: Limit state fragilities L/D = 2, ρ_l = 2.5%, ALR = 15%.

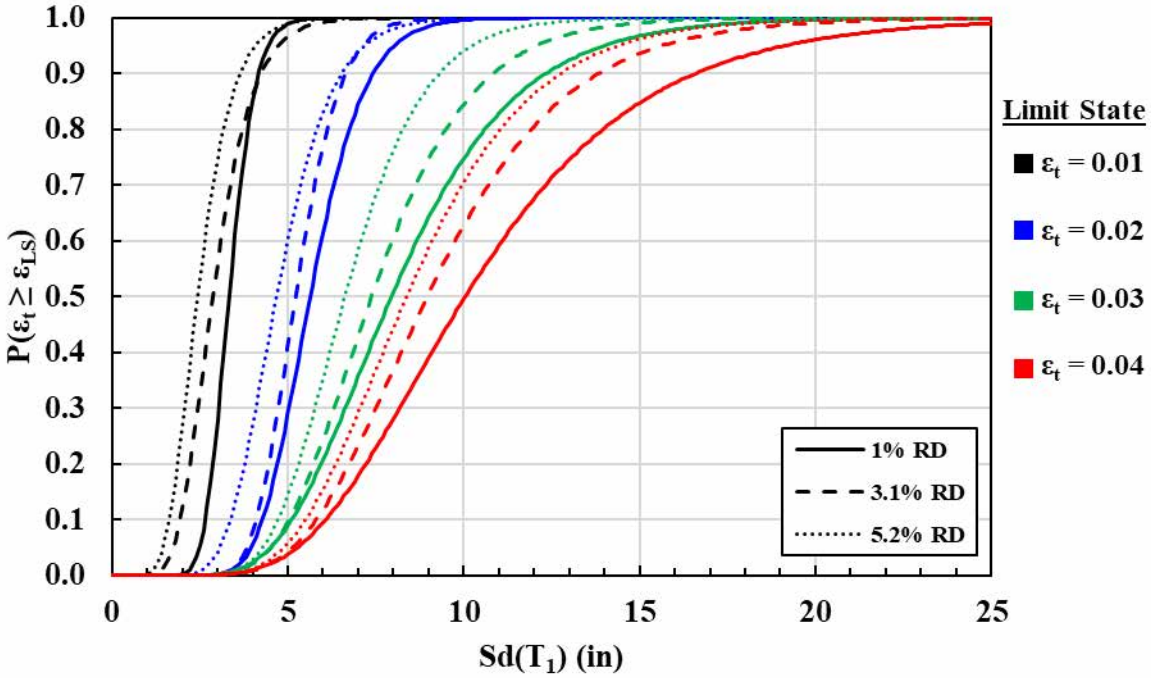

Figure B. 8: Limit state fragilities L/D = 2, ρ_l = 2.5%, ALR = 20%.

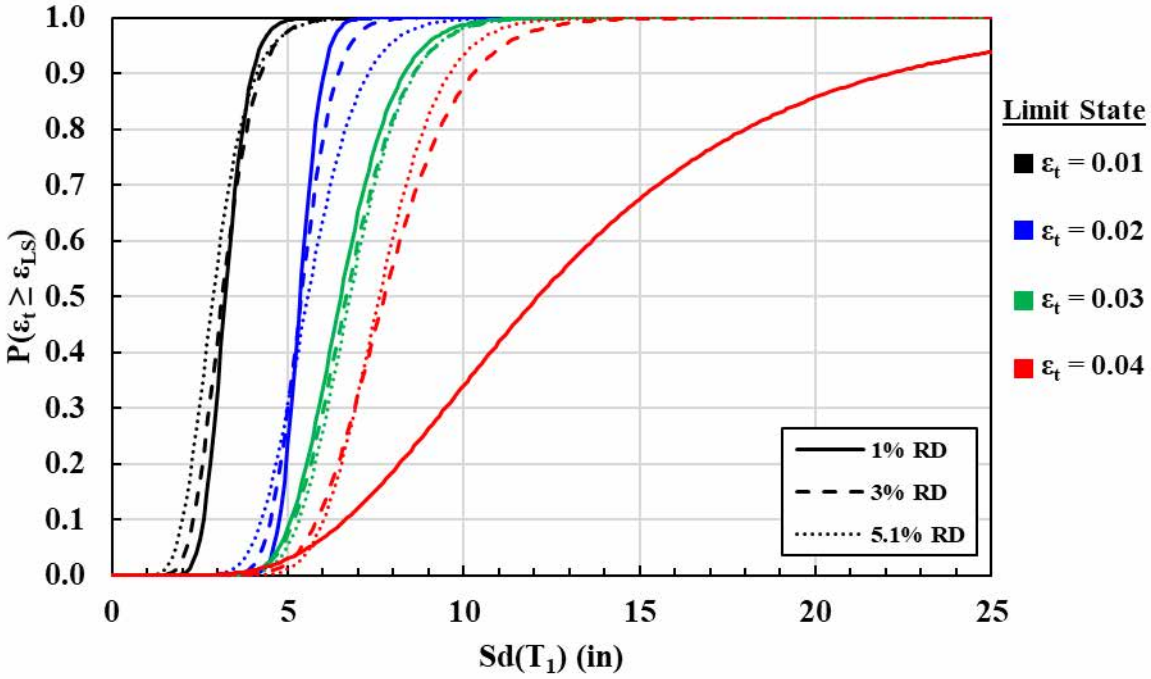

Figure B. 9: Limit state fragilities L/D = 2, ρ_l = 4.0%, ALR = 10%.

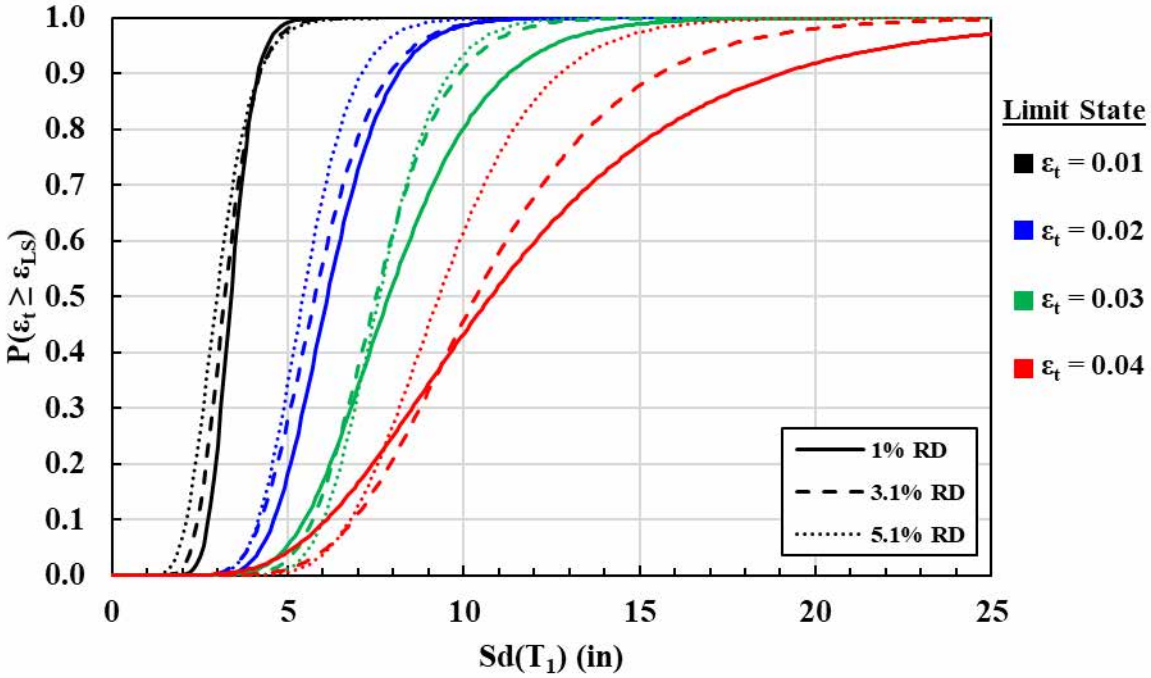

Figure B. 10: Limit state fragilities L/D = 2, ρ_l = 4.0%, ALR = 15%.

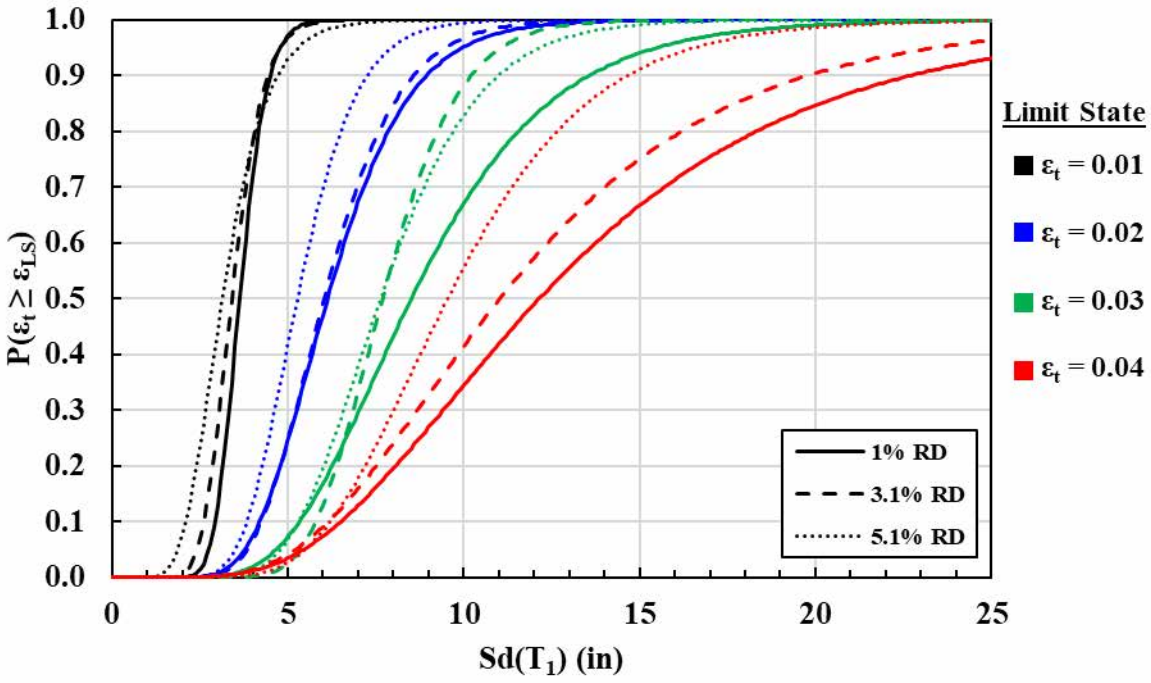

Figure B. 11: Limit state fragilities L/D = 2, ρ_l = 4.0%, ALR = 20%.

L/D Ratio = 4

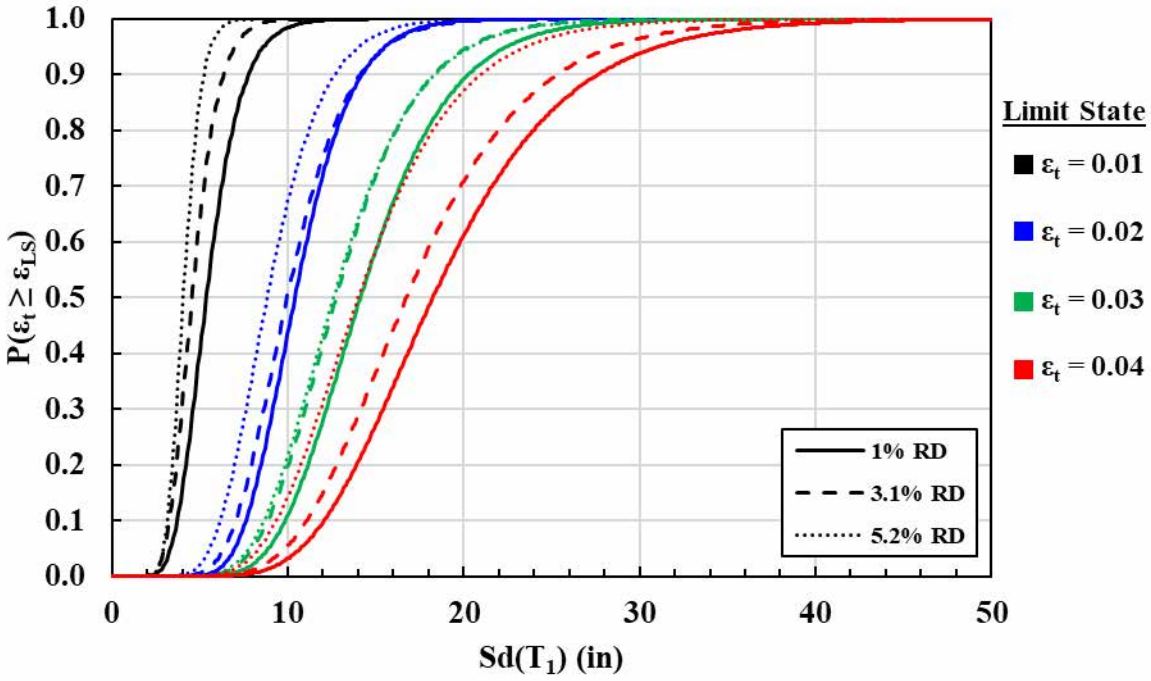

Figure B. 12: Limit state fragilities L/D = 4, ρ_l = 1.0%, ALR = 5%.

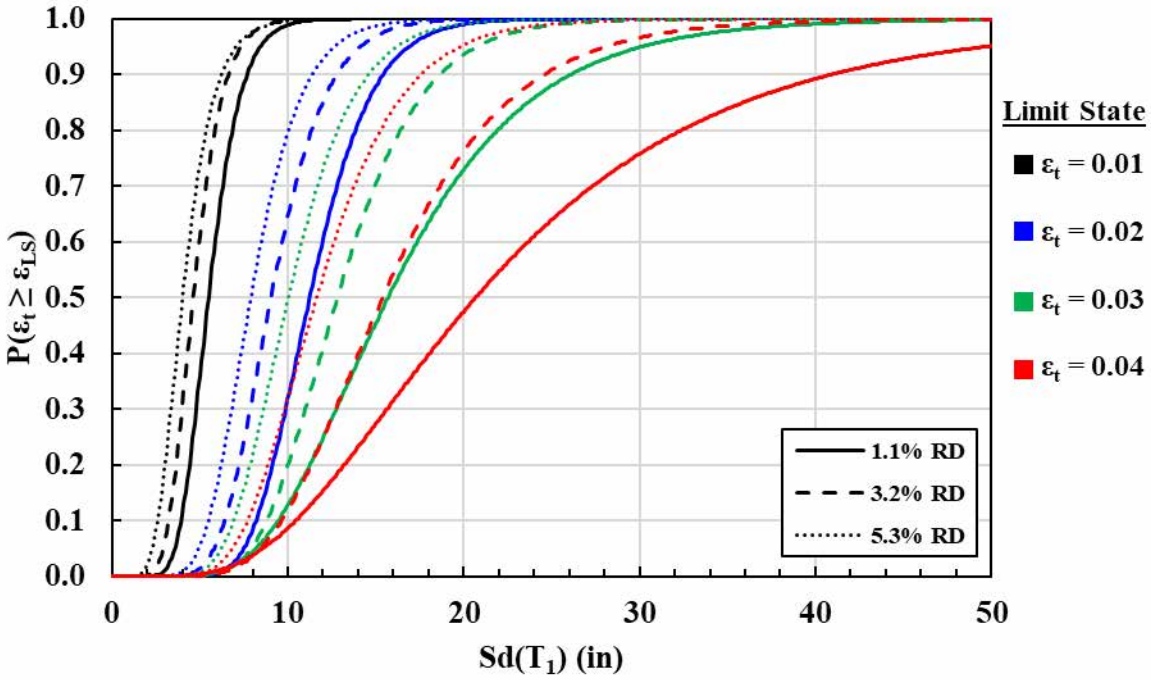

Figure B. 13: Limit state fragilities L/D = 4, ρ_l = 1.0%, ALR = 10%.

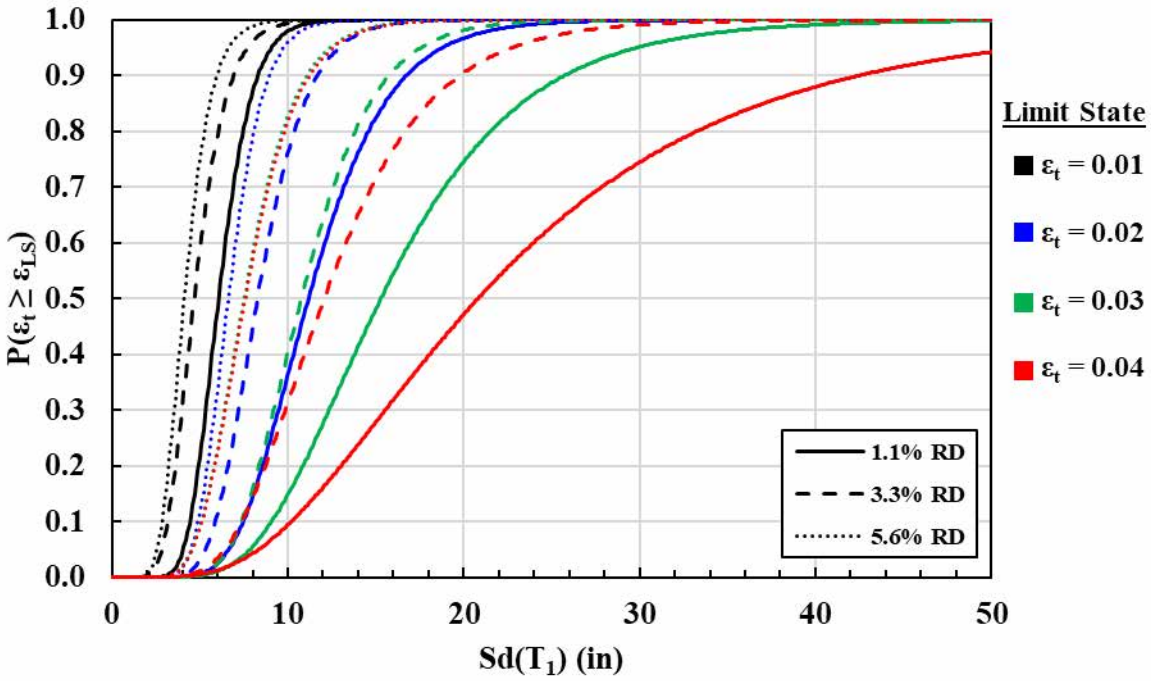

Figure B. 14: Limit state fragilities L/D = 4, ρ_l = 1.0%, ALR = 15%.

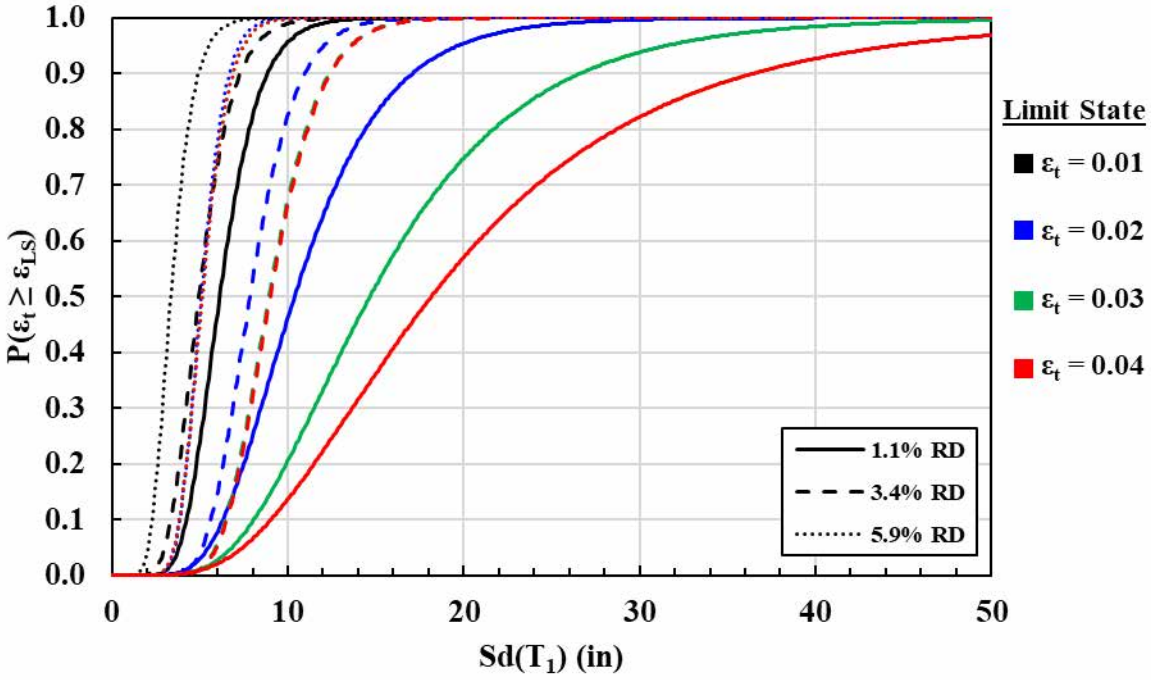

Figure B. 15: Limit state fragilities L/D = 4, ρ_l = 1.0%, ALR = 20%.

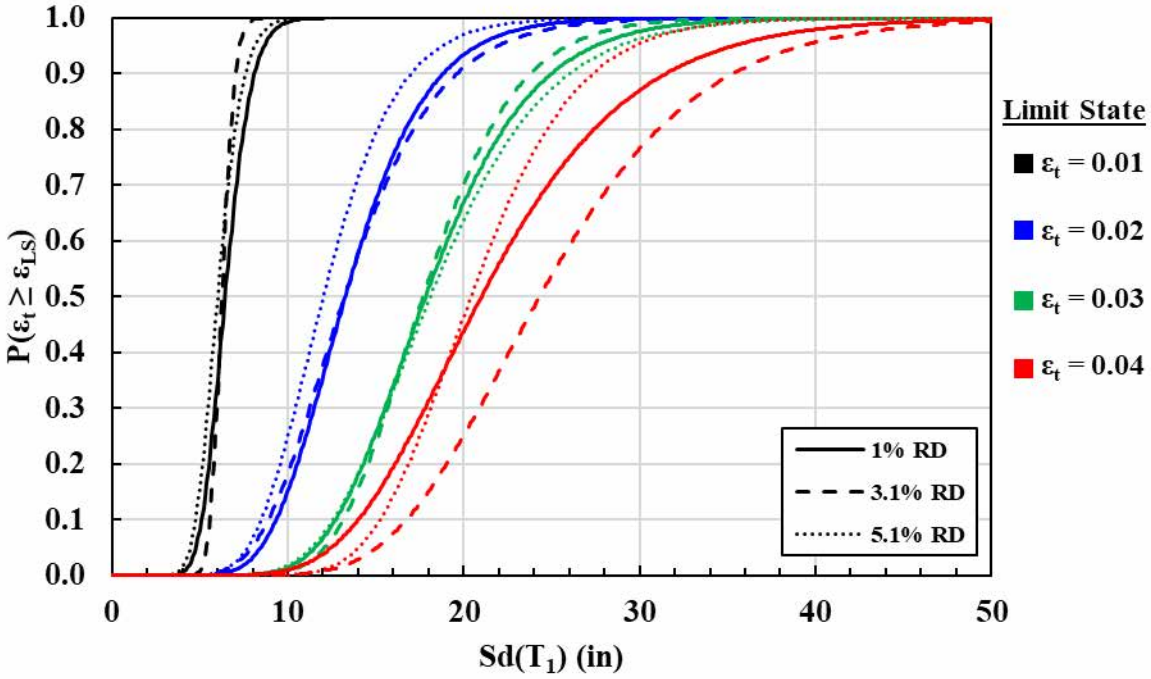

Figure B. 16: Limit state fragilities L/D = 4, ρ_l = 2.5%, ALR = 5%.

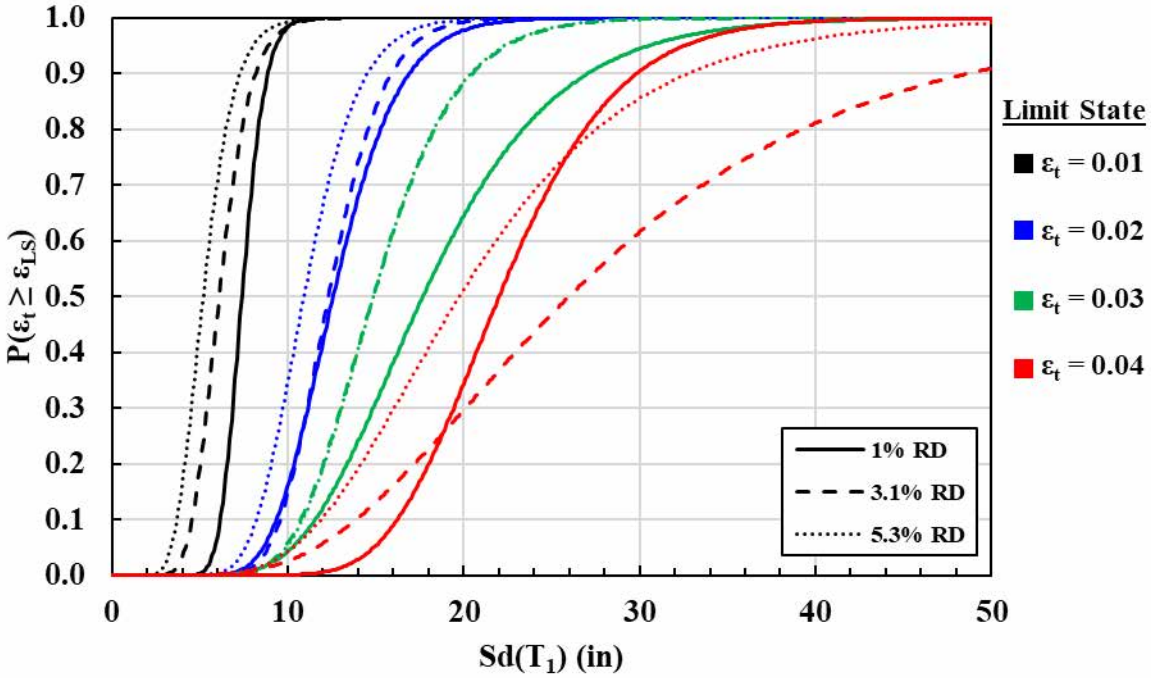

Figure B. 17: Limit state fragilities L/D = 4, ρ_l = 2.5%, ALR = 10%.

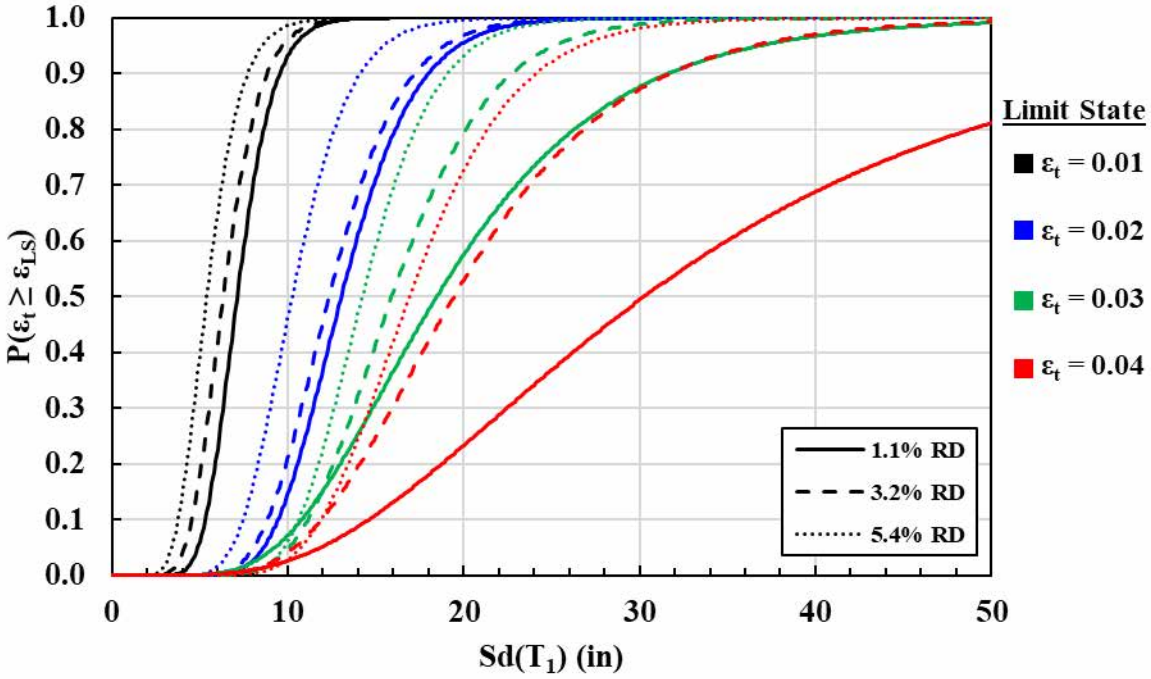

Figure B. 18: Limit state fragilities L/D = 4, ρ_l = 2.5%, ALR = 15%.

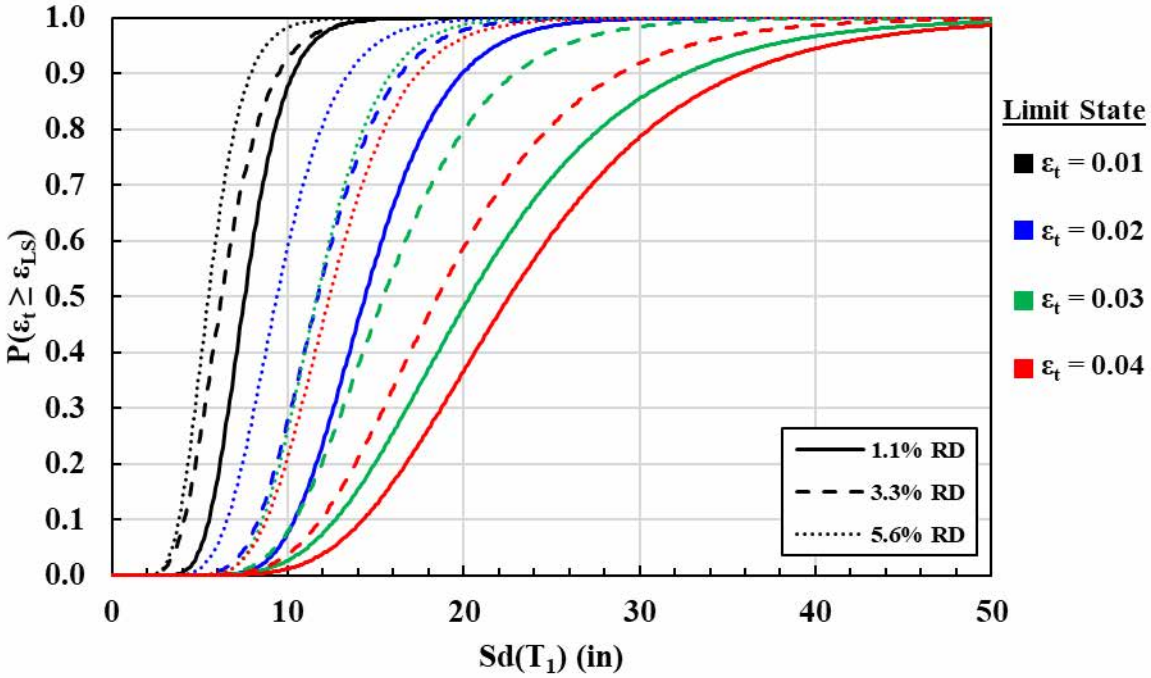

Figure B. 19: Limit state fragilities L/D = 4, ρ_l = 2.5%, ALR = 20%.

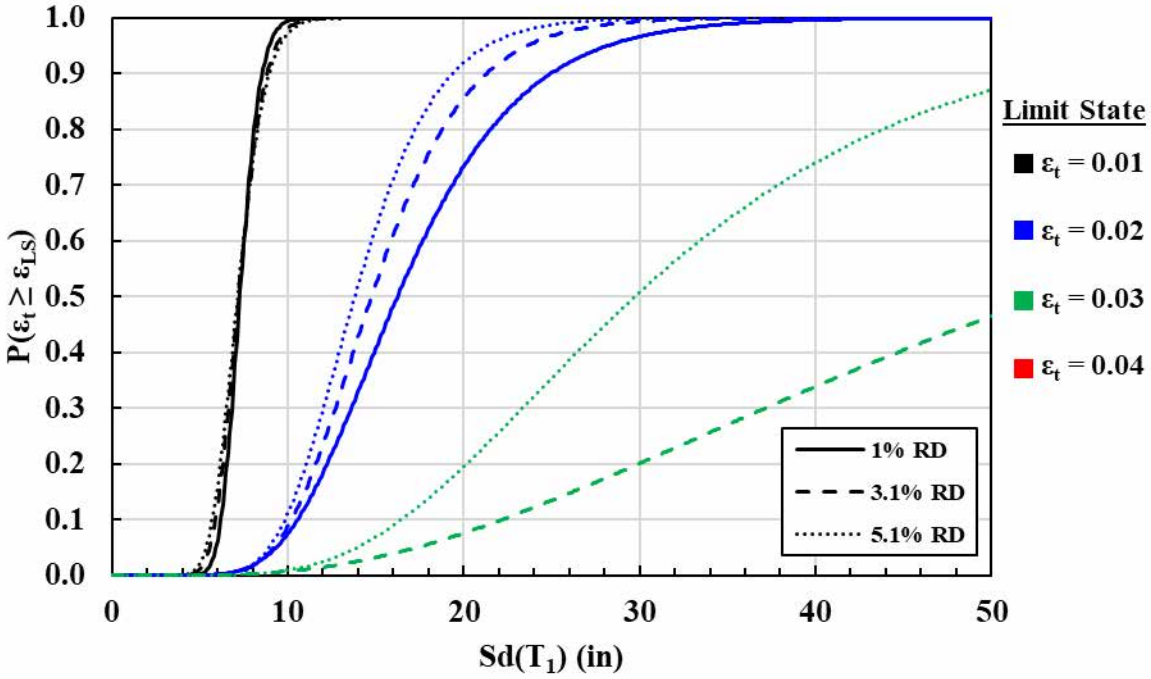

Figure B. 20: Limit state fragilities L/D = 4, ρ_l = 4.0%, ALR = 5%.

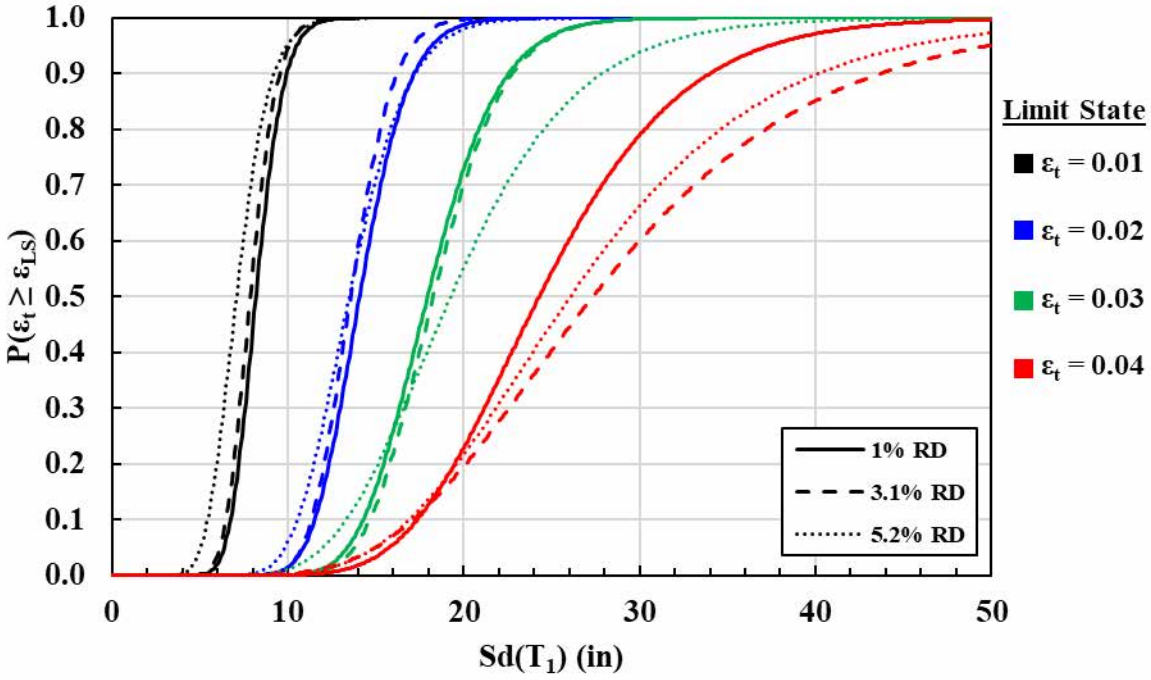

Figure B. 21: Limit state fragilities L/D = 4, ρ_l = 4.0%, ALR = 10%.

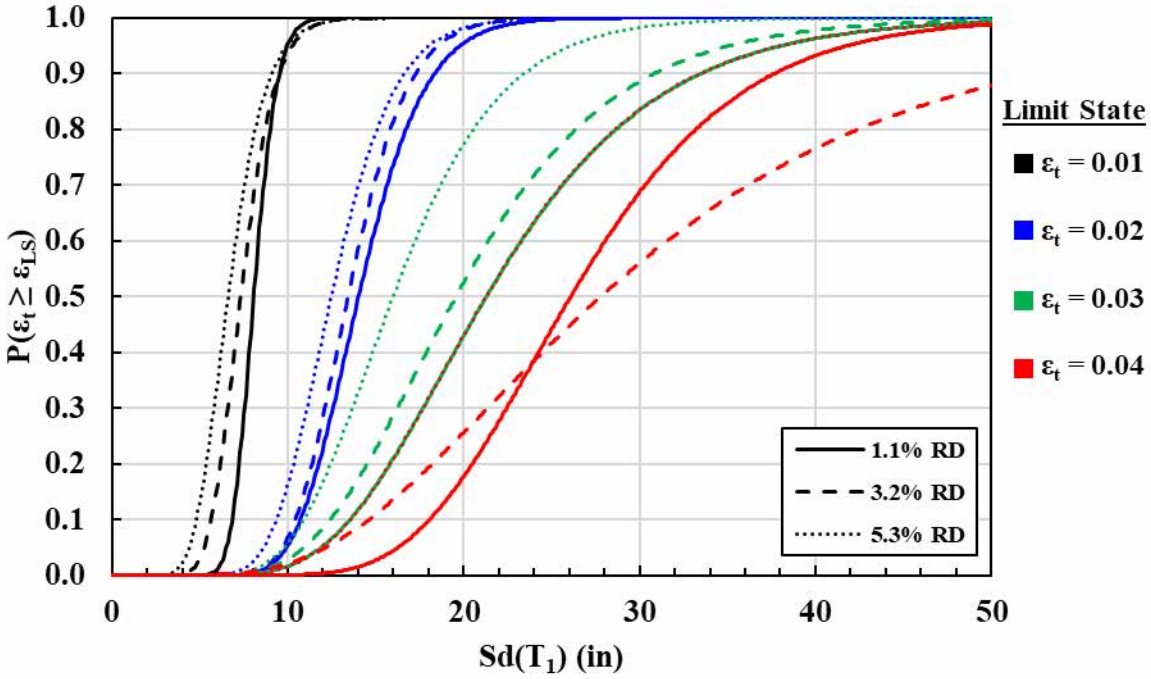

Figure B. 22: Limit state fragilities L/D = 4, ρ_l = 4.0%, ALR = 15%.

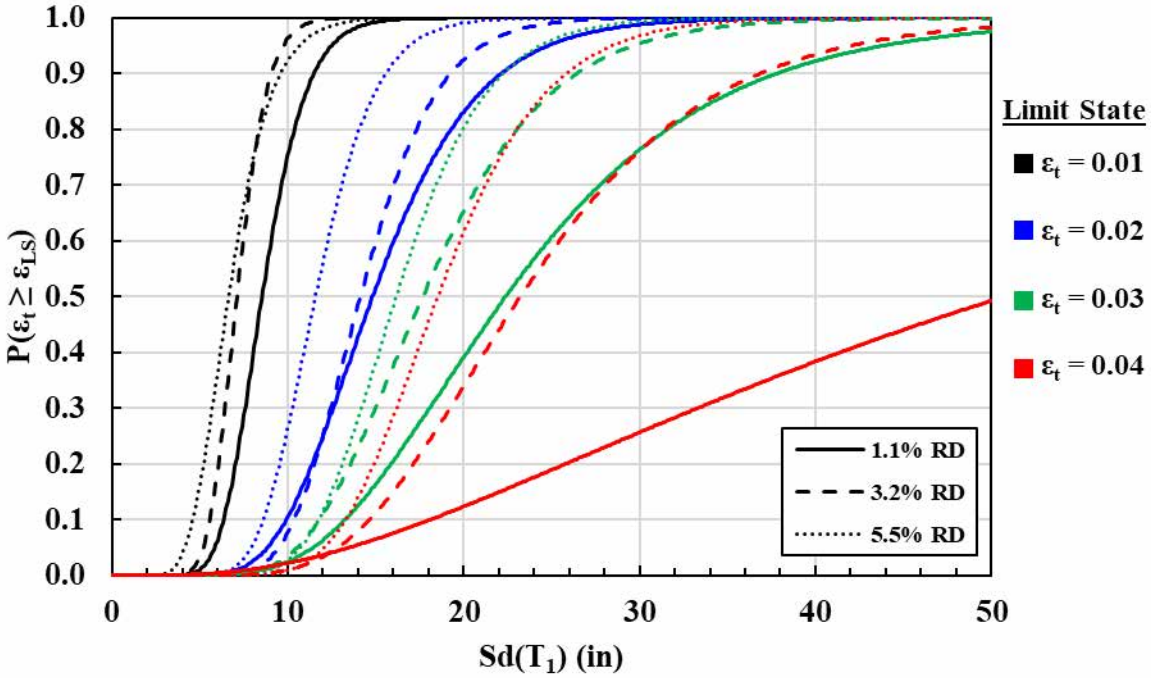

Figure B. 23: Limit state fragilities L/D = 4, ρ_l = 4.0%, ALR = 20%.

L/D Ratio = 6

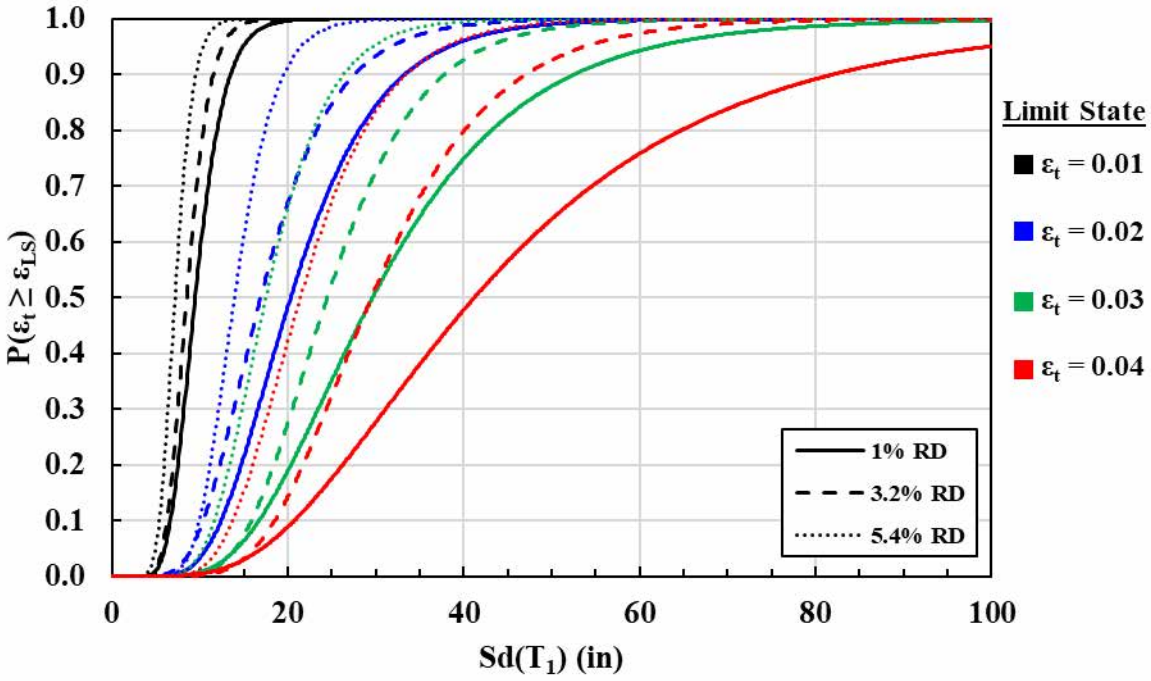

Figure B. 24: Limit state fragilities L/D = 6, ρ_l = 1.0%, ALR = 5%.

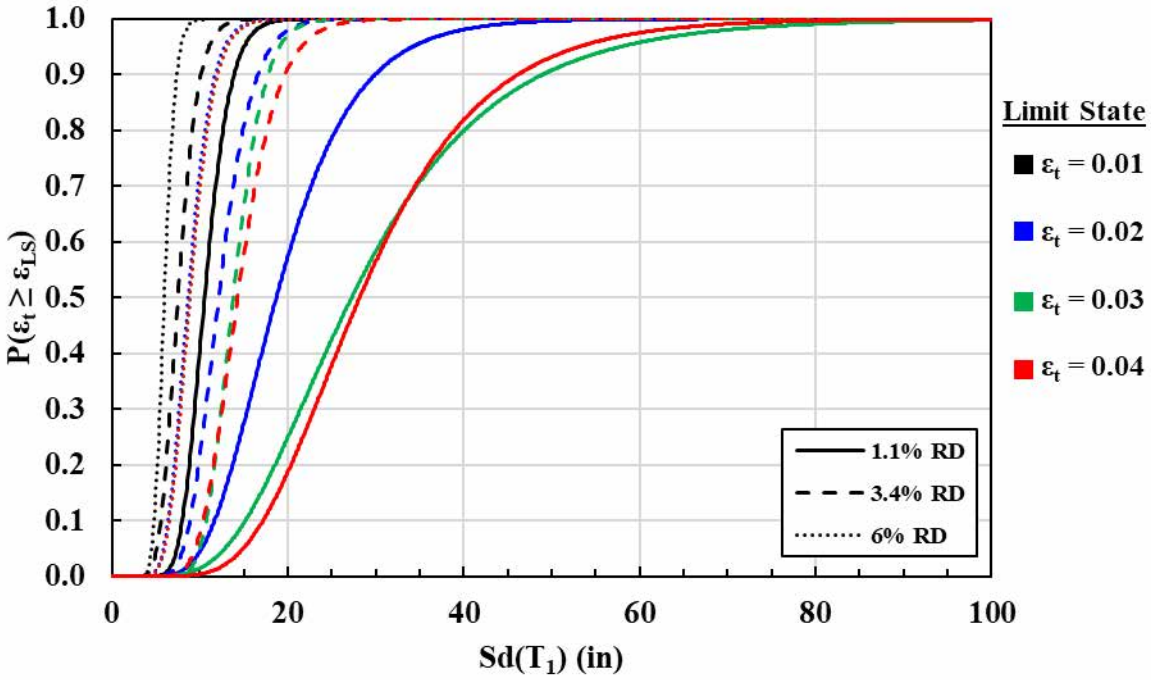

Figure B. 25: Limit state fragilities L/D = 6, ρ_l = 1.0%, ALR = 10%.

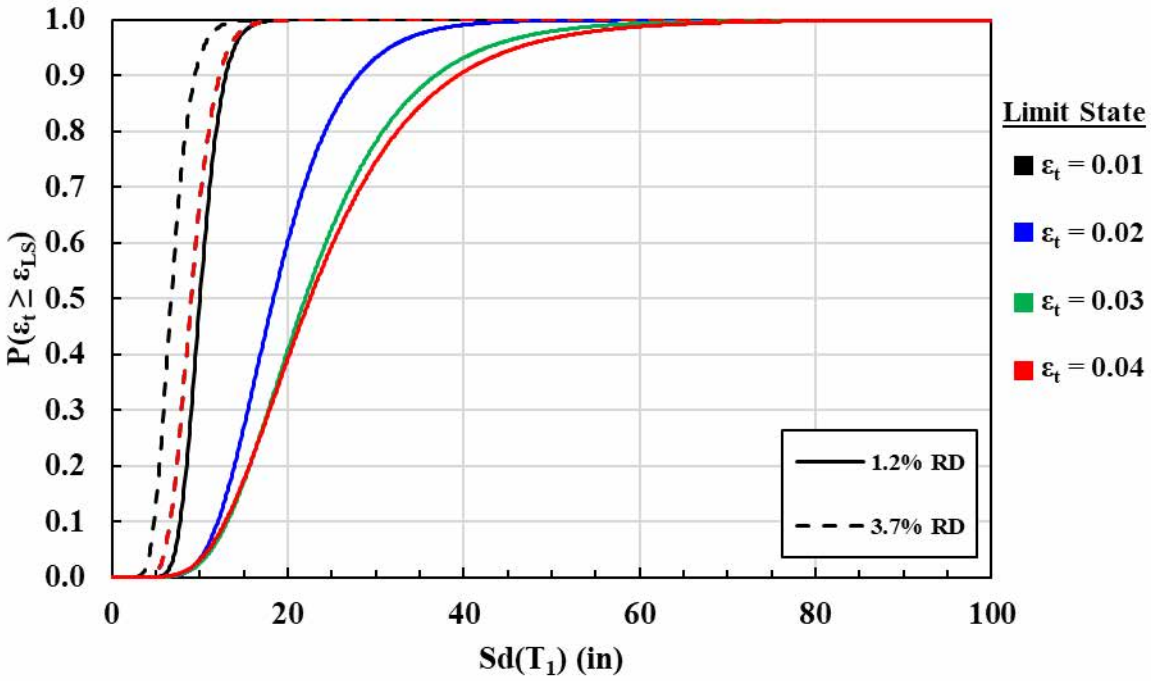

Figure B. 26: Limit state fragilities L/D = 6, ρ_l = 1.0%, ALR = 15%.

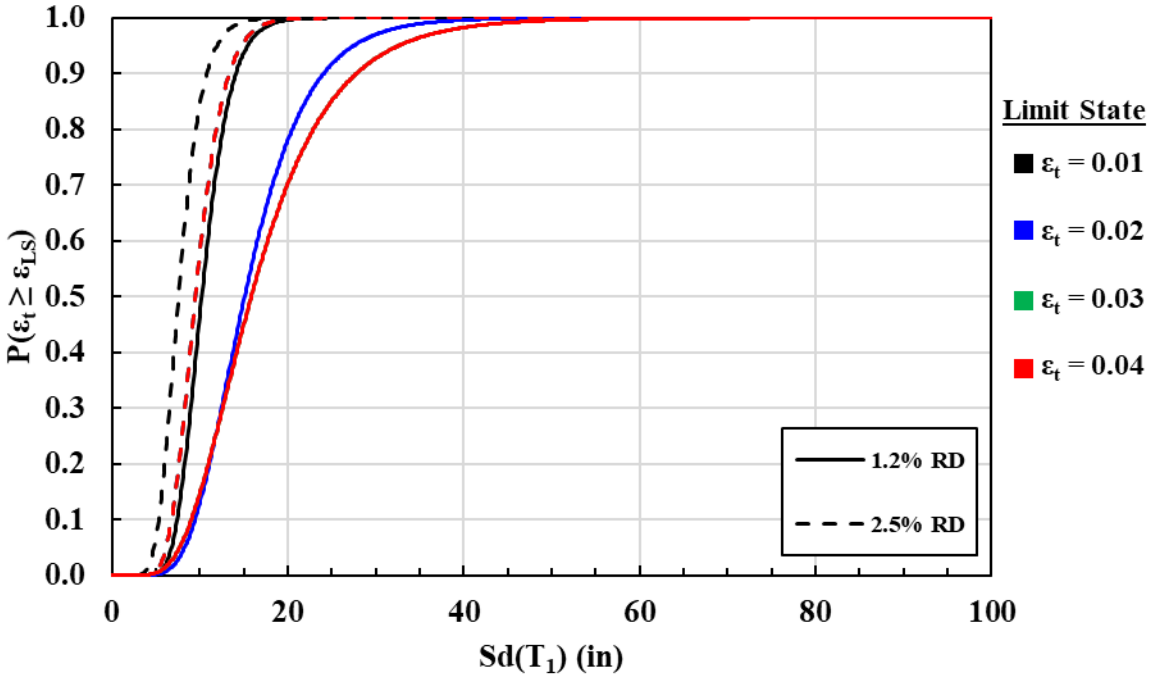

Figure B. 27: Limit state fragilities L/D = 6, ρ_l = 1.0%, ALR = 20%.

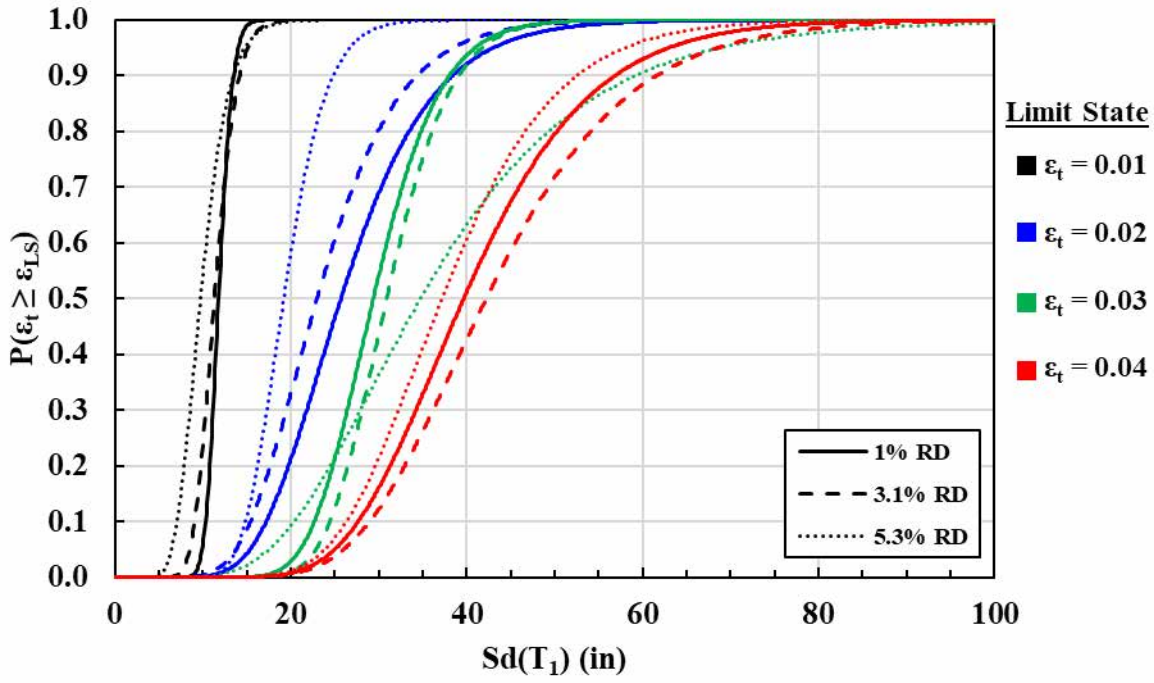

Figure B. 28: Limit state fragilities L/D = 6, ρ_l = 2.5%, ALR = 5%.

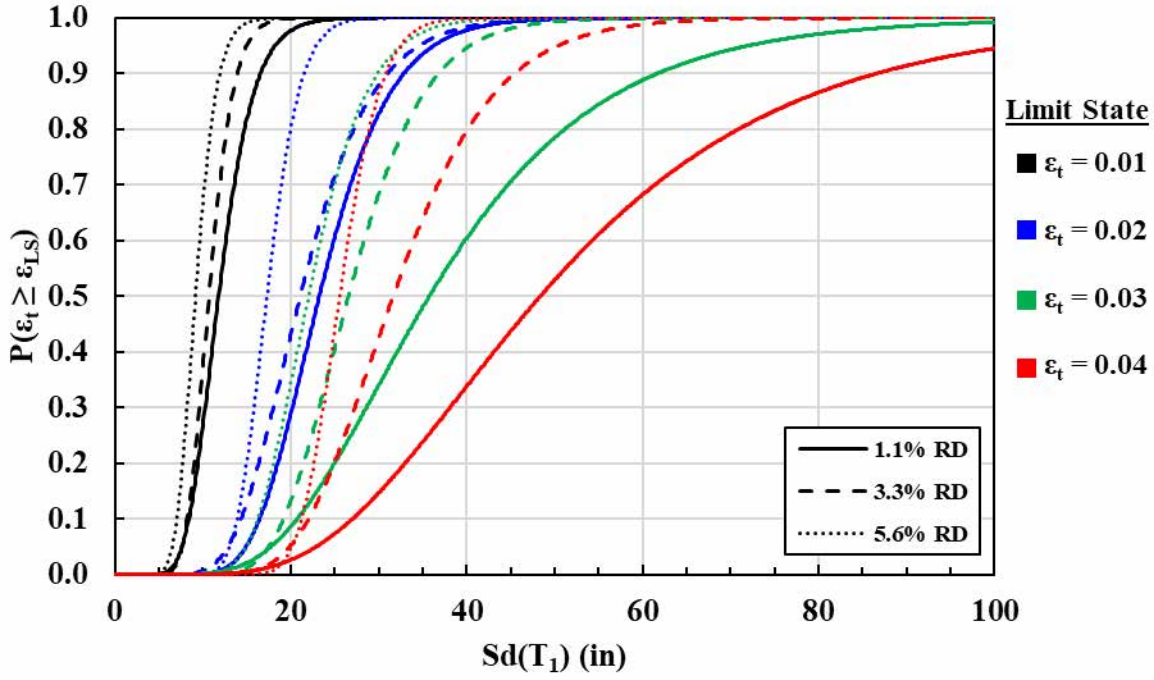

Figure B. 29: Limit state fragilities L/D = 6, ρ_l = 2.5%, ALR = 10%.

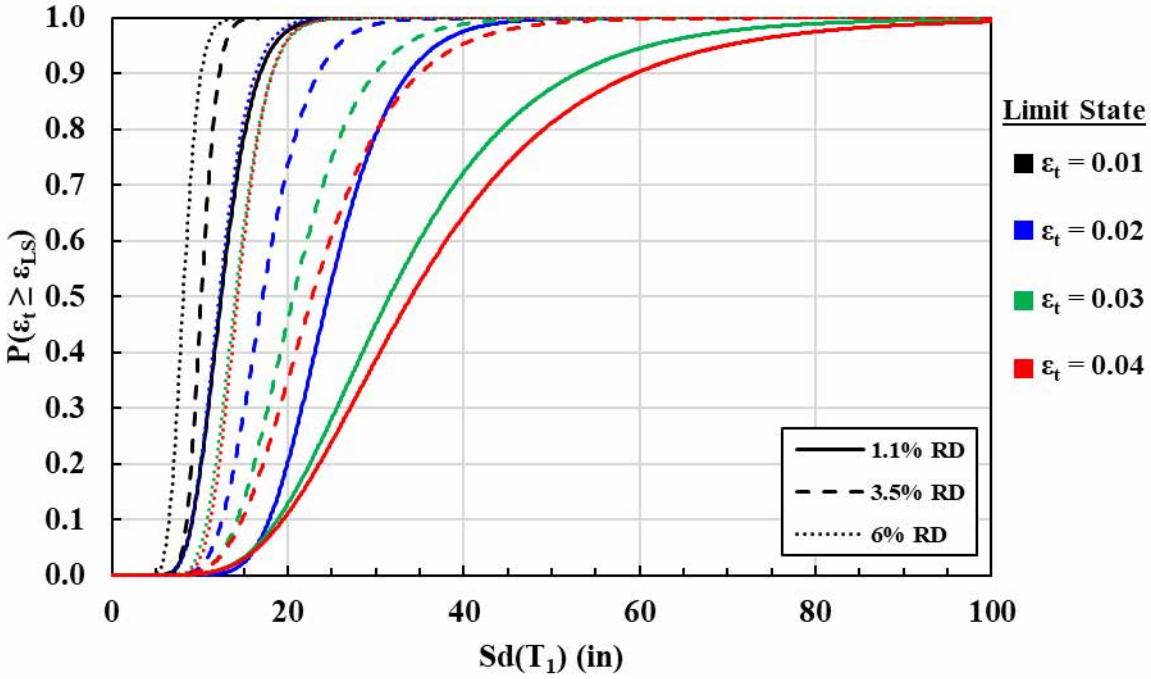

Figure B. 30: Limit state fragilities L/D = 6, ρ_l = 2.5%, ALR = 15%.

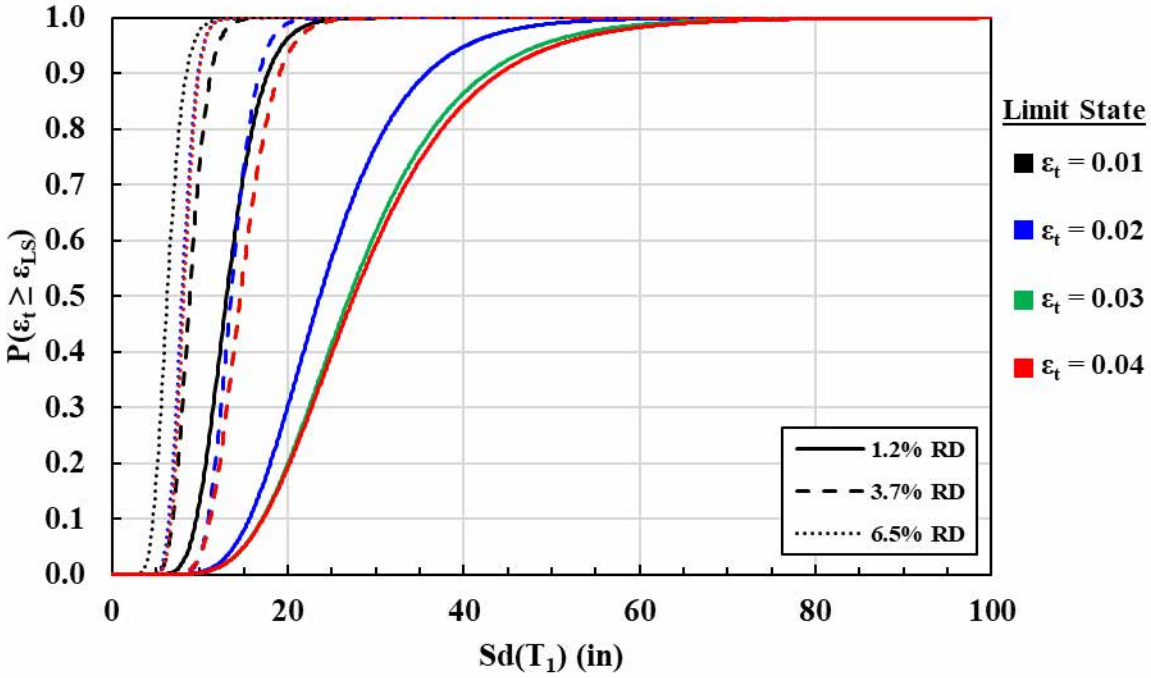

Figure B. 31: Limit state fragilities L/D = 6, ρ_l = 2.5%, ALR = 20%.

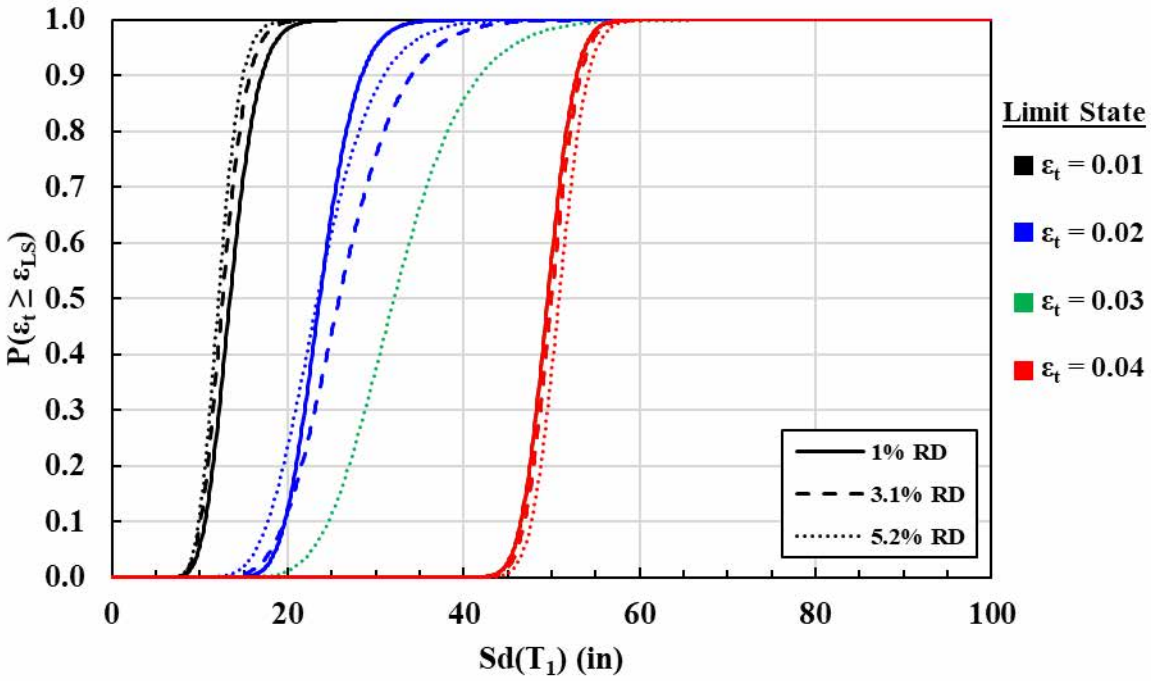

Figure B. 32: Limit state fragilities L/D = 6, ρ_l = 4.0%, ALR = 5%.

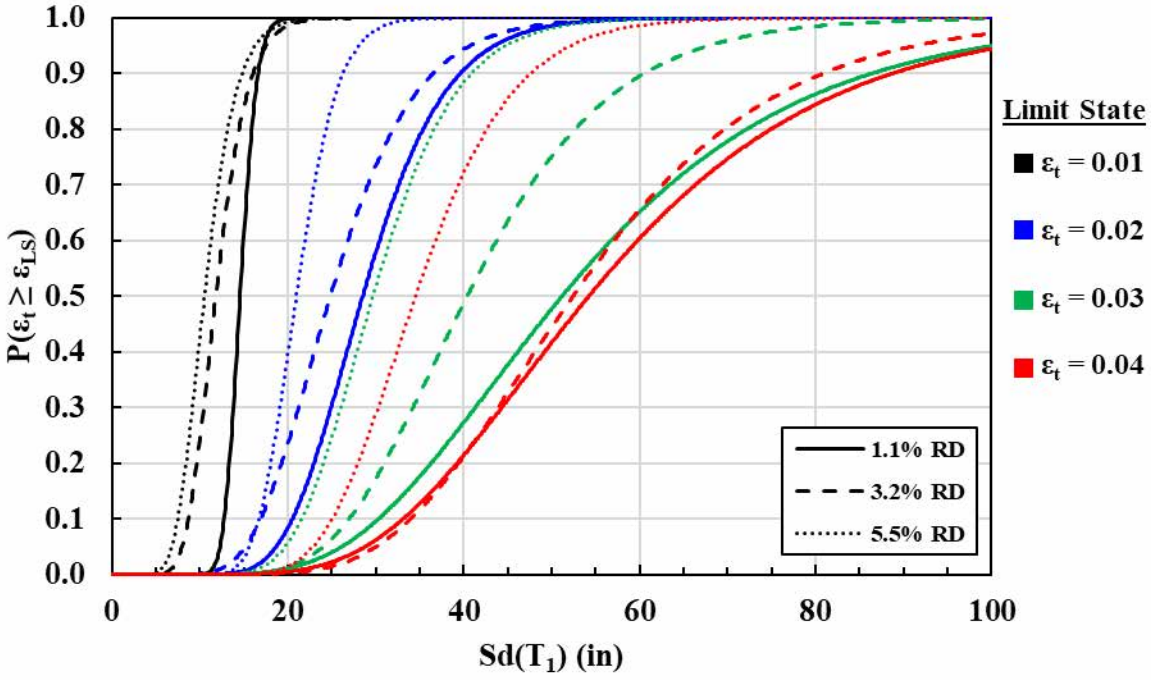

Figure B. 33: Limit state fragilities L/D = 6, ρ_l = 4.0%, ALR = 10%.

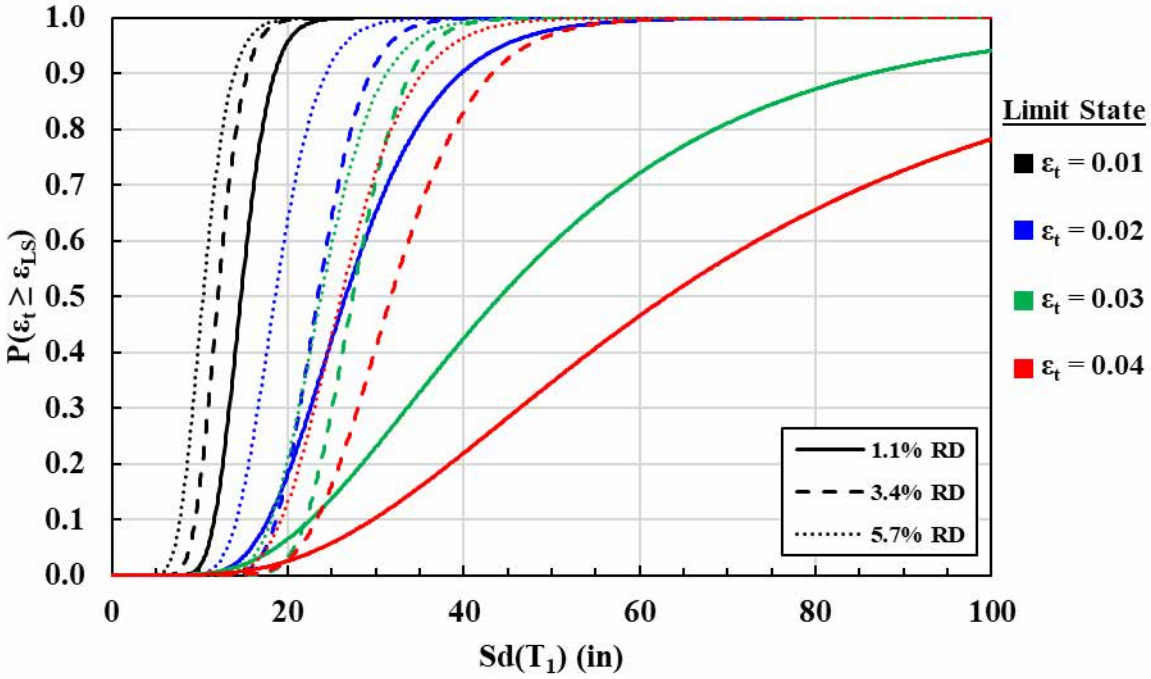

Figure B. 34: Limit state fragilities L/D = 6, ρ_l = 4.0%, ALR = 15%.

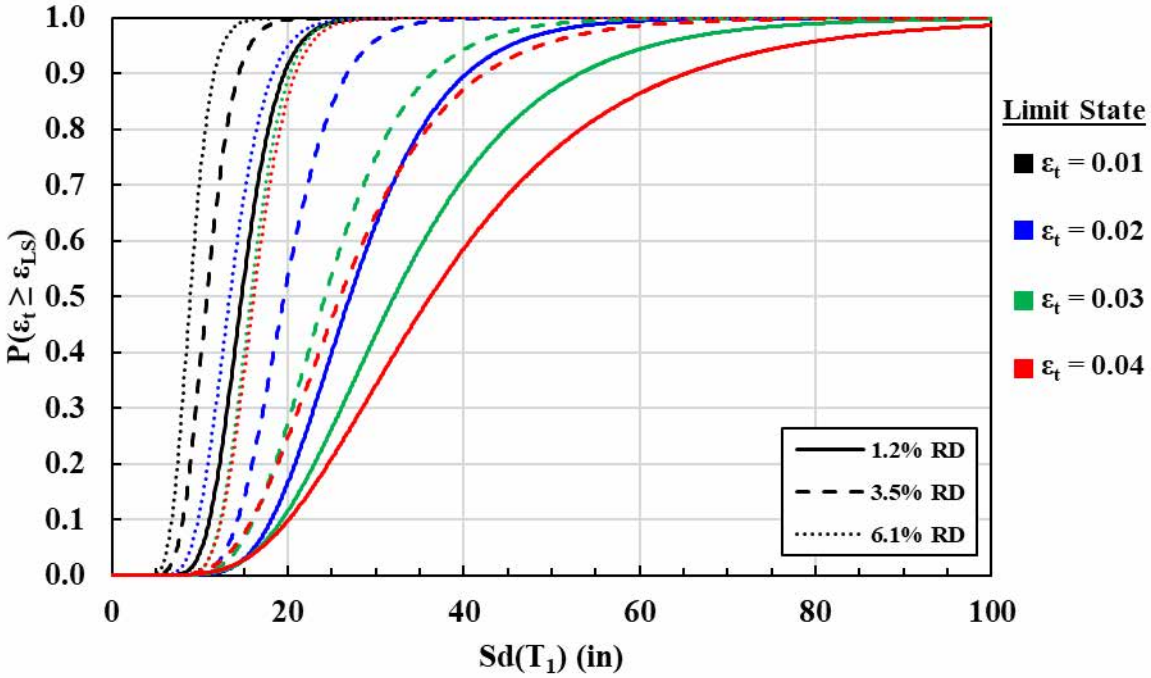

Figure B. 35: Limit state fragilities L/D = 6, ρ_l = 4.0%, ALR = 20%.

L/D Ratio = 8

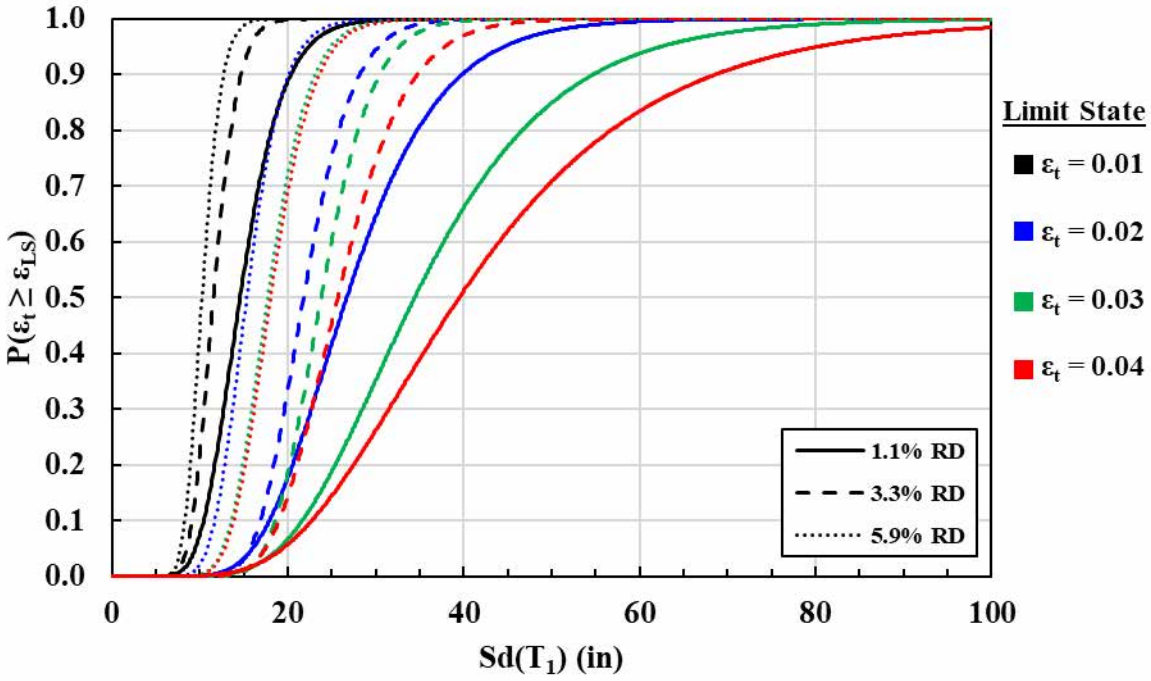

Figure B. 36: Limit state fragilities L/D = 8, ρ_l = 1.0%, ALR = 5%.

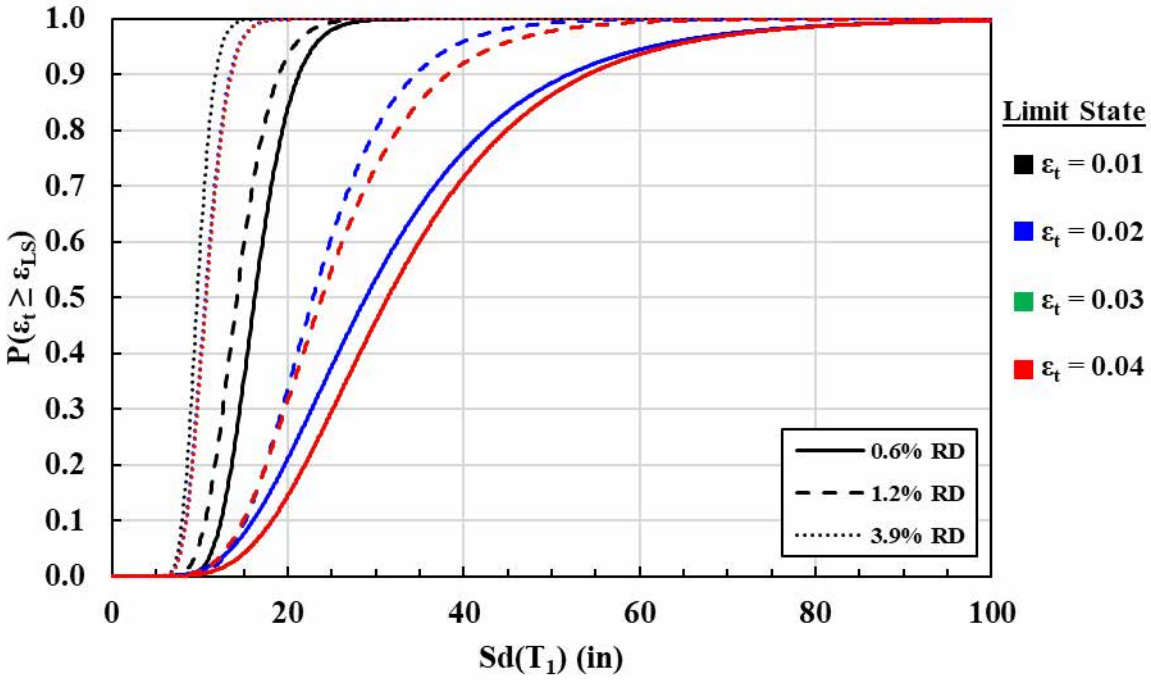

Figure B. 37: Limit state fragilities L/D = 8, ρ_l = 1.0%, ALR = 10%.

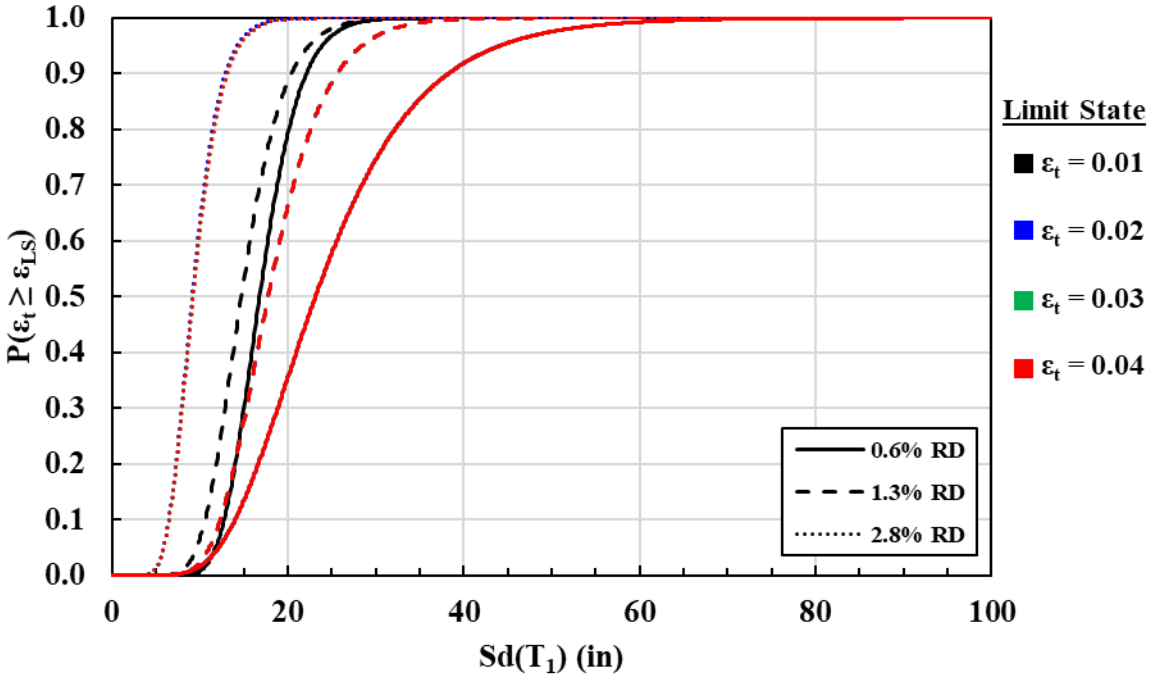

Figure B. 38: Limit state fragilities L/D = 8, ρ_l = 1.0%, ALR = 15%.

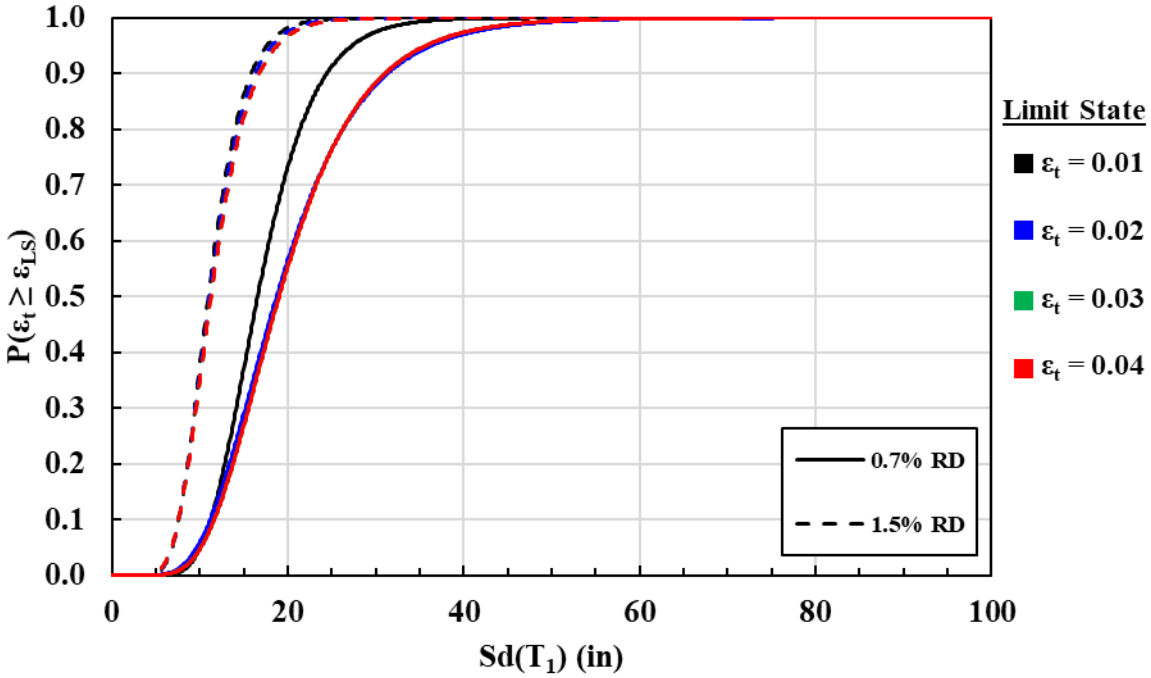

Figure B. 39: Limit state fragilities L/D = 8, ρ_l = 1.0%, ALR = 20%.

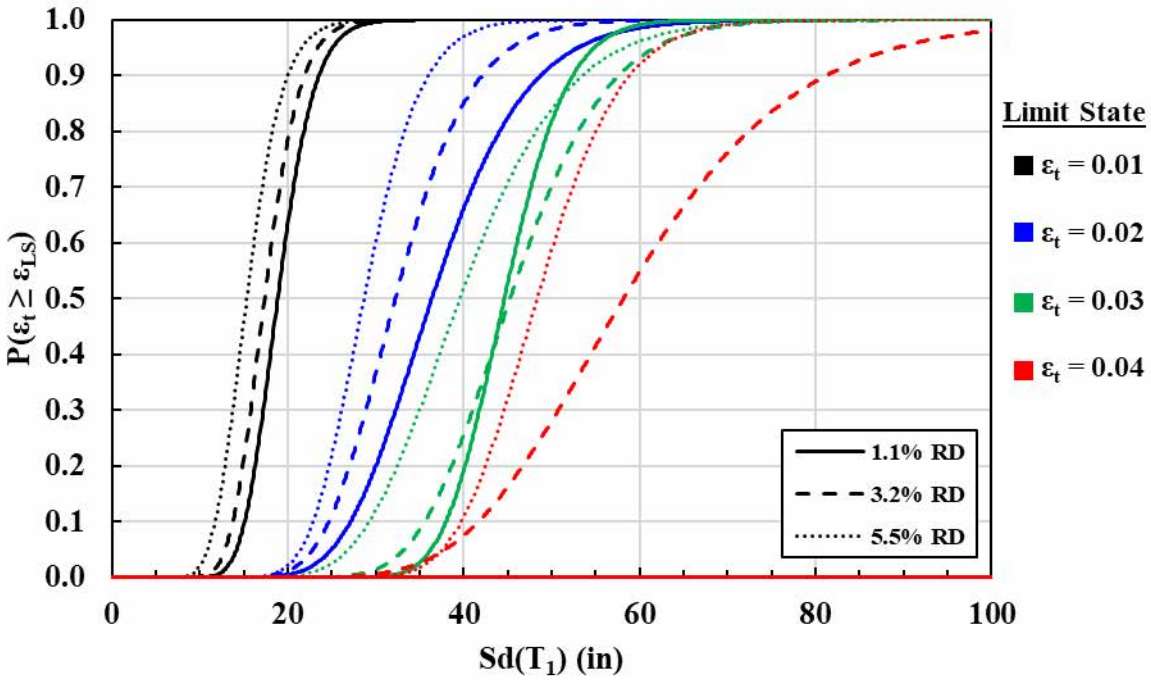

Figure B. 40: Limit state fragilities L/D = 8, ρ_l = 2.5%, ALR = 5%.

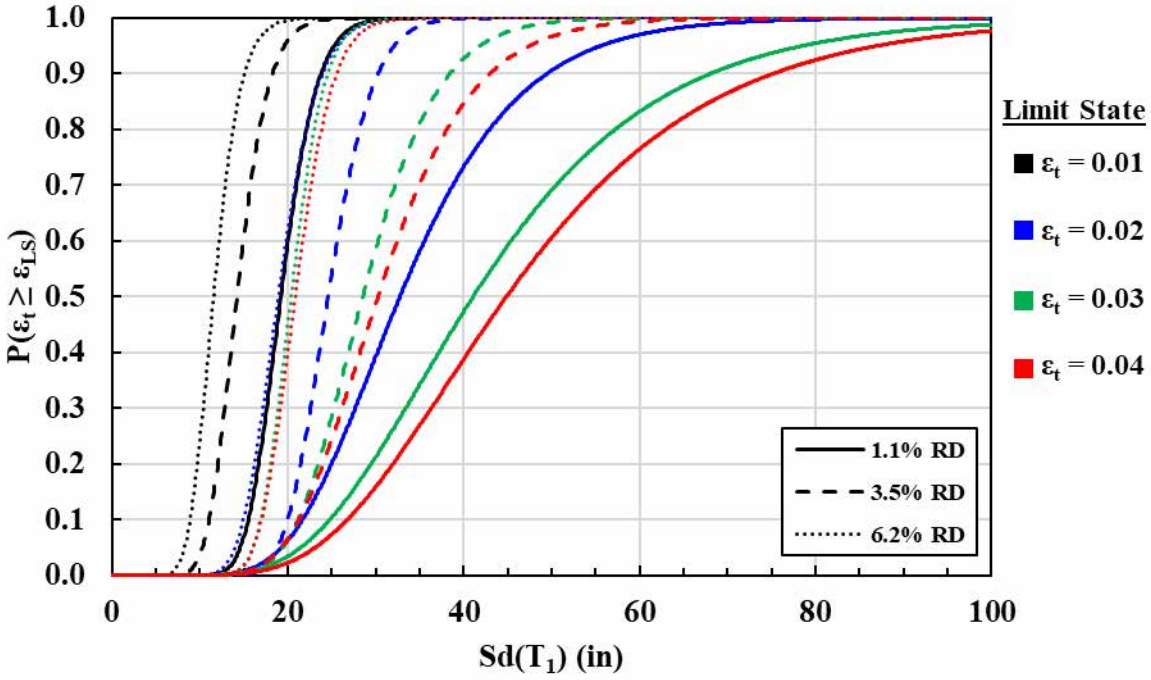

Figure B. 41: Limit state fragilities L/D = 8, ρ_l = 2.5%, ALR = 10%.

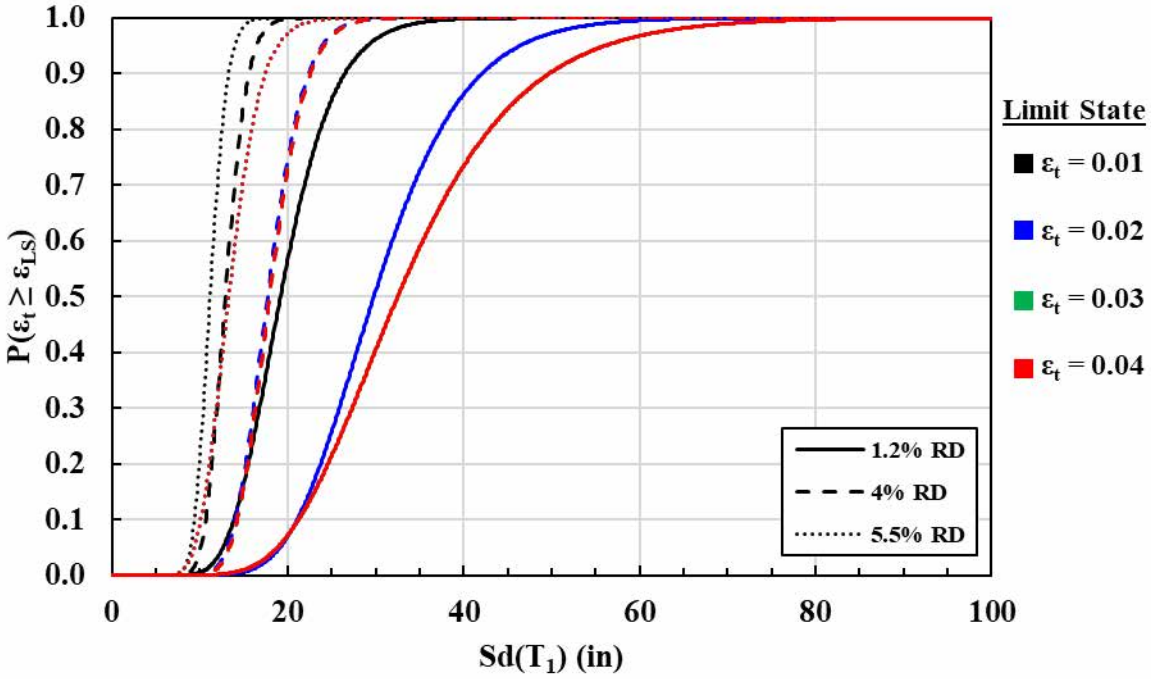

Figure B. 42: Limit state fragilities L/D = 8, ρ_l = 2.5%, ALR = 15%.

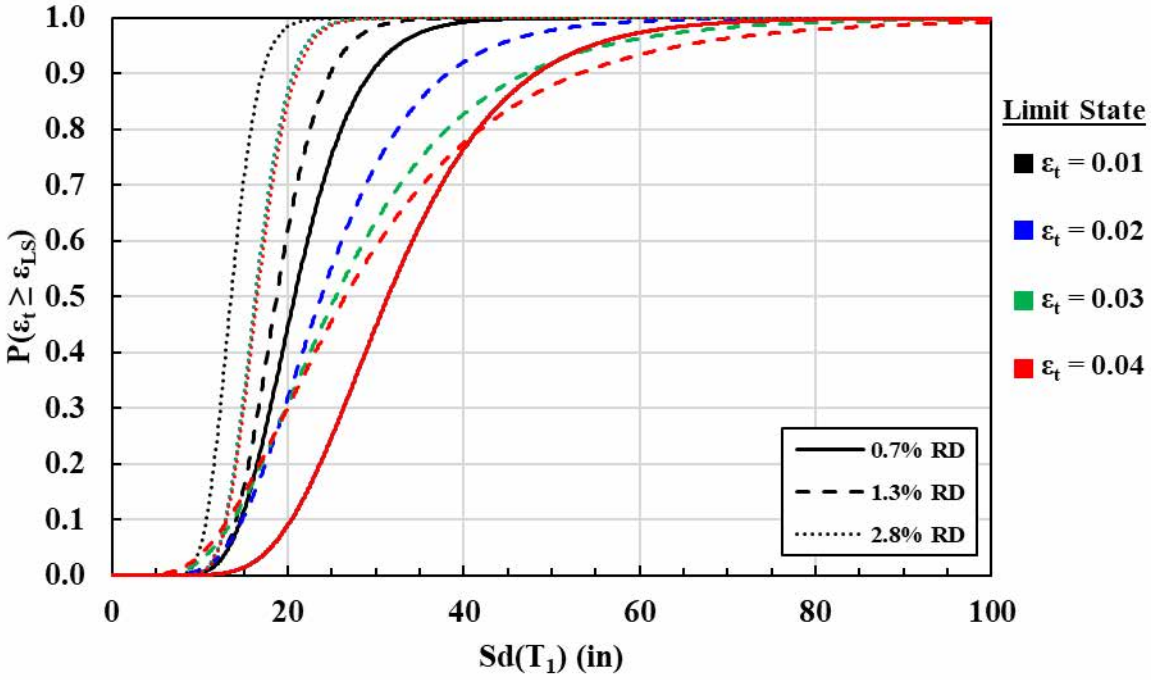

Figure B. 43: Limit state fragilities L/D = 8, ρ_l = 2.5%, ALR = 20%.

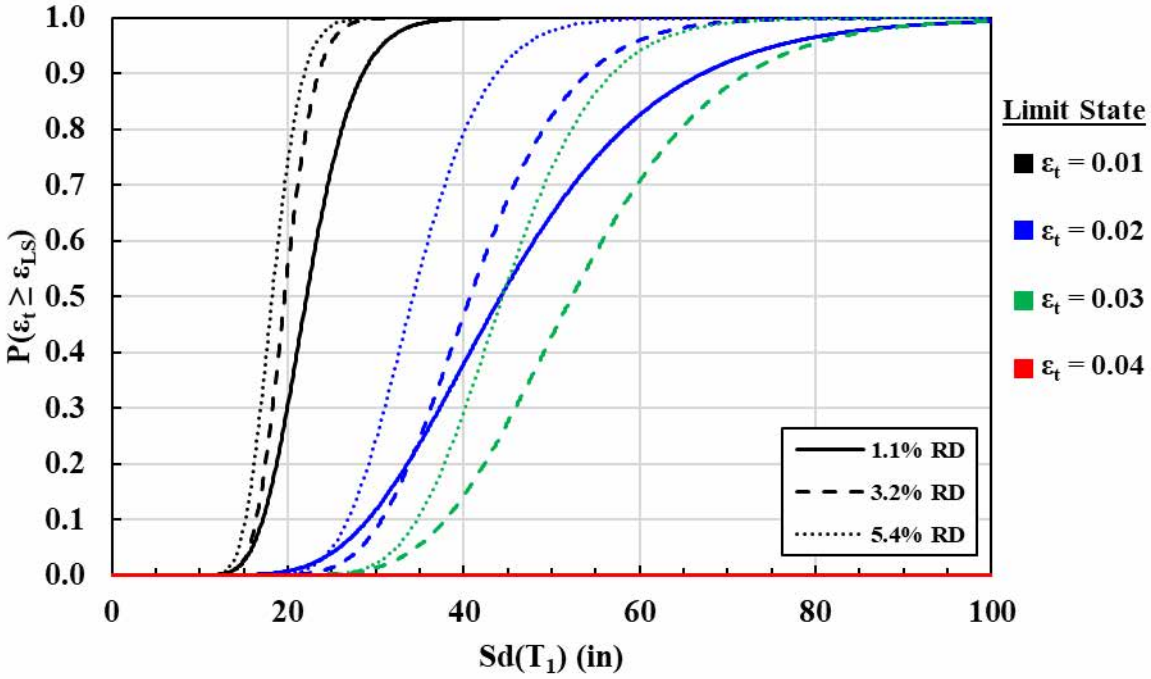

Figure B. 44: Limit state fragilities L/D = 8, ρ_l = 4.0%, ALR = 5%.

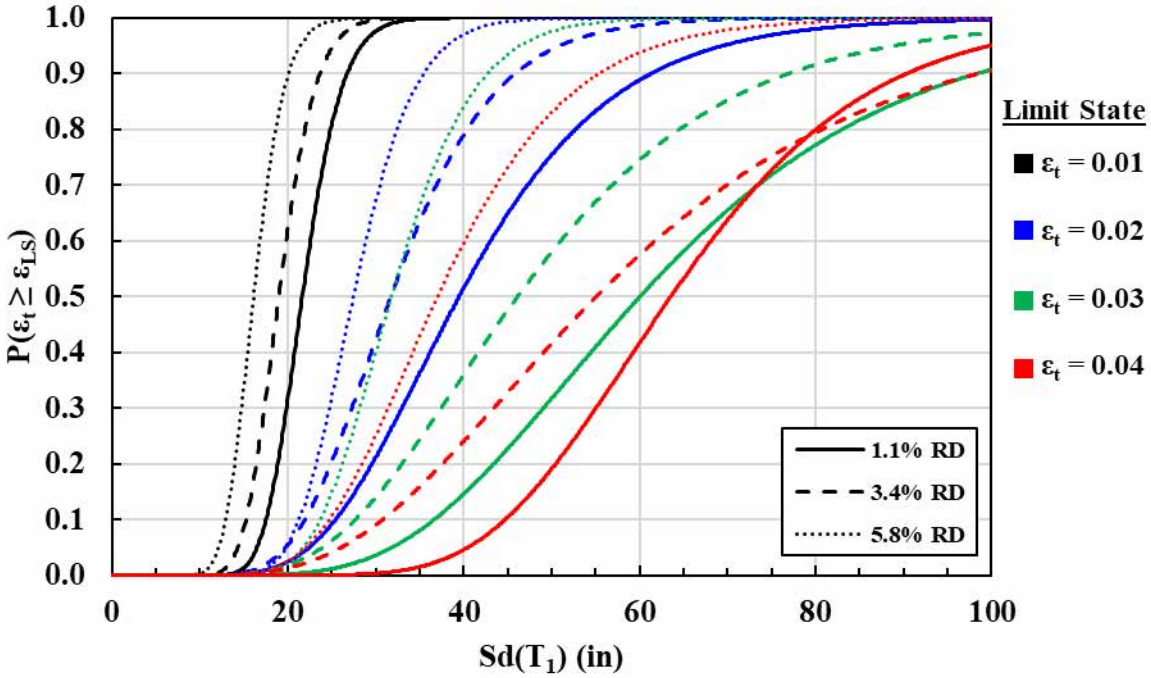

Figure B. 45: Limit state fragilities L/D = 8, ρ_l = 4.0%, ALR = 10%.

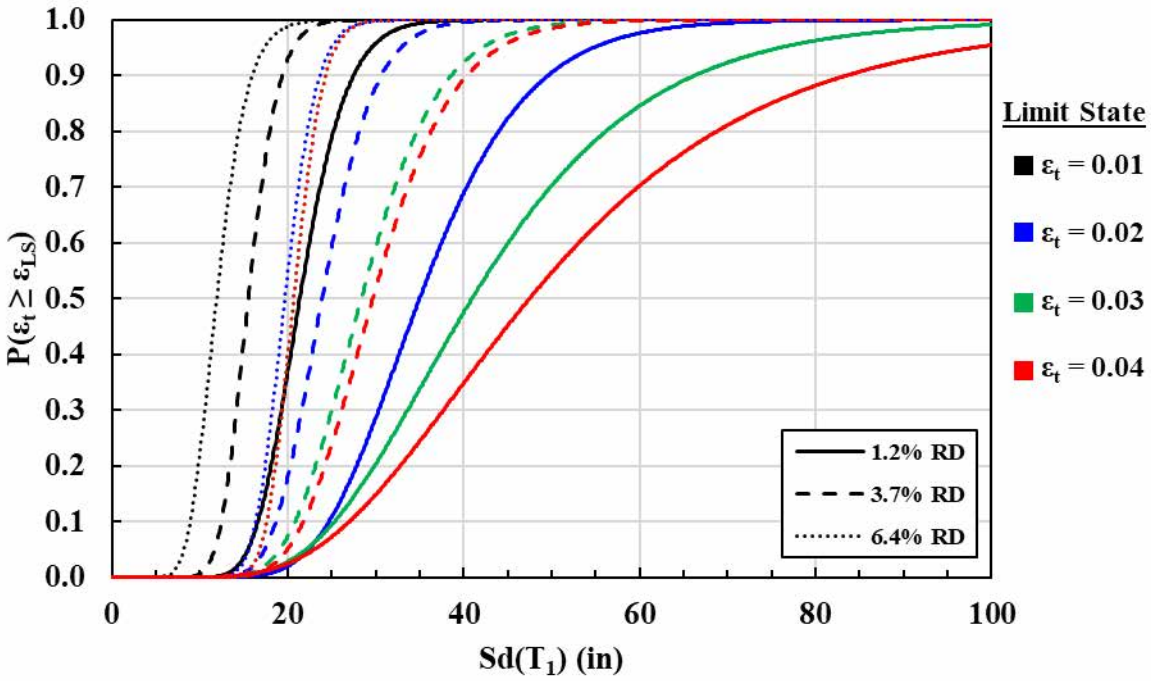

Figure B. 46: Limit state fragilities L/D = 8, ρ_l = 4.0%, ALR = 15%.

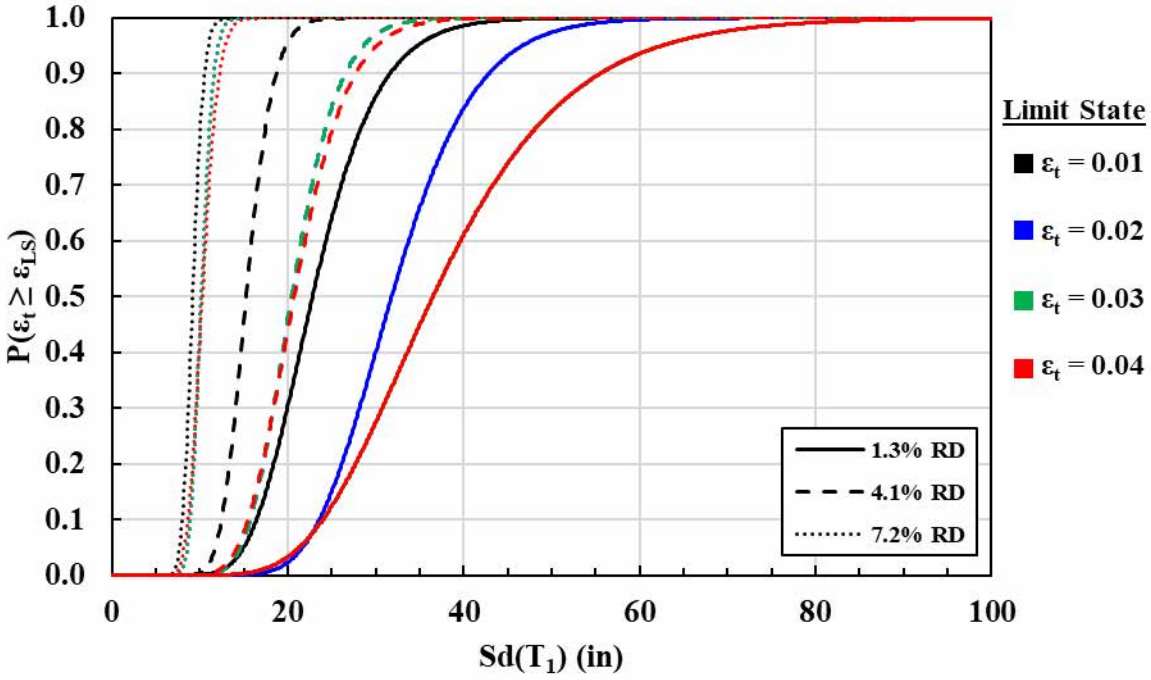

Figure B. 47: Limit state fragilities L/D = 8, ρ_l = 4.0%, ALR = 20%.